Technical University of Munich
TUM School of Engineering and Design

Geological and Geotechnical Evaluation of a Landslide Prone Slope in an Informal Settlement in Medellín, Colombia

Tamara Breuninger

Complete reprint of the dissertation approved by the TUM School of Engineering and Design of the Technical University of Munich for the award of the

Doktorin der Ingenieurwissenschaften (Dr.-Ing.)

Chair:

Prof. Dr. Michael Krautblatter

Examiners:

1. Prof. Dr. Kurosch Thuro
2. Prof. Dr. Christian Zangerl

The dissertation was submitted to the Technical University of Munich on 3 July 2024 and accepted by the TUM School of Engineering and Design on 1 October 2024.

Table of Contents

Abstract III
Zusammenfassung IV
Resumen V
List of Figures VI
List of Tables IX
Acknowledgements X
1 Motivation 1
1.1 Project Inform@Risk 1
1.2 Tasks and Problems 3
1.3 Aims 5
1.4 Project Work 5
2 Geography and Geology of the Project Area 7
2.1 Colombia 7
2.2 Medellín and the Aburrá Valley 7
2.3 Study Site Bello Oriente 12
3 State of the Art 14
3.1 Medellín Dunite 14
3.2 Landslides in the Aburrá Valley 15
3.3 Landslide Risk and Hazard Assessment 18
4 Methodology 21
4.1 Mapping of Past Landslides (Process Map) 21
4.2 Mapping of Geological Features (Geological Map) 21
4.3 Drillings 22
4.4 Joint Recording 22
4.5 ERT Measurements 23
4.6 Laboratory Tests 24
4.6.1 Uniaxial Compressive Strength Test 24
4.6.2 Brazilian Test 26
4.6.3 Grain Size Analysis 26
4.6.4 Atterberg Limits Analysis 28
4.6.5 Direct Shear Test 29
4.6.6 Thin Section Analysis of Dunites 29
4.6.7 X-Ray Diffractometry of Soil Samples 30
4.7 Underground Model 31
4.8 Hazard Assessment 31
4.9 Social Integration 32

5 Results and First Evaluation 34
5.1 Process Map 34
5.2 Geological Map 34
5.3 Drillings 37
5.3.1 Drilling A1 37
5.3.2 Drilling A2 38
5.3.3 Drilling B1 39
5.3.4 Drilling B2 40
5.4 Joint Record 41
5.5 ERT Measurements 43
5.5.1 ERT Transect BO-01 43
5.5.2 ERT Transect BO-03 45
5.5.3 ERT Transect BO-04 45
5.6 Laboratory Tests 48
5.6.1 Rock Tests 48
5.6.2 Soil Tests 50
5.6.3 Thin Section Analysis 57
5.6.4 XRD Analysis 60
5.7 Social Integration 62
6 Interpretation of Results 64
6.1 General Evaluation of the Results 64
6.2 Underground Model of the Study Site 66
6.2.1 Visual Interpretation of ERT Transects 66
6.2.2 Colluvial Map 70
6.3 Hazard Assessment 70
6.3.1 Characterization of Events 72
6.3.2 Hazard Map 75
7 Discussion 80
7.1 Underground Model 80
7.2 Hazard Assessment 86
8 Conclusion 90
9 Outlook and Future of the Project 93
Bibliography 95
Standards 100
Internet Sources 101
Annex 103

Abstract

The project Inform@Risk was aiming towards a landslide early warning and evacuation system in the informal settlements of the city of Medellín, which have been subject to several fatal landslide events in the last decades. In order to cover the events properly with this early warning system, the study site Bello Oriente was investigated thoroughly regarding (1) the subsurface conditions promoting landslide events, (2) the landslide dynamics typical for the study site, and (3) the areas with the highest hazard potential. This information was obtained by (1) determining the geological composition of the study site, (2) determining the geotechnical parameters of the subsurface, (3) determining the geotechnical behavior of the landslides in the study site, and (4) determining high hazard areas on the basis of these three factors. Additionally, due to the dense population of the study site, the development of trust among the community in the project, the scientists and the early warning system itself was vital.

The study site Bello Oriente is located in the geological unit of the Medellín Dunite, an ultramafic, ophiolitic body, formed in the Triassic. It has been altered significantly and can, therefore, not be categorized as a dunite, but rather a serpentinite. This alteration and the long tectonic history, causing extreme fracturing of the rock, have led to the rock being highly disintegrated and deeply weathered, making it the most landslide prone unit in the city of Medellín and the region.

To achieve the scientific goals, several direct and indirect methods were applied. Mappings of the geological and process characteristics were conducted, as well as four drillings, joint recordings on the surface, four geoelectric measurements (ERT) and several laboratory tests on rock and soil samples from the drillings and the surface.

All investigations found a very heterogenic composition of the subsurface regarding mineralogy, structure, and weathering. The presence of the phenomenon pseudokarst, already observed by other investigations in different parts of the Medellín Dunite, was obvious from the cavities encountered in the drillings, the high amount of soil in depths of up to 50 m, and the degree of disintegration of seemingly unaltered rock. This heterogeneity was visualized in three subsurface profiles and a colluvial thickness map, using the information from the geological mapping, the drillings and the geoelectric (ERT) transects.

The landslides in the study site were characterized as shallow to mid-seated (max. 10 m depth) and having a maximum area of 15,000 m² on the surface. It was not expected for a larger event to occur in the study site. Therefore, the categorization of the events used the biggest event (approx. 15,000 m²) as the maximum magnitude of a 100 year event. Events of a size up to 4,000 m² were categorized as 30 year events, while events > 15,000 m² were categorized as residual hazard. The hazard areas of all three magnitudes were visualized in three magnitude hazard maps; a synthesis map, depicting all three magnitudes at once, was the final hazard map for the study site. This map was used for an optimal distribution of the sensor system in the study site and to develop evacuation routes and safe areas.

A vital aspect during the course of the project was the social integration of the system into the community in Bello Oriente. In addition to several workshops held by project partners regarding landslides, risk and early warning and community walks in the neighborhood, all scientific and technical operations in the study site were conducted with the assistance and knowledge of voluntaries from the community. The installation of most of the equipment of the early warning system was done with the community members as employees of the construction company responsible. These expressions of mutual trust led to a comfortable working environment for all parties involved and has prevented vandalism on the sensor system until now.

Zusammenfassung

Das Projekt Inform@Risk verfolgte das Ziel, ein Frühwarn- und Evakuierungssystem für Hangbewegungen in den informellen Siedlungen der Stadt Medellín einzurichten, in denen es in den letzten Jahrzehnten zu mehreren Hangbewegungen mit Todesfolge gekommen ist. Um die Ereignisse mit diesem Frühwarnsystem angemessen erfassen zu können, wurde das Untersuchungsgebiet Bello Oriente ausführlich untersucht, hinsichtlich (1) der Untergrundbedingungen, die Hangbewegungen begünstigen, (2) der für das Untersuchungsgebiet typischen Hangbewegungsdynamik und (3) der Gebiete mit dem höchsten Gefährdungspotenzial. Diese Informationen wurden gewonnen, indem (1) die geologische Beschaffenheit des Untersuchungsgebiets bestimmt wurde, (2) die geotechnischen Parameter des Untergrunds ermittelt wurden, (3) das geotechnische Verhalten der Hangbewegungen im Untersuchungsgebiet bestimmt wurde und (4) die Gebiete mit dem höchsten Gefährdungspotenzial auf der Grundlage dieser drei Faktoren ermittelt wurden. Aufgrund der dichten Besiedlung des Untersuchungsgebiets war es außerdem von entscheidender Bedeutung, das Vertrauen der Bevölkerung in das Projekt, die Wissenschaftler und das Frühwarnsystem selbst zu stärken.

Das Untersuchungsgebiet Bello Oriente befindet sich in der geologischen Einheit des Medellín-Dunits, einem ultramafischen, ophiolitischen Gesteinskörper aus der Trias. Er erfuhr starke Umwandlung und kann daher nicht als Dunit, sondern muss eher als Serpentinit eingestuft werden. Diese Umwandlung und die lange tektonische Geschichte, die zu einer extremen Zerlegung des Gesteins geführt hat, hatten zur Folge, dass das Gestein bis in hohe Tiefen verwittert ist, was den Medellín Dunit zur Einheit mit dem höchsten Potential für Hangbewegungen in der Stadt Medellín und der Region macht.

Um die wissenschaftlichen Ziele zu erreichen, wurden mehrere direkte und indirekte Methoden angewandt: Kartierung der geologischen Eigenschaften und Prozesse, vier Bohrungen, Kluftaufnahmen an der Oberfläche, vier Geoelektrik-Messungen (ERT) und mehrere Laboruntersuchungen an Gesteins- und Bodenproben aus den Bohrungen und von der Oberfläche.

Alle Untersuchungen ergaben eine sehr heterogene Zusammensetzung des Untergrundes in Bezug auf Mineralogie, Struktur und Verwitterung. Das Phänomen Pseudokarst, das bereits bei Untersuchungen in anderen Abschnitten des Medellín-Dunits beobachtet wurde, wurde durch die in den Bohrungen entdeckten Hohlräume, die große Menge an Boden in Tiefen von bis zu 50 m und den Grad der Zerlegung von scheinbar unverwittertem Gestein deutlich. Diese Heterogenität wurde anhand der Informationen aus der geologischen Kartierung, den Bohrungen und den ERT-Profilen in drei Untergrundprofilen und einer Mächtigkeitskarte des Verwitterungsmaterials (Kolluvium) dargestellt.

Die Hangbewegungen im Untersuchungsgebiet wurden als flach- bis mittelgründig (max. 10 m Tiefe) und mit einer maximalen Fläche von 15.000 m² an der Oberfläche charakterisiert. Es wurde nicht erwartet, dass im Untersuchungsgebiet ein größeres Ereignis auftritt. Daher wurde bei der Kategorisierung der Ereignisse das größte Ereignis (ca. 15.000 m²) als maximales Ausmaß eines 100-jährigen Ereignisses ausgewiesen. Ereignisse mit einer Größe von bis zu 4.000 m² wurden als 30-jährige Ereignisse eingestuft, während Ereignisse > 15.000 m² als Residualgefahr eingestuft wurden. Die Gefährdungsgebiete aller drei Größenordnungen wurden in drei Gefährdungskarten dargestellt. Eine Synthesekarte, die alle drei Größenordnungen zusammen darstellt, wurde als finale Gefährdungskarte erstellt. Diese Karte wurde für eine optimale Verteilung des Sensorsystems im Untersuchungsgebiet und für die Entwicklung von Evakuierungsrouten und Sicherheitsbereichen verwendet.

Ein wichtiger Aspekt im Verlauf des Projekts war die soziale Integration des Systems in die Gemeinschaft in Bello Oriente. Zusätzlich zu mehreren Workshops, die von den Projektpartnern zu den Themen Hangbewegungen, Risiko und Frühwarnung abgehalten wurden, und zu Exkursionen im Gebiet wurden alle wissenschaftlichen und technischen Arbeiten im Untersuchungsgebiet mit der Unterstützung und dem Wissen von Freiwilligen aus der Gemeinde durchgeführt. Bei der Installation des Equipments des Frühwarnsystems waren die Gemeindemitglieder als Mitarbeiter der verantwortlichen Baufirma angestellt. Dieser Ausdruck des gegenseitigen Vertrauens führte zu einem angenehmen Arbeitsumfeld für alle Beteiligten und verhinderte Vandalismus am Sensorsystem bis heute.

Resumen

El proyecto Inform@Risk tiene como objetivo crear un sistema de alerta temprana y evacuación por deslizamientos en los asentamientos informales de la ciudad de Medellín, que han sufrido varios deslizamientos mortales en las últimas décadas. Con el fin de cubrir adecuadamente los eventos con este sistema de alerta temprana, el sitio de estudio Bello Oriente fue investigado a fondo con respecto a (1) las condiciones del subsuelo que promueven los eventos de deslizamiento, (2) la dinámica de deslizamiento del sitio de estudio, y (3) las áreas con mayor potencial de amenaza. Esta información se obtuvo (1) determinando la composición geológica del sitio de estudio, (2) determinando los parámetros geotécnicos del subsuelo, (3) determinando el comportamiento geotécnico de los deslizamientos en el sitio de estudio, y (4) determinando las zonas de alto amenaza en función de estos tres factores. Además, debido a la densa población del sitio de estudio, era vital el desarrollo de la confianza entre la comunidad, los científicos y el propio sistema de alerta temprana.

El sitio de estudio Bello Oriente se localiza en la unidad geológica de la Dunita de Medellín, un cuerpo ofiolítico ultramáfico, formado en el Triásico. Ha sufrido una profunda alteración, por lo que no puede considerarse una dunita, sino una serpentinita. Esta alteración y la larga historia tectónica, causando un nivel de fracturación extrema en la roca, han provocado que la roca esté muy desintegrada y profundamente meteorizada, convirtiéndola en la unidad más propensa a deslizamientos de la ciudad de Medellín y de la región.

Para alcanzar los objetivos científicos, se aplicaron varios métodos directos e indirectos; se realizaron mapeos de las características y procesos geológicos, cuatro perforaciones, levantamiento de diaclasas en superficie, cuatro adquisiciones geoeléctricas (TRE) y varios ensayos de laboratorio en muestras de roca y suelo de las perforaciones y de la superficie.

Todas las investigaciones encontraron una composición muy heterogénea del subsuelo en su estructura, mineralogía, y estado de meteorización. La presencia del fenómeno pseudokarst, ya observado por otras investigaciones en otras partes de la Dunita de Medellín, era obvia por las cavidades encontradas en las perforaciones, la gran cantidad de suelo en profundidades de hasta 50 m, y el grado de desintegración de roca aparentemente inalterada. Esta heterogeneidad se visualizó en tres perfiles del subsuelo y en un mapa de espesores coluviales, utilizando la información de la cartografía geológica, las perforaciones y los cortes transversales (TRE).

Los deslizamientos en el sitio del estudio se caracterizaron por ser de poca profundidad a media profundidad (máx. 10 m de profundidad) y tener una superficie máxima de 15.000 m². No se espera que ocurra un evento mayor en el sitio de estudio. Por lo tanto, la categorización de los eventos utilizó el evento más grande (aprox. 15.000 m²) como la magnitud máxima de un evento de 100 años. Los eventos de un tamaño de hasta 4.000 m² se categorizaron como eventos de 30 años, mientras que los eventos > 15.000 m² se categorizaron como amenaza residual. Las zonas de amenaza de las tres magnitudes se visualizaron en tres mapas de amenaza de magnitud; un mapa de síntesis, que representaba las tres magnitudes a la vez, este fue el mapa de amenza final para el sitio de estudio. Este mapa se utilizó para una distribución óptima del sistema de sensores en el sitio de estudio y para desarrollar rutas de evacuación y zonas seguras.

Un aspecto vital durante el transcurso del proyecto fue la integración social del sistema en la comunidad de Bello Oriente. Además de varios talleres organizados por los socios del proyecto sobre deslizamientos, riesgo y alerta temprana y de paseos comunitarios por el barrio, todas las operaciones científicas y técnicas en el sitio del estudio se realizaron con la ayuda y los conocimientos de voluntarios de la comunidad. La instalación de la mayoría de los equipos del sistema de alerta temprana se hizo con los miembros de la comunidad como empleados de la empresa constructora responsable. Estas muestras de confianza mutua propiciaron un entorno de trabajo cómodo para todas las partes implicadas y han evitado el vandalismo en el sistema de sensores hasta ahora..

List of Figures

Figure 1: Project partners of the project Inform@Risk (WERTHMANN 2019:). 2

Figure 2: Map of Colombia's environmental regions (after LEISGANG 2021, www-04 and www-05). . 8

Figure 3: Location of Antioquia and the Aburrá Valley in Colombia (after www-04, HERMELIN 2016 and LEISGANG 2021). 9

Figure 4: The comunas of the city of Medellín and the location of the study site (after www-09). 10

Figure 5: Geological Map of the Aburrá Valley (after DEMHARTER 2021, LEISGANG 2021 and CASAS & MONSALVE 2018). 11

Figure 6: Study Site in Bello Oriente and Santa Elena. 12

Figure 7: Forms of karst found in the Medellín Dunite; A = spitzkarren , B = karst cavern, C = rillenkarren, D = rundkarren (after TOBÓN-HINCAPIÉ et al. 2011). 16

Figure 8: Landslide hazard map of Colombia (after LEISGANG 2021, OJEDA & DONNELLY 2006 and www-01). 17

Figure 9: Landslide events with more than 10 fatalities in the Aburrá Valley since 1920 (after ECHEVERRI et al. 2012). 18

Figure 10: Risk Management Cycle, depicting all stages of risk management (www-13). 19

Figure 11: Landslide risk in Medellín at city scale and precarious/informal settlements of the city (WERTHMANN et al. 2024). 20

Figure 12: Locations of the drillings and ERT transects in Bello Oriente (after BREUNINGER et al. 2023a). 23

Figure 13: Location of all scanlines, trench samplings, and surface samplings in the project. 25

Figure 14: Process map of the study site created during the first field campaign in August 2019 and revised in 2022 (after BREUNINGER et al. 2021c and BREUNINGER et al. 2023a). 35

Figure 15: Geological map of the study site created during the second field campaign in February 2020 (after Breuninger et al. 2021c and BREUNINGER et al. 2023a). 36

Figure 16: Drilling cores of drillings A1 (left) and A2 (right) (after BREUNINGER et al. 2021c). 38

Figure 17: Drilling core of drilling B1 (after BREUNINGER et al. 2021c). 39

Figure 18: Drilling core of drilling B2. 41

Figure 19: Structural map of the study site (after BREUNINGER et al. 2023a and WERTHMANN et al. 2024). 42

Figure 20: Structural analysis of 11 scanlines (after GAMPERL et al. in review). 42

Figure 21: Result and interpretation of ERT profile BO-01 (after GAMPERL et al. in review). 44

Figure 22: Result and interpretation of ERT profile BO-03 (after GAMPERL et al. in review). 46

Figure 23: Result and interpretation of ERT profile BO-04 (after GAMPERL et al. in review). 47

Figure 24: Uniaxial compressive strength values plotted against sampling depth of all four drillings. 49

Figure 25: Tensile strength values plotted against sampling depth of all four drillings. 50

Figure 26: Grain size distribution of all drilling core samples depicted according to DIN EN ISO 14688-2 (2020) (after BREUNINGER et al. 2021c). 51

Figure 27: Grain size distribution of all trench samples depicted according to DIN EN ISO 14688-2 (2020) (after BREUNINGER et al. 2021c). 52

Figure 28: Spatial distribution of the grain size distribution of the trench samples. 53

Figure 29: Atterberg limits of all drilling core and trench samples depicted according to DIN EN ISO 14688-2 (2020) (after BREUNINGER et al. 2021c). 54

Figure 30: Friction angle plotted against the cohesion of the shear tests of the samples from drilling core B2 and the trench samples. 55

Figure 31: Spatial distribution of the friction angle of the trench samples. 56

Figure 32: Spatial distribution of the cohesion of the trench samples. 57

Figure 33: Microscopic photos of the thin sections related to the sample numbers: (**a**) = D-01; (**b**) = D-02; (**c**) = D-03; (**d**) = D-04; (**e**) = D-05; (**f**) = D-06 (ol = olivine, ant = antigorite, chr = chrysotile, pyr = pyroxene, chl = chlorite, op = opaque phase) (after AMBOS 2020 and BREUNINGER et al. 2021c). 58

Figure 34: Microscopic photos of the thin sections related to the sample numbers: (**a**) + (**b**) = D-07; (**c**) = D-08.1; (**d**) = D-08.2; (**e**) = D-09; (**f**) = D-10 (ol = olivine, ant = antigorite, chr = chrysotile, pyr = pyroxene, amp = amphibole) (after AMBOS 2020 and BREUNINGER et al. 2021c). 59

Figure 35: Spatial distribution of the mineralogical composition of the trench samples. 61

Figure 36: Visual interpretation of ERT transect BO-01 (after GAMPERL et al. in review). 67

Figure 37: Visual interpretation of ERT transect BO-03. 68

Figure 38: Visual interpretation of ERT transect BO-04. 69

Figure 39: Colluvial map of the study site. 71

Figure 40: Age of the landslide events recorded in Bello Oriente plotted against their size. 73

Figure 41: Sketch of the typical appearance of the three event magnitudes in the study site. 74

Figure 42: Hazard assessment after the Swiss model with the three event magnitudes of the project (after BAFU 2016). 75

Figure 43: Hazard map depicting the hazard and runout area for 30 year events (after BREUNINGER et al. 2023a and WERTHMANN et al. 2024). 76

Figure 44: Hazard map depicting the hazard and runout area for 100 year events. 77

Figure 45: Hazard map depicting the hazard and runout area for the residual hazard. 77

Figure 46: Synthesis hazard map of the study area. 78

Figure 47: Synthesis hazard map of the study area, categorized regarding the slope inclination. 79

Figure 48: First attempt at a profile through the study site, along ERT transect BO-01 (after GAMPERL et al. in review). 80

Figure 49: Second attempt at the depiction of the subsurface along the profile line depicted in Figure 50. 81

Figure 50: Colluvial map before the drillings with the profile line shown in Figure 49. 82

Figure 51: Final colluvial map, as depicted in Figure 39 and Figure A7, in comparison. 83

Figure 52: Development of the understanding of the weathering profile during the project: (a) weathering model after WERTHMANN & ECHEVERRI (2013), (b) pseudokarst model after

TOBÓN-HINCAPIÉ et al. (2011), (c) in-situ conditions encountered during the investigations (after GAMPERL et al. in review)..... 84

Figure 53: Synthesis hazard map depicting the slope inclination, including the outlines of the registered landslide events, as presented in Figure 14. 88

Figure 54: Final installation plan of the EWES in Bello Oriente, created by AGR, on the basis of the inclination hazard map of Figure 47, as seen in the background (GAMPERL et al. 2023).... 94

List of Tables

Table 1: Bachelor's and Master's theses supervised in the project by the Chair of Engineering Geology of TUM. 5

Table 2: Publications by project members with contributions of this dissertation's author. 6

Table 3: USC test conditions according to ASTM D 7012-14e (2014) and DGGT (2022a) (after PETZI 2022). 24

Table 4: Number of UCS tests and Brazilian tests per drilling. 26

Table 5: Splitting tensile strength test (Brazilian test) conditions according to ASTM D 3967 (2016) and DGGT (2022b) (after PETZI 2022). 26

Table 6: Comparison of mesh sizes used in the project according to I.N.V. E-123 (2013) and DIN EN ISO 17892-4 (2017) (after DEMHARTER 2021)..... 27

Table 7: Comparison of minimum sample quantity per largest grain size of I.N.V. E-123 (2013) and DIN EN ISO 17892-4 (2017) (after DEMHARTER 2021). 27

Table 8: Comparison of test conditions of the hydrometer analysis of I.N.V. E-124 (2013) and DIN EN ISO 17892-4 (2017) (after PETZI 2022)..... 28

Table 9: Comparison of test conditions for the determination of the liquid limit between I.N.V. E-125 (2013) and DIN EN ISO 17892-12 (2020) (after PETZI 2022). 28

Table 10: Comparison of test conditions for the determination of the plastic limit between I.N.V. E-126 (2013) and DIN EN ISO 17892-12 (2020) (after PETZI 2022)..... 29

Table 11: Comparison of the test conditions for the shear test between I.N.V. E-154 (2013) and DIN EN ISO 17892-10 (2019) (after PETZI 2022)..... 29

Table 12: Soil tests performed on the samples from the drillings and the trenches. 50

Table 13: List of landslide events in the study site and their event date, size, slide geometry and information source. 72

Acknowledgements

I would like to thank the following people for their support during the preparation of this thesis:

Prof. Dr. Kurosch Thuro, for the opportunity to work on this dissertation in the first place, his continued support in all matters related to it, especially the input during the writing process, and for his confidence in me as a lecturer, researcher, and scientist.

Dr. Moritz Gamperl, for the productive cooperation and mutual support throughout this project during field work, writing processes, travel and shipping preparations and organisations and, especially, for his friendship since the start of our Bachelor's programme and for the joy we had while working together in Colombia.

Dr. Bettina Menschik, for her guidance and input in the evaluation of the results and in the writing process, and the support in the legal and customs matters of the project.

Dr. John Singer, for his incredible support far beyond and in addition to the aspects of his own part in the project.

Dr. Marion Nickmann, for her mentorship during the doctorate, her input in the evaluation of the laboratory results and the supervision of my Master's thesis.

Dr. Carolina Garcia-Londoño, for all the support and project coordination in Colombia, without which the project could not have been realized, her hands-on approach to difficult negotiations and the friendship we built during and after work.

David Cerón-Hernandez and Julián Castañeda-Valderrama, for their incredibly dedicated on-site work, without which the pandemic would have terminated the project, and the friendships we developed.

The residents of Bello Oriente, for their immediate acceptance, incredible support, and friendly and joyful inclusion of us into their community. It was a privilege to get to know them and to spend so many wonderful hours working and laughing together.

Prof. Christian Werthmann, Dr. Heike Schäfer, and Lisa Seiler form LUH, and Isabel Basombrío and Alejandro Echeverri from Urbam, for the project coordination, the great cooperation in Germany and Colombia during meetings and field work, the ongoing dedication for the project, and the personal relationships built in the project.

Josephine Ziegler, Patricia Ambos, Agnes Demharter, Isabelle Leisgang, and Julia Petzi, for the research and the evaluation of the results of the field and laboratory work in their theses, that took a lot of work off my shoulders.

Prof. Dr. Hans-Albert Gilg and Dr. Gerhard Lehrberger, for the realization, guidance, and input regarding the mineralogical investigations of the project.

Dr. Katja Lokau and Dr. Bernhard Lempe, for the great collaboration during the lectures and field curses, and for teaching me how to teach.

Prof. Dr. Michael Krautblatter, for his help regarding the evaluation of the geoelectrical measurements, the chairmanship of the examining board of my thesis, and the countless coffee breaks over the years.

Catharina Drexl, Saskia Eppinger, Dr. Martin Potten, Dr. Georg Stockinger, Matthias Brugger, Justin Mattheis, and Riccardo Scandroglio, for being my siblings in arms for all these years, for the after-work beers and pizzas, and the comic relief when it was needed the most.

Rosemary Marin-Loebard, for her continued support concerning the administrative and financial processes of the project, especially during its finalization, and the occasional emotional support.

Renate and Joachim Breuninger, for their lifelong support, guidance, and love.

1 Motivation

Parts of this chapter have already been published in BREUNINGER et al. (2021a), BREUNINGER et al. (2021b) and BREUNINGER et al. (2023b).

Due to global warming and climate change in general, extreme draughts on the one side and heavy rainfalls on the other side became more frequent in the past decades and are expected to continue to intensify in the future (KOPP et al. 2017, LIU et al. 2022). Since rainfall is the main trigger for landslide events, the frequency of those events is expected to increase as well (CROZIER 2010). Especially tropical regions with high topographic changes suffer from this development, for example countries in the Andean region in South America (ARISTIZÁBAL et al. 2022, MOREIRAS & PONT 2017, FROUDE & PETLEY 2018).

At the same time, many regions around the world, especially in developing countries, experience an exponential growth in population (GU et al. 2021). Additionally, large cities in those countries are subject to major influx of people from rural areas in search of easier and better paid work than in agriculture (GU et al. 2021, WERTHMANN & ECHEVERRI 2013, OJEDA & DONNELLY 2006). Due to a high price level in the city centre, these people settle at the city border (BREUNINGER et al. 2021b, OJEDA & DONNELLY 2006). In case the city is situated in a mountain area, like Medellín, Colombia, the people settle on steep and unstable slopes (BREUNINGER et al. 2021b, OJEDA & DONNELLY 2006). This overpopulation leads to considerable changes in land use, deforestation, embankment cutting for roads and uncontrolled/increased infiltration of water (wastewater and watering for plants) (JAYASINGHA 2016, Breuninger et al. 2021b). The constructed houses lack preliminary ground investigation and proper foundation and weaken the already unstable ground in steep slopes in mountainous areas (BREUNINGER et al. 2021b). All these actions are taken with no or only little understanding of landslide dynamics and their promoting and triggering factors (JAYASINGHA 2016, BREUNINGER et al. 2021b). In Medellín numerous landslides have occurred in these informal settlements in the past decades, some of them claiming several human lives (WERTHMANN & ECHEVERRI 2013), the most horrendous one being the Villa Tina landslide in 1987 with over 500 casualties (TOKUHIRO 1988, HERMELÍN 2005, OJEDA & DONNELLY 2006, BREUNINGER et al. 2023b).

The increase of frequency and intensity of landslide events and the exponential growth of precarious settlements due to rural exodus in tropical and mountainous regions cause an increasing number of deaths per landslide in urban areas (SEPÚLVEDA & PETLEY 2015, WERTHMANN & ECHEVERRI 2013).

Since long term mitigation measure, like relocation of endangered citizens and implementation of physical mitigation measures, are neither economically nor socially feasible for affected communities, Early Warning and Evacuation Systems (EWES) are the only effective measure to provide a short- to midterm relief for affected communities (GAMPERL et al. 2021, UCHIMURA et al. 2015). Though subject to a wide range of failures like false alarms and short evacuation times, these systems give the people living under these circumstances a chance to get to safety before a catastrophic event (JAYASINGHA 2016).

1.1 Project Inform@Risk

The project Inform@Risk is a German-Colombian collaboration with the goal to develop and install a prototype landslide early warning and evacuation system in an informal settlement in Medellín, Colombia. It is funded by the German Federal Ministry of Education and Research in its program “Client II”, a promotion of international partnerships in science and research (BREUNINGER et al. 2021a, LEIBNIZ UNIVERSITY HANOVER 2018). A key goal is to strengthen the resilience of residents against the risk of landslides, that is rapidly increasing due to climate change, especially in the tropical regions (BREUNINGER et al. 2021a). To approach this task, the created system has to be replicable, precise, low-cost, spatially integrated, socially integrated, multiscale, and multisectoral. The following information regarding the project Inform@Risk is derived from LEIBNIZ UNIVERSITY HANOVER 2018, the jointly agreed upon working plan of all project partners:

To create a successful prototype of an EWES the project has several requirements to the system itself. Most importantly, the system has to be **replicable** in other parts of the city, Colombia, and the Andean region. This does not mean that the system needs to be able to be copied exactly, but it must be adaptable in other but similar social, geological, and political environments.

Additionally, the sensor system has to be **precise** enough to detect the most frequent events typical for the study site. In the last years the emphasis of Colombian risk management was on regional risk analysis (PEÑA 2017). This approach mostly uses remote sensing and limited to no field investigations. The EWES created in the project needs a much more detailed and small-scale understanding of the subsurface and the geotechnical behavior of the study site. This includes a very precise geological and geotechnical investigation.

Due to the limited public resources of the city the system also needs to be **low-cost** in procurement, installation, operation, and maintenance to ensure the replicability.

Since the project takes place in a densely populated area (see chapter 2.3), a main focus is the **spatial and social integration** of the project and the system into the neighbourhood and, especially, into the community to ensure the acceptance of the sensor system, avoid vandalism and ensure an adequate response to alarms and evacuation orders.

The risk and vulnerability assessment took place on three different levels (**multiscale**): city level, neighbourhood level and quarter level (study site). The city and neighbourhood levels were analysed using remote sensing, the quarter level was studied in detail using drone flights, mappings, and geotechnical investigations (see chapter 4).

Since meeting all of the above-mentioned criteria requires several different fields of expertise, the project also has to be **multisectoral**. The cooperation of many actors from the German and the Colombian side is vital for the success of the project and the system (Figure 1).

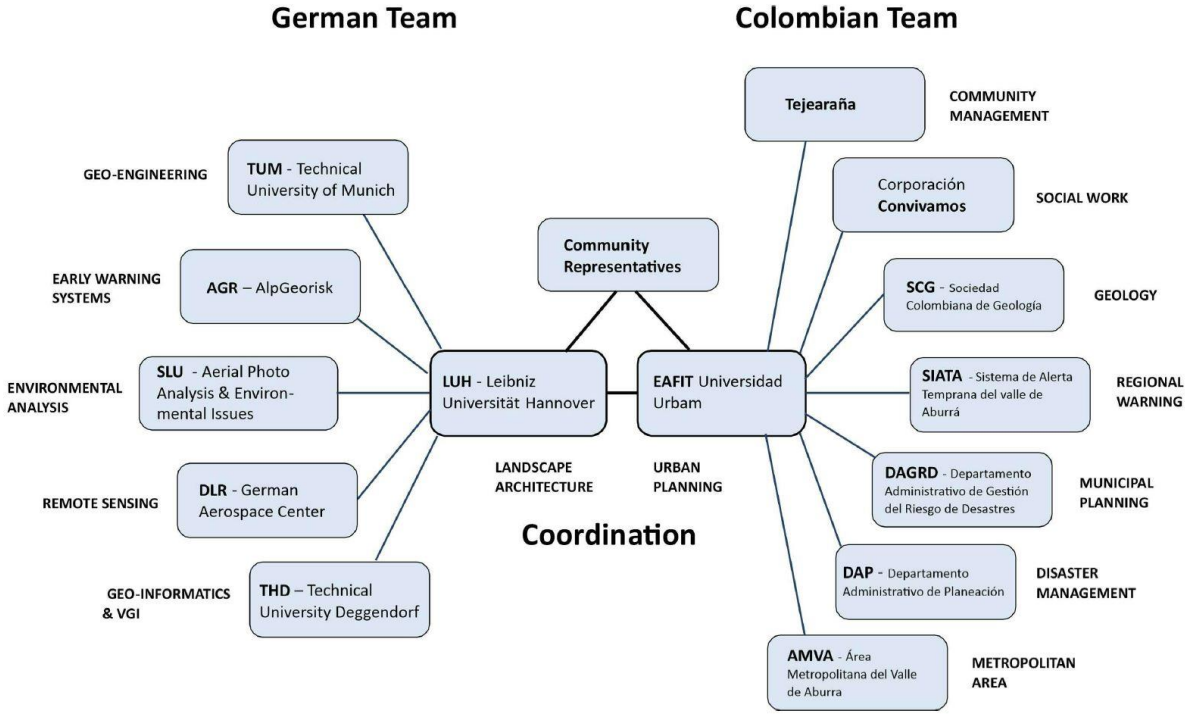

Figure 1: Project partners of the project Inform@Risk (WERTHMANN 2019:).

The project leader and main coordinator on the German side is the Institute of Landscape Architecture of the Leibniz University of Hanover (**LUH**). In addition to that leader role, the tasks of the project partner included community work in the study site, demographic mappings and analyses, and integrating

the sensors of the EWES into the public space of the study site by designing different encasements, covers, and other items for those sensors.

The Technical University of Deggendorf (**THD**) is responsible for the drone flights and their digital processing and the development of an early warning app, while the German Aerospace Center (**DLR**) and the small enterprise Expert Office for Aerial Image Analysis and Environmental Issues (**SLU**) are responsible for the remote sensing data and their processing and analyses on all three levels (city, neighbourhood, and quarter).

All geological and geotechnical investigations in the study site (quarter level) are the task of the Chair of Engineering Geology of the Technical University of Munich (**TUM**). These investigations include several mappings, drillings, laboratory tests, joint recordings, and geoelectrical measurements as well as the evaluation and analysis of the obtained data and their merging into a simple underground model to understand the landslide dynamic of the study site. To choose the best spatial distribution of the sensors of the EWES, a hazard map is developed on the basis of the conclusions of these investigations and evaluations. These tasks are the main object of this thesis.

The sensor system of the EWES is designed, planned, and implemented by the small enterprise AlpGeorisk (**AGR**). This includes the designing and building of about 150 single sensors (LoRa nodes) to be put on houses (infrastructure nodes) and into small drillings of up to 6 m depth in the ground (subsurface nodes), the planning and implementation of CSM lines in trenches of 50 cm depth, and the designing, building, implementation, and programming of a communication system between the sensors, the communication gateways, and the data server. The obtained data is than visualized and can be used to modify the underground model. The development of the sensor system is subject of the dissertation of Moritz Gamperl from TUM. Both dissertation were done in close cooperation.

On the Colombian side the project leader and coordinator is the Center for Urban and Environmental Studies of the EAFIT University in Medellín (Urbam). Its tasks are the coordination of the project partners on site, the community work, and assistance for LUH in the integration of the sensors into the public space.

The government of Medellín, the Aburrá Valley and Colombia are also part of the project through the municipal disaster management agency of Medellín (DAGRD), the municipal planning agency of Medellin (DAP), the regional warning agency of the Aburrà Valley (SIATA), the Defensa Civil (DC) and the Ministry of Environment and Sustainable Development of Colombia (MADS). Their responsibilities include assistance with transportation and import, granting permissions to work on public land, and, most importantly, the future operation of the EWES (DAGRD or SIATA).

Non-governmental organisations, namely Tejerañas, Convivamos, Oficina de Resiliencia de Medellín (ORM), and Fundacion Sumapaz (FS) are the main partners concerning community work and the development of trust in the project and the scientists by the community members. Their tasks include assistance during field work and co-hosting of workshops on landslide risk as well as communicating the project within the social scientific community in Medellín.

Another vital partner in the project is the Geological Society of Colombia (SCG) represented by Carolina Garcia-Londoño. Her role in the project is the communication between all stakeholders on the Colombian side, assistance in field and community work and communicating the project within the social scientific community in Medellín as well as abroad.

1.2 Tasks and Problems

As already mentioned in chapter 1.1, this thesis primarily focusses on the geotechnical investigations of the study site as preparation for the distribution of the sensor system of the EWES.

The EWES is to be implemented in a landslide-prone, densely populated, informal settlement at the steep slopes at the city border of Medellín. In addition to the investigations themselves, this location presents some special challenges not typically encountered by geologists from southern Germany.

A general understanding of the subsurface is necessary for any landslide early warning system regardless of location. This includes the geological composition of the area, the geotechnical parameters of the subsurface and the geotechnical behavior of the landslides typical for the study site. All of this information can only be obtained by mapping of the geological and geomorphological features of the surface and different non-invasive and direct measurements of the subsurface. Since the study site is densely populated, the surface is already highly disturbed by anthropogenic measures and sealed by roads, houses, and other constructions. Geomorphological and geological data is therefore either highly altered or not obtainable at all, subsurface data can only be obtained at certain, non-sealed locations rather than at locations with the highest expected information content. When performing the geotechnical investigations, the special circumstances of the study site have to be considered, especially when evaluating the collected data.

Another important factor are the elements at risk when designating areas at risk. The geotechnical and demographic data obtained by LUH (see chapter 1.1) have to be combined into a multisectoral hazard map rather than only determining the hazard of a certain area by the probability and size of a landslide event. Even the time of day has to be considered; some areas are only populated by day (schools), others primarily at night (homes).

During all the investigations by all the project partners, the works are carried out with multiple spectators of all ages. The people living in the study site are mostly not used to scientists working at their homes and have either fear of or anger towards authorities from the city and the state, depending on their experiences. It is therefore necessary to earn the trust of the population through various measures. Some project partners are tasked with the education of the population about landslide risk, early warning, reaction to alarms, and evacuation routes and strategies during multiple workshops (see chapter 1.1). Since some scientists, especially the landscape architects (LUH), the geologists (TUM), and the technicians (AGR), work within the community for a considerable amount of time (2-6 weeks at a time, every three months for four years), they need to build relationships with the people living in the study site as well to be able to do their work without creating a hostile environment. Most importantly, the sensor system must be accepted by the community members to avoid vandalism and evoke an adequate reaction to warnings, alarms, and evacuation orders.

These tasks lead to the following main research questions to be answered in this thesis:

- What are the specific mineralogical, geological, and geotechnical factors promoting the landslide processes in the study site?
- What landslide processes are to be expected at the study site and what is their typical size and depth?
- Which areas of the study site are most prone to landslides and which areas have the highest hazard potential?

1.3 Aims

To approach the above-mentioned topics, this thesis is focusing on pursuing the following scientific goals:

- Determining the geological composition of the study site.
- Determining the geotechnical parameters of the subsurface.
- Determining the geotechnical behavior of the landslides at the study site.
- Determining high hazard areas on the basis of the three factors mentioned above.
- Developing trust among the community in the project and the EWES.

In the chapters 2 and 3, the study site and its landslide characteristics will be explained in more detail, before the methodology is presented in chapter 4, addressing the above-mentioned goals regarding the characteristics of the study site.

1.4 Project Work

Several Bachelor's and Master's theses were supervised at the Chair of Engineering Geology of TUM in the course of this project. A great part of the data obtained was presented and evaluated in these theses and is partly presented in this dissertation. The following Table 1 gives an overview of the Bachelor's and Master's theses supervised in the project and their contribution to this dissertation and the dissertation of Moritz Gamperl.

Table 1: Bachelor's and Master's theses supervised in the project by the Chair of Engineering Geology of TUM.

Title – thesis type, year	Contribution	Author	Supervisor
Petrographische Analyse der ultramafischen Gesteine am Osthang der Stadt Medellín. – BA 2020.	Thin section analysis of the dunite samples from the surface (chapters 4.6.6 and 5.6.3).	Patricia Ambos	Tamara Breuninger
XRD Analysis of the Weathered Material from the Igneous Rocks on the Eastern Slope of Medellín (Inform@Risk). – BA 2020.	XRD-analysis of the soil samples taken from the surface (chapters 4.6.7 and 5.6.4).	Josefine Ziegler	Tamara Breuninger
Geological-geotechnical characterization of the "Medellín Dunite" along the eastern slope of the city of Medellín, Colombia. – MA 2021.	Analysis of the first three drillings and their laboratory tests (chapter 4.3, 4.6, 5.3 and 5.6).	Agnes Demharter	Tamara Breuninger
Risk-Based Selection and Positioning of Sensors for a Geosensor Network for Landslide Monitoring, in Medellín (Colombia). – MA 2021.	Sensor distribution (dissertation Moritz Gamperl 2024).	Isabelle Leisgang	Tamara Breuninger
Hydrological modelling of informal settlements in Medellín, Colombia. – MA 2021.	Hydrological analysis of the study site.	Christian Kerczek	Moritz Gamperl
Geological-geotechnical characterization of the "Medellín Dunite" along the eastern slope of the city of Medellín, Colombia. – MA 2022.	Analysis of the fourth drilling and its laboratory tests and those from the test trench (chapters 4.3, 4.6, 5.3 and 5.6).	Julia Petzi	Tamara Breuninger

The findings of the project were discussed within the scientific community in journal papers and by attributions to international and national conferences. Table 2 shows all publication with contributions by this dissertation's author. All publications were written in close cooperation with the author of the second dissertation from TUM in this project, Moritz Gamperl.

Table 2: Publications by project members with contributions of this dissertation's author.

Publication title	Publication type	Main author
Hazard assessment of landslide-prone areas on highly weathered dunite rock in Bello Oriente, Medellín, Colombia (Project Inform@Risk).	Online Presentation, EGU 2020, Vienna	Tamara Breuninger
Development of an early warning system for landslides in the tropical Andes (Medellín, Colombia).	Journal Paper 2020, Geom. and Tunneling	Kurosch Thuro
Hazard assessment and monitoring of landslide prone areas in Medellín, Colombia	Conference Proceedings, EURENGEO 2021, Athens	Kurosch Thuro
Development of a low cost geosensor network for detection and monitoring of rainfall induced landslides in soil.	Conference Proceedings, EURENGEO 2021, Athens	John Singer
Technical Concepts for an Early Warning System for Rainfall Induced Landslides in Informal Settlements.	Conference Proceedings, WLF 2021, Kyoto	John Singer
Initial Experiences of Community Involvement in an Early Warning System in Informal Settlements in Medellín, Colombia.	Conference Proceedings, WLF 2021, Kyoto	Tamara Breuninger
Investigation of Critical Geotechnical, Petrological and Mineralogical Parameters for Landslides in Deeply Weathered Dunite Rock (Medellín, Colombia).	Journal Paper 2021, International Journal of Environmental Research and Public Health	Tamara Breuninger
First Field Findings and their Geological Interpretations at the Study Site Bello Oriente, Medellín, Colombia.	Conference Proceedings, ISL 2021, Cartagena	Tamara Breuninger
Development of a Landslide Early Warning System in informal settlements in Medellín, Colombia.	Conference Proceedings, ISL 2021, Cartagena	Moritz Gamperl
Geologische Vorerkundung für ein Hangbewegungsfrühwarnsystem in den informellen Siedlungen von Medellín, Kolumbien.	Conference Proceedings, DGGT Conference 2023, Würzburg	Tamara Breuninger
Determination of Crucial Shear Parameters in Highly Landslide Prone Tropical Soils in Bello Oriente, Medellín, Colombia.	Conference Proceedings, IAEG 2023, Chengdu	Tamara Breuninger
Insights into the development of a landslide early warning system prototype in an informal settlement: the case of Bello Oriente in Medellín, Colombia.	Journal Paper 2024, Natural Hazards and Earth Systems	Christian Werthmann
Improvement of landslide investigation in deeply weathered ultramafites by parallelizing ERT with direct field observations.	In review	Moritz Gamperl

2 Geography and Geology of the Project Area

Parts of this chapter have already been published in BREUNINGER et al. (2021a), BREUNINGER et al. (2021b) and BREUNINGER et al. (2021c) and in the Master's theses of AGNES DEMHARTER (2021) and ISABELLE LEISGANG (2021).

2.1 Colombia

Colombia lies in the northwestern corner of the South American continent and is bordered by Panama to the Northwest, the Caribbean Sea to the North, Venezuela to the Northeast, Brazil to the Southeast, Peru to the South, Ecuador to the Southwest, and the Pacific Ocean to the West (Figure 2) (www-01). It has an area of 1.14 Mio. km² and 52.09 Mio. inhabitants (www-02). The capital city Bogotá is located in the Andean mountains at 2,640 m a.s.l., the highest mountain in Colombia is the Pico Cristóbal Colón with 5,775 m a.s.l. (www-02). Colombia is divided by the Andean mountains from southwest to northeast (Andes); southwest of the mountain range are the Orinoco Basin (Orinoquía) and the Amazonas Basin (Amazonía), west of the mountain range is the Pacific Coast (Pacífico), to the north the Caribbean Coast (Caribe), and the Pacific and Caribbean islands in the Pacific Ocean and the Caribbean Sea (Insular) (Figure 2) (www-01). Most of the inhabitants live in cities at the two coasts and in the Andes, the two basins are scarcely populated (www-03). Due to its location at the equator between 13° 34' north and 4° 14' south latitude, Colombia has a tropical climate at the coasts and in the basins, and a subtropical climate in the valleys of the Andean mountains (www-02).

The Andes in Colombia are split into three mountain ranges: the Cordillera Occidental (Western Ranges), the Cordillera Central (Central Ranges) and the Cordillera Oriental (Eastern Ranges) (Figure 3). These three branches are united in the Nudo de los Pastos (Knot of the Pastos) at the border between Colombia and Ecuador (HERMELÍN 2016, CEDIEL & SHAW 2019). All three cordilleras are mostly composed of different terranes and island arcs, that were accreted since the Paleozoic from the Pacific Plate and the Nazca Plate to the South American Continent during the orogeny of the Andes, and parts of oceanic plate (CEDIEL & SHAW 2019, CASAS & MONSALVE 2018, ARISTIZÁBAL & YOKOTA 2008). This origin causes many fault systems striking NNE-SSW parallel to the accumulation from an eastern direction, like the dominant Romeral Fault System in the Cordillera Central, and volcanic activity (CEDIEL & SHAW 2019).

Petrologically, the Colombian Andes consist mainly of Paleozoic and Mesozoic metamorphic and igneous rocks, the Cordillera Occidental also contains younger sedimentary rocks (CEDIEL & SHAW 2019).

2.2 Medellín and the Aburrá Valley

The city of Medellín is the capital of the region Antioquia in the Central Cordillera of the Andean mountains (Figure 3) and is the second most populated city in Colombia after the capital Bogotá (www-02, www-06). It has an altitude of approx. 1,500 m a.s.l., an area of 382 km², and 2.7 Mio. inhabitants (www-06, www-07). Medellín lies within the Aburrá Valley at the northwestern border of the Cordillera Central (Figure 3) and borders the cities of Bello to the north and Itagüí and Envigado to the south (www-08). The city consists of 16 comunas, the most famous one being Comuna 13 San Javier due to its murals, escalators, and history within the Medellín Cartel and Pablo Escobar (Figure 4) (www-09). Since the subtropical climate and the vicinity to the equator lead to very similar temperatures of about 22 – 24 °C daily mean year-round and 1,752.3 mm annual rainfall, the city is nicknamed "La Ciudad de la Eterna Primavera" (the city of eternal spring) (www-10).

The Aburrá Valley cuts into the Antioqueño Plateau, which is represented in the region by the San Pedro Altiplano (2,800 m a.s.l.) west of the valley and the Santa Elena Altiplano (2,750 m a.s.l.) east of the valley (CASAS & MONSALVE 2018, ARISTIZÁBAL & YOKOTA 2008). It is approx. 65 km long, has an area of 1,152 km², and the Medellín River flows through it from south to north (Figure 4) (ARISTIZÁBAL & YOKOTA 2008). Between the valley floor and the altiplanos on both sides the terrain rises in very

steep slopes, that are prone to landslides, especially due to the tropical climate with frequent heavy rainfall events (HERMELIN 2016).

Figure 2: Map of Colombia's environmental regions (after LEISGANG 2021, www-04 and www-05).

The geological basement of the Aburrá Valley is the Cajamarca Complex (Figure 5), an island arc, that was accumulated during the Ordovician and Silurian. It consists mostly of high to medium-grade metamorphic schists, granulites, gneisses, and migmatites (CASAS & MONSALVE 2018, CEDIEL & SHAW 2019, CORREA-MARTÍNEZ 2009). Together with the Devonian Caldas Group (orthogneisses, amphibolites) and the Jurassic Iguaná Gneiss (mylonitic granite), both also exposed in the Aburrá Valley (Figure 5), it is part of the Central Tectonic Realm (CTR) of the Cordillera Central, a group of accumulated island arcs (CASAS & MONSALVE 2018, CORREA-MARTÍNEZ 2009). The Caldas Group and the Cajamarca Complex are separated by the Santa Isabel Fault, most likely part of the Romeral Fault System, the major fault system in the Cordillera Central (CASAS & MONSALVE 2018).

Figure 3: Location of Antioquia and the Aburrá Valley in Colombia (after www-04, HERMELIN 2016 and LEISGANG 2021).

Most of the various ultrabasic rocks, namely the Permian Santa Elena Amphibolite (or Medellín Amphibolite), the Triassic Medellín Dunite, the Triassic Picacho Metagabbros and the Cretaceous Romeral Gabbros (Figure 5), are considered to be one dismembered ophiolitic complex by some sources (ÁLVARES-AGUDELO 1987, CORREA-MARTÍNEZ & MARTENS 2000). However, it is mostly hypothesized, that at least the Santa Elena Amphibolite is not part of this dismembered ophiolitic complex but is instead part of the Cajamarca Complex (BOTERO-ARANGO 1963, RESTREPO & TOUSSAINT 1984, CASAS & MONSALVE 2018). The Medellín Dunite possibly overlies another amphibolitic body instead, the Espadera Amphibolite (not exposed on the surface) (RESTREPO et al. 2012, CASAS & MONSALVE 2018). It is not clear, if this is indeed a different amphibolite or part of the Santa Elena Amphibolite (RODRÍGUEZ et al. 2005, CASAS & MONSALVE 2018). The Medellín Dunite and the Santa Elena Amphibolite are separated by the 65-90° E dipping La Acuarela Fault, where the amphibolite was lifted

(RODRÍGUEZ et al. 2005, RESTREPO & TOUSSAINT 1984, RESTREPO 2008). The Rodas Fault, dipping subhorizontally 10° E, separates the supposed Espadera Amphibolite and the Medellín Dunite and unites with the La Acuarela fault at the surface, then named Rodas Fault (Figure 5) (RODRÍGUEZ et al. 2005). This thrust fault is believed to strike out at the level of the valley floor (1,500 m a.s.l.) or slightly higher, but covered by deposits (RODRÍGUEZ et al. 2005, ECHEVERRI et al. 2012).

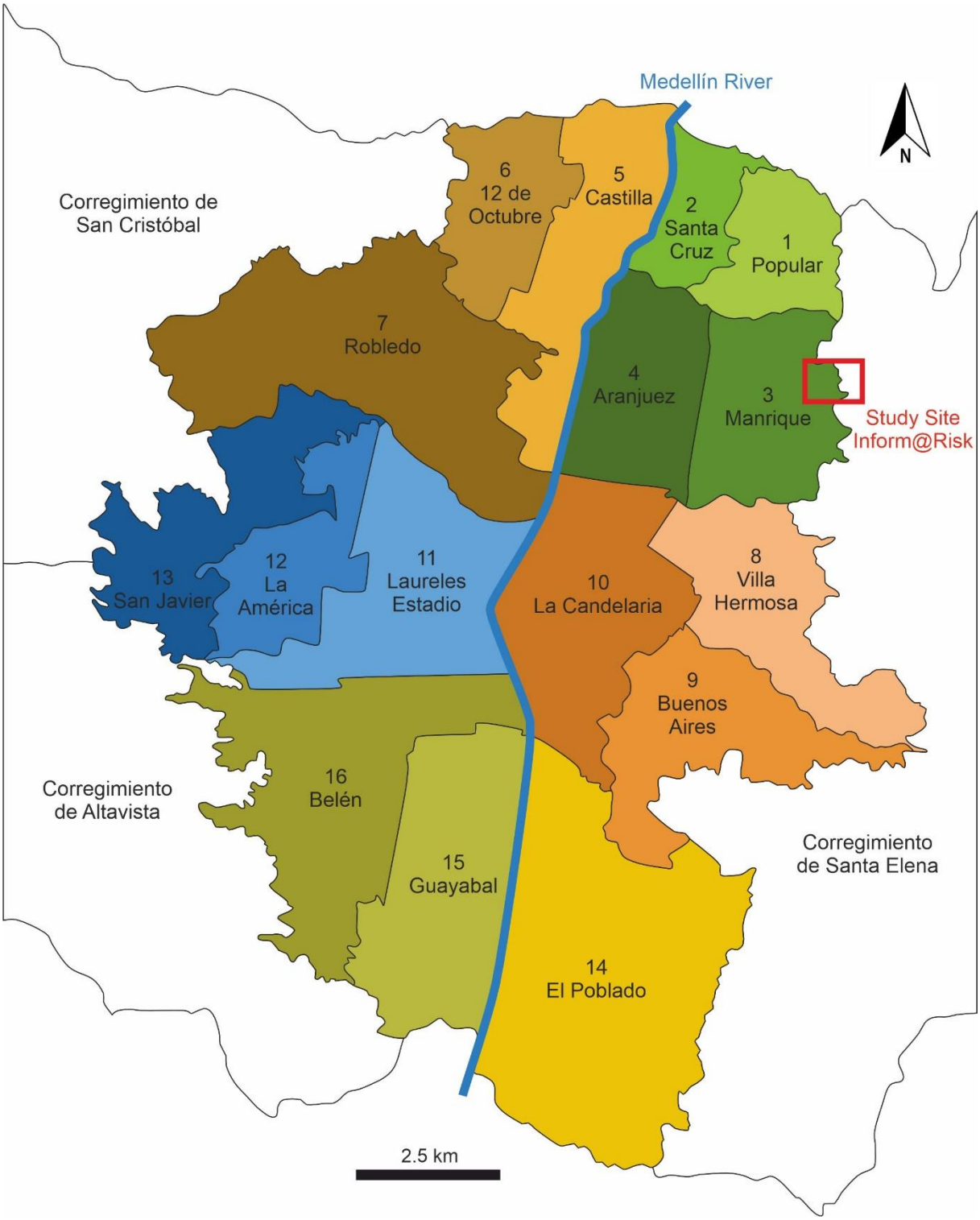

Figure 4: The comunas of the city of Medellín and the location of the study site (after www-09).

The Cretaceous Quebradagrande Complex is separated from the other geological units by the San Jeronimo Fault, most likely also part of the Romeral Fault system like the Santa Isabel Fault east of it (RESTREPO 2008, CEDIEL & SHAW 2019). It is composed of low-graded metamorphic andesitic and

basaltic vulcanites and sediments (CORREA-MARTINEZ 2009). Its origin is either as part of an ophiolitic complex or as an accumulated island arc (CORREA-MARTINEZ 2009).

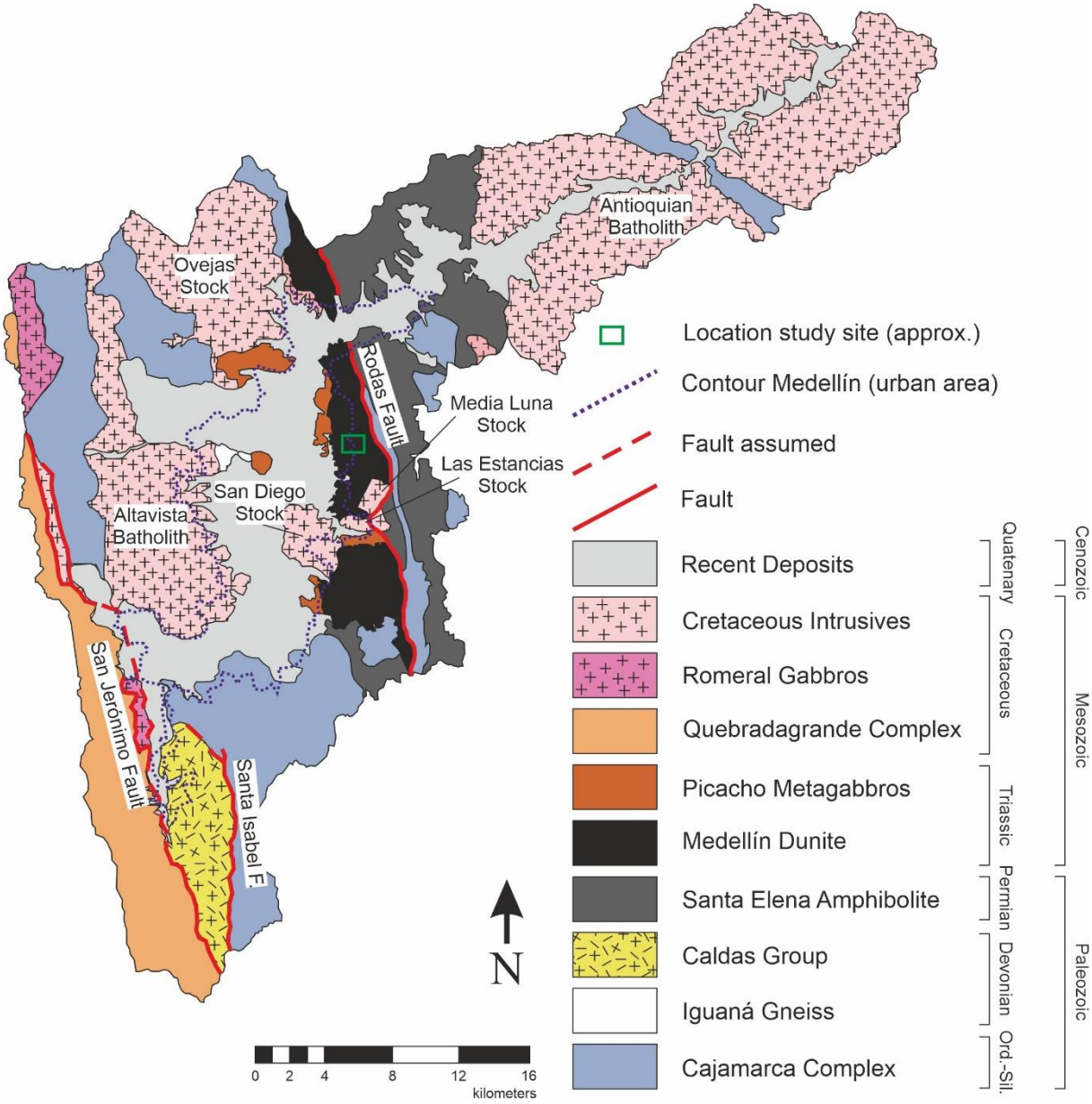

Figure 5: Geological Map of the Aburrá Valley (after DEMHARTER 2021, LEISGANG 2021 and CASAS & MONSALVE 2018).

These units are intruded by various Cretaceous plutonic structures (Figure 5). Two of those structures are of batholitic dimensions, namely the granodioritic-tonalitic Antioquia Batholite in the northeastern part of the valley and the dioritic Altavista Batholite in the western part (RODRÍGUEZ et al. 2005). Additionally, four plutonic stocks are present. The Las Estancias Stock, the Media Luna Stock and the dioritic-tonalitic Ovejas Stock are considered to be parts of or connected to the Antioquia Batholite due to similar lithological and petrological properties (CORREA-MARTÍNEZ 2009, RESTREPO 2008, RODRÍGUEZ et al. 2005). The fourth stock, the San Diego Stock consists of gabbro and is put into contact with the Altavista Batholite due to geochemical analyses (RODRÍGUEZ et al. 2005).

The valley floor is covered by alluvial and colluvial deposits and from the Medellín River and several creeks from the slopes as well as deposits from landslides (ARISTIZÁBAL & YOKOTA 2008).

The findings regarding the exact tectonic standings of the different units are still subject of investigations and new interpretations, as is apparent by some different opinions mentioned above.

2.3 Study Site Bello Oriente

The study site of the project Inform@Risk lies in the upper part of the barrio Bello Oriente in the Comuna 3 Manrique at the northeastern slope of the city of Medellín and the rural Corregimiento de Santa Elena, adjoining to the east (Figure 4, Figure 6) and has about 4,600 inhabitants (WERTHMANN et al. 2024). As is visible in Figure 5, the study site lies within the geological unit of the Medellín Dunite, an ultramafic body of a former ophiolitic complex (chapter 2.2 and chapter 3.1). Most of the landslides recorded in the Aburrá Valley have occurred in this unit due to the dunite's high degree and depth of weathering and its location at the steep eastern slope (WERTHMANN & ECHEVERRI 2013) (chapter 3.2). The Medellín Dunite and the landslides in the Aburrá Valley will be presented in chapters 3.1 and 3.2.

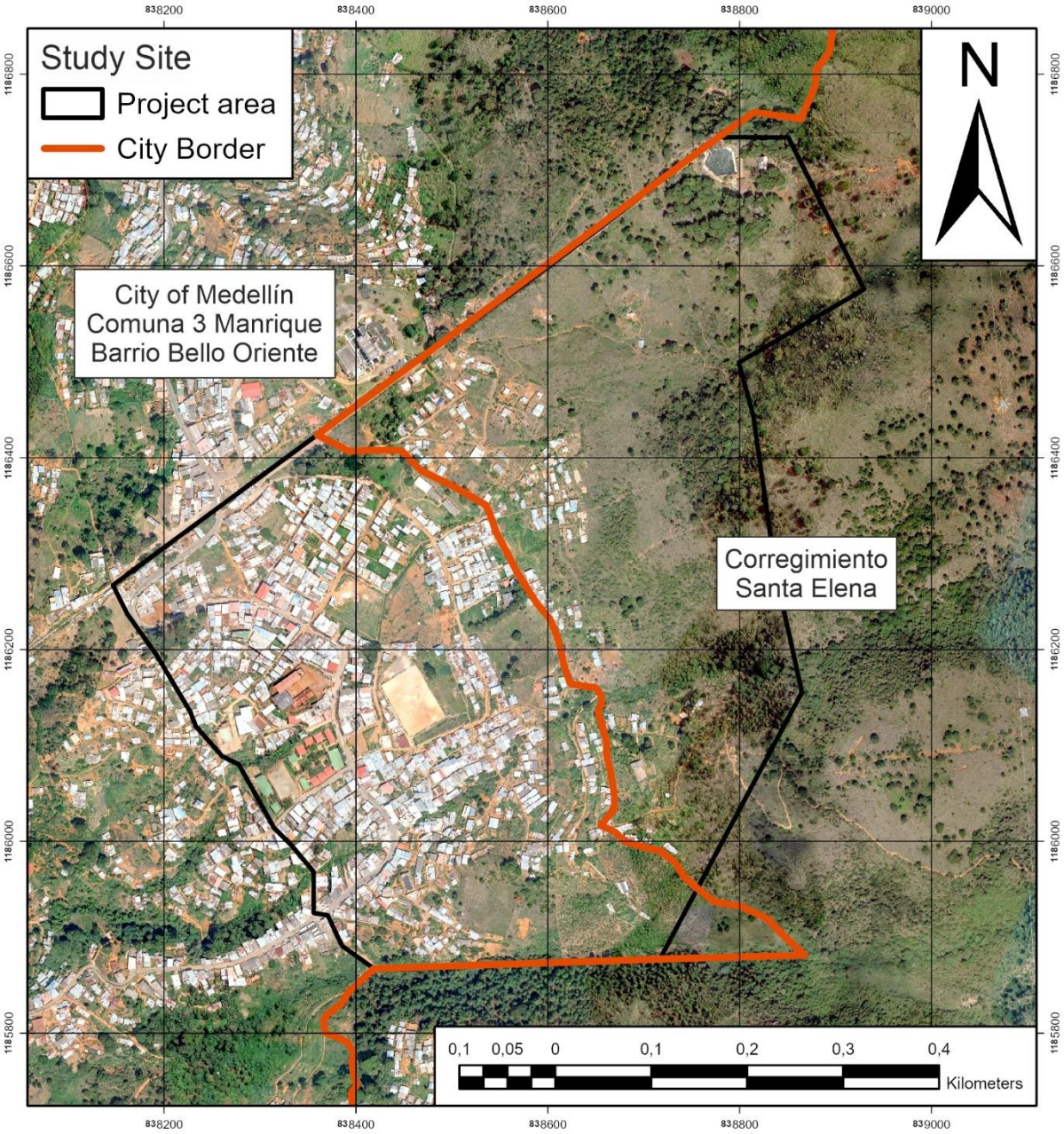

Figure 6: Study Site in Bello Oriente and Santa Elena.

This barrio has been chosen on the basis of several geotechnical, social, and administrative parameters defined at the beginning of the project. The study site had to be in a mostly immitigable landslide prone area (preferably within the Medellín Dunite) with loose building development to allow a better insight into the geological structure and an easier implementation of the sensors for the EWES. The social

requirements included low crime rates (safety for the scientists and community workers) and already existing community work by NGOs (preferably with experience in risk management). From the administrative side, the main requirement was the classification as an informal settlement.

Bello Oriente met all the required criteria and was chosen as the study site for Inform@Risk in May 2019 during the first field visit. Four other barrios were visited, but they had a much denser building development and were therefore not as suited. Additionally, two NGOs (Tejerañas and Convivamos) were already working on risk management within the barrio and supported the project until the end.

In June of 2017, a small landslide occurred in the uppermost part of Bello Oriente, that was filmed and subsequently shared on local TV and YouTube. No person or animal was killed or injured, but it showed the urgency to intervene in this particular part of the city and encouraged the decision for this barrio as the study site of Inform@Risk. This landslide, as many landslides in Medellín, was triggered by leaking water from a broken water pipe. These pipes cross the entire slope above the populated area and provide the houses below with fresh water from the main water pipe north of the barrio. This water distribution system is built by the community members, not by the supply agency of the city (EPM), and is, therefore, mostly using insufficient pipes, connections, and joints, that are not properly sealed and tend to leak. This leads to a high local infiltration of water into the slope, further promoting landslide hazard. Depending on the volume of the leakage and the time of day, this infiltration might not be detected by the community for several hours or even days. Unlike precipitation, this type of trigger cannot be predicted.

The study area stretches from 2,050-2,350 m a.s.l., which results in a height difference to the valley floor of approx. 550-850 m. This means, that the Medellín Dunite is approx. 500-1,000 m thick at the study site, considering the thrust fault to the underlying Espadera Amphibolite is dipping subhorizontally 10° E and strikes out slightly above the level of the valley floor (chapter 2.2).

3 State of the Art

Parts of this chapter have already been published in BREUNINGER et al. (2021c), BREUNINGER et al. (2023b) and in the Master's theses of AGNES DEMHARTER (2021) and ISABELLE LEISGANG (2021).

3.1 Medellín Dunite

This chapter is derived from BREUNINGER et al. (2021c) with some changes and additions.

The Medellín Dunite is an ultramafic unit at the eastern slopes of Medellín with a length of approx. 35 km and a width of 0.2-5.0 km. It is divided by other geological units into three rock bodies (Figure 5) with areas of 10-36 km², which strike between 10° and 24° NW-SE (CORREA-MARTÍNEZ 2009, GONZALES 2001). The petrologic nature of the unit is described as a homogeneous, fine-grained, massive, olive-green to dark-green rock with occasional yellowish-green shear surfaces (GONZALES 2001). It consists mainly of magnesium-rich olivine with transformations into serpentine, amphibole, talc and chlorite and hardly contains pyroxene (GONZALES 2001). In addition, the dunite is folded as well as partially banded or foliated and contains serpentine and chlorite lenses (ÁLVARES-AGUDELO 1987).

Although the Medellín Dunite has been studied by scientists for decades (BOTERO-ARANGO 1963, RESTREPO & TOUSSAINT 1984, ÁLVARES-AGUDELO 1987, GONZALES 2001, RODRÍGUEZ et al. 2005, CORREA-MARTÍNEZ 2009, RESTREPO 2008, HERNÁNDEZ-GONZÁLEZ 2014, GARCIA-CASCO et al. 2020), there are still uncertainties regarding its regional characteristics. Its significant small-scale changes in petrology and tectonics are especially a challenge for geologists and hydrogeologists when generating a geological subsurface model.

The Medellín Dunite is part of an ophiolite sequence formed in the Triassic (250–205 Mya b. p.) before the Andean orogenesis in the Pacific Ocean and has already partly been serpentinized by ocean floor metamorphosis (BOTERO-ARANGO 1963, GARCIA-CASCO et al. 2020). Therefore, the Medellín Dunite has already undergone a significant transition. Depending on the study area, the dunite can already be identified as serpentinite (BOTERO-ARANGO 1963). There are regions within the unit that consist of less than 90 % (serpentinized) olivine and more than 10 % orthopyroxene and hence the rock must be called harzburgite (GARCIA-CASCO et al. 2020). Other minerals that exist in the unit are amphibole (tremolite, actinolite), talc, chlorite, clinopyroxene, magnesite, mica and serpentine minerals (GARCIA-CASCO et al. 2020). Due to these deviations from a pure dunite, the unit was renamed several times and has been called Medellín Serpentinite (BOTERO-ARANGO 1963), Medellín Dunite Tectonite (ÁLVARES-AGUDELO 1987), Medellín Dunite (RESTREPO & TOUSSAINT 1984), Medellín Serpentinized Dunite (RODRÍGUEZ et al. 2005), Medellín Ultramafic Massif (CORREA-MARTÍNEZ 2009), Medellín Metadunite (RESTREPO 2008), Medellín Metaperidotite (HERNÁNDEZ-GONZÁLEZ 2014) and Medellín Metaharzburgitic Unit (GARCIA-CASCO et al. 2020). The term "Medellín Dunite", however, has prevailed.

Due to the tectonic history, several joint sets can be observed (TOBÓN-HINCAPIÉ et al. 2011). The first and oldest of those joint sets is the foliation created by ocean floor metamorphosis and the transport to the unit's current location (BOTERO-ARANGO 1963, GARCIA-CASCO et al. 2020). This foliation (joint set 1) is oriented subhorizontally SW-NE with an incidence angle of max. 30° towards SE (TOBÓN-HINCAPIÉ et al. 2011). It is characterized by mylonitic structures showing banding of mica, chrysotile, and chlorite (TOBÓN-HINCAPIÉ et al. 2011). The contact to the underlying Espadera Amphibolite (Rodas Fault) has the same orientation (RODRÍGUEZ et al. 2005). The second joint set (joint set 2) strikes NNW-SSE with a subvertical angle of 75–90° towards WSW (TOBÓN-HINCAPIÉ et al. 2011). This orientation resembles the fault between the Medellín Dunite and the Santa Elena Amphibolite (La Acuarela Fault), where the amphibolite was uplifted (RESTREPO & TOUSSAINT 1984, RESTREPO 2008). A third joint set (joint set 3) strikes SW-NE with a dip of 25–60° towards NW (TOBÓN-HINCAPIÉ et al. 2011). Due to these three main joint sets and several other discontinuities, the whole dunite body is highly disintegrated.

Since Medellín is located in a tropical environment, chemical weathering is a strong influencing factor on the subsurface composition. When in contact with water, the rock is altered by hydration into serpentine minerals, degradation into clay minerals and oxidation into iron oxides and hydroxides, which weakens the rock's structure and decreases its compressive strength continuously (ÜNDÜL et al. 2015). The higher the content of olivine in the rock ("pure" dunite), the stronger the weathering (ÜNDÜL & TUĞRUL 2016). Therefore, the weathering highly depends on the specific petrological composition of the rock and can change within the Medellín Dunite. The typical weathering profile of the unit consists of organic soil and volcanic ashes on the surface overlaying the saprolite deposits which show a decreasing weathering with increasing depth. This saprolite mostly consists of blocks of at least 50 cm in diameter in a silt-clay matrix with a ratio of approximately 1:1 (block-in-matrix structure). The content of loose material decreases with the depth. The depth of the top of the fractured dunite below the saprolite varies extremely within 0–20 m (TOBÓN-HINCAPIÉ et al. 2011). This simplified and idealized cross section is influenced by landslide processes taking place along the slope surface (uppermost 10 m), creating a further block-in-matrix structure which occurs to be similar to the one formed by weathering processes (TOBÓN-HINCAPIÉ et al. 2011).

The phenomenon "pseudokarst" (term here explicitly used as a differentiation from the real karst in carbonate rock) occurs in highly fractured crystalline rock masses. Water circulation in the fractures causes increased weathering and corrosion and, therefore, the solution, and, in other places, precipitation of minerals. In the case of the Medellín Dunite, the magnesium-rich olivine Forsterite is hydrated by meteoric water and transformed into serpentine minerals (in-situ) and Brucite precipitations, mostly at springs or in bigger caverns (TOBÓN-HINCAPIÉ et al. 2011, GARCIA-CASCO et al. 2020):

$$2\ Mg_2SiO_4 + 3\ H_2O \rightarrow Mg_3Si_2O_5(OH) + Mg(OH)_2.$$

$$\text{Forsterite} + \text{Water} \rightarrow \text{Serpentine} + \text{Brucite}.$$

The Medellín Dunite shows various forms of karst such as dolines, spitzkarren, rundkarren and karst caverns (Figure 7) (TOBÓN-HINCAPIÉ et al. 2011). Some fractures created by the pseudokarst are filled with clayey material, others are open discontinuities of up to 1 m opening width. This pseudokarst phenomenon reaches a depth of at least 60 m (RENDÓN-GIRALDO 2020). The block-in-matrix structure in combination with the joints, further opened up by the pseudokarst, lead to increased water conductivity which results in an increase of subsurface weathering and pseudokarst formation which again leads to increased water conductivity and subsurface weathering, creating a cycle.

Due to the water retaining properties of the fine material, the block-in-matrix structure is highly affected by landslides (TOBÓN-HINCAPIÉ et al. 2011) since water infiltration is the main reason and trigger for landslides in the Medellín Dunite (see chapter 3.2). The retained water is absorbed over several days, the pore water pressure increases, the structure "floats" upwards, the friction angle decreases below the slope angle, and the slope fails. The blocks tend to float in the matrix and their geotechnical properties do not influence the mechanics of motion once the full detachment occurs (RENDÓN-GIRALDO 2020).

3.2 Landslides in the Aburrá Valley

The main natural disasters in Colombia are landslides (49 %) and floods (42 %), while earthquakes (9 %) and volcanic eruptions (1 %) do not occur on a regular basis (LEISGANG 2021, OJEDA & DONNELLY 2006). This suggests that the most hazardous areas are located in the Andes and at the two coast lines. These areas are also the most populated ones, which is mirrored in the landslide hazard map for Colombia (Figure 8); the hazard areas mostly coincide with the most densely populated areas.

The hazard map (Figure 8) was based on the promoting factors (lithology, erosion, weathering, tectonics, relief) and the triggering factors (rainfall, seismic events, volcanism, anthropologic interventions) in these areas (OJEDA & DONNELLY 2006).

The Aburrá Valley and its inhabitants suffered from several landslides during the last century, with 854 fatalities in total (ECHEVERRI et al. 2012). Figure 9 shows events with more than 10 fatalities between

1920 and 2010. The biggest event was the Villa Tina Landslide in 1987 with 500 fatalities. One of the main triggers of these events was human intervention (ECHEVERRI et al. 2012).

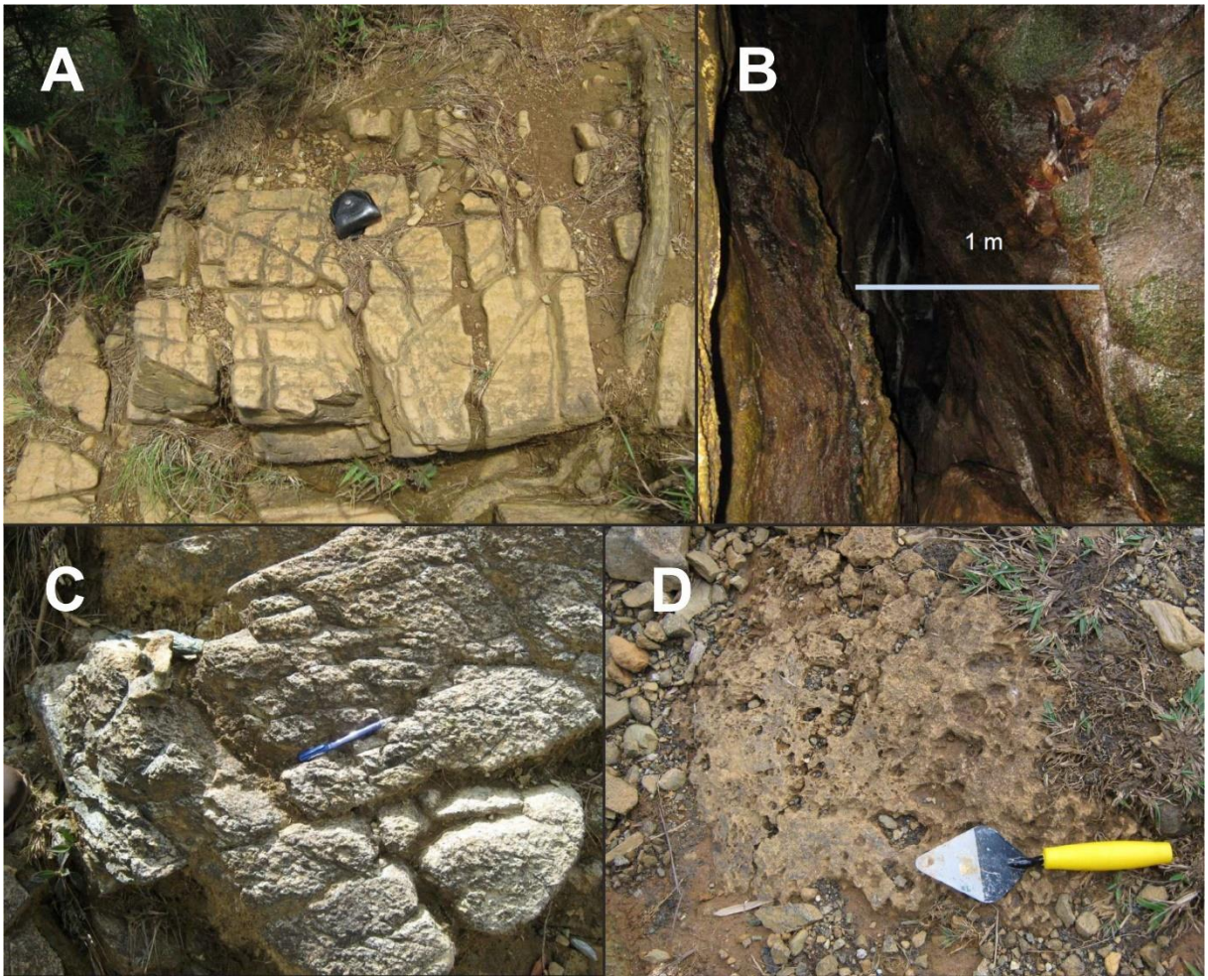

Figure 7: Forms of karst found in the Medellín Dunite; A = spitzkarren , B = karst cavern, C = rillenkarren, D = rundkarren (after TOBÓN-HINCAPIÉ et al. 2011).

The subtropical climate with periodically heavy rainfall events, the topography with a high relief and the geology with highly weathered mafic and ultramafic units make the Aburrá Valley susceptible to landslide events (HIDALGO & VEGA 2014). At present, 200,000 inhabitants of the Aburrá Valley live in informal settlements and are especially exposed to the dangers of landslides, since these settlements reach into the steep valley slopes (THURO et al. 2020). The exposure towards landslides is further increasing due to an exponentially growing habitation of these steep slopes due to rural exodus and refugees from Venezuela coming to the city (www-11, www-12).

The four main factors that promote landslides in the Aburrá Valley are slope inclination, lithology, hydrology, and human intervention (ECHEVERRI et al. 2012). Slopes with an inclination of more than 20 % are generally prone to landslides (Figure 9: medium hazard), slopes of around 50 % inclination represent a high hazard (Figure 9) (ECHEVERRI et al. 2012). The red marked area in Figure 9 (very high hazard) is mainly dominated by the weathered Medellín Dunite presented in chapter 3.1. This weathered material is highly unstable especially when saturated, since the water reduces soil strength and finally leads to slope failure (ARISTIZÁBAL et al. 2015, CROSTA & FRATTINI 2008). The total annual precipitation in Medellín lies between 1,500 and 2,300 mm/a (ECHEVERRI et al. 2012), therefore, landslides occur especially during the rainy seasons in May and November (OJEDA & DONNELLY 2006). Typical human interventions in the Aburrá Valley promoting landslides are small constructions (e.g. slope foot cutting), civil engineering constructions (roads, dams, bridges, buildings), incorrect land management and discharge of wastewater, overloading of slopes, deforestation, and fires (OJEDA & DONNELLY 2006). These

measures either decrease the soil stability (slope foot cutting, deforestation, fires) or increase the weight on the slope (buildings, water infiltration).

Figure 8: Landslide hazard map of Colombia (after LEISGANG 2021, OJEDA & DONNELLY 2006 and www-01).

The main triggers for landslides in the Aburrá Valley are human activities and rainfall, already explained above as promoting factors (ECHEVERRI et al. 2012, OJEDA & DONNELLY 2006). Since intense rainfalls often lead to shallow (0.3-2.0 m) to mid-seated landslides (2.0-10.0 m) according to the Swiss BUNDESAMT FÜR UMWELT (BAFU 2016), especially in weathered rock on steep terrain (WIECZOREK 1997), shallow to mid-seated landslides are dominant. The most devastating landslide in Medellín, the Villa Tina landslide in 1987, was only 1.0–8.0 m deep but had 20,000–40,000 m^3 of volume (TOKUHIRO 1988, OJEDA & DONNELLY 2006, HERMELÍN 2005). This indicates that the landslides in the Medellín Dunite are, in fact, mostly shallow to mid-seated, but the possibility of a deep-seated landslide cannot be ruled out completely (BREUNINGER et al. 2021c). The dominating landslide types at the Aburrá Valley are

rotational/translational slides as well as, subordinately, earth, debris, and mud flows (ECHEVERRI et al. 2012). The size of a landslide and its runout is controlled by the area and the slope angle it occurs in and cannot be predicted, which is the main challenge for any form of early warning in Medellín and one of the key problems for the design and implementation of the EWES of Inform@Risk.

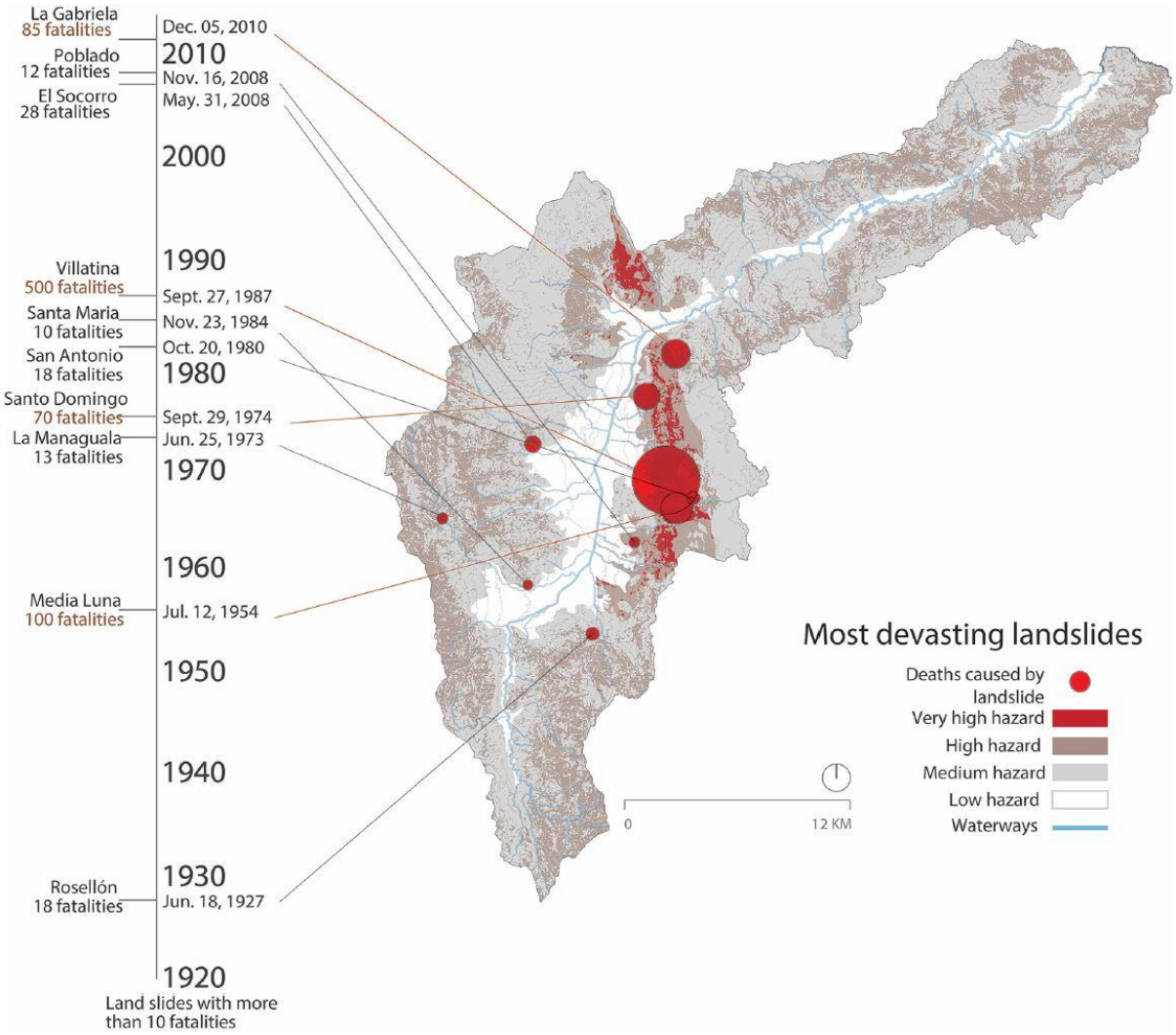

Figure 9: Landslide events with more than 10 fatalities in the Aburrá Valley since 1920 (after ECHEVERRI et al. 2012).

3.3 Landslide Risk and Hazard Assessment

Landslide risk is defined as the product of the hazard and the damage it is expected to cause to infrastructure, property, animals, and humans (BAFU 2016). In this context, hazard is the appearance of a natural disaster, like a landslide, with potentially damaging outcome (THURO et al. 2020). As visible in the risk cycle in Figure 10, the key elements of risk management are the identification, analysis, evaluation, and assessment of the prevailing risks, resulting in various measures covering the three phases preparedness, response, and recovery. The development of an EWES is a key tool within the risk cycle and a specific measure of the "preparedness" phase (emergency provisions – warning and alert systems) (LEISGANG 2021).

In Medellín the landslide risk and hazard assessment is established in a methodological guideline (SERVICIO GEOLÓGICO COLOMBIANO 2015). This local guideline aims towards a detailed risk analysis, using basic cartography (1 : 2,000), digital terrane models (1 : 2,000), remote sensing data, topographic profiles, cadastral information (1 : 2,000), and rainfall and seismic records to create a geotechnical model of a study area. The output of this analysis is a hazard map categorizing the probability of failure of that study area in low (green), medium (yellow) and high (red). This assessment is based on existing and

remote sensing data and should also include field observations and investigations like physical mappings, drillings, electrical measurements, and laboratory tests. In addition to the fatal landslide events, Figure 9 also shows a hazard map of the Aburrá Valley. In this analysis, the hazard is solely determined using the slope inclination and lithology:

- low hazard: < 20 % inclination;
- medium hazard: 20-50 % inclination in all units but the Medellín Dunite;
- high hazard: > 50 % inclination or > 20 % inclination in Medellín Dunite;
- very high hazard: > 50 % inclination in Medellín Dunite (ECHEVERRI et al. 2012).

Figure 10: Risk Management Cycle, depicting all stages of risk management (www-13).

Despite the above-mentioned guideline advising detailed field investigations, this rough, general, and solely numerical approach is common in the Aburrá Valley and Colombia when analysing hazard and risk, since hazard is mostly determined on a regional scale (HIDALGO & VEGA 2014, HIDALGO & VEGA 2015, KLIMEŠ & RIOS ESCOBAR 2010, VEGA et al. 2017, ARISTIZÁBAL et al. 2017, ARISTIZÁBAL & GARCÍA-ARISTIZÁBAL 2020). All these studies use inclination information, hydrological and general lithological data, and landslide inventories/databases, etc. for their numerical models and calculations and do not include actual field observations. It is a GIS-based approach to analyse the slip susceptibility

using sensitivity analyses, earthquake activity and rainfall data to obtain information on hazard potential on a regional scale (HIDALGO & VEGA 2015, VAN WESTEN & TERLIEN 1996, THURO et al. 2020).

This approach was also used by the project partners DLR and SLU to create a hazard map on city level (Figure 11) (WERTHMANN et al. 2024). It depicts the developed areas and the precarious/informal settlements of the city. The study site of the project is within the high hazard area. Since the approach for the creation of this map was similar to the one used to create the map in Figure 9, the hazard area also has a very similar extent in both maps.

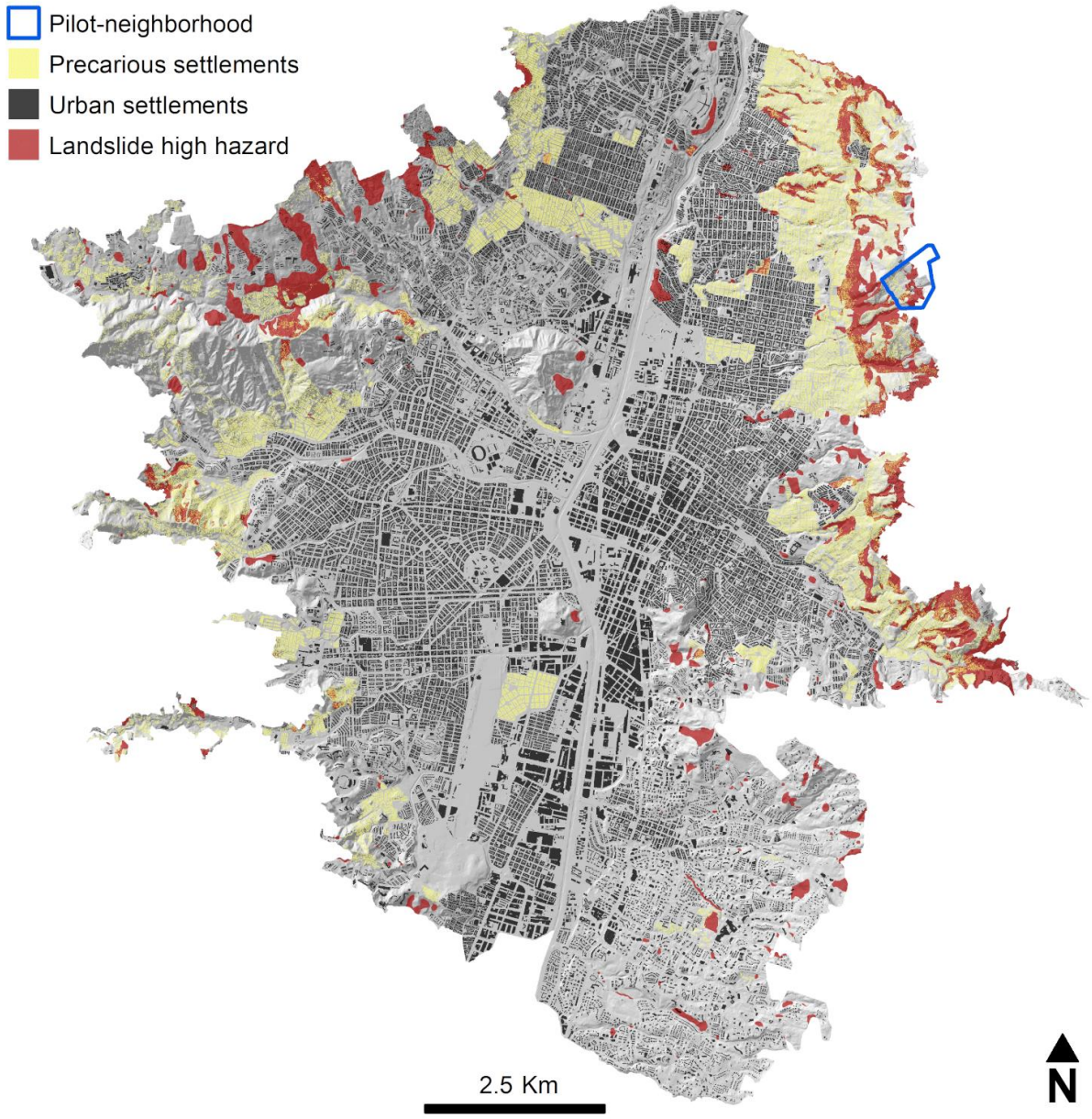

Figure 11: Landslide risk in Medellín at city scale and precarious/informal settlements of the city (WERTHMANN et al. 2024).

A more detailed approach is used in Switzerland (BAFU 2016): The maps serving as input data for numerical models and hazard/risk assessments include detailed field studies and optional laboratory analyses of the study area. The output is a hazard map, depicting the five hazard levels high (red), medium (blue), low (yellow), residual (white-yellow crosshatched), and no hazard (white), that are a combination of the probability and the intensity of an event; the intensity is defined by the impact of an event on infrastructure, animals, and humans and is categorized into three intensity levels (high, medium, low); the probability is defined as the return period of an event, categorized into 30, 100, and 300 years return period. With increasing event size, the intensity increases, while the probability usually decreases.

4 Methodology

Parts of this chapter have already been published in BREUNINGER et al. (2021a), BREUNINGER et al. (2021b), BREUNINGER et al. (2021c), BREUNINGER et al. (2023b), in the Master's theses of AGNES DEMHARTER (2021) and JULIA PETZI (2022), and in the Bachelor's theses of PATRICIA AMBOS (2020) and JOSEFINE ZIEGLER (2020).

Most of the landslides and the most devastating ones have occurred in the very high hazard area in the Medellín Dunite (Figure 9). To create an effective EWES for a small area like the study site in Bello Oriente, the hazard assessment and the resulting hazard map of the area need to have a higher spatial precision than these regional analyses. The distribution of the sensors of this system is highly dependent on the risk distribution, which in turn is dependent on the hazard category and the density of elements at risk in a certain area. To reach a detailed hazard assessment designating different hazard levels, the study site needs to be investigated using various methods.

The geological investigation of the study site Bello Oriente was conducted using a combination of field mapping, geo-electrical measurements, drillings, joint recordings, and laboratory tests (chapters 4.1-4.6). This combination of methods enabled the synthesis of different types of data, obtained by these investigations, into a simple underground model of the study site (chapter 4.7). This model served as the basis for the hazard assessment (chapter 4.8). The investigations took place during several field campaigns over 2½ years:

- first field campaign in August 2019 (process map and ERT measurements),
- second field campaign in February 2020 (geological map, sampling for thin section analysis and first XRD measurements),
- first drilling campaign in fall 2020 (drillings A1/A2/B1, including laboratory tests on the cores),
- second drilling campaign in fall 2021 (drilling B2, including laboratory tests on the core),
- laboratory tests on the trench samples from the test installation of the CSM system in fall 2021,
- laboratory tests on the trench samples from the final installation of the CSM system in winter 2021/2022.

Since the study site is densely populated, all these investigations were performed with the acceptance and help of the community members. Therefore, the social integration of the scientists working in the field into the community of the study site was vital and the social scientific approach will also be discussed in this chapter (chapter 4.9).

4.1 Mapping of Past Landslides (Process Map)

During the first field campaign in August 2019 the landslide features (tear-off edges, accumulative ridges, depressions, trenches, ridges, fissure etc.) of several historic landslides were recorded to understand the landslide dynamics in this area and to be able to validate numerical models using back analysis methods (BREUNINGER et al. 2021c). This mapping took place over four days. The recording of former events was only possible with the help of the residents, since the whole study site is anthropogenically changed and densely vegetated, which makes the registration of morphological landslide indicators difficult. The residents provided information on age, size, and speed of several mass movements in the study site (BREUNINGER et al. 2021c). Additionally, the depth of each landslide was estimated based on the height of the tear-off edges, the depth of the depressions, and the volume of the accumulative ridges.

4.2 Mapping of Geological Features (Geological Map)

In February 2020, during the second field campaign, the geological composition of the study site was recorded. Since the whole area lies within the geological unit of the Medellín Dunite, the different conditions of the Medellín Dunite were assessed. The main goal was to determine the ratio of blocks and matrix in the block-and-matrix structures, since these are most prone to landslides with increasing content of fine material (water storage properties) and the areas with in-situ rock, which are not likely to

fail (BREUNINGER et al. 2021c). During the works conducted in this field campaign, the help of the residents was again of great importance.

4.3 Drillings

The first drilling campaign was planned for May 2020. Due to the COVID-19-caused lockdown in both Germany and Colombia starting in March 2020, the drillings have been performed in fall 2020 (A1, A2, B1). A fourth drilling was conducted in October and November 2021 (B2). All drilling locations can be seen in Figure 12. Their locations were chosen regarding the expected thickness of soil cover (at least 10 m) and their contribution to the early warning system with CSM cables, piezometers and inclinometer casings being installed after the drilling campaign (SINGER et al. 2021). Additionally, the drillings are all located along ERT transects, B1 and A2 are located at or very near a crossing of two ERT transects (see chapter 4.5). This spatial link of different methods was chosen to better combine the information retrieved. A drilling depth of 30.4 m for A1, 30.3 m for A2 and 50.0 m for B1 and B2 could be achieved. Drillings B1 and B2 are among the deepest drillings ever performed in the Medellín Dunite (RENDÓN-GIRALDO 2020). All drillings were performed by the company Integral S.A.S., based in Medellín, using the double core rope drilling method without oriented cores. The inner diameter of drillings B1 and B2 is 101.6 mm, the inner diameter of the drillings A1 and A2 is 63.5 mm. The bigger diameter in drillings B1 and B2 was chosen to fit an inclinometer casing in the borehole in addition to two CSM cables and four piezometers. A1 and A2 do not include an inclinometer casing.

Due to the travel restrictions caused by the pandemic the drillings were supervised and surveyed by the local geologist David Cerón-Hernandez. Using his descriptions and pictures taken in the field all drilling cores were evaluated regarding the core loss, weathering stages (DIN EN ISO 14689 2018), RQD (DEERE 1964), fracture ratio *k* (STINY 1922), joint sets, and alteration type. Based on all these parameters, seven homogeneous areas were established; Homogenous area 0 is fresh core, homogeneous areas 2–6 show increasing decomposition of the core, homogeneous area 1 is topsoil and fillings.

The core loss was calculated from the core recovery data. In contrast to common practice in Germany, their exact depth in the drilling sections is not marked by placeholders in the core boxes, so that the exact position remains unclear. The orientation of the joints and their categorization into joint sets was based solely on their dip angle, as the boreholes were drilled without orientation. To visualize the joint sets a non-oriented tadpole presentation with 15° steps was chosen. The three forms of weathering – oxidation, serpentinisation and fragmentation – were identified based on the drilling core photos. To be able to present the evaluation of the drilling cores more clearly, the properties were then graphically depicted at a scale of 1:100 using CorelDraw Graphics Suite 2019 (DEMHARTER 2021).

4.4 Joint Recording

For a better understanding of the tectonic conditions of the study site and an adequate categorization of the joint sets encountered in the drillings in the context of these conditions, joint recordings on two different scales took place: (1) a hillshade (DEM) analysis which provided the general distribution of fractures in the study area, and (2) scanlines on some outcrops in the study area which provided a very detailed account of the local fracture network (GAMPERL et al. in review).

The hillshade analysis was performed on a digital elevation model which was generated using UAV elevation data of the study site. The data was received and analysed by the Technical University of Deggendorf (THD) as part of the Inform@Risk research project (WERTHMANN et al. 2024). The structures visible in the hillshade were combined with the pre-existing structural geology of the Aburrá Valley (GARCIA-CASCO et al. 2020, GAMPERL et al. in review).

The scanline analysis was performed by David Cerón-Hernandez on eleven outcrops in the study site with 2.5 to 7.0 m width after PRIEST (1993) (Figure 13). The results of the scanlines were compared with the fracture distribution in the drillings and the fracture dip angle and dip direction of the city model

and checked for plausibility. The resulting fracture system for the study area was combined to a map and a structural model using "Dips" by "Rocscience" (GAMPERL et al. in review).

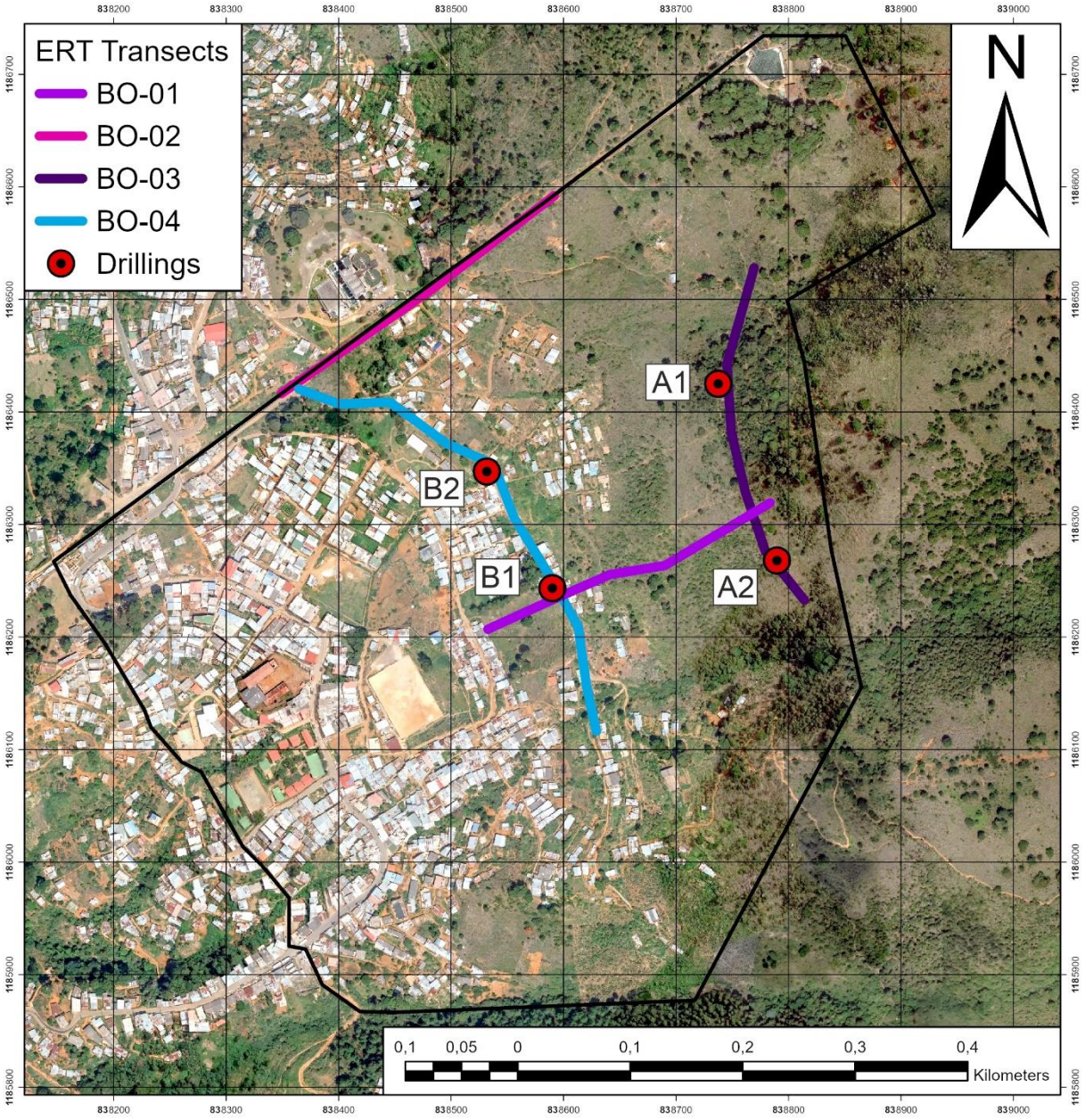

Figure 12: Locations of the drillings and ERT transects in Bello Oriente (after BREUNINGER et al. 2023a).

4.5 ERT Measurements

During the first field campaign in August 2019 four ERT transects were measured in the study site, after the process mapping (chapter 4.1). Their location in visible in Figure 12. The transects were chosen perpendicular along and across the slope to create a 2.5D picture of the subsurface (GAMPERL et al. in review).

The measurements were performed using an ABEM LS2 system (Guideline Geo) and two ABEM Lund cable sets. The electrode spacing was 5 m and with two 32 electrode cables, a total profile length of about 315 m can be achieved, with roll along measurements naturally yielding longer profiles. Transects BO-01, BO-02 and BO-03 are 315 m long, transect B-04 reached 475 m using one roll along measurement (GAMPERL et al. in review). An experimental measurement on a short transect was performed earlier (May 2019) in order to find out the most suitable electrode configuration. It was observed that

the Wenner-Array yields the best results, especially for the expected mostly horizontal geological features (OTTO & SASS 2006). The power line frequency was adapted to the local value (60 hz for Colombia). Since the measurements were performed during the dry season, some electrodes had to be treated with salt water in order to create sufficient contact between the electrodes and the ground (GAMPERL et al. in review).

The inversion and display of the ERT-profiles was carried out using the software RES2DINV by Geotomo software. Due to high resistivity gradients on the surface, robust inversion was chosen, and the mesh was refined to allow for more contrast in the inversion, resulting in an RMS Error of 5.9 % (BO-01) and 5.7 % (BO-03). The results were first calibrated by measuring a dunite block of about 20x15x10 cm with visually little weathering at TUM. The result was a mean apparent resistivity of 22 kΩm (GAMPERL et al. in review). Secondly, the direct information retrieved by the drillings was used to revalidate and calibrate the interpretation of the ERT results (GAMPERL et al. in review).

4.6 Laboratory Tests

Like the drillings, the laboratory tests performed in the project were conducted by the company Integral S.A.S. in Medellín. The rock samples tested were all taken from the cores of the four drillings, while the soil tests were also conducted on some samples from the drilling cores, but most of them on samples taken from trenches (up to 0.5 m depth) dug for the installation of the CSM cables for the EWES. All trench sampling locations are visible in Figure 13.

The rock tests included the uniaxial compressive strength test according to ASTM D 7012-14e1 (2014) and the tensile strength test/Brazilian test according to ASTM D 3967 (2016). The soil tests included the grain size analysis according to I.N.V. E-123 (2013) and I.N.V. E-124 (2013), the Atterberg limits test according to I.N.V. E-125 (2013) and I.N.V. E-126 (2013), and the direct shear test according to I.N.V. E-154 (2013). Additionally, mineralogical tests were conducted on some samples; a thin section analysis of rock samples collected on the surface and an x-ray diffractometry (XRD) on samples collected on the surface and on samples taken from the trenches for the CSM cables for the EWES. The sampling locations of the samples taken from the surface are visible in Figure 13. The thin sections were made and analysed at the TUM in Munich, the XRD samples were made and analysed partly in Munich and partly in Medellín.

4.6.1 Uniaxial Compressive Strength Test

The uniaxial compressive strength tests (USC tests) were conducted according to ASTM D 7012-14e1 (2014). This standard includes four methods: method A and B cover triaxial compressive strength tests, methods C and D uniaxial compressive strength tests. All tests were conducted according to method C "Uniaxial Compressive Strength of Intact Rock Core Specimens" (ASTM D 7012-14e1 2014).

The test conditions are stated and compared to the German recommendation for uniaxial compressive strength tests of the DEUTSCHE GESELLSCHAFT FÜR GEOTECHNIK (DGGT 2022a) in Table 3. Uniaxial compressive strength tests were performed on 22 samples from all four drilling cores, Table 4 shows the number of tests per drilling.

Table 3: USC test conditions according to ASTM D 7012-14e (2014) and DGGT (2022a) (after PETZI 2022).

Parameter	ASTM D 7021-14e (2014)	DGGT (2022a)
Specimen length-to-diameter ratio	2.0-2.5	2.0
Minimum diameter of the specimen	47 mm	30 mm
Applied stress rate	0.5-1.0 MPa/s	0.1-0.5 MPa/s
Applied strain rate	constant	constant
Time until failure	2-5 minutes	minimum 5 minutes

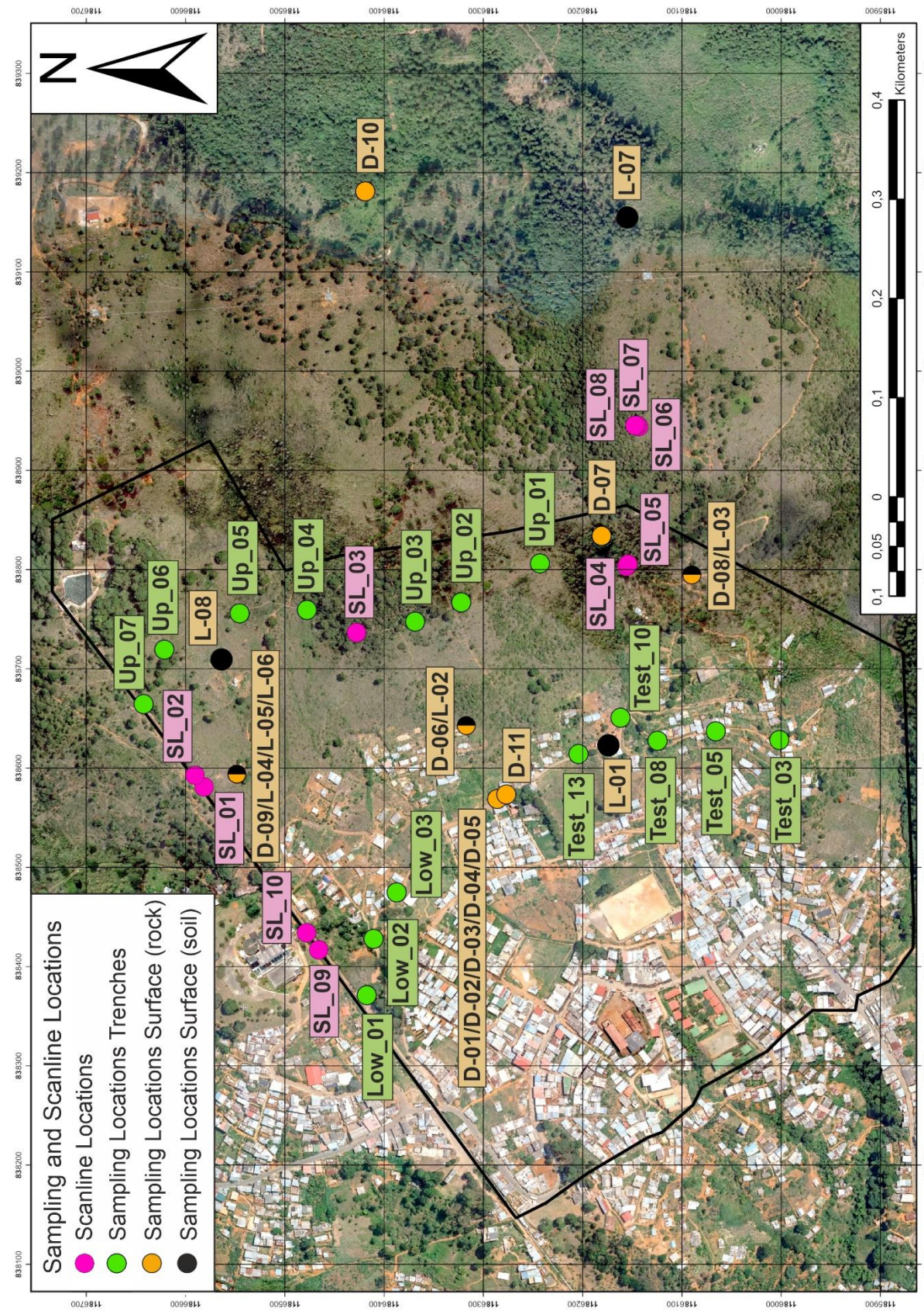

Figure 13: Location of all scanlines, trench samplings, and surface samplings in the project.

Table 4: Number of UCS tests and Brazilian tests per drilling.

Drilling	Number of USC tests	Number of Brazilian tests
A1	6	6
A2	6	6
B1	6	6
B2	4	4

4.6.2 Brazilian Test

The tensile strength tests (Brazilian tests) were conducted according to ASTM D 3967 (2016). Unlike stated in the standard (length-diameter-ratio of 0.5–0.6) the length-diameter-ratio of the samples used was 0.68 on average.

The conditions of the test are stated and compared to the German recommendation for indirect tensile strength tests DGGT (2022b) in Table 5. Brazilian tests were performed on 22 samples from all four drilling cores. Table 4 shows the number of tests per drilling.

Table 5: Splitting tensile strength test (Brazilian test) conditions according to ASTM D 3967 (2016) and DGGT (2022b) (after PETZI 2022).

Parameter	ASTM D 3967 (2016)	DGGT (2022b)
Specimen thickness-to-diameter ratio	0.20-0.75	0.50
Minimum diameter of the specimen	50 mm	10x size of biggest grain
Allowed deviation in the smoothness	± 0.5 mm	-
Time until failure	1-10 minutes	2-5 minutes
Loading rate	0.50-0.35 MPa/s	(0.01-0.05 MPa/s)

4.6.3 Grain Size Analysis

The grain size analysis was conducted according to I.N.V. E-123 (2013) and I.N.V. E-124 (2013), the evaluation of the results, however, was done after DIN EN ISO 14688-1 (2020) due to the international standardization level of the ISO standards. The analysis was conducted on ten drilling samples and 14 trench samples.

The main differences between the Colombian and German standards are the used mesh sizes for the sieving and the minimum sample quantity. The mesh sizes used in I.N.V. E-123 (2013) and those used in the German standard DIN EN ISO 17892-4 (2017) are compared in Table 6, the minimum sample quantity is compared in Table 7. In general, the mesh sizes in the Colombian standard have a closer spacing than in the German one.

Every sample is in divided into the two fractions > 2 mm and < 2 mm. The fractions are analysed separately. Both fractions are sieved, the coarse fraction (> 2 mm) with mesh sizes of 75.0-2.0 mm, the fine fraction (< 2 mm) with mesh sizes 2.0 mm - 75 µm (0.075 mm). If the clayey material in the fine fraction is too bonded, the material is sieved wet.

The fraction < 75 µm is analysed using the sedimentation method with hydrometer according to I.N.V. E-124 (2013). The used hydrometer must be in conformity with the requirements for hydrometers 151H or 152H, specified in ASTM E 100 (2019). The scale is either the specific gravity or g/l of suspension. According to DIN EN ISO 17892-4 (2017), the hydrometer must be conform with a national standard without naming a specific standard and show a scaling between 0.995 g/ml and 1.030 g/ml (PETZI 2022).

Table 6: Comparison of mesh sizes used in the project according to I.N.V. E-123 (2013) and DIN EN ISO 17892-4 (2017) (after DEMHARTER 2021).

I.N.V. E-123 (2013) [mm]	I.N.V. E-123 (2013) Sieve number	DIN EN ISO 17892-4 (2017) [mm]
63.0	2 1/2“	63.0
50.0	2“	-
37.5	1 1/2“	-
25.0	1“	-
19.0	3/4“	20.0
12.5	1/2“	-
9.5	3/8“	-
4.75	No. 4	6.3
2.0	No. 10	2.0
0.85	No. 20	0.63
0.425	No. 40	0.4 (if needed)
0.250	No. 60	0.2
0.150	No. 100	0.125 (if needed)
0.075	No. 200	0.063

Table 7: Comparison of minimum sample quantity per largest grain size of I.N.V. E-123 (2013) and DIN EN ISO 17892-4 (2017) (after DEMHARTER 2021).

I.N.V. E-123 (2013)		DIN EN ISO 17892-4 (2017)	
Largest grain size [mm]	Minimum quantity (dry) [g]	Largest grain size [mm]	Minimum quantity (dry) [g]
-	-	2.0	100
-	-	6.3	300
9.5	1,000	10.0	500
12.5	2,000	-	-
19.0	5,000	20.0	2,000
25.0	10,000	-	-
37.5	15,000	37.5	14,000
50.0	20,000	-	-
63.0	35,000	63.0	40,000

The differences in the hydrometer analysis between the Colombian standard (I.N.V. E-124 (2013) and the German standard DIN EN ISO 17892-4 (2017) are listed in Table 8. Both standards require sodium hexametaphosphate with a concentration of 40 g/l as suspension agent, a sieve analysis of the material

> 0.075 mm (Colombia standard)/> 0.063 mm (German standard), 1,000 ml suspension in distilled water, shaking of the cylinder for one minute before starting the analysis, and a constant water temperature (PETZI 2022).

Table 8: Comparison of test conditions of the hydrometer analysis of I.N.V. E-124 (2013) and DIN EN ISO 17892-4 (2017) (after PETZI 2022).

	I.N.V. E-124 (2013)	**DIN EN ISO 17892-4 (2017)**
Required amount of sample	65 g for silty/clayey samples 115 g for sandy samples	20-30 g of grains < 0.063 mm
Amount of suspension agent	125 ml	10 % of total suspension
Soaking of suspension agent and stirring	Soaking of 16 hours, then stirring for 1-15 minutes	Stirring of 4 hours directly after adding suspension agent
Sieving of fine material	After hydrometer analysis	Before hydrometer analysis
Smallest grain size for sieving	0.075 mm	0.063 mm
Temperature requirements	Temperature in cylinder 20 °C	Allowed deviation of 3 °C
End of hydrometer analysis	After reading at minute 1,440	After determination of fraction < 0.002 mm
Placing of hydrometer into cylinder	20-25 seconds before reading	15 seconds before reading
Recommended times for readings in minutes	2, 5, 15, 30, 60, 250, 1,440	0.5, 1, 2, 4, 8, 30, 60, 120, 360, 1,440
Accuracy	not specified	0.0005 g/ml

4.6.4 Atterberg Limits Analysis

The Atterberg limits tests were conducted according to I.N.V. E-125 (2013) (liquid limit) using the Casagrande device and I.N.V. E-126 (2013) (plastic limit and plasticity index). Ten drilling samples and 14 trench samples were analysed. Both standards correspond with the German standard DIN EN ISO 17892-12 (2020).

The differences between the Colombian and the German standard in conducting the liquid limit analysis are listed in Table 9, the differences regarding the conduction of the plastic limit analysis are listed in Table 10.

Table 9: Comparison of test conditions for the determination of the liquid limit between I.N.V. E-125 (2013) and DIN EN ISO 17892-12 (2020) (after PETZI 2022).

	I.N.V. E-125 (2013)	**DIN EN ISO 17892-12 (2020)**
Sample Quantity [g]	150-200	200
Max. grain size [mm]	0.425	0.400-0.425
Length of contact [mm]	13	10
Range of number of strokes	15-35	15-40
Number of trials	min. 3	min. 4
Testing methods	Multi-point of single point	Four-point of single point
Requirements on samples used for the water content analysis	Conditions about sampling location	15 g

Table 10: Comparison of test conditions for the determination of the plastic limit between I.N.V. E-126 (2013) and DIN EN ISO 17892-12 (2020) (after PETZI 2022).

	I.N.V. E-126 (2013)	**DIN EN ISO 17892-12 (2020)**
Total sample quantity [g]	15-20	20
Max. grain size [mm]	0.425	0.4
Diameter of the roll [mm]	3.2	3.0
Sample quantity for one water content analysis [g]	6.0	Not specified
Number of portions for water content analysis	2	3

The calculation of liquid limit, plastic limit, and plasticity index is the same in the Colombian standard as it is in the German standard. The consistency index, the liquidity index, and the activity index are not explicitly calculated in the Colombian standard.

According to the Colombian standard, the soil classification is based in the US standards USCS (Unified Soil Classification System) (ASTM D 2487-17e1 2017) and AASHTO (American Association of State Highway and Transportation Officials) (ASTM D 3282 2015). Because of the international standardization level of the ISO standards the classification was additionally done after DIN EN ISO 14688-2 (2020).

4.6.5 Direct Shear Test

The direct shear tests were conducted drained and consolidated after the Colombian standard I.N.V. E-154 (2013) on three drilling samples and 13 trench samples. The corresponding German standard is the DIN EN ISO 17892-10 (2019).

For each test three separate samples were used, which is the minimum sample quantity for each test (I.N.V E-154 2013). The standards (Colombian vs. German) differ regarding the minimum sample height, the minimum diameter-height-ratio, and the conditions for the termination of the test (Table 11) (DEMHARTER 2021).

Table 11: Comparison of the test conditions for the shear test between I.N.V. E-154 (2013) and DIN EN ISO 17892-10 (2019) (after PETZI 2022).

	I.N.V. E-154 (2013)	**DIN EN ISO 17892-10 (2020)**
Minimum sample thickness [mm]	12	20
Minimum diameter-height ratio	2.0	2.5
End of test	Shear stress constant or displacement of 10 %	Max. horizontal shear stress reached or displacement of 15 %

The test was conducted with a shear velocity of 0.2 mm/min after 60 min. of consolidation. The samples were taken with cut-out cylinders directly from the drilling cores and the trenches and had a diameter of 50.0 mm and a height of 25.4 mm, with a diameter-height-ratio of approximately 2.0.

4.6.6 Thin Section Analysis of Dunites

All thin sections analysed in the project were produced in the laboratories of the Chair of Engineering Geology of the TUM by technician Cordula Bode and Patricia Ambos within the scope of the latter's

Bachelor's thesis. The size of each thin section is 24x32 mm, the thickness is 30 µm, and the embedding agent is a mixture of epoxy casting resin and a hardener with a ratio of exactly 100:35 (AMBOS 2020).

The analysis of the thin section was conducted at the TUM by Patricia Ambos and Dr. Gerhard Lehrberger with a polarization microscope and the minerals were determined using the works TRÖGER (1969) and TRÖGER (1982) and additionally MACKENZIE & ADAMS (1995), MARKL (2015), and OKRUSCH & MATTHES (2014).

All ten analysed samples (resulting in 11 thin sections) were collected from the surface during the field campaign in February 2020. The sampling locations are visible in Figure 13 (samples D-01–D-10). Sample D-11 was not analysed.

4.6.7 X-Ray Diffractometry of Soil Samples

The x-ray diffractometry (XRD) was conducted on eight samples taken from the surface during the field campaign in February 2020 and on ten samples taken from the trenches for the CSM cables.

With the XRD analysis minerals can be detected using the wave length λ of x-rays, used to irradiate a sample, in a specific diffraction angle θ (DESLATTES & HENINS 1973). This diffraction angle θ is used to determine the lattice space d between the different layers/lattices of a mineral where the beams are diffracted (DESLATTES & HENINS 1973). Since this lattice space d is very distinctive for each mineral and, therefore, also the diffraction angle θ, minerals can be determined using the Bragg equation (BRAGG & BRAGG 1915):

$$n\lambda = 2d\,\sin(\theta)$$

The path difference or diffraction order n is the number of the layer/lattice, where the beam is diffracted. One mineral diffracts multiple beams, since x-rays reach every layer of the mineral, not only the uppermost (ERMRICH & OPPER 2011). The wavelength of the anode is known, the diffraction angle is recorded during the test. The final diagram shows the intensities measured for each 2θ angle. The intensity depends on crystal structure, phase quantities, and preferred orientation (ERMRICH & OPPER 2011).

During the field campaign in February 2020 eight soil samples were taken from the surface in the study site (see Figure 13; samples L-01–L-08). These samples were prepared and tested at the Chair of Engineering Geology of the TUM in Munich. The sample preparation was done by Josefine Ziegler within the scope of her Bachelor's thesis, the XRD analysis was conducted by Prof. Dr. Hans Albert Gilg using Cu-Kα radiation, the evaluation was done by Josefine Ziegler. To prepare the oriented samples the material was grinded in an agate mortar and then transferred to an Atterberg cylinder with distilled water (ZIEGLER 2020). After 15.5 h, when the suspension only contained clay, a small amount of the suspension was centrifuged, drained and enriched (ZIEGLER 2020). The material was then treated with 0.3 M sodium citrate ($Na_3C_6H_5O_7$), 1 M sodium bicarbonate ($NaHCO_3$), and dithionite ($Na_2S_2O_4$) after MEHRA & JACKSON (2013) to extract the iron oxides and hydroxides, which overlay the diffraction of other minerals (ZIEGLER 2020). After the first measurement of the oriented samples, they were glycolized and measured again to be able to see shifts in the diffraction peaks of the clay minerals due to swelling (ZIEGLER 2020). The graphs were made with Profex 4.1.0 and analysed after BRINDLEY & BROWN (1982) and using empirical structure files provided by Prof. Dr. Hans-Albert Gilg.

The XRD of the ten trench samples was performed by the company Integral S.A.S. in Medellín, using a Rigaku Miniflex 6GC with Cu tube anode for measurements. All samples were first pulverized with an agate mortar. For the pulverized samples, the material was then sieved to only use the fraction of < 70 µm and pressed into tablets. The oriented samples were prepared using only the fraction of < 2 µm of the pulverized material, which was dispersed in deionized water. After 10 minutes one cm^3 of the suspension was dropped on a piece of glass, where it dried and left a thin layer of oriented minerals. After the oriented samples were tested, they were saturated with ethylene glycol in a vacuum of 0.3 atm

and dried at 500 °C for three hours. These three different types of samples (pulverized, oriented, glycolized) allow to differentiate the clay minerals by their different reaction to these treatments. The evaluation was done after the Rietvelt method (RIETVELD 2010).

4.7 Underground Model

The underground model of the study site was created by using all information retrieved from the results of the measures described in chapters 4.1-4.6.

A first, preliminary model was created after the first field campaign in August 2019. The information retrieved during that campaign included the process map (chapter 4.1) and the four ERT transects (chapter 4.5). This model was not yet complemented by any direct measurements or observations, since the only subsurface information came from an indirect method (ERT transects).

After the results of the first three drillings, the laboratory tests performed on the drilling cores, and the joint recordings were analysed, a second underground model, including all this information, was developed (late 2020/early 2021). This model was further adjusted with new information from the fourth drilling and the laboratory results from this drilling core and the trench samples being available.

The subsurface was visualised in two different ways, three profiles along three of the ERT transects and a colluvial map of the study area.

Three of the four ERT transects measured (Figure 12) were interpreted and transferred into visual 2D profiles under the direction of Prof. Dr. Michael Krautblatter, head of the Chair of Landslides at the TUM. The first interpretation only included the information from the ERT measurements. After the drillings and the results from the laboratory tests on the drilling cores were performed, this data was used to create a second, more detailed version of the profiles. The fourth ERT measurement (BO-02) could not be evaluated (see chapter 5.5).

Since the weathered and colluvial material (block-in-matrix-structure, see chapter 3.1) was recognized as the most landslide prone, the determination of the approximate thickness of this material and its border to the in-situ rock in the study site was crucial for the approximation of the magnitude of a possible event and the designation of areas at risk. A colluvial map depicting this depth was created using the results of the first three drillings and the ERT measurements. After the fourth drilling was evaluated, this map was adjusted according to the newly acquired information.

4.8 Hazard Assessment

The hazard assessment in the project aimed towards the determination of hazard areas and subsequently into a hazard map of the study site. This map was created after the Swiss model (BAFU 2016), categorizing the hazard areas of the study site according to the frequency and the magnitude of potential events. The main input into the analysis were the two maps created during field work and the underground model: the process map (see chapter 4.1), the geological map (see chapter 4.2), and the colluvial map (see chapter 4.7).

The geological map was used to generally determine areas that are prone to landslides: the block-in-matrix-structure (see chapter 3.1) and, potentially, the saprolite, since this unit is already heavily altered and could fail during heavy rainfall. The in-situ rock was not considered to fail under normal circumstances.

The frequency and magnitude of the typical events in the study site were derived from the process map created during the first field campaign in August 2019 (see chapter 4.1) and the SIMMA (www-14) database from AMVA (Àrea Metropolitana Valle de Aburrá). All registered landslides were plotted into a magnitude-frequency diagram and categorized according to both properties.

With the information of the critical slope angle and the runout derived from the information of the registered events and the distribution of block-in-matrix-structure and saprolite visible in the geological

map, a hazard map for each process magnitude was created; areas with the same or a higher slope angle than the typical angle of failure determined for that magnitude and containing block-in-matrix-structure or saprolite were categorized as hazard areas. Depending on the size of a typical event of that magnitude, smaller areas of no hazard between areas of hazard were included into the hazard area. The runout was determined using an angle of 5° as the maximum angle of movement, with the starting point of the runout at the end of a potential event of each magnitude.

The results of this assessment were hazard maps depicting the potential hazard of a landslide of a certain magnitude. All magnitude hazard maps combined resulted in a "synthesis map" which was used to determine evacuation routes and safe areas by LUH and the optimal sensor distribution of the EWES by AGR.

4.9 Social Integration

This chapter is derived from BREUNINGER et al. 2021b with some changes and additions.

The biggest challenge in developing an EWES is to manage the human factors in the best possible way to improve the EWES and ensure safety for all parties involved. One of the biggest social problems in early warning is miscommunication between the different stakeholders, not only between the local population and the experts (NADIM & INTRIERI 2011). This leads to false responses and in the worst case to devastating losses in case of an event. A way to reach people in general are social media and TV, already effectively applied in Hong Kong and by the project SafeLand (NADIM & INTRIERI 2011). In some countries and societies these measures are not enough. The people need to be addressed directly, which, in this project, is achieved by (1) various workshops managed by the NGO's, LUH and Urbam and involving input from all stakeholders, (2) assistance of the geologists and technicians in the field work, (3) the construction and installation of the sensors and measurement cables, and (4) the maintenance of the sensor network.

Every month workshops were held in Bello Oriente, sometimes at the schools, sometimes at the community centre. In these workshops the Colombian partners educated the residents about preventive measures and preparation in advance of a landslide event using presentations, charts, models, and games and by creating flow charts with the people. Most importantly, there were community walks at the end of some workshops, where the residents applied their knowledge of their environment and inserted their observations into a map of the barrio. Once the geo-sensor network for the landslide detection was completed, the workshops also included talks about possible evacuation routes, safe houses and how to react to an alarm depending on the area one is in at that time. There were already some residents very eager to work in the program. It is possible, that those will be educated on first responding in case of an emergency.

During all field campaigns (August 2019, February 2020, November 2021, April 2022), there were several voluntaries from the local community helping with the work, together with voluntaries from the Geological Society of Colombia. The mapping in the rural part of the study area had to be done with at least two of the residents, otherwise it was impossible to find a way through the dense forest and high grass in this area. The people know their own home very well and were eager to show it to the scientists working with them. Also, the ERT measurements conducted in August 2019 were done with the help of the residents. This cooperation built a strong bond of trust between the residents and the scientists. Every day after the work was done, jam sessions or talks in a local bar took place, which increased the mutual trust even more.

Starting in 2021 the sensor network was installed in the barrio in several stages. To increase the residents' risk awareness and their knowledge of the sensors, the people helped building the sensors and the transmission devices. They also assisted installing them in the field in order to stay updated on the locations of the sensors. Most importantly, the excavation of the trenches for the CSM cables and their

installation was mostly done by the residents. They were employed by the executing construction company. For the workers this meant a stable income for several weeks or months. Most of the community members earn their money through day-by-day jobs, so this work meant at least some financial stability.

It is planned that the sensor network will be maintained by SIATA or DAGRD and the community. The residents have already and will further be trained in basic maintenance activities such as changing batteries in the transmission devices and make simple measurements that can be transmitted to SIATA or DAGRD via app.

The aspired outcome of these measures is that these expressions of confidence in the residents increase their sense of responsibility regarding the technology in the barrio and therefore decrease the probability of vandalism. The community members should embrace the system as their own in order to increase trust in the system and, consequently, create accurate responses to warnings and evacuation orders.

5 Results and First Evaluation

Parts of this chapter have already been published in BREUNINGER et al. (2021c), BREUNINGER et al. (2023a), BREUNINGER et al. (2023b), and in GAMPERL et al. (in review), in the Master's theses of AGNES DEMHARTER (2021) and JULIA PETZI (2022), and in the Bachelor's theses of PATRICIA AMBOS (2020) and JOSEFINE ZIEGLER (2020).

5.1 Process Map

The following chapter is derived from BREUNINGER et al. (2021c) and BREUNINGER et al. (2023a) with some changes and additions.

During the first field campaign in August 2019, an extensive map of the landslide phenomena at the study site was created (Figure 14, Figure A5) on an original mapping scale of 1:3,500. It was revised in 2022 after two new landslides had occurred. The map shows the outlines of former landslide events (the oldest being about 110 years old, the youngest occurred in 2022), and their detachment and accumulation areas. Older landslides may be existent but are masked by younger ones.

The biggest registered landslide has an area of about 15,000 m², the smallest registered landslide has an area of about 230 m². The latter occurred during the installation of the sensor system in 2022. According to the typical depth of landslides, the depth of the registered landslides was estimated to 0.5-10 m. These numbers indicate an estimated volume of about 230-150,000 m³ for the typical landslides in Bello Oriente. Most landslides are rotational slides, only one landslide was identified as a translational slide.

As a main outcome, it is suggested that most of the landslides are rotational slides, occurring to an increased extent in soil or highly weathered rock (HUNGR et al. 2014). The depths of the landslides can be specified in a range of 0.5–10 m, which could be classified as shallow to mid-seated (BAFU 2016), reflecting the majority of the landslides in Medellín in the last decades (see chapter 3.2) (TOKUHIRO 1988, HERMELÍN 2005, OJEDA & DONNELLY 2006). Within the borders of the study area, there are no indications of deep-seated landslides in the past, even though the bedrock is expected to be highly weathered and fractured up to a depth of 60 m or more. However, a deep-seated landslide could not be excluded since the morphological elements would have been eliminated due to anthropogenic influence, such as road, building and plantation construction.

Based on these current results, the probability for a detachment surface exceeding 10 m or a deep-seated landslide in the future is suggested not to be evident, but the possibility cannot be ruled out.

5.2 Geological Map

The following chapter is derived from BREUNINGER et al. (2021c) with some changes and additions.

The geological map of the study site is shown in Figure 15 and Figure A6 (original mapping scale 1 : 3,500). Two outcrops of in situ rock are ridge structures on the north-western border of the study site and in the south, both structures striking more or less SW-NE. A few other outcrops exist in the eastern part of the site (uphill). All these structures are visible on the surface as ridges, which indicates that these parts of the slope are more resistant and were not moved, e.g., due to landslides, in the past (BREUNINGER et al. 2021c).

Another prominent observation is that the strike direction of these ridges could be parallelized with one of the three joint sets mentioned in chapter 3.1 (joint set 3). Therefore, the ridges could have been lifted tectonically creating a horst-and-graben structure in the study site with the trenches being filled by weathering products of the described ridges and landslide material (block-and-matrix structure). The in-situ rock is heavily weathered and can hardly be distinguished from the saprolite formation.

The saprolite borders the outcrop on the north-western border and also occurs in the mid-eastern part of the study site, surrounding another outcrop. Two other saprolite structures are to the west in the main body of the site and to the far west, adjacent to the southern rock ridge. The saprolite and the in-situ rock

are not separated by a sharp line, but by a smooth transition from one to the other. Like the in situ rock, the saprolite has not been moved in the past but, unlike the in situ rock, is likely to fail in the future.

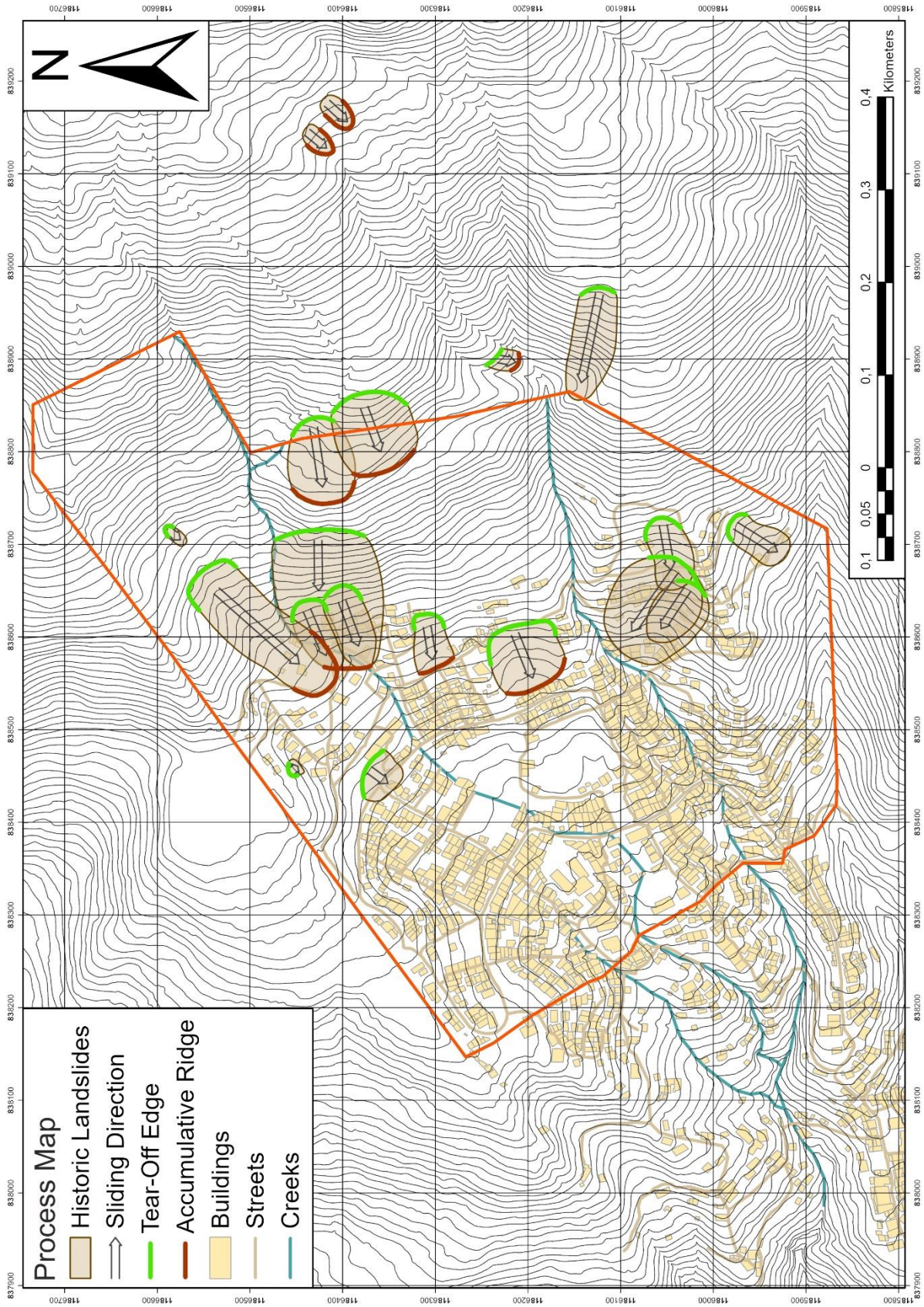

Figure 14: Process map of the study site created during the first field campaign in August 2019 and revised in 2022 (after BREUNINGER et al. 2021c and BREUNINGER et al. 2023a).

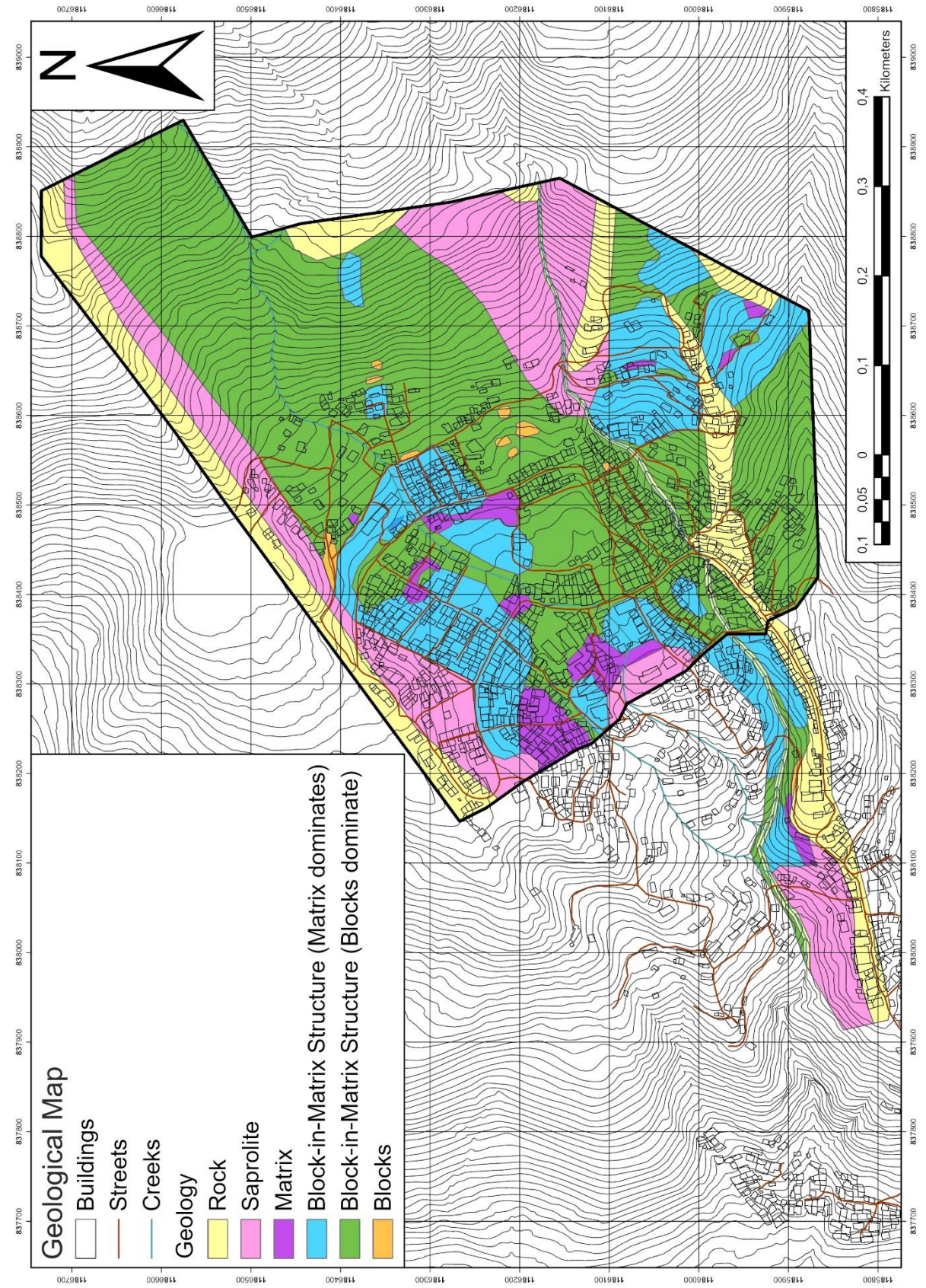

Figure 15: Geological map of the study site created during the second field campaign in February 2020 (after Breuninger et al. 2021c and BREUNINGER et al. 2023a).

The block-in-matrix structures that make up the rest of the area (trenches) are subdivided by their block-matrix ratio. Though the main part of the area (green) is dominated by blocks, there are also areas (blue)

dominated by matrix. All areas made up of these block-and-matrix structures are very prone to landslides as already discussed in chapters 3.1 and 3.2. A distinction between block-and-matrix structure created by former landslides or created by weathering cannot be made. The origin of the structure, however, does not influence its geotechnical behavior, which is why it is not of immediate importance.

5.3 Drillings

The following chapter is derived from BREUNINGER et al. (2021c) with some changes and additions.

Figure 16, Figure 17 and Figure 18 show pictures of the drillings cores, Figures A1–A4 in the annex include the drilling core documentations (drilling profile) and evaluations with several columns (core loss, weathering profile, RQD, facture ratio, joint set, alteration type and homogeneous area). The evaluations of the drillings were done in collaboration with the Master's theses of AGNES DEMHARTER (2021) and JULIA PETZI (2022). The drillings took place in fall 2020 (drillings A1, A2 and B1) and fall 2021 (drilling B2)

Some parts of the cores were wrapped into plastic foil to preserve their original humidity for laboratory testing (for the shear and Atterberg limits tests) (Figure 16, Figure 17 and Figure 18).

The core loss is not directly visible in the core boxes, since the cores were put next to each other, without leaving space, when a section was not retrieved.

As depicted in Figure 16, Figure 17 and Figure 18, the thickness of the soil on the surface hardly reaches 2 m, except for drilling B1. In all drillings, there is significant core loss (Figures A1–A4). Except for the first 3.00 m of drilling B1, this core loss is most likely a combination of flushed out, loose material due to the drilling flushing and holes in the ground created by pseudokarst. The first 3.00 m of drilling B1 are fillings from the road construction; the core loss here is most likely a combination of flushed out loose material and holes due to insufficiently compacted ground.

All three cores show fractures that dip predominantly with 0–15° (foliation/joint set 1) and 30–60° (joint set 3). The few joints dipping > 60° are suggested to be parallelized with joint set 2.

5.3.1 Drilling A1

In this drilling, the residual soil only reaches 40 cm depth. The material shows a deep brown color and mostly consists of sand, silt, and clay. The rest of the core has one of the best rock quality of all the cores (Figure 16/left and Figure A1).

Meters 2.60–12.10 show the weathering stage II after DIN EN ISO 14689 (2018), have an RQD of at least 53 (fairly good) and show joints, which are oriented subhorizontally (most likely foliation/joint set 1) or dip with 30–45° (most likely joint set 3). In this area, some joints show serpentinization and brown colors indicating water circulation through these joints. Other joints show no color changes. These could have been closed prior to drilling due to vertical pressure and, therefore, were not altered by water circulation. The whole area is therefore designated as homogeneous area 2, except for the areas of core loss and meters 0.40–2.60, where the core is more fractured and, therefore, belongs to homogeneous area 3.

Below 12.10 m, the core quality decreases in strength with increased weathering visible due to the brown colors on the core.

The area of meters 12.10–13.50 includes an area of highly destroyed, almost pulverized, but not deep brown colored, loose material. In Colombia, this material is called "salbanda" meaning "fault clay" (RENDÓN-GIRALDO 2020). It is formed by mechanical grinding without weathering (water circulation). This might indicate a tectonic movement in the past, without an information on the age of this movement. The area has a weathering stage of V and the RQD is 0 (very poor). Therefore, this part of the core is in homogeneous area 5.

The rest of the core (13.50–30.40 m) shows weathering stages III and IV, an RQD of 12–37 (poor to very poor) and mostly contains the joint sets 1 and 3, in meters 13.50–17.40 also one joint of joint set 2, leading to the homogeneous area 4. Brown weathering material dominates the core's appearance, serpentinization is not or only slightly visible. Two areas in this part of the core show a considerable better quality (19.20–20.10 m and 29.30–30.40 m) with weathering stage II and an RQD of 72 and 75 (fairly good), which results in homogeneous area 2.

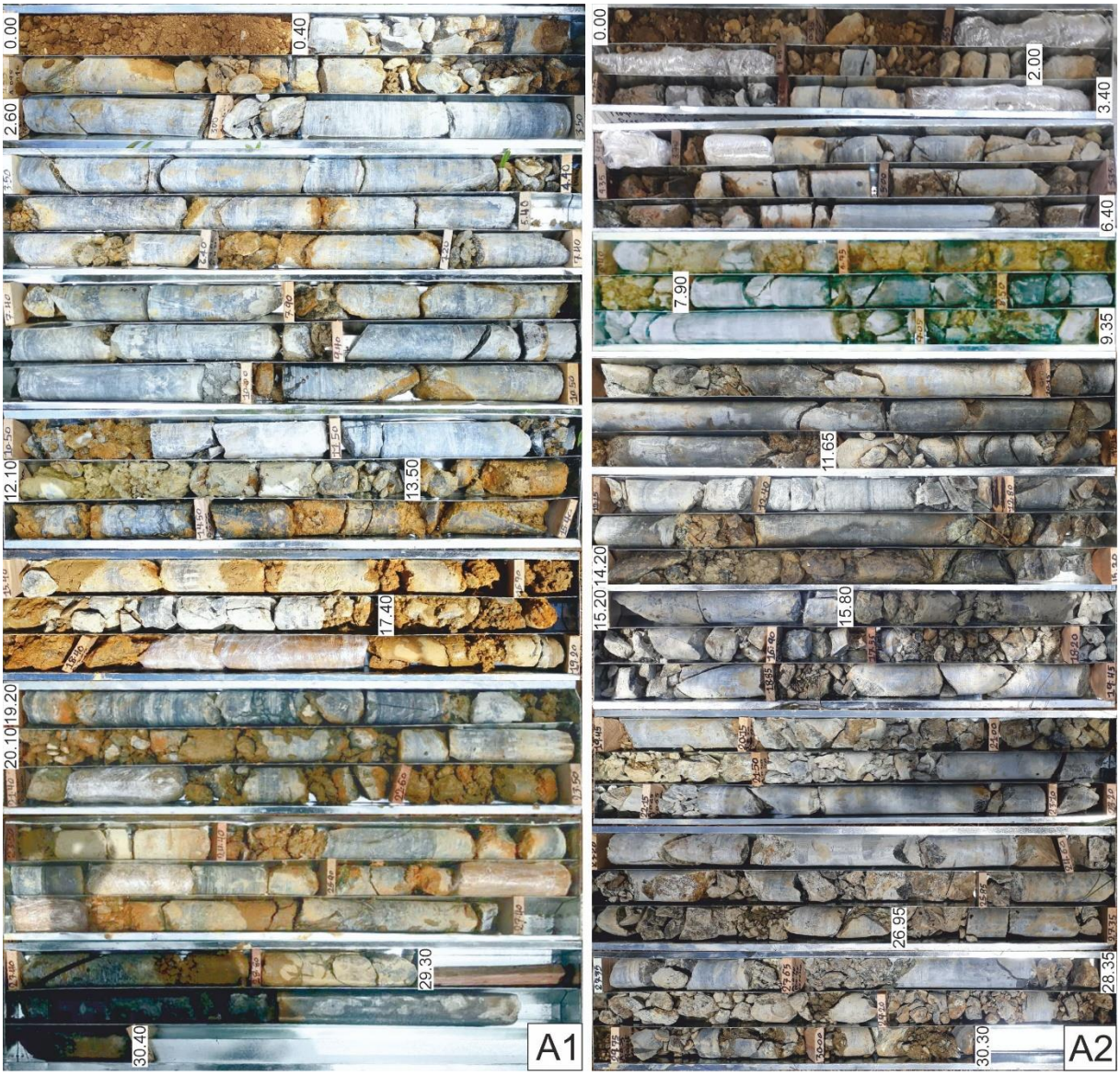

Figure 16: Drilling cores of drillings A1 (left) and A2 (right) (after BREUNINGER et al. 2021c).

5.3.2 Drilling A2

In general, this drilling core shows less brown fine material compared to the core of drilling A1, but the material is more fractured and fragmented. It also shows more small-scale changes, since the rock quality, weathering and joint numbers change significantly within a few centimeters (Figure 16/right and Figure A2).

With up to 2.00 m, the thickness of loose material and soil on the top in drilling A2 is higher than in drilling A1.

Meters 2.00–6.40 show weathering stages of II to IV, an RQD of 16–60 (very poor to fairly good) and all three joint sets mentioned before (only one fracture of joint set 2). Only one area shows serpentinization, the weathered material mostly shows brown colors. As it is only lightly weathered, this area

belongs to homogeneous area 3, except for a small part around 3.40 m which belongs to 4 (in Figure 16/right, this part is already wrapped in plastic foil).

The next section of 6.40–7.90 m shows the strongest weathering in the whole core. It has the weathering stage IV with brown and fragmented weathered material, and the ROD is not quantifiable due to the lack of enough rock material. Therefore, this area belongs to homogeneous area 4.

Below 7.90 m, the drilling core shows interchanges of homogeneous area 2 and 3. Homogeneous area 2 is characterized by weathering stage II, an RQD of 36–64 (poor to fairly good), only a few areas with color changes (9.35–11.65 m and 26.95–28.35 m), indicating a lack of water circulation in the joints and fractures, and mostly joint sets 1 and 3 (joint set 2 only at 15.20–15.80 m). In contrast, homogeneous area 3 shows weathering stages III to IV, an RQD of mostly 0 with spikes of up to 39 (very poor to poor), the weathering types of brown weathered material and fragmentation and the joint sets 1 and 3.

The section 14.20–15.20 m belongs to the homogeneous area 4, because the weathering is much stronger here (weathering stage V).

5.3.3 Drilling B1

As the drilling A2, drilling B1 (Figure 17 and Figure A3) shows significant small-scale changes and extreme differences regarding the weathering type. All three dominant joint sets are present throughout the core. To a depth of 8.90 m, core loss is the dominating feature. Only 3.05 m of this section are recovered. This phenomenon is most likely caused by flushed out loose material and in the upper 3.00 m additionally by insufficiently compacted ground.

Figure 17: Drilling core of drilling B1 (after BREUNINGER et al. 2021c).

The first 3.00 m of this core are fillings from road construction, mostly gravel and blocks in brown sand and clayey silt.

Meters 3.00–6.90 show weathering stages IV and V and except for one section (3.15–3.40 m/75 (good)), the RQD is not quantifiable. The upper part belongs to homogeneous area 3, since the weathering is still moderate, but the fragmentation is high. The lower part is homogeneous area 4, because of the strong weathering.

In the area of 6.90–11.20 m, the core is still intact but shows extreme weathering (stage V) with brown colors, an RQD of 20 (very poor) and, therefore, belongs to homogenous area 3. This part of the core could be identified as the saprolite overlaying the dunite rock, since the structure of the rock is still visible, but the material is extremely weathered.

The meters 11.20–12.40 are made up of the before mentioned “salbanda” (fault clay); here it appears as grey-greenish silty clay. This indicates movement in the past along this area with no water infiltration, since brown colors are not visible. Due to its crushed structures and clay content, this area belongs to homogenous area 5.

Below 12.40 m, the core shows a variation between homogeneous areas 2 and 3, with some exceptions. Homogeneous area 2 is characterized by the weathering stage II (except for 42.60–44.50 m with IV/V), an RQD of 0–80 (mostly good, but some exceptions) and varying weathering types. Homogenous area 3 shows weathering stages of II–V, an RQD of 0–58 (generally lower than in homogeneous area 2) and more intense weathering colors than in homogeneous area 2.

Some sections in this area show homogeneous area 6. These sections are characterized by weathering stage V, an RQD of 0–50 (mostly under 15) and mostly fragmented cores without brown colors but showing serpentinization. The most prominent characteristic is that the blocks in this area can easily be broken by hand. Therefore, especially the area of 18.20–31.40 m is extremely unstable.

5.3.4 Drilling B2

The topsoil of drilling B2 reaches a depth of 9.95 m, as opposed to the other three drillings, where the topsoil only reaches 2.00 m (Figure 18 and Figure A4). Only half of that section is recovered (5.00 m), the other half is registered as core loss, due to flushed out loose material from the water flushing and holes from insufficiently compacted ground, since the drilling is located next to a dirt road. This topsoil consists of fine-grained material as well as loose gravel to stone sized dunite rock.

Starting at 9.95 m downwards the core shows fractures dipping into three dominant directions: 0-15° (joint set 1), 60-90° (joint set 2) and 30-45° (joint set 3), as was observed in the other three drillings.

Compared to the other three drillings, drilling B2 has the longest sections of solid, lightly altered rock, but still shows very small-scale changes. The first section (9.95-16.10 m) has the best quality with weathering stage I, an RQD of 93-99, a joint ratio of 4.4-4.9 and only slight serpentinization and oxidation. It is, therefore, categorized as homogeneous area 0 (core, fresh), which was introduced for this drilling, as the other drilling cores did not show unaltered rock. Homogeneous area 0 is also present at 19.05-20.15 m and 31.70-39.45 m, but with a slightly lower quality due to weathering stage I-II, an RQD of 60-66, a joint ratio of 5.5-10.0 and visible serpentinization and oxidation.

At 13.80-14.05 m and 35.05-37.10 m two of the sections of homogeneous area 0 are interrupted by homogeneous area 6, highly fragmented rock, that does not seem to be strongly altered or weathered but is still highly disintegrated.

The rest of the drilling core shows homogeneous areas 2-5 with strongly varying rock quality and small-scale changes (longest section of one homogeneous area < 3.00 m). In general, the drilling core shows a decrease of alteration intensity (serpentinization and oxidation) with depth, but an increase in fragmentation. As with the other drillings, drilling B2 does not reach undisturbed or unweathered bedrock.

Figure 18: Drilling core of drilling B2.

5.4 Joint Record

Figure 19 shows the mapped joints in the study site on a hillshade projection. This mapping can only give information on the striking direction of the fault systems, it does not depict dipping direction or angle. Therefore, the mapped fault systems were complemented by the scanline analysis, visualized in Figure 20. Both sources combined give a complex picture of the tectonic structure of the subsurface in the study site.

The hillshade analysis recognizes four different striking directions, N-S (green), SW-NE (pink), WSW-ENE (orange), and WNW-ESE (yellow), whereas the scanline analysis shows three fault systems, (1) striking NNW-SSE and dipping 0-30° WSW, (2) striking NW-SE and dipping 85-90° SW, and (3) striking WSW-ENE and dipping 30-60° NWN. All these fault systems show a high dispersion rate.

Combining both information results in the color scheme depicted in Figure 20; the green fault system from Figure 19 corresponds to the subhorizontally dipping (0-30° WSW), NNW-SSE striking fault system in Figure 20; the pink and the orange fault systems correspond to the two main directions of the WSW-ENE striking and 30-60° NWN dipping fault system in Figure 20; the yellow fault system in Figure 19 corresponds to the steep dipping (85-90° SW), NW-SE striking fault system in Figure 20.

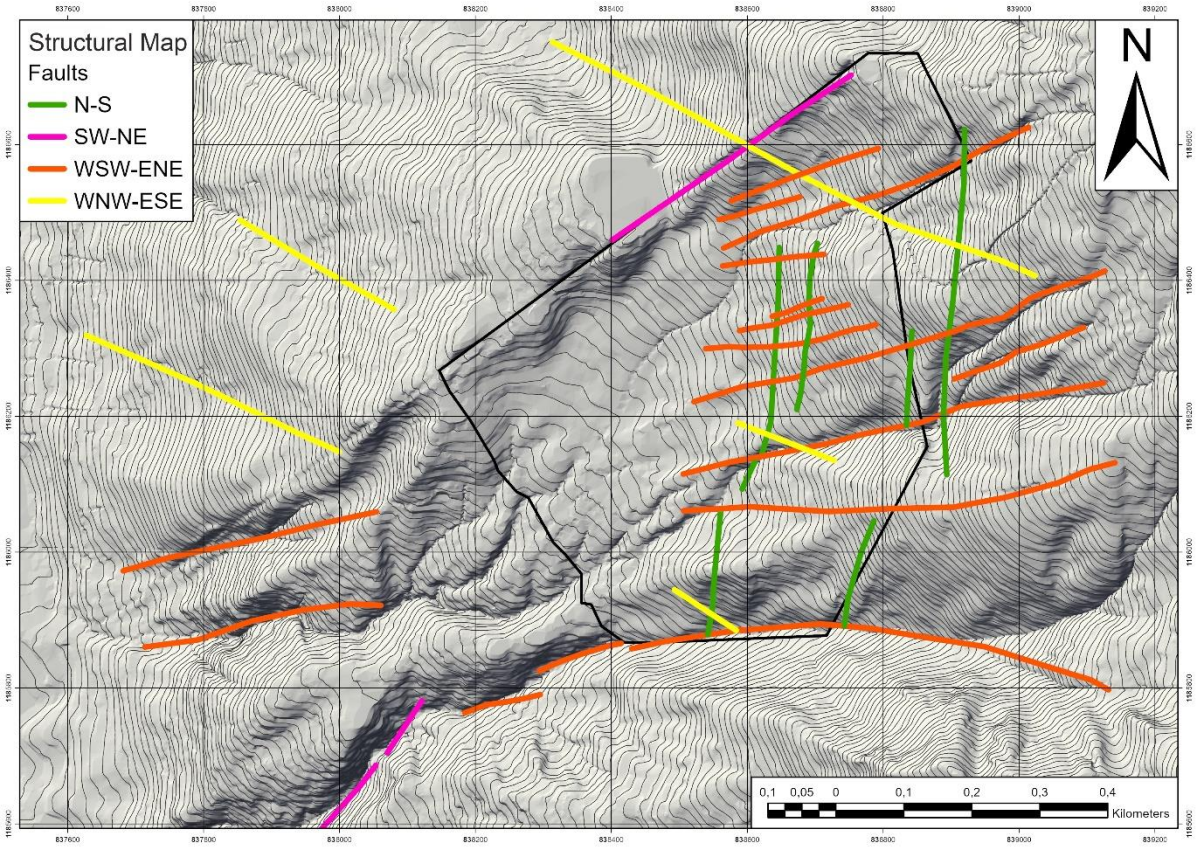

Figure 19: Structural map of the study site (after BREUNINGER et al. 2023a and WERTHMANN et al. 2024).

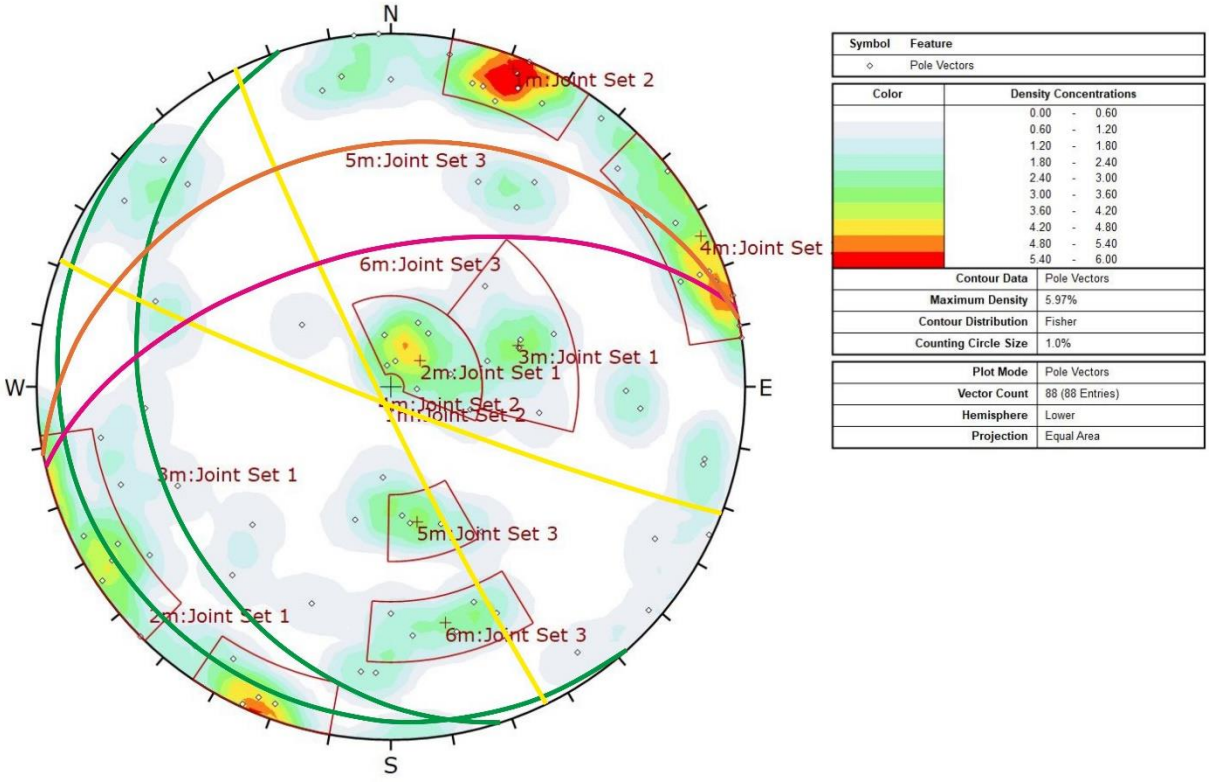

Figure 20: Structural analysis of 11 scanlines (after GAMPERL et al. in review).

The three fault systems correspond with the joint sets described in chapter 3.1: Joint set 1, the foliation of the Dunite and direction of the Rodas Fault to the underlying Espadera Amphibolite (striking SW-

NE, dipping 0-30° SE (TOBÓN-HINCAPIÉ et al. 2011)), is possibly represented by the green fault system; Joint set 2 (striking NNW-SSE, dipping 75-90° WSW (TOBÓN-HINCAPIÉ et al. 2011)), the direction of the La Acuarela Fault, where the Santa Elena Amphibolite was uplifted, possibly corresponds to the yellow fault system; Joint set 3 (striking SW-NE, dipping 25-60° NW (TOBÓN-HINCAPIÉ et al. 2011), is possibly represented by the pink and the orange fault systems.

None of these assignments of the fault systems to the fault systems of the literature fit exactly. Especially joint set 1 (foliation) has a completely different striking and dipping direction (SW-NE, SE) than the corresponding fault system in the study site (NNW-SSE, WSW). Since this fault system in the study site is the only one with a subhorizontal dipping angle, it is the only possible fault system representing the foliation in the study site. In addition, the low dipping angle can also lead to an overturning of the foliation in another direction at some places, which would explain the different striking and dipping directions. Joint set 2 and joint set 3 have a perfect fit with their corresponding fault systems in the study site regarding the dipping angle and a reasonable fit regarding the striking and dipping directions with only little deviations, that are within the scope of the dispersion rate of the fault systems recorded by the scanline analysis.

5.5 ERT Measurements

The results of the ERT measurements have already been published in GAMPERL et al. (in review). For the full understanding of the subsurface, the results are included in this thesis as well.

As mentioned in chapter 4.5, profile BO-02 could not be interpreted due to an RMS (root-mean-square) deviation of 48.6 % (GAMPERL et al. in review). The profiles BO-01, BO-03 and BO-04 had an RMS deviation of 5.7-7.1 % (GAMPERL et al. in review). The high RMS error of ERT profile BO-02 can be attributed to a concrete structure for a water pipe located close to the transect which caused extremely low resistivity values in the profile (GAMPERL et al. in review). A clear boundary between soil material and solid rock in the depth could not be seen in any of the transects.

5.5.1 ERT Transect BO-01

As is visible in Figure 21 the left part of the transect BO-01 (red/brown colors) shows resistivity values of 600-2,400 Ωm. This area is sharply separated from the right part of the transect (yellow/light blue colors), that shows much lower resistivity values of 100-600 Ωm. One area on the surface (dark blue) shows resistivity values of under 50 Ωm.

The sharp separation between the two areas of different resistivity values was interpreted as a fault system, striking NW-SE and dipping very steep (70°) towards NE in the profile, with the left part (uphill, NE) being uplifted. In combination with the other ERT transects, the real direction of the fault system will be determined, but it is likely to be part of the steep dipping joint set 2 (chapters 3.1 and 5.4). The dipping direction is not correct, but due to the steepness of joint set 2 and the complex tectonic history, the fault might be overturned in that area.

The left part of the transect (uphill) was interpreted as weathered (surface) and fractured (depth) Dunite rock, as is evident from the evaluation of drilling core A2 (chapter 5.3.2). In the middle of the transect the Dunite was interpreted to be covered by block-in-matrix structure, in the upper (far-left) part by saprolite, as mapped in the geological mapping (chapter 5.2).

The evaluation of drilling B1 was used to interpret the low resistivity values of the right part of the transect (chapter 5.3.3). Since the drilling core is highly fragmented, the low resistivity values might be explained by the condition of the Dunite at that area. The subsurface was, therefore, interpreted as fractured Dunite material. At the far-right end of the profile, a water source was recorded, suggesting a high water content at that part of the slope, which might add to the low resistivity values in that area.

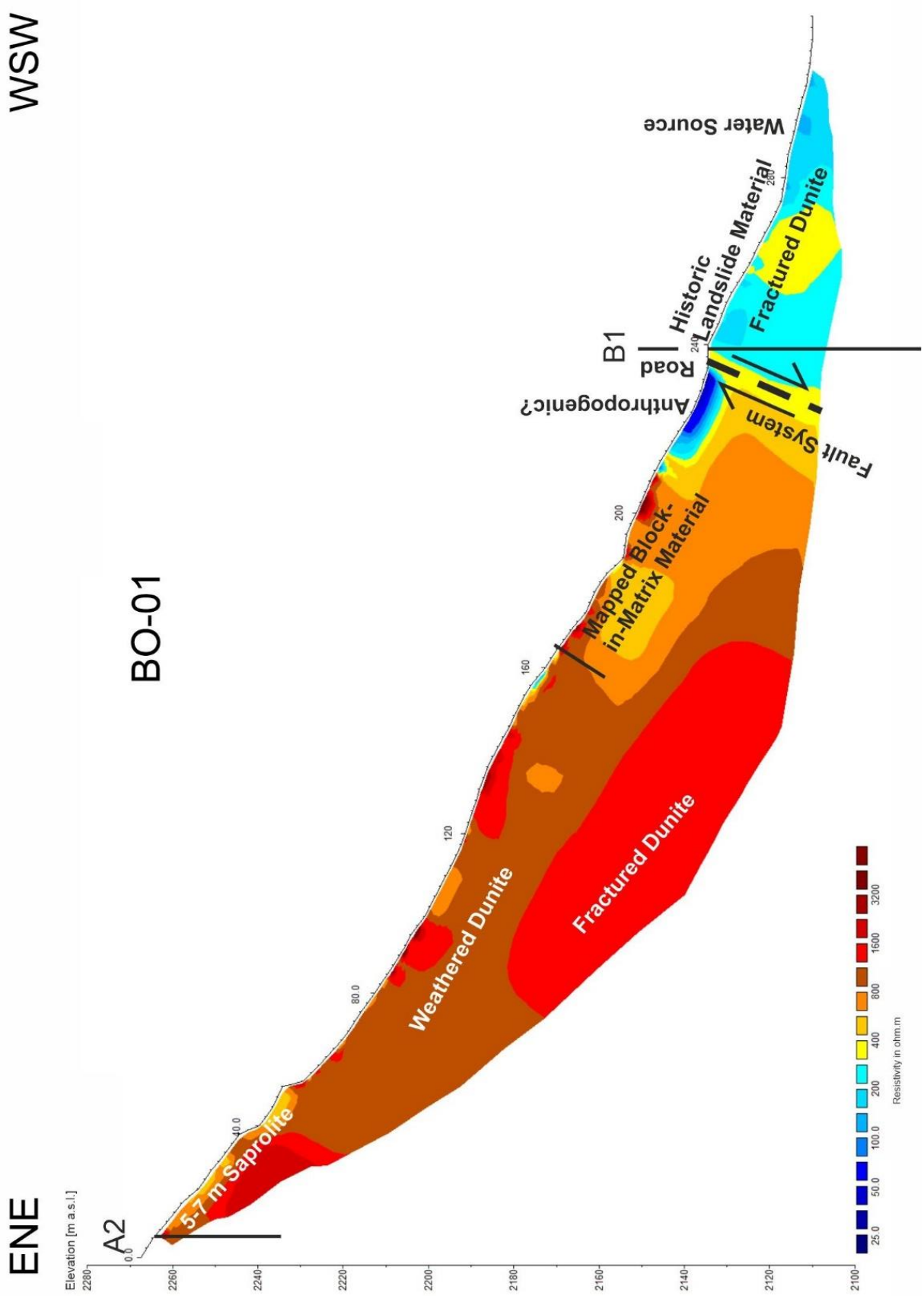

Figure 21: Result and interpretation of ERT profile BO-01 (after GAMPERL et al. in review).

Regarding the extremely low resistivity values on the surface left of the suggested fault system, this was interpreted as anthropogenic material, since this area contains several houses and a concrete staircase, interfering with the measurement.

5.5.2 ERT Transect BO-03

Transect BO-03, depicted in Figure 22, is divided into five parts of different resistivity values. (1) The far-left side of the profile shows low resistivity values of 150-400 Ωm, as does (2) the far-right side. Between these two ends the profile shows varying resistivity values; (3) the area adjacent to the far-right shows high resistivity values (red colors) of 1,200-6,400 Ωm, with increasing values in depth. (4) To the left of this high resistivity area is a large area with lower resistivity values (yellow/blue colors) of 200-600 Ωm. Between this area and the far-left area is (5) a zone with medium resistivity values (red/brown colors) of 600-3,200 Ωm.

The areas to the far- left and the far-right are most likely made up of soil material/block-in-matrix structure, as is suggested by their low resistivity values.

The area showing high resistivity values in the transect was pierced by drilling A2 (chapter 5.3.2). This drilling showed a high fragmentation but a low serpentinization and oxidation rate. Therefore, the upper part of this high resistivity area, punctured by the drilling, is interpreted as fractured and slightly weathered dunite. Since the resistivity values increase with depth in that area, the part below the drilling was interpreted as apparently unweathered bedrock, possibly fractured by the joint systems in the study site.

To the left of this area, the resistivity levels drop with an approximate angle of 50°, dipping NW in the profile. After this decrease of resistivity values, the values stay low towards the left side in the depth. This structure was interpreted as a complex fault system, where the material is highly weathered and fragmented resulting in mylonitic material with a high water intake capacity, resulting in low resistivity values. This structure is very broad (about 50 m) and reaches deeper than the profile. The dipping direction and angle of the profile suggest that the fault system might correspond to joint set 3.

The area showing medium resistivity values left of this suggested fault system was pierced by drilling A1 (chapter 5.3.1). While the profile shows higher resistivity values towards the surface and decreasing resistivity values with increasing depth, the core of drilling A1 seams to confirm this: The drilling core shows less fracturing and weathering in the upper 10 m than the rest of the core, suggesting an increase of weathering and fracturing with increasing depth, as is visible in the profile. One explanation for this reversed weathering profile might be the fault system next to this area, creating a higher water conductivity in the depth, further promoted by pseudokarst.

The steep transition between the area with medium resistivity values and the area to the far-left of the profile might suggest another, very steep fault system between those areas, dipping about 80-90°SE. Given the steep dipping angle, this fault might correspond to joins set 2. The directions and angle of these fault systems indicate a horst-graben-structure in the study area.

5.5.3 ERT Transect BO-04

Visible in Figure 23, transect BO-04 shows the most areas with low resistivity values of all profiles, and can be divided into four parts; (1) the area to the far-left shows the highest resistivity values with 1,200-6,400 Ωm. To the right there is a sharp transition to (2) an area with low resistivity values of 50-400 Ωm, making up half of the profile. Starting at the middle of the profile in 50 m depth, rising towards the surface to the right, (3) appears an area with medium resistivity values of 400-1,600 Ωm. (4) To the far-right the resistivity values are very low again with 100-400 Ωm.

The high resistivity values to the left of the profile were interpreted as bedrock dunite, as is also apparent in the geological mapping (chapter 5.2), showing an in-situ rock ridge in that area.

The transition to the low resistivity area to the right is very sharp and was interpreted as a fault system, dipping 40-60° towards SE in the profile. This fault system might correspond to joint set 3, given the dipping angle. However, the normal dipping direction of that joint set is NW, so the fault system encountered in transect BO-04 might be a joint set standing vertically to joint set 3 but created by the same tectonic regime.

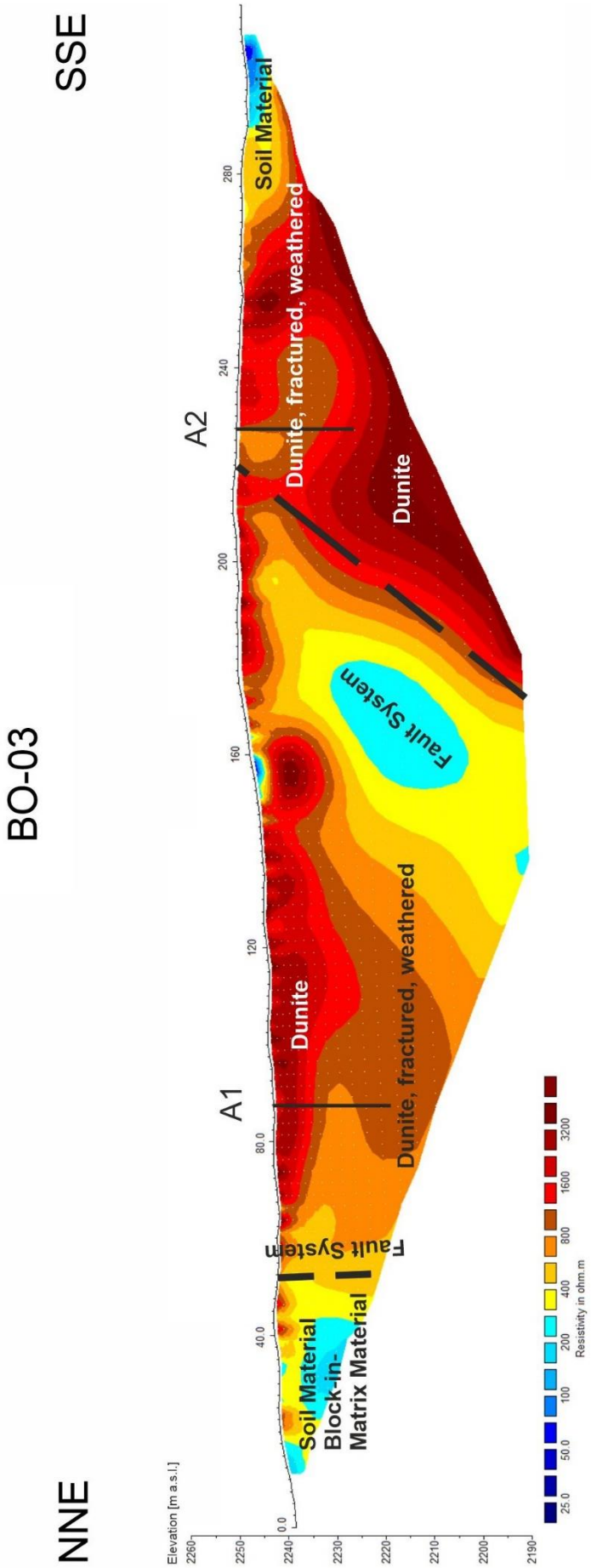

Figure 22: Result and interpretation of ERT profile BO-03 (after GAMPERL et al. in review).

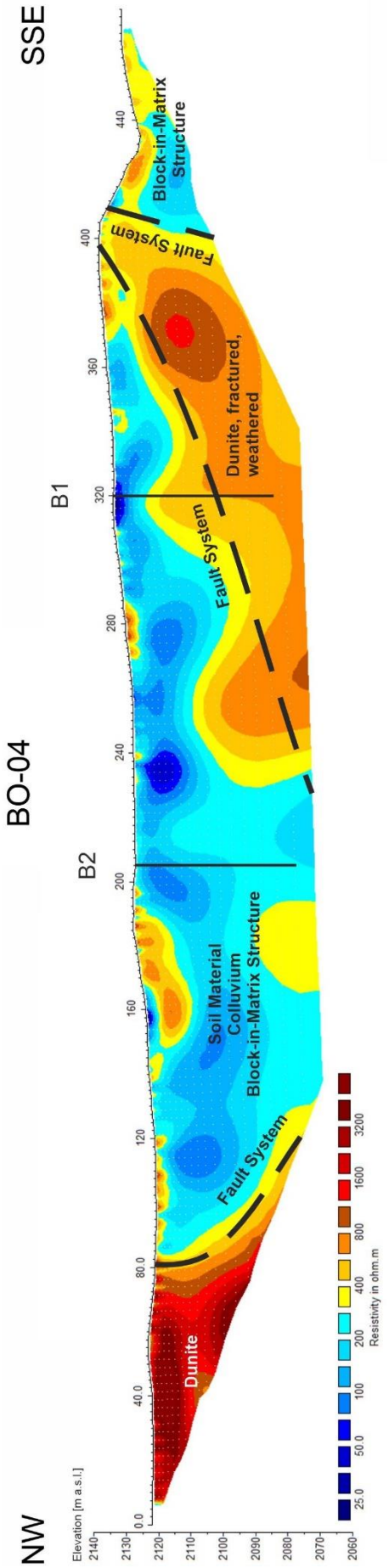

Figure 23: Result and interpretation of ERT profile BO-04 (after GAMPERL et al. in review).

The adjacent area, displaying low resistivity values, was interpreted as soil and colluvial material. This block-in-matrix structure was most likely created by weathering, pseudokarst and landslide events. The structure reaches deeper than the ERT measurement, being at least 50 m deep. Drilling B2 pierces this area but does not reflect the low resistivity values encountered in the ERT measurement (chapter 5.3.4). The drilling core is fractured and weathered, but not to a higher degree than the other drilling cores, piercing areas of higher resistivity values in the other transects. This deviation cannot be explained yet.

As was the case to the left side of this structure, the area is bordered by a sharp transition to the right side as well. This transition, however, is not straight but waved. This transition was interpreted as a fault system, dipping about 20-25° towards NW in the profile. Like the fault system to the other side of the area of low resistivity values, this fault system most likely corresponds to joint set 3, here with the normal dipping direction. The waved surface of the fault system, which can be encountered in carbonate rocks, might reflect the uneven surface of the dunite below due to pseudokarst structures,

The area with medium resistivity values was pierced by drilling B1 (chapter 5.3.3). At the same point in the profile, transect BO-01 crosses transect BO-04. The upper 15 m of the transect at the drilling location show similar low resistivity values than in BO-01 at that location. Transect BO-04, however, reaches deeper at this point, into the medium resistivity area. This section was interpreted as highly fractured and weathered dunite, which is confirmed by the drilling core of drilling B1.

To the far right, an area of low resistivity values follows. This area was interpreted as block-in-matrix structure, but not further investigated upon. The transition to this area might again indicate a fault system, dipping 70-80° NW, corresponding to an overturned fault system of joint set 2.

At some areas in the middle of the profile towards the surface, there are areas of extremely low resistivity values (25-75 Ωm). These structures within the block-in-matrix structure might be areas where the matrix dominates and water is retained by the fine material, leading to very low resistivity values.

The low resistivity values up to a great depth in all the transects contribute to the picture of the Medellín Dunite as extremely weathered, fractured and disturbed, suggesting that the pseudokarst phenomenon explained in chapter 3.1 is in fact present in the study site as it is in other areas in the Medellín Dunite. It contributes to the weathering and fracturing in the depth and leads to cavities enabling water infiltration into a depth of at least 60 m or more, destabilizing the slopes and making them susceptible to (possibly even deep-seated) landslides.

5.6 Laboratory Tests

5.6.1 Rock Tests

The following chapter is derived from BREUNINGER et al. (2021c) with some changes and additions.

Uniaxial Compressive Strength

Figure 24 and Table A1 show the values of uniaxial compressive strength of the samples of all four drilling cores plotted against the sampling depth. Since the compressive strength decreases with increasing weathering, it is expected to show lower values with increasing weathering (ÜNDÜL et al. 2015). All samples show weathering stage II on the exterior with little differences.

The values vary from 10 MPa to 132 MPa and show little to no correlation between depth and strength; the high deviation of strength values shows the high variation within the Medellín Dunite. In drilling B1, the four stratigraphically deepest samples show a constant increase of compressive strength with increasing depth, but the two uppermost values do not fit into this correlation. In drillings A1 and A2, only a slight tendency can be seen. The samples from drilling B2 show no correlation between depth and strength. The deepest sample even shows the lowest value (39 MPa) of all samples from this drilling.

Most samples (12) have a high compressive strength of 50–100 MPa (DIN EN ISO 14689 2018). One sample has a low compressive strength of 5–25 MPa, seven samples have a moderately high compressive strength of 25–50 MPa (DIN EN ISO 14689 2018). Two samples show a very high compressive strength of 100–250 MPa (DIN EN ISO 14689 2018).

An explanation of this bad correlation between depth and strength might be that the primary rock conditions are affected by serpentinization and tectonic damage already before weathering. Another one might be that the normal weathering from top to bottom could not be applied in the Medellín Dunite, most likely due to the pseudokarst present in this unit, but also due to landslides, which disturb the uppermost 2–10 meters of the unit causing a mix of top layers. Most likely, it is a combination of both.

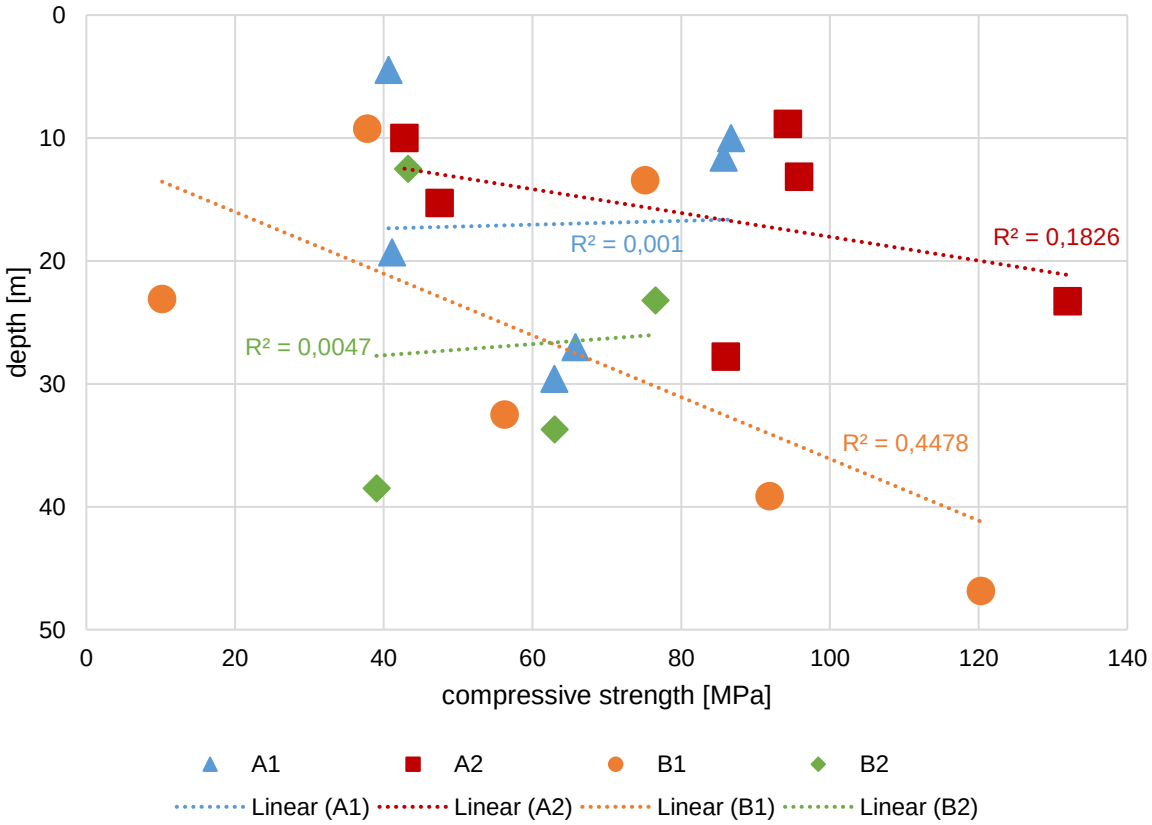

Figure 24: Uniaxial compressive strength values plotted against sampling depth of all four drillings.

Tensile Strength (Brazilian Test)

The results of the Brazilian test are depicted in Figure 25 and Table A1. Like the results of the uniaxial compressive strength test, the tensile strength is expected to decrease with increased weathering (ÜNDÜL et al. 2015). All samples show weathering stage II on the exterior with little differences.

The values of the tensile strength vary to a high extent between 4.1 and 17.5 MPa. Although the compressive strength showed at least a slight correlation with depth, the tensile strength seems not to increase with the sampling depth at all. This also might correspond to the fact that the primary rock conditions were already affected by serpentinization and tectonic damage before weathering, as discussed above.

The results of the tensile strength test of the drilling core samples confirm the heterogenic composition of the subsurface at the study site and emphasize the factors leading to that heterogeneity. Even the intact rock sections can be highly weathered internally in great depths as both rock tests prove, since the exterior of the samples suggested similar weathering conditions.

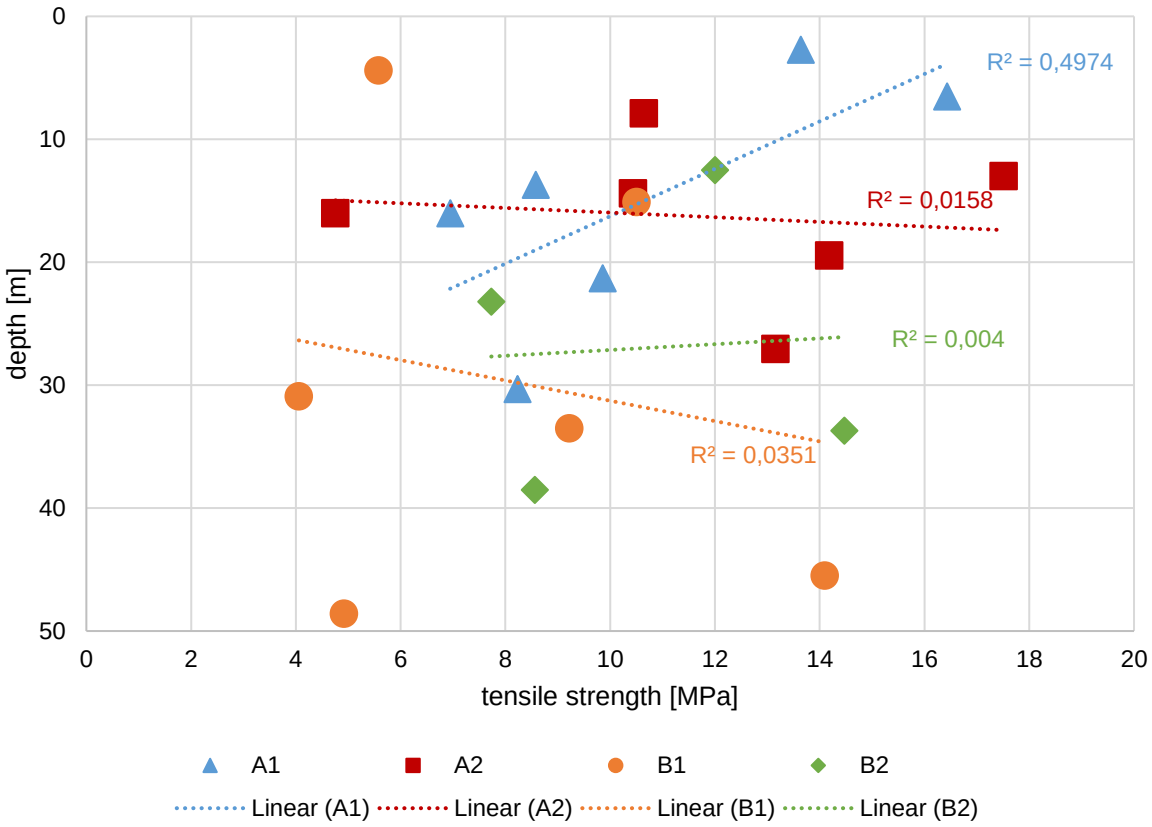

Figure 25: Tensile strength values plotted against sampling depth of all four drillings.

5.6.2 Soil Tests

The soil tests were performed on samples from all four drillings as well as on samples from the trenches dug for the CSM cables of the EWES (see chapter 4.6). The number of tests is listed in Table 12.

Table 12: Soil tests performed on the samples from the drillings and the trenches.

Test Performed	Number of Tests (Drillings)	Number of Tests (Trenches)
Grain Size Analysis	10 (4xA1, 1xA2, 2xB1, 3xB2)	14
Atterberg Limits	10 (4xA1, 1xA2, 2xB1, 3xB2)	14
Direct Shear Test (CD)	3 (3xB2)	13

The following chapter is derived from BREUNINGER et al (2021c) with some changes and additions.

Grain Size Distribution

The grain size distribution was determined on ten samples in all four drillings, four of them in drilling A1, one in drilling A2, two in drilling B1, and three in drilling B2, which are depicted in Figure 26 and Table A2. Even though the tests were performed after INV E 123 (2013), the evaluation was done after DIN EN ISO 14688-2 (2020), due to the intercultural collaboration and because ISO standards provide an international standardization level for rock and soil testing and evaluation. Except for drilling B2, the grain size distribution on the drilling core samples was only determined using the sieving test. Therefore, the graphs end at the sand-silt border and a distinction between clay and silt cannot be made.

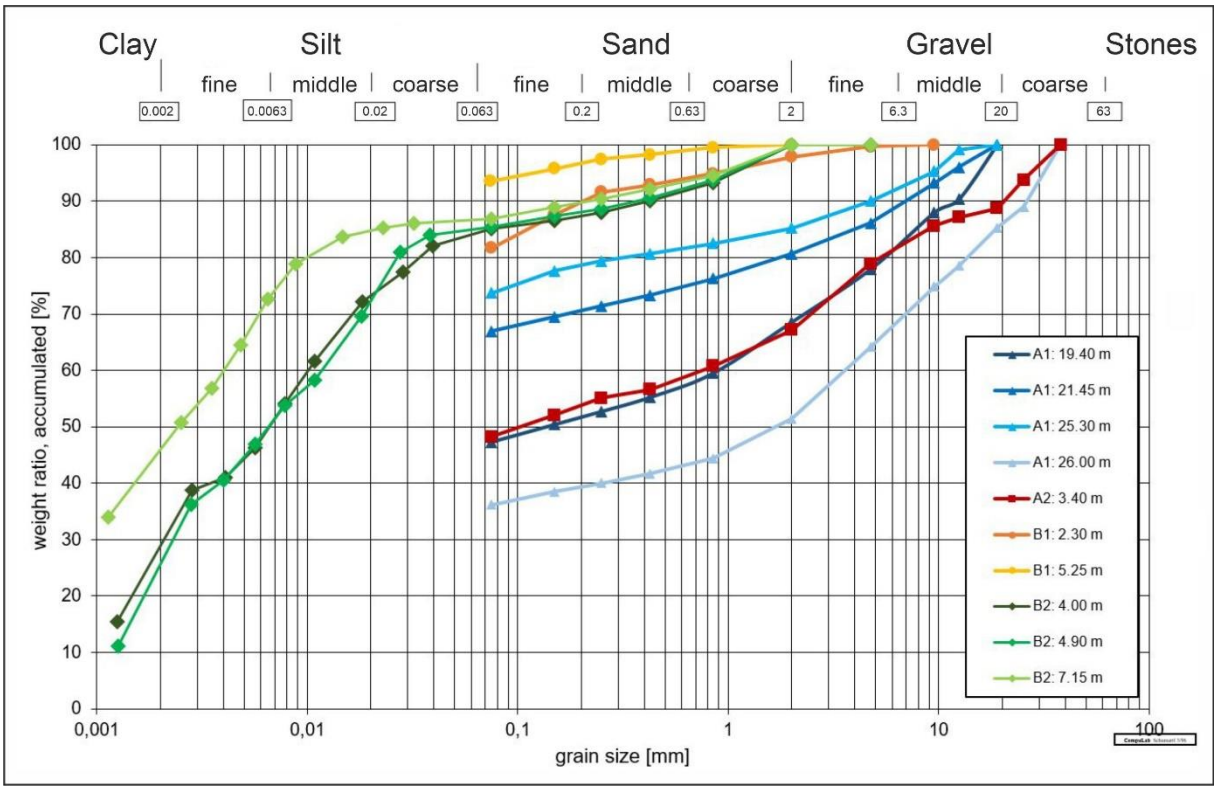

Figure 26: Grain size distribution of all drilling core samples depicted according to DIN EN ISO 14688-2 (2020) (after BREUNINGER et al. 2021c).

The results of the grain size analysis indicate that the loose material in the drilling cores consists of at least 37 % fine material, in most cases much more. One sample (drilling B1, 5.25 m) even shows an amount of about 93 % fine material. All samples are fine-grained soils, except for one sample (A1, 26.00 m), where gravel is the dominating grain size (48 %). The samples of drilling B2 show the most similarities, which might be due to their very close sampling location, especially the samples from 4.00 m and 4.90 m depth.

Like the rock tests before, this investigation shows no correlation between depth and the values determined. In a weathering profile, the grain size would be expected to increase with increasing depth. This fact could not be observed, which underlines the presence of pseudokarst and disturbance due to landslides.

Additionally, 14 trench samples were analysed and those results are depicted in Figure 27 and Table A2. Like all trench samples, the sampling depth was 0.50 m. All samples can be categorized as fine-grained soils after DIN EN ISO 14688-2 (2020).

The results can roughly be divided into three groups of samples: Nine samples (Test_03, Test_08, Test_10, Test_13, Low_03, Up_04, Up_05, Up_06, Up_07) have a coarse grain content of under 20.0 % with a gravel content of under 10.0 % and can be classified as grsaclSi/clsaSi/saclSi/sasiCl/saSi after DIN EN ISO 14688-1 (2020). Three samples (Low_01, Up_01, Up_03) have a coarse grain content of 33.0-34.0 % with a gravel content of 13.8-19.0 % and can be classified as clgrsaSi after DIN EN ISO 14688-1 (2020). The other two samples (Test_05, Up_02) have a coarse grain content of 45.0-46.1 % with a gravel content of 31.4-37.3 % % and can be classified as saclgrSi/casagrSi after DIN EN ISO 14688-1 (2020).

Figure 28 shows the spatial distribution of the grain size distribution of the trench samples. There is no correlation between sampling location (north-south, east-west, uphill-downhill) and grain size distribution. As already observed in the uppermost part of all drillings and the geological mapping (BREUNINGER et al. 2021c) the topsoil in the study site seems to consist of fine-grained material with only a

small content of sand, gravel, and stone sized particles. Large blocks, however, are present on the surface all over the study site.

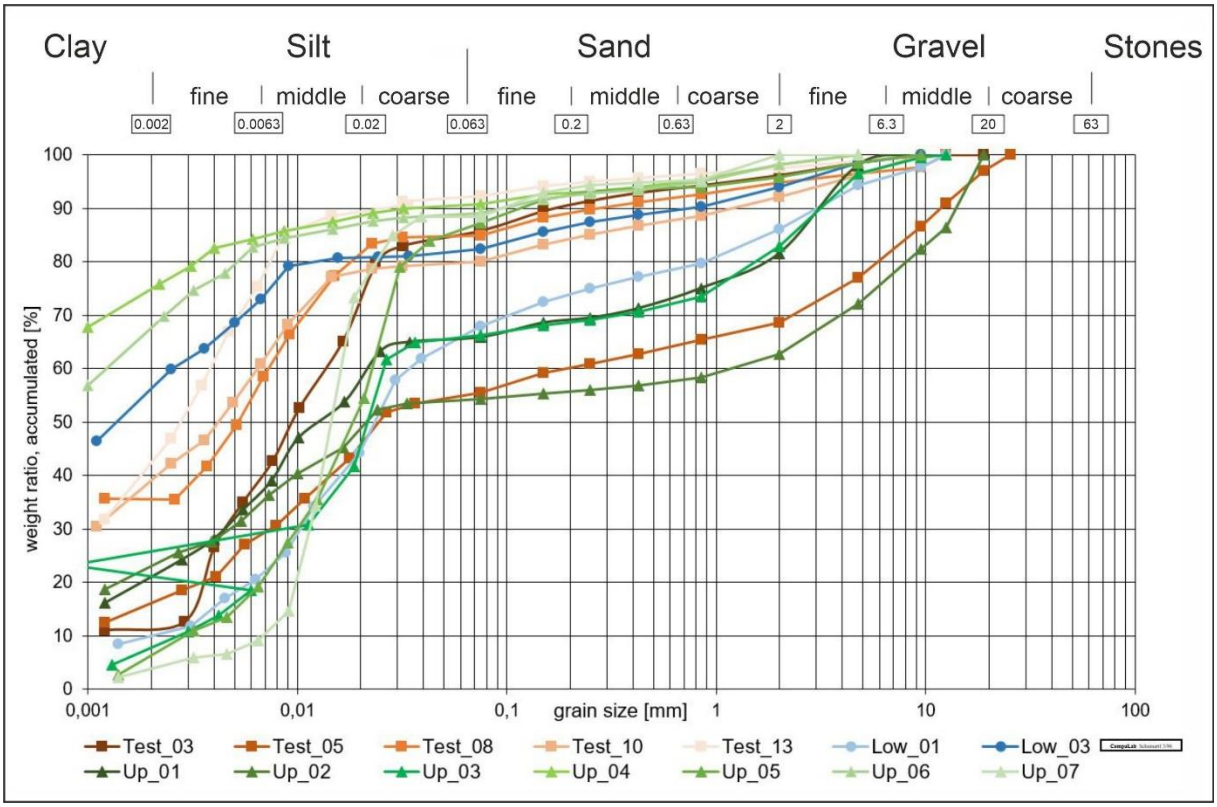

Figure 27: Grain size distribution of all trench samples depicted according to DIN EN ISO 14688-2 (2020) (after BREUNINGER et al. 2021c).

Atterberg Limits

The following chapter is derived from BREUNINGER et al (2021c) with some changes and additions.

All results of the Atterberg limits tests on the drillings core samples and the trench samples are visible in Figure 29 and listed in Table A2.

The samples of drilling A1 vary to a considerable degree; Two samples can be classified as clay with low plasticity (ClL) after DIN EN ISO 14688-2 (2020) and as clay with low liquid limit (CL) after USCS (ASTM D 2487—17e1 2017), one as silt with medium plasticity (SiM) after DIN EN ISO 14688-2 (2020) and as silty gravel (GM) after USCS (ASTM D 2487—17e1 2017), and one as clay with high plasticity (ClH) after DIN EN ISO 14688-2 (2020) and as clayey sand (SC) after USCS (ASTM D 2487—17e1 2017). The plastic limits vary moderately, between 20 % and 27 %, the liquid limits to a higher degree, between 31 % and 53 %, while the plasticity index ranges from 11 % to 27 %.

Very similar to one sample from drilling A1, the single sample from drilling A2 is classified as silt with medium plasticity (SiM) after DIN EN ISO 14688-2 (2020) and as silty sand (SM) after USCS (ASTM D 2487—17e1 2017). It shows a plastic limit of 31 %, a liquid limit of 49 %, and a plasticity index of 18 %.

Both samples from drilling B1 are classified as silt with very high plasticity (SiV) after DIN EN ISO 14688-2 (2020) and as silt with high liquid limit (MH) after USCS (ASTM D 2487—17e1 2017). Their plastic limits are very high, at 56 % and 72 %, as are the liquid limits, at 77 % and 106 %, with plasticity indices of 21 % and 34 %.

All three samples from drilling B2 can be classified as silt with high plasticity (SiH) after DIN EN ISO 14688-2 (2020) and as silt with high liquid limit (MH) after USCS (ASTM D 2487—17e1 2017). The plastic (40-43 %) and liquid (60-63 %) limits as well as the plasticity indices (18-20 %) vary to a very

low degree, as was the case with those samples' grain size distribution, which is possibly, again, due to their close sampling locations (4.00 m, 4.90 m, 7.15 m depth)

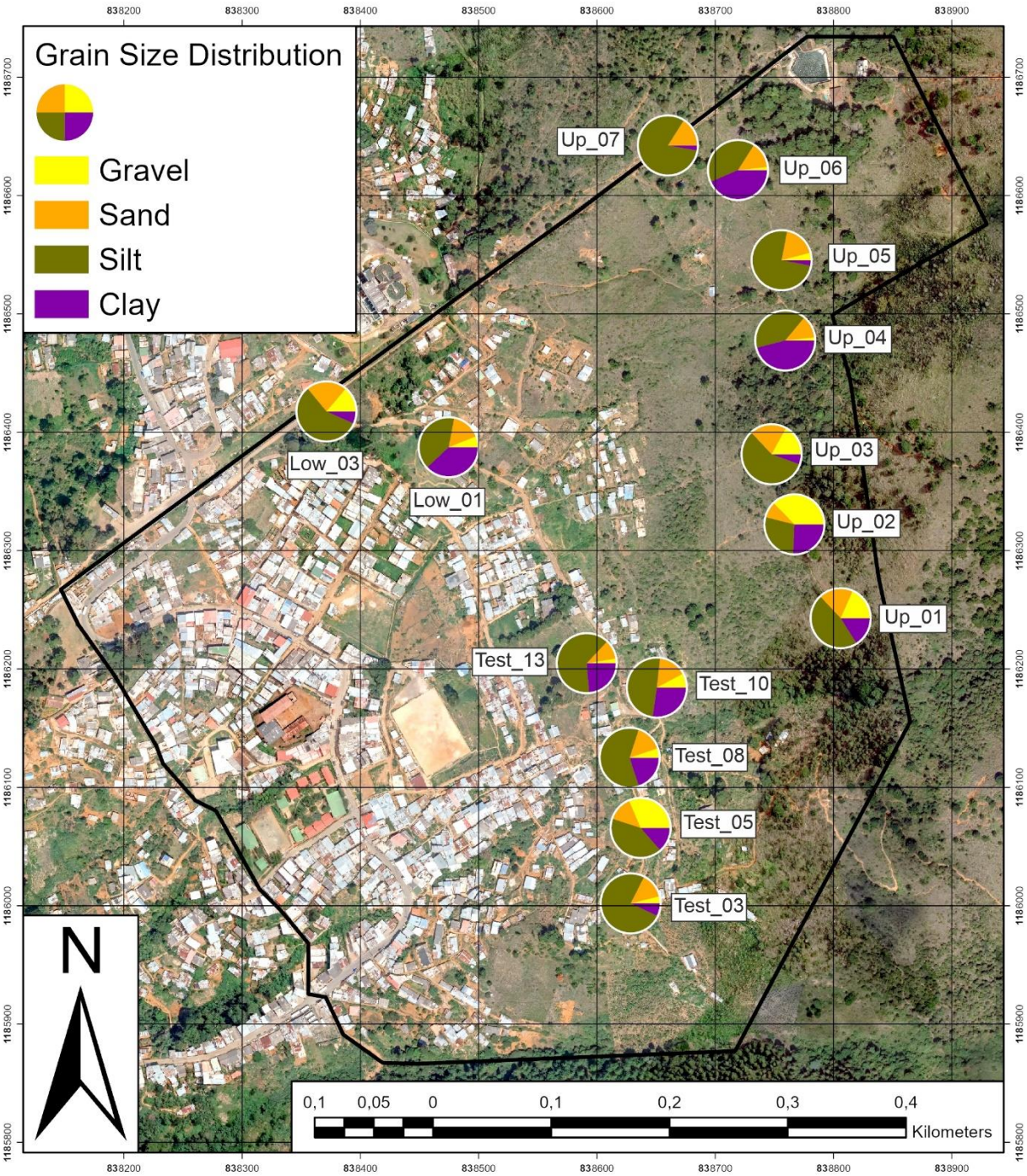

Figure 28: Spatial distribution of the grain size distribution of the trench samples.

Except for two samples of drilling A1 the material shows a considerable plastic behavior in the Atterberg limits test, indicating a possibly high content of swelling clay minerals. As is evident from Table A2, no correlation between sampling depth or location and the values can be made.

All trench samples are classified as silt with high or very high plasticity (SiH, SiV) after DIN EN ISO 14688-2 (2020) and as silt with high liquid limit (MH) after USCS (ASTM D 2487—17e1 2017), as were the samples from the drillings B1 and B2.

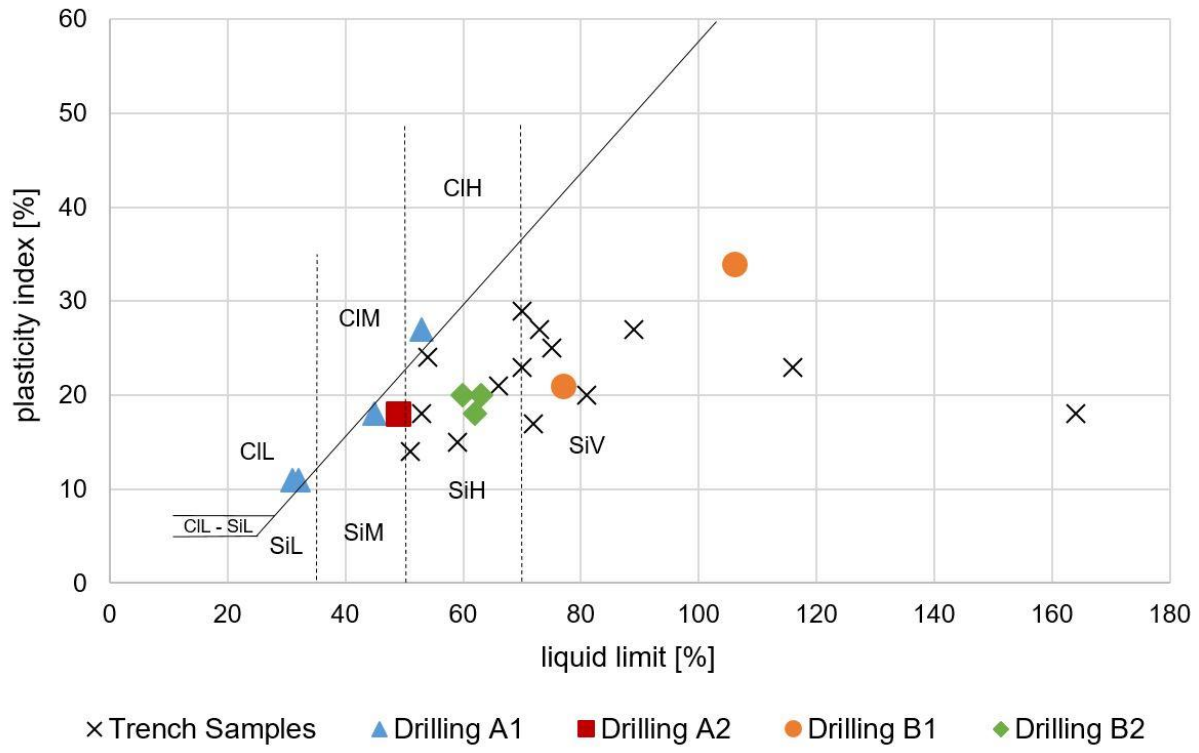

Figure 29: Atterberg limits of all drilling core and trench samples depicted according to DIN EN ISO 14688-2 (2020) (after BREUNINGER et al. 2021c).

The values of plastic limit vary between 30 % and 62 % with two outliers of 91 % and 146 %. The liquid limit varies between 51 % and 89 % with two outliers of 116 % and 164 %, which are the same samples as the two outliers of the plastic limit. These values create a plasticity index of 14-29 %. Eleven samples show plastic behavior (plasticity index of 10-25 %), three samples show high plastic behavior (plasticity index of 25-75 %) after DIN EN ISO 14688-2 (2020).

The values of the plastic limit and liquid limit vary to a high extend, the plasticity, however, only varies moderately. The two samples with the extreme high values regarding plastic and liquid limit might contain a very high amount of swelling clay minerals, that can hold a high amount of water. The values of the other samples also imply the presence of swelling clay minerals, to a lesser extent.

As was the case for the drillings core samples and the grain size distribution, there is no correlation between sampling location (north-south, east-west, uphill-downhill) and Atterberg limit values, as is evident from Table A2.

Shear Parameters

The following chapter is derived from BREUNINGER et al (2021c) and BREUNINGER et al. (2023b) with some changes and additions.

Since the one shear test conducted on drilling core B1 was only done using two single samples due to a lack of soil material in the drilling, this test was not suitable for the evaluation of reliable shear parameters. Only the results of the tests conducted on the samples from drilling core B2 and the trench samples will be presented. Table A3 lists the results and conditions of all shear tests, whereas in Figure 30 the friction angle is plotted against the cohesion of each sample.

The friction angle of the three samples from drilling B2 is very high and varies between 31.3° and 36.0°, as is the cohesion with values between 30.0 kPa and 37.7 kPa. Especially the high values of the friction angle are unusual, since fine-grained non-organic soils normally show values of 17.5-27.5° (DIN 1055-2 2010). There is no correlation between sampling depth and shear values (Table A3).

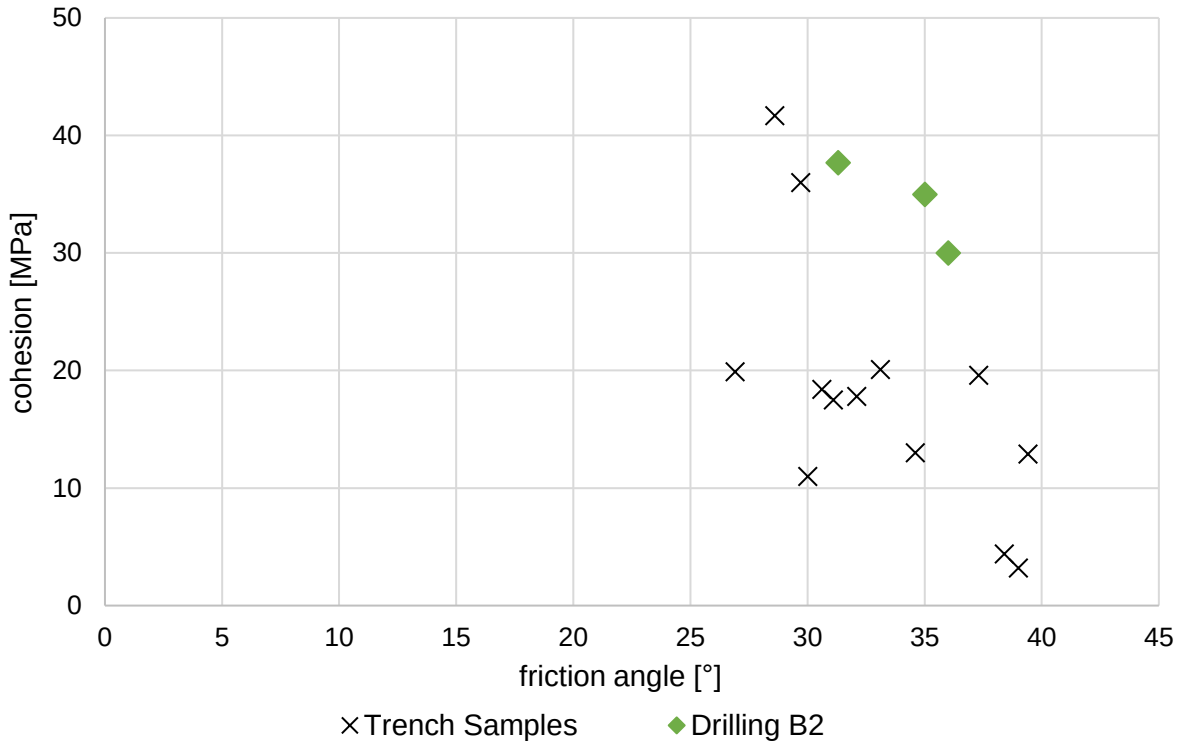

Figure 30: Friction angle plotted against the cohesion of the shear tests of the samples from drilling core B2 and the trench samples.

Regarding the trench samples, there are only 13 results, one less than of the other tests conducted on the soil samples from the trenches, since the tests on the three samples from Up_02 failed due to pre-existing shear surfaces in the samples. All trench samples were taken next to a dirt road or a highly frequented path. It is, therefore, expected that the samples have a slightly higher friction angle then is typical for cohesive soils due to a higher degree of compaction, especially those from the dirt road.

The friction angle varies between 26.9° and 39.4°. As is the case with the samples from drilling B2, these high friction angle values are normally only to be expected in coarse-grained soils or in mixed-grained soils with a higher content of coarse-grained material as is the case with these samples. Typical friction angle values of material of this sort are 17.5-27-5° (DIN 1055-2 2010). As mentioned above, the high friction angles are suggested to mirror the over-consolidation of the soil (road/path).

The cohesion varies considerably between 3.2 kPa and 41.7 kPa. The highly varying cohesion might be explained with a varying amount of swelling clay minerals, that was already suspected in the results of the Atterberg limits test and the grain size distribution analysis. The x-ray diffractometry was conducted to determine the existence and amount of swelling clay minerals in the samples. As is evident from Table A2 and Table A3, the differences in the cohesion values cannot be explained with varying water content, grain size distribution or density values (BREUNINGER et al. 2023b).

Other factors possibly contributing to differing values of the shear parameters might be mineralogical differences, varying organic content and minor differences in sampling quality. The generally low values of density (Table A3) suggest a high amount of organic material in all samples (SN 670 010b 1998), the mineralogical composition of the material is determined in chapter 5.6.4.

In Figure 31 the spatial distribution of the friction angle values and in Figure 32 the spatial distribution of the cohesion values of the trench samples is depicted. As is apparent from these figures there is no correlation between sampling location (north-south, east-west, uphill-downhill) and shear values, as was the case for the grain size distribution results and the Atterberg limits values. The samples from the dirt road (downhill, SW) do not show higher friction angles than the ones from the path (uphill, NE), as might be the case due to higher compaction of the soil.

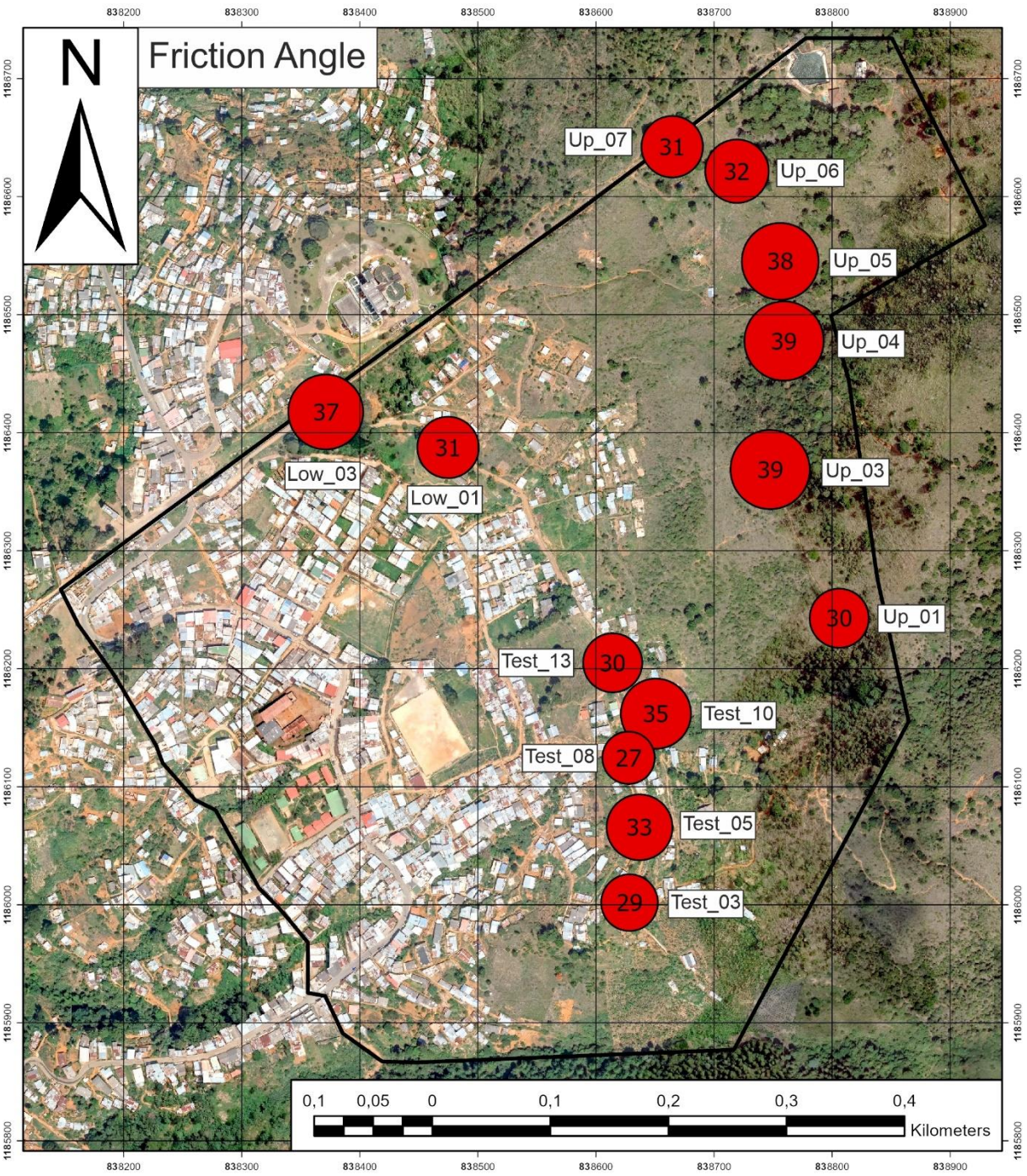

Figure 31: Spatial distribution of the friction angle of the trench samples.

Since the shear tests show friction angles between 26.9° and 39.4° on the surface and 31.3° and 36.0° in drilling B2 and the slope angle in Bello Oriente lies between 22° and 35°, the measured friction angles are suggested to create a critical state of equilibrium in the slope. Heavy rainfall events could lead to a decrease of the friction angle, the equilibrium is exceeded, and the slope fails.

Due to the fine-grained and highly plastic nature of the material, it is almost water stagnant. Therefore, it is highly likely, that rainwater infiltrates into the ground over several hours or even days before the pore water pressure increases and a slope failure occurs, allowing for adequate preparation.

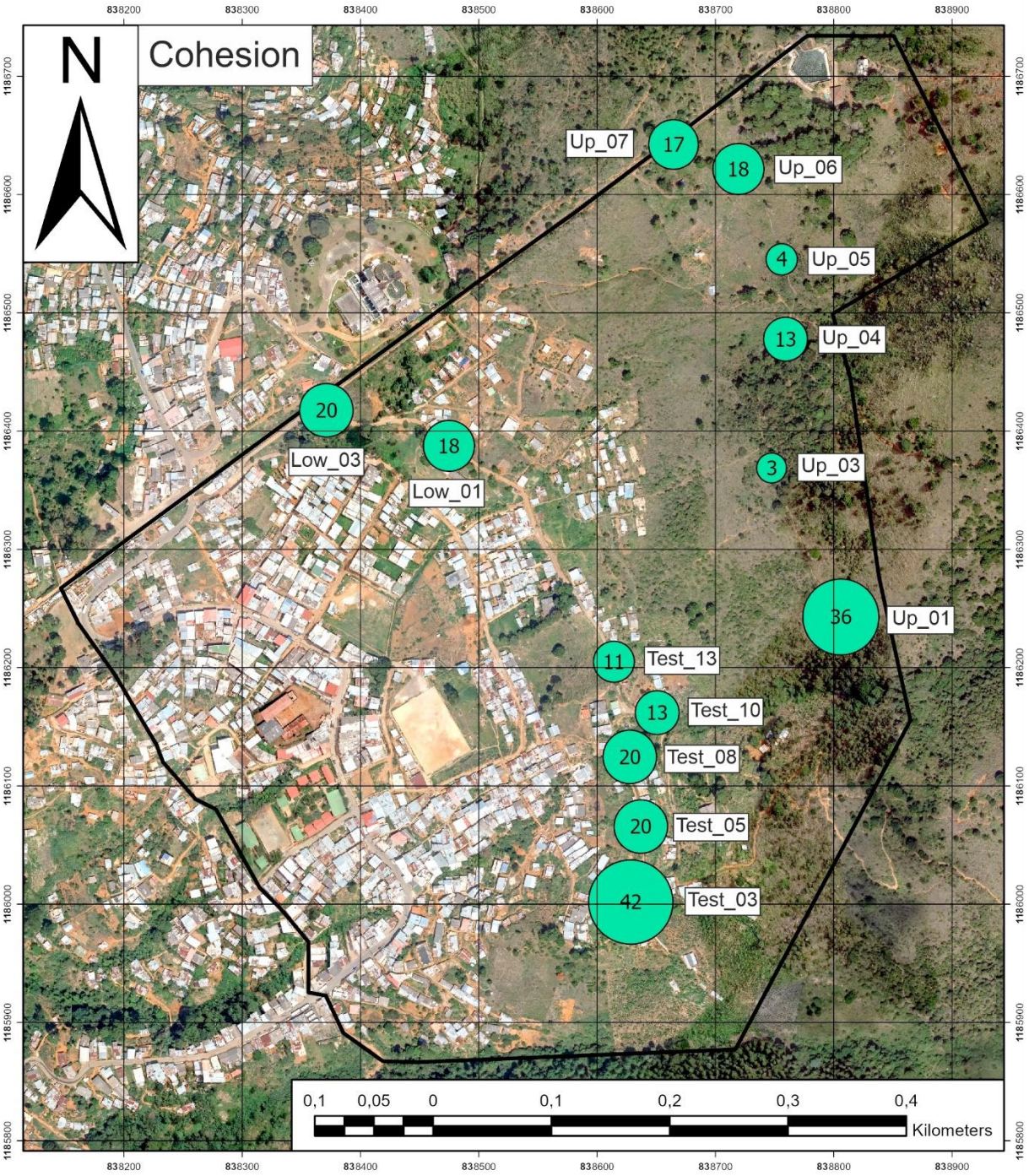

Figure 32: Spatial distribution of the cohesion of the trench samples.

5.6.3 Thin Section Analysis

The following chapter is derived from BREUNINGER et al. 2021c with some changes and additions.

During the analysis of the thin sections, six minerals or mineral groups could be identified frequently (Table A4): olivine, serpentine, pyroxene, amphibole, chlorite, and opaque phase (most likely ferrous minerals). There are also other minerals in the samples, but in very small frequency and quantity. In Figure 33 and Figure 34, some microscopic pictures of the thin sections show typical shapes of the minerals in the rocks and their weathering, which is visible in some samples.

Since dunite consists of olivine, pyroxene, and amphibole, the presence of these minerals has been expected. The serpentinization is very advanced in most samples, as is the weathering which is creating

chlorite. The opaque phases could be ferrous minerals such as hematite and magnetite, which are common in ultramafic rocks.

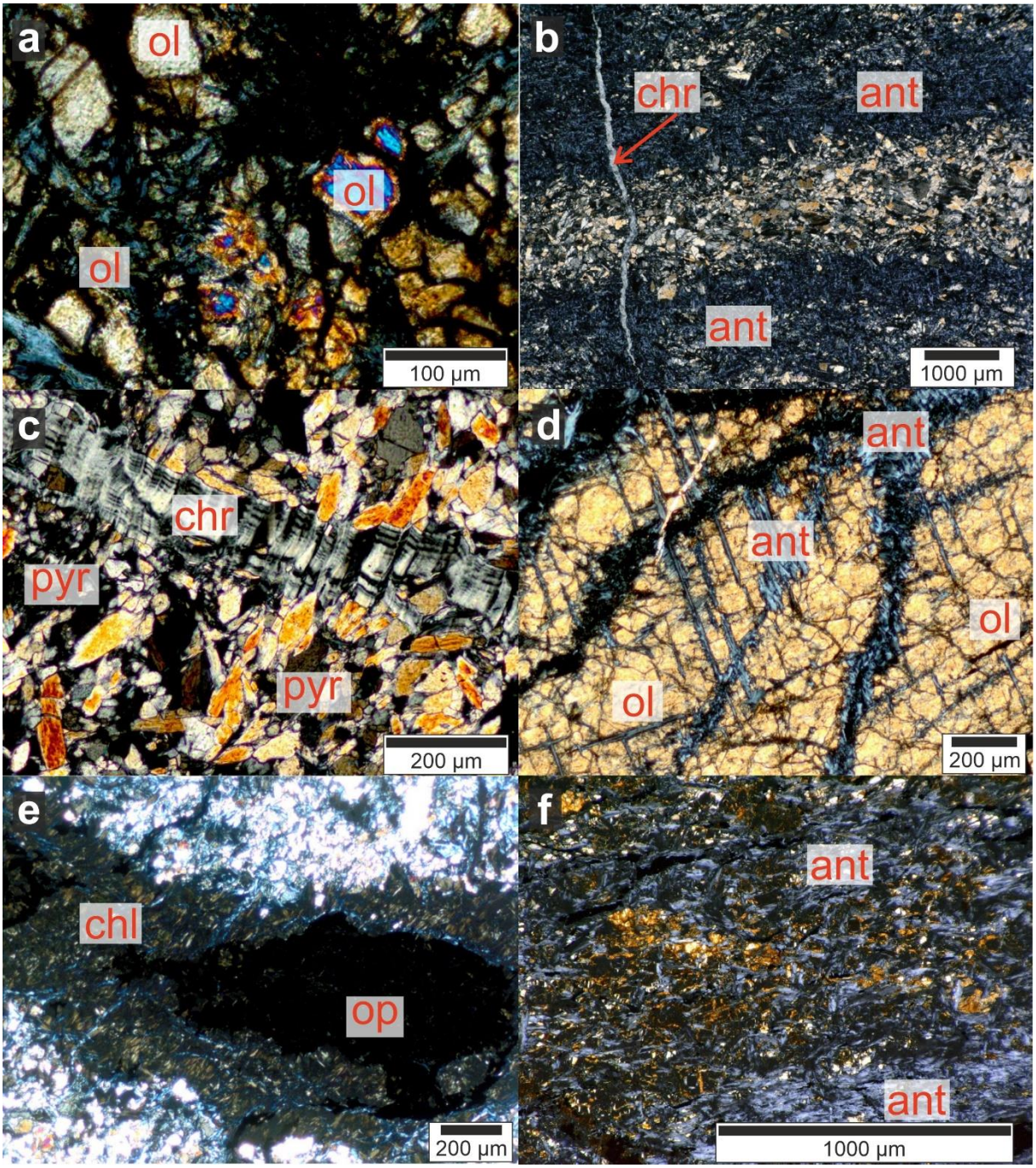

Figure 33: Microscopic photos of the thin sections related to the sample numbers: (**a**) = D-01; (**b**) = D-02; (**c**) = D-03; (**d**) = D-04; (**e**) = D-05; (**f**) = D-06 (ol = olivine, ant = antigorite, chr = chrysotile, pyr = pyroxene, chl = chlorite, op = opaque phase) (after AMBOS 2020 and BREUNINGER et al. 2021c).

The olivine crystals in the samples are mostly broken and heavily weathered at their exterior, as is visible in Figure 33a,d and Figure 34f.

Pyroxene (Figure 33c and Figure 34c) is not present in all samples, suggesting these parts of the rock might either be dunite in a strict sense without any pyroxene or that the pyroxene minerals have already been altered by serpentinization or weathering.

Five samples contain amphibole (Figure 34c, e), which is commonly present in ultramafic rocks. Its absence in the other thin sections indicates that it has already been serpentinized.

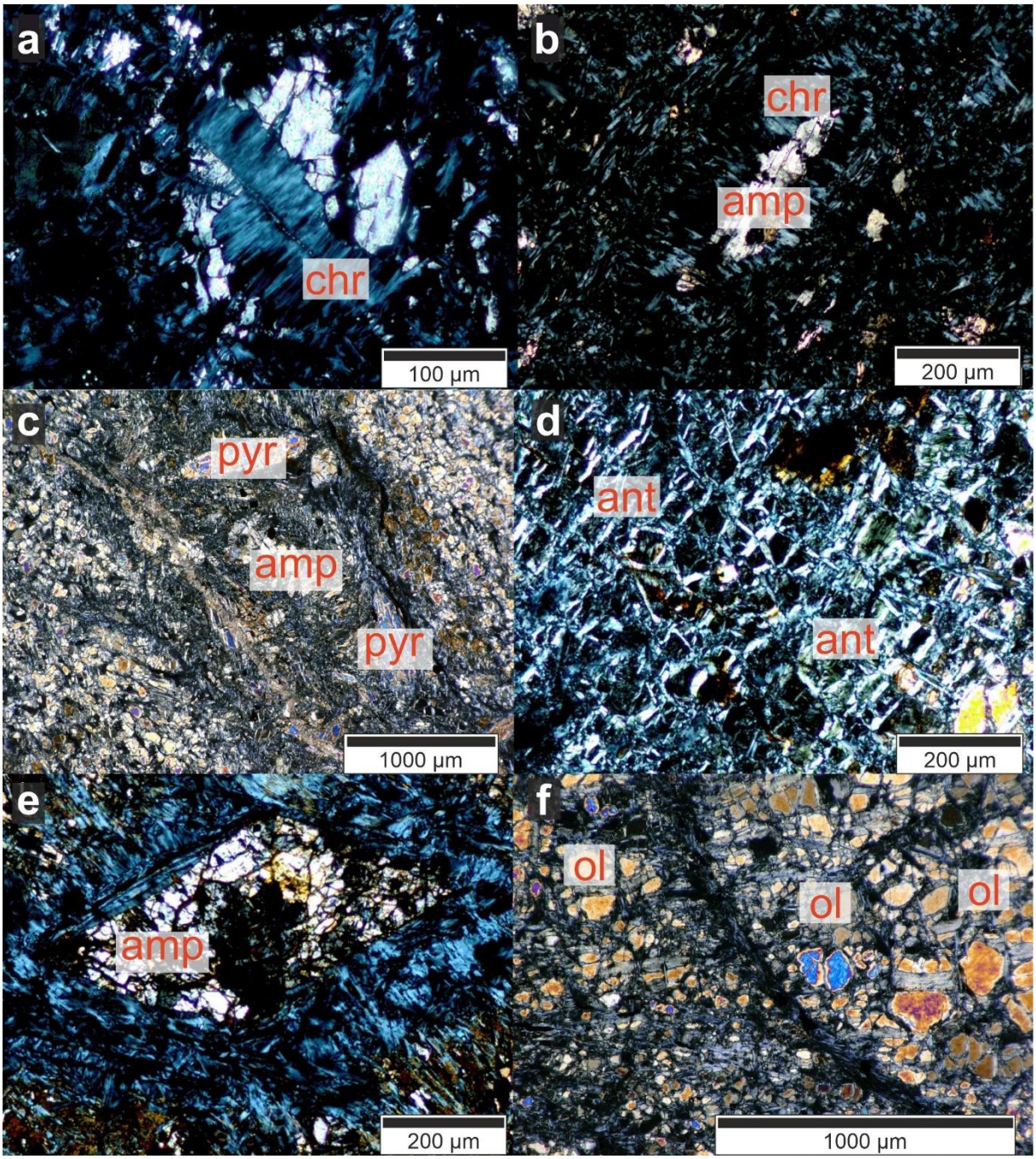

Figure 34: Microscopic photos of the thin sections related to the sample numbers: (**a**) + (**b**) = D-07; (**c**) = D-08.1; (**d**) = D-08.2; (**e**) = D-09; (**f**) = D-10 (ol = olivine, ant = antigorite, chr = chrysotile, pyr = pyroxene, amp = amphibole) (after AMBOS 2020 and BREUNINGER et al. 2021c).

Figure 34b shows serpentinization of an amphibole from the outside. Serpentine was found in most samples, either chrysotile (fiber serpentine, Figure 33b, c and Figure 34a, b) or antigorite (foil serpentine, Figure 33b, d, f and Figure 34d). The serpentinization starts at fractures (Figure 33d and Figure 34a) and grows into the minerals from there.

Chlorite (Figure 33e) is found in all samples. It is a common mineral in metamorphized ultramafic rocks and, therefore, was expected to appear in the Medellín Dunite (RESTREPO 2008). It is also a weathering product of silicates such as olivine (TRÖGER 1969).

Sample D-07 also contains several quartz veins. These veins are created by precipitation of SiO_2 in fractures. The SiO_2 is dissolved in water circulating in the fractures, its origin lies in other silicate minerals in the rock (olivine, pyroxene, amphibole, etc.).

Samples D-01, D-04, D-05, D-06 and D-09 contain small amounts of goethite. Goethite is a FeO(OH) mineral formed by weathering of iron containing minerals like pyroxene, amphibole, and olivine and, therefore, its presence in the Medellín Dunite is to be expected.

The differences in the mineral content show that the Medellín Dunite is not homogeneous regarding its mineralogical composition. Serpentine, olivine, and chlorite seem very common, but other samples were free of at least one of those minerals. Additionally, the domination of serpentine in the rock suggests that the dunite has already been transformed into a serpentinite.

Since all samples were taken from the surface without knowledge of their origin in the slope but as typical representative specimens of the rock material, there is no possibility of correlating the results with the sampling location.

5.6.4 XRD Analysis

The mineralogical composition of eight surface samples and ten trench samples was determined using x-ray diffractometry. The results of all tests are depicted in Table A5. The minerals of the surface samples analysed at the TU Munich were not quantified, the minerals of the trench samples analysed by Integral S.A.S. in Medellín were quantified (Table A5).

All surface samples contain chlorite, amphibole (tremolite), quartz and hematite. Except for sample L-07, goethite is present in all samples; serpentine (lizardite) is missing only in samples L-05 and L-07. Other minerals that were found in some samples are gibbsite, magnetite and olivine (forsterite).

Those minerals found in the surface samples are to be expected in weathered material of ultramafic rocks. The quartz content seems uncharacteristic at first sight. Quartz, however, is very resistant to weathering and, therefore, even a very small amount of it (veins in the rock, see chapter 5.6.3) is enriched very fast in its weathering material. Another source of quartz could be construction sand. Since the study site is located in a densely populated area, the contamination of the samples by anthropogenic material like this sand is very likely.

The lack of olivine in most samples shows the high degree of serpentinization of the rock and the fast degradation of the remaining olivine during weathering.

Serpentine and magnetite are not found in all of the samples; they could already be completely dissolved by weathering. The serpentine is mostly lizardite, which forms in the presence of meteoric-hydrothermal water (CAILLAUD et al. 2006), which fits this setup.

Hematite, goethite (iron oxides), chlorite (iron/aluminum hydroxide) and gibbsite (aluminum hydroxide) are typical weathering products of iron containing minerals. The absence of some of the minerals in some samples indicates different educts, which underlines the theory of the inhomogeneous composition of the Medellín Dunite.

Sample L-07 differs the most from the others. It also contains a small amount of a swelling clay mineral, most likely nontronite (ZIEGLER 2020). This difference could be due to its remote sampling location separated from the other samples (see Figure 13).

There is no pyroxene found in any of the samples. Pyroxenes are very hard to detect in X-ray diffraction, since their peaks are not very precise but have a range. Their peaks could also be overlapping with the peaks of other minerals.

All surface samples were taken in an anthropogenically altered region. Therefore, a contamination, as well as a content of external minerals could not be excluded completely, which is also why it is impossible to correlate the results spatially. The collected material might not be from its original location.

The mineral content of the trench samples is very different, depending on the sampling location, in contrast to the results from the analysis of the surface samples. The results of the trench samples and their spatial distribution is depicted in Figure 35.

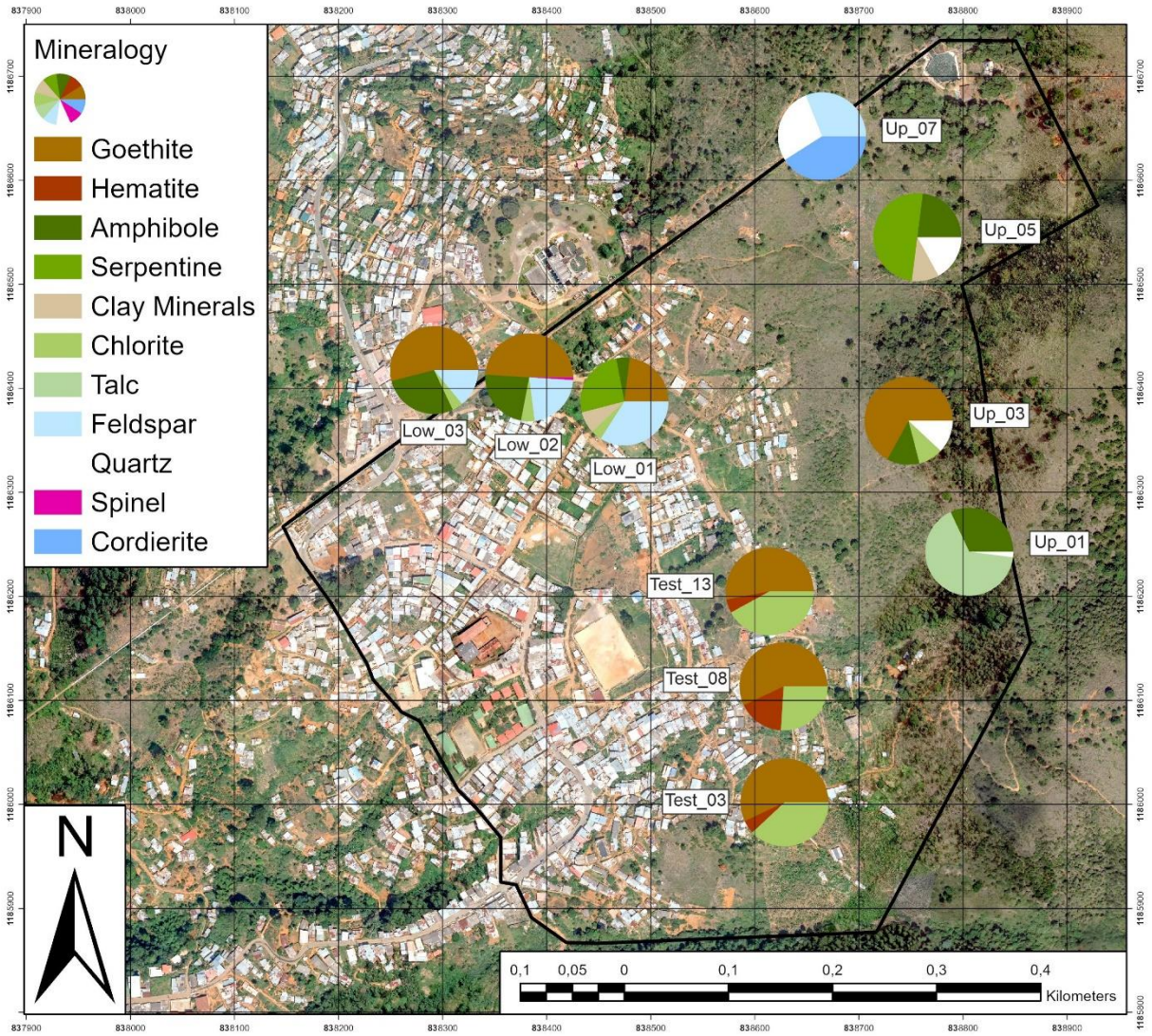

Figure 35: Spatial distribution of the mineralogical composition of the trench samples.

The most common minerals in the ten trench samples are chlorite and goethite, which were found in seven samples, and amphibole, found in six samples. If iron oxides are present in the sample, they normally add up to over 50 % of the material. Quartz and feldspar were each found in four samples, hematite was found in three samples. The rarest minerals detected are serpentine and clay minerals in two samples and spinel, cordierite and talc in one sample each.

The three samples from the southern downhill sampling locations (Test_03, Test_08, Test_13) all contain the same minerals, chlorite, goethite, and hematite. The three northern downhill sampling locations (Low_01, Low_02, Low_03) also have a very similar mineral content with chlorite, amphibole, goethite, and feldspar found in all of those samples. Low_02 additionally contains spinel, Low_03 additionally contains serpentine and clay minerals. The four uphill samples (Up_01, Up_03, Up_05, Up_07) only share the two minerals amphibole and quartz, Up_07 only quartz. The sample Up_01 additionally contains talc; sample Up_03 chlorite and goethite, sample Up_05 serpentine and clay minerals; sample Up_07 feldspar and cordierite, but no amphibole.

Most samples lack highly expected swelling clay minerals, that could have explained the differences in cohesion values and the highly plastic behavior in the Atterberg limits tests. The surface samples also did not show clay minerals in the x-ray diffractometry, except for one (L-07). It is possible that the peaks of these minerals overlap with those of other minerals and can, therefore, not be identified. This is a

common problem of this testing method. However, the glycolyzed samples should show some differences to the other samples, if clay minerals were present. These differences were not nearly as high as expected, but the presence of clay minerals is still not ruled out.

The total absence of olivine also in these samples can be explained by the high degree of serpentinization of the mineral in the rock in the first place and the fast degradation of this mineral by weathering due to its high iron content, as mentioned above.

As is the case for olivine, the absence of serpentine in most samples can be explained with the high degree of weathering of the soil. Due to that process the serpentine minerals might already be dissolved completely at some locations at the study site.

The typical weathering products of iron rich soils, goethite, hematite, and chlorite are present in most samples, but not in all. This underlines the degree of variation within the unit of the Medellín Dunite. The absence of all those minerals in some samples (Up_01, Up_05, Up_07) is very unusual. It could be, that some minerals were present, but not detected by the test.

The mineral pyroxene, normally present in this unit, has not been detected, as was the case for the surface samples. As mentioned above, pyroxene is hard to detect with X-ray diffractometry.

The presence of quartz and feldspar in some samples was not expected, since these minerals are not commonly present in dunite rock. Since quartz is very weathering resistant, even a small amount of it in the rock is enriched highly in the weathering material, as was discussed for the surface samples. The main reason for the presence of these two minerals, however, is anthropogenic alteration. The whole study site is densely populated, and all samples are very likely to be contaminated by human activity. Both minerals might come from construction material like sand and cement. One sample (Up_07) only contains quartz, feldspar, and cordierite. This sample was taken directly next to the concrete wall of an artificial waterway. It was, therefore, highly contaminated by the construction and does not represent the natural soil.

The XRD analysis is the only test that shows a correlation between sampling location and results, in this case mineral content. The downhill samples seem to be further weathered, since they show a high amount of iron oxides and hydroxides (goethite/hematite), which were only found in one uphill sample (Up_03). The southernmost samples (Test_03, Test_08, Test_13) only show weathering products (goethite, hematite, chlorite), whereas the samples Low_01, Low_02 and Low_03 show the highest degree of anthropogenic alteration (feldspar content) in addition to sample Up_07. These three samples were collected next to a dirt road in the most densely population area of all sampling locations.

The low clay mineral content or the lack of them in most samples was very unexpected, since these minerals were considered to be responsible for the high plasticity values and friction angles. It is possible that the minerals were underrepresented in the x-ray diffractometry due to overlapping peaks. According to HANS-ALBERT GILG (2024) in a geological setting like this, the ions of the clay minerals are most likely washed away before the minerals can form and are precipitated at springs, where the clay minerals are formed. Another, less likely explanation is, that the clay minerals were formed within the soil material but are already washed out (GILG 2024).

5.7 Social Integration

Thanks to the early and intense approach on community involvement none of the installed sensors and other equipment has been vandalized or stolen so far. The only problem, that occurred, were minor issues with the infrastructure nodes (LoRas) at private houses, since some house owners removed the sensors for construction works and did not put them back on the walls properly. Neither the CSM system nor the subsurface nodes were stolen or vandalized.

This shows the success of the community work in the project by the Colombian partners, the integration of the sensors in the neighborhood and the inclusion of the community members in the installation process. The project could not have been carried out without any of these aspects of social integration and

the further operation of the EWES would be next to impossible. All measures taken are replicable in other parts of Medellín, Colombia and the Andean region. They are labor-intensive and time-consuming, but affordable also for poorer communities and as part of the ‚last mile' extremely important for the success of an EWES.

6 Interpretation of Results

Parts of this chapter have already been published in BREUNINGER et al. (2021c) and in GAMPERL et al. (in review).

6.1 General Evaluation of the Results

The following chapter is derived from BREUNINGER et al. (2021c) with some changes and additions.

The landslide feature map shows only small-sized (max. 15,000 m^2) and shallow- to mid-seated (max. 10 m depth) landslides. A former, deep-seated landslide could not be excluded, but is nevertheless not very likely. These observations fit into the descriptions of landslides in the eastern slope of Medellín of the past decades (see chapter 3.2).

As depicted in Figure 16, Figure 17, Figure 18 and Figures A1-A4, the thickness of the soil below the surface hardly reaches 2 m in drillings A1 and A2, less than 10 m in drillings B1 and B2. This was very unexpected and underlines the importance of a detailed and exhaustive investigation of the subsurface in the Medellín Dunite, since this unit shows extreme variations.

Discontinuity Sets

The three joint sets mentioned in chapter 3.1 were observed in the parallel to joint set 3 striking ridges of dunite rock in the geological map (chapter 5.2), all four drillings (chapter 5.3), the joint recording using hillshade analysis and scanlines (chapter 5.4), and the ERT measurements (chapter 5.5). They do not strike or dip in the exact direction and the exact angle mentioned in the literature, some stand vertically to the typical direction; given the high variation of the Medellín Dunite and its tectonic history, these discrepancies are to be expected.

Weathering Processes – Serpentinization and "Pseudokarst" Structures

The expected weathering profile of decreasing weathering stages with the depth was not observed in any of the four drillings. However, the drillings did confirm the theory of block-in-matrix structures and especially pseudokarst cavities in the dunite body, as described by previous studies (TOBÓN-HINCAPIÉ et al. 2011, RENDÓN-GIRALDO 2020) and chapter 3.1. The high ratio of core loss in all drillings provide certain evidence of some smaller cavities in the rock mass. Additionally, the presence of large amounts of loose material in deep parts of the drillings indicate a high degree of water circulation within the rock along the pseudokarst structures and other fractures, accumulating the soil material in these cavities and contributing to the high degree of weathering at depth. This phenomenon also creates a block-in-matrix structure in the end.

In all drillings, a serpentinization, especially along fractures and joints, could be observed, besides oxidation processes (brown colored areas). According to literature dealing with weathering of ultramafic rocks (GARCIA-CASCO et al. 2020, TOBÓN-HINCAPIÉ et al. 2011, ÜNDÜL et al. 2015, ÜNDÜL & TUĞRUL 2016), this serpentinization is a characteristic weathering process of dunite rock. Normally, serpentinization only takes place in hydrothermal regimes with water temperatures above 100 °C (CAILLAUD et al. 2006). Antigorite can only be formed above 250 °C (CAILLAUD et al. 2006). However, since we do observe antigorite and chrysotile in the thin sections, but only lizardite in the X-ray diffraction, lizardite could be the serpentine mineral being formed during weathering processes of dunite rocks (pseudokarst/'second serpentinization'), while antigorite and chrysotile were created earlier during ocean floor metamorphosis in a hydrothermal process ('first serpentinization') and are already weathered in the soil samples.

The outcomes of the laboratory tests conducted on the samples of the drilling cores show generally no correlation with the depth of the drillings or the drilling locations. This underlines the extreme heterogeneous structure and behavior of the Medellín Dunite. A common weathering profile (decreasing weathering with increasing depth) would show increasing compressive strength, tensile strength and grain sizes with increasing depth (ÜNDÜL et al. 2015, ÜNDÜL & TUĞRUL 2016). Despite the missing

correlation between the depth and the values of the rock test results, the values do vary extremely with 10-132 MPa for uniaxial compressive strength and 4.1–17.5 MPa for tensile strength. Most samples showing low values were already expected to be weak because of their weathering or serpentinization. However, some samples showed no alteration on the outside, but still had low values in the compressive and tensile strength tests. This shows a varying internal disintegration of the rock's structure without visible weathering signs even in seemingly intact bedrock to a depth of at least 50 m. Disintegrated rock without oxidation or visible weathering is also observed in the drillings B1 and B2 in the homogeneous area 6. These samples seem to be fractured formerly intact rock parts, but can be crushed by hand, indicating an advanced weathering throughout this part of the dunite body without any visible evidence of weathering or tectonic damage already before weathering. However, these parts of the rock show a high degree of serpentinization. In this case, this could be due to pseudokarst formation, as mentioned above, which disintegrates the whole rock without oxidation or degradation into clay minerals.

The soil tests on the drilling cores also show no correlation of depth with grain size and plasticity of the fine material, the samples taken from the trenches show no correlation between sampling location and grain size and plasticity. Highly plastic soil is distributed throughout the depth of the dunite, accumulating in pre-existing fractures and pseudokarst cavities, which indicates that it originated in weathering of the rock. The cavities and fractures are further widened by the water flowing through them and are continuously filled with the weathering products. The loose material is not only oxidized but also shows green colors or no discoloration at all. The green areas could contain lizardite and chlorite, since both minerals are weathering products of the serpentinized dunite rock and show light green colors (CAILLAUD et al. 2006). Most soil samples provide a high content of fine material, as already observed during field work. This is also visible in the drilling cores since the cores either show intact rock parts or completely disintegrated loose material that does not contain high amounts of gravel. This indicates that the loose material was not formed by tectonic forces (which would have produced gravel and sand alike), but primarily by weathering processes. The plastic behavior of some samples suggests a considerable amount of swelling clay minerals, which were, however, not found in the x-ray diffractometry.

Thin Section Analysis and X-Ray Diffraction Analysis

The mineralogical composition observed in the thin sections of some rock samples is coherent with previous data (BOTERO-ARANGO 1963, RESTREPO & TOUSSAINT 1984, ÁLVARES-AGUDELO 1987, GONZALES 2001, RODRÍGUEZ et al. 2005, CORREA-MARTÍNEZ 2009, RESTREPO 2008, HERNÁNDEZ-GONZÁLEZ 2014, GARCIA-CASCO et al. 2020, TOBÓN-HINCAPIÉ et al. 2011). Most parts of the samples are highly serpentinized, antigorite and chrysotile can be distinguished easily, and lizardite could not be found. Therefore, pyroxene, amphibole and olivine (forsterite) are already being transformed to varying degrees, depending on the sample. These differences in the samples regarding the ratio of olivine (forsterite), amphibole and pyroxene and the degree of serpentinization are severe, i.e., amphibole and pyroxene are already dissolved in some samples. The weathering of the material could also be observed, the minerals are mostly transformed into the iron oxide goethite. Even though the presence of olivine in all samples indicates an originally high amount of this mineral in the rock, the amphibole and pyroxene found in most samples indicate that the rock is, in fact, not exactly a dunite, but rather a peridotite. The high degree of serpentinization, however, provides evidence that the unit is mostly made up of serpentinite and not peridotite, harzburgite or dunite.

In the x-ray diffractometry on the surface samples, lizardite was found, but no antigorite or chrysotile, indicating a transformation of those two serpentine minerals and the forming of lizardite, possibly by weathering processes. This might underline the theory of a second serpentinization by weathering (GARCIA-CASCO et al. 2020, TOBÓN-HINCAPIÉ et al. 2011, ÜNDÜL et al. 2015, ÜNDÜL & TUĞRUL 2016), as explained above. All other minerals observed in the x-ray diffractometry of the surface samples were expected after reviewing the thin sections. The quartz in the soil samples could also originate in contamination by construction material in this highly populated area, since quartz was only found in one thin section but in many surface samples taken for the x-ray analyses.

The mineralogical composition of the samples from the trenches differs from the surface samples. All surface samples contained chlorite, amphibole, quartz and hematite, most contained serpentine, and goethite, as would be expected in an ultramafic environment. These minerals were also detected in the trench samples, but they are not present in all samples, some only in a few. Especially serpentine, which would be expected in weathering material of an ultramafic rock, is missing in most samples. The serpentine minerals may already be dissolved completely in most samples. The results of the x-ray diffractometry generally fit with the results from the surface samples, but the lack of essential minerals in some samples suggests an even more diverse composition of the rock as expected after the results of the surface samples.

Shear Parameters

The values of the friction angle detected in the shear tests on the samples taken from the trenches and drilling B2 are much higher than anticipated (26.9-39.4°). Typical values for plastic fine-grained soil do not exceed 27.5° (DIN 1055-2 2010). Some sampling locations showed a content of coarse-grained material of up to 46 %, which can lead to values of more than 30° and, therefore, explain friction angles of up to 40°. The cohesion varies extremely between 3.2 kPa and 41.7 kPa. Since the cohesion depends on clay mineral content, water content, saturation, and compaction of the soil (DIN 1055-2 2010), these variations might be created by a combination of all four factors.

As observed during the field investigations over three years, the fine-grained material in the study site can easily create vertical walls, for example cuts for a construction site. Additionally, the slope angle at the study site exceeds 35° at some locations, without immediate signs of a landslide developing, like fissures or depressions. The high friction angles detected in the shear tests mirror this field behavior. The landslides of the landslide database of Medellín (SIMMA, www-14) and the historic landslides mapped in 2019 occurred with different slope angles of 20-25°. These different angles of failure already indicated varying friction angles, water retention capacities and grain size distributions throughout the study site and confirm the extreme heterogeneity of the underground. The values of friction angle determined in the shear tests are higher than the angle of failure of the historic landslides but are within the angles of the stable slopes in the study site. This indicates that the slope and friction angles are not the only factors to be considered when determining the landslide probability in the study site.

6.2 Underground Model of the Study Site

6.2.1 Visual Interpretation of ERT Transects

Figure 36, Figure 37 and Figure 38 show the visual interpretations of the three ERT transects presented in chapter 5.5. The profiles show the tectonic destruction by fault systems, the high fragmentation by joint systems and the deep weathering, including pseudokarst structures, in the Medellín Dunite, evident from the results of the field and laboratory investigations (chapters 5 and 6.1). Since the resistivity values of the ERT measurements correspond with the degree of weathering and fragmentation (ÜNDÜL et al. 2015, ÜNDÜL & TUĞRUL 2016, DEMHARTER 2021, BREUNINGER et al. 2021c, GAMPERL et al. in review), this disintegration was also made visible in the profiles. The areas showing very low resistivity values are depicted in the profiles as soil material including dunite blocks of varying sizes (block-in-matrix structure).

It is evident from these profiles, that there is no clear distinction between or layering of soil/loose/colluvial material, saprolite and bedrock in the depth. This last boundary (saprolite/bedrock) would be the deepest possible sliding surface for a potential landslide. Due to the extremely rough surface of the bedrock in the depth, the possibility of such a deep-seated event is very low, but cannot be ruled out, as already suspected in chapters 3.2, 5.1 and 6.1. It is still possible for a sliding surface to form deeper down than the observed 10 m (chapter 5.1), if extensive cavities filled with weathered, water-saturated material develop in the slope.

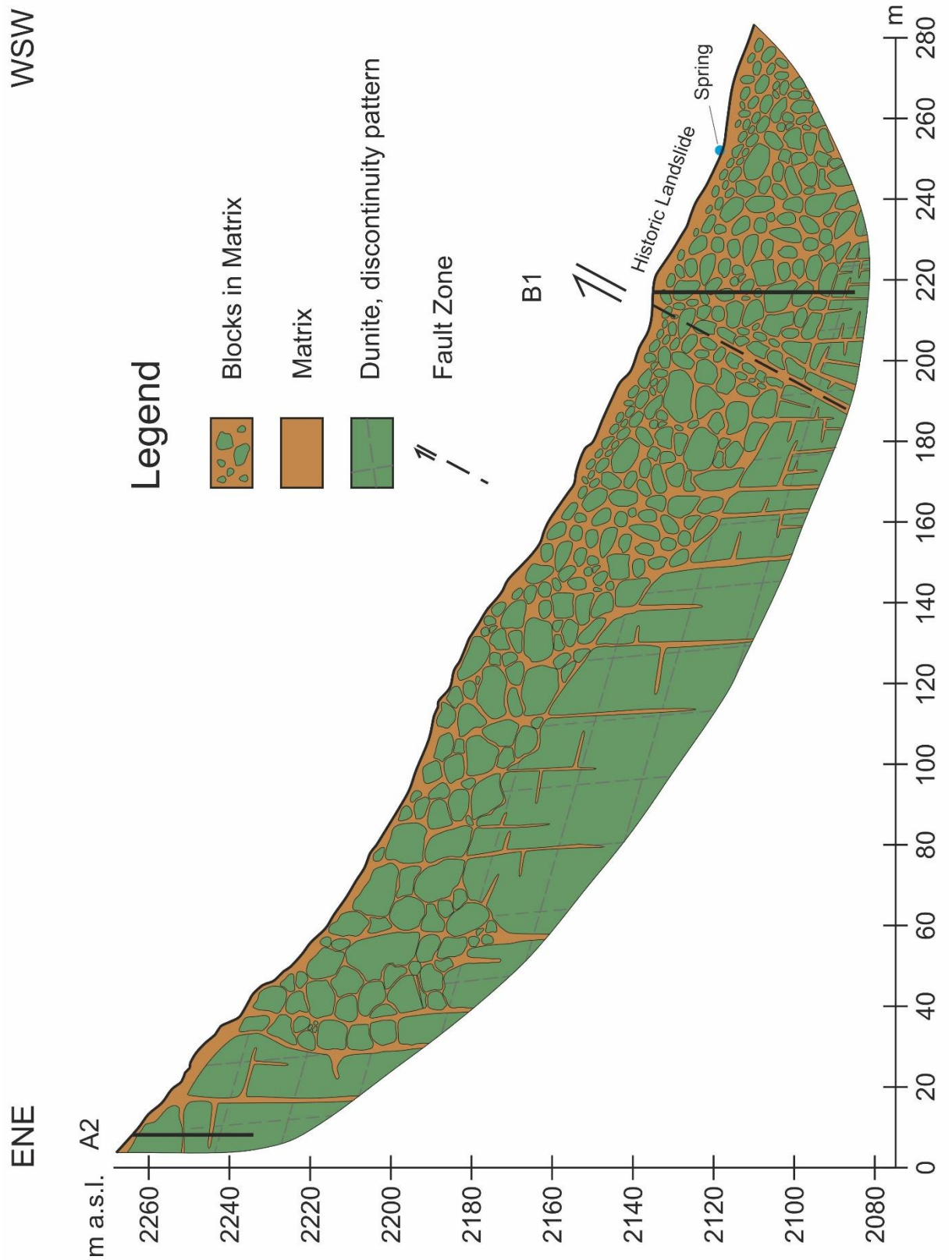

Figure 36: Visual interpretation of ERT transect BO-01 (after GAMPERL et al. in review).

Figure 37 shows two very broad fault systems in transect BO-03. These areas with low resistivity values in the ERT transect BO-03 do not allow for a more distinctive interpretation of the location of these faults. Therefore, in both cases the entire area of low resistivity was depicted as a fault system, in reality those areas are most likely not as broad.

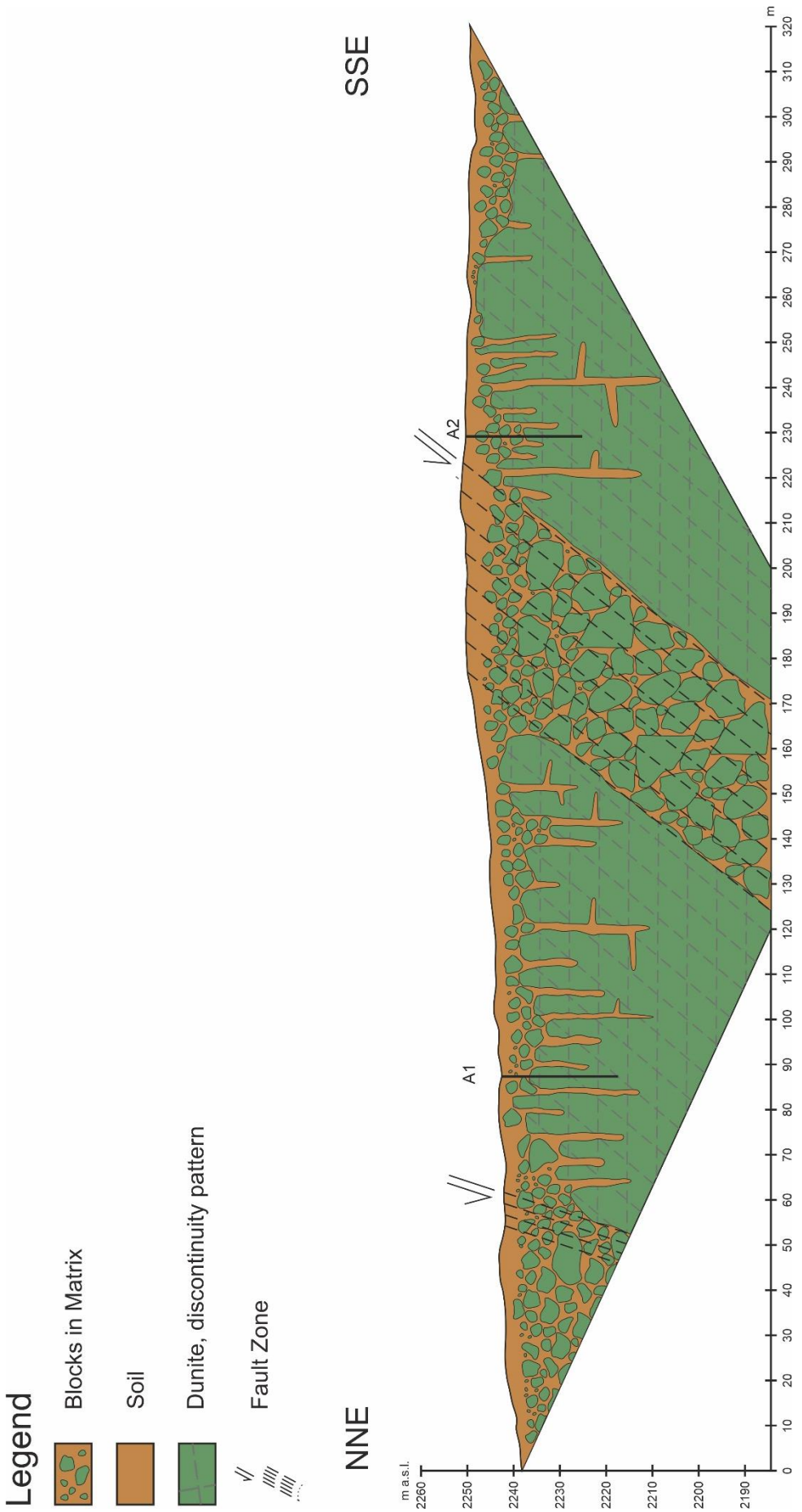

Figure 37: Visual interpretation of ERT transect BO-03.

Figure 38: Visual interpretation of ERT transect BO-04.

6.2.2 Colluvial Map

The geological map (chapter 5.2, Figure 15), the results of the ERT measurements (chapter 5.5), specifically the visualization of these (chapter 6.2.1), and the drilling evaluations (chapter 5.3) were used to create the colluvial map depicted in Figure 39 and Figure A7.

The areas consisting of in-situ rock and saprolite in the geological map (Figure 15) are also categorized as those in the colluvial map (green and light green). The areas, that were categorized as block-in-matrix structure of varying amounts of block and matrix are depicted in the colluvial map regarding the depth of the colluvial thickness (beige/brown colors), irrespective of block or matrix content. The blocks in this structure are defined as less than 5 m in diameter. Areas with bigger blocks are not defined as colluvium, since blocks of these sizes in the subsurface are most likely in-situ weathered due to advanced pseudokarst formation. In addition, these areas are not believed to have been moved in the past and are also not likely to be moved in the future due to the wedging of the blocks.

Most of the colluvial material in the study area is considered to be up to 5 m thick. In the middle of the study site, striking SW-NE, there appears to be a broad depression or trench, where the colluvial material reaches a thickness of over 10 m. This structure was mostly retrieved from ERT transect BO-03 (Figure 22, Figure 37). In this transect this area shows extremely low resistivity values, indicating the presence of block-in-matrix structure, possibly with a high amount of matrix due to its water absorption capacity. These low resistivity values reach a depth of at least 50 m, which is the vertical limit of the ERT measurement. Due to the results of drilling B2, which punctures the ground in the middle of that depression in the ERT transect BO-03, the depth of the colluvial material in this area was reduced to the term “over 10 m”. This drilling’s core shows a high amount of continuous unaltered to lightly altered but fractured rock parts, starting at a depth of 9.95 m (Figure 18, chapter 5.3.4). These parts of fresh to lightly altered dunite rock are separated by layers of soil material. Therefore, this area is, additionally, marked as “heavily fractured” in the colluvial map, explaining the low resistivity values in the depth in transect BO-03 despite having recovered dunite rock instead of mainly soil material in drilling B2.

6.3 Hazard Assessment

The hazard assessment was a collaborative effort in the project and is included in this thesis as the final result of the field and laboratory work and the development of the underground model. It is presented in the form of a short overview of the methods and results. Some results of the hazard assessment have already been published in WERTHMANN et al. (2024).

The heterogeneity of the subsurface in the study site is the main difficulty for the development of an EWES. This heterogeneity is created by the varying mineralogical composition and fragmentation of the dunite, which leads to differences in the intensity of the weathering processes, mainly the occurrence and depth of pseudokarst. These different weathering intensities (and, therefore, differing amount of soil in the depth) lead to a small-scale varying character of the block-in-matrix structure, the most landslide prone structure in the study site, reaching to a depth of at least 50 m, as is evident from the drillings. All historic landslides mapped are mostly or entirely located in that structure. Its soil content is not as high as expected, but the soil material exists even with increasing depth, is very fine and is therefore suggested to act as a shear surface for landslides, even with a thickness of only a few centimeters. The thicker and finer the soil (matrix) between the blocks, the higher the probability of a shear surface developing in that soil layer. The probability increases due to water saturation during the rainy season or due to anthropogenic reasons, e.g., a leakage in the water pipe system.

Since the unit of the Medellín Dunite is so heterogeneous, it is impossible to forecast the location, size, depth and velocity of a landslide event.

The friction angles of the trench and drilling samples (chapter 5.6.2) are much higher than anticipated (26.9-39.4°) by taking the local landslide database (SIMMA, www-14) into account, which shows a typical angle of failure of 20-25°. However, stable slopes of up to 35° inclination or more show, that these angles of failure are not valid for all parts of a slope. Differences in mineralogical composition,

grain size and, therefore, water retention capacity play an important role in slope stabilization. Since most landslides occur within a range of angles between of 20° and 25° the landslide hazard assessment must take these values into account as well.

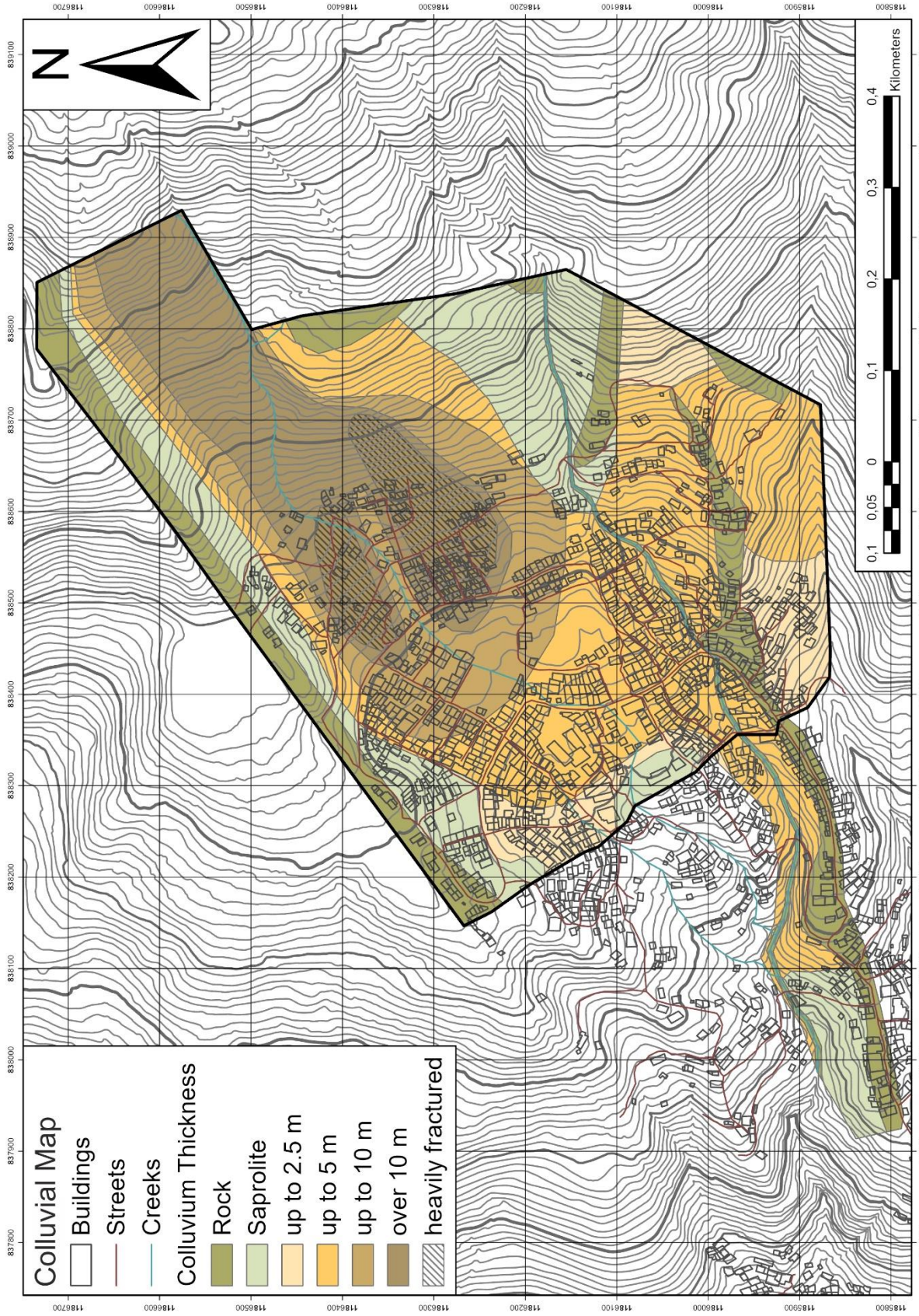

Figure 39: Colluvial map of the study site.

6.3.1 Characterization of Events

The landslides recorded during the first field campaign in the process map (chapter 5.1) are listed in Table 13. They were categorized regarding their size and age into a magnitude-frequency graph, which is depicted in Figure 40.

Table 13: List of landslide events in the study site and their event date, size, slide geometry and information source.

Event date [year]	Event size [m²]	Slide geometry	Source
1910s	4,980	rotational	Community
1980s	5,560	rotational	Community
1980s	6,558	rotational	Community
2000	849	rotational	Community
2000	699	rotational	Community
2002	9,783	rotational	Community/SIMMA (www-14)
2003	1,668	rotational	Community/SIMMA (www-14)
2007	14,981	rotational	Community
2007	3,013	rotational	Community
2008	2,746	rotational	Community
2008	3,376	rotational	Community
2009	10,786	translational	Community
2010	567	rotational	Community
2017	2,084	rotational	Community
2017	2,973	rotational	Community/SIMMA (www-14)
2022	228	rotational	Community
2022	312	rotational	Community
?	5,031	rotational	Community
?	2,316	rotational	Community

Of the 19 events registered in the study area, eleven had a size of < 4,000 m² and an event date of 2000-2022, six had a size of 4,000-15,000 m² and an event date of 1915-2009. Two landslides could not be categorized, because there was no information about their age. The information about the ages of the landslides was given by the community members and, if possible, verified by the SIMMA data base (www-14). All landslides were classified as shallow (0.3-2.0 m) to mid-seated (2.0-10.0 m) landslides according to BAFU (2016), but the exact depth was not visible due to the high degree of anthropogenic activity.

The two event magnitudes were categorized as small and as medium events. The smaller events happen more frequently and were, therefore, classified as typical 30 year events, similar to the Swiss model (BAFU 2016). The medium sized events were subsequently classified as typical 100 year events. Since no events with an area of > 15,000 m² and a depth of > 10 m were registered in the study site, neither in the SIMMA database (www-14) nor during the field trips, these events were classified as very rare > 300 year events. An event of this size is not expected, since there is no record of it having happened in the past in the study site, but it cannot be ruled out, as already discussed in chapters 3.2, 5.1 and 6.2.1.

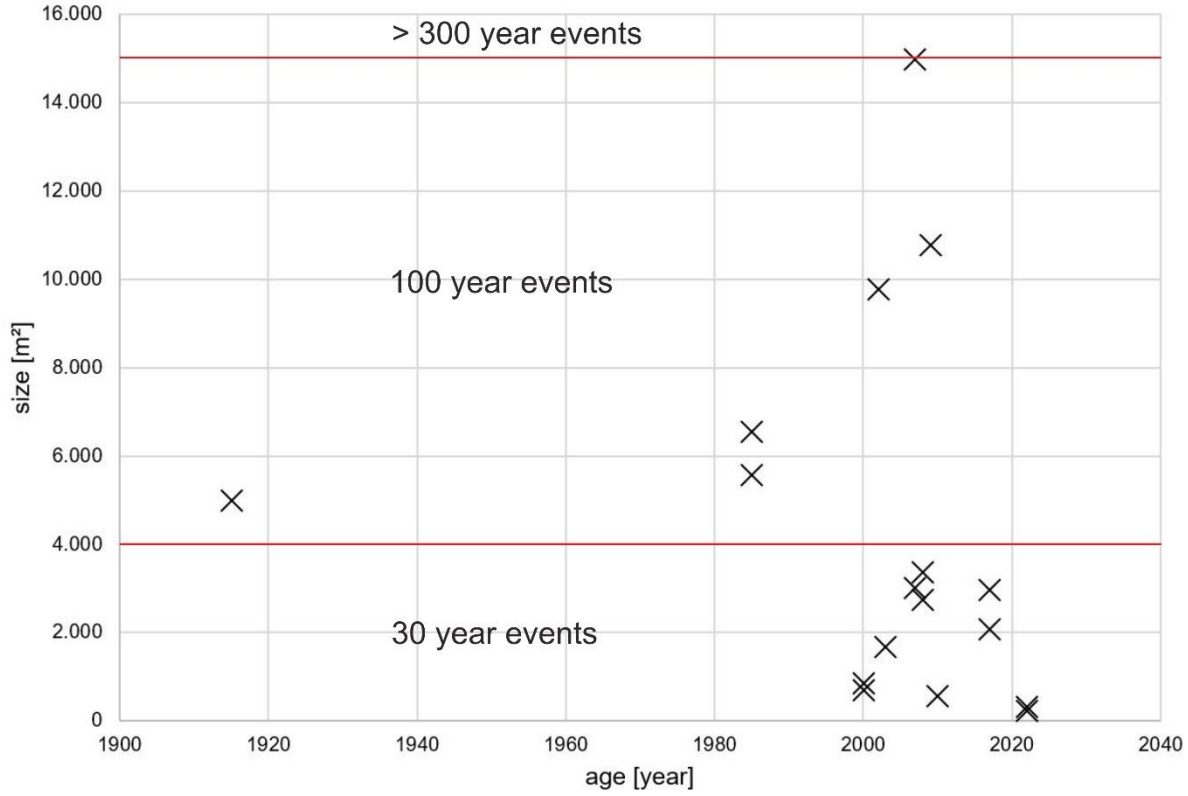

Figure 40: Age of the landslide events recorded in Bello Oriente plotted against their size.

The field observations and event categorization allowed a definition of the three magnitudes of events, depicted in Figure 41:

A typical 30 year event, as registered in the study site, is 15-100 m long and up to 10 m deep, but mostly more shallow. It is a simple, single shear surface detachment and normally forms rotational slides. No translational slides were found for this magnitude in the study site.

The 100 year event is much larger, with a length of 100-200 m and also a depth of up to 10 m. The maximum depth does not differ from the depth of the 30 year event, since the registered events of both event magnitudes showed similar event depth; the 30 year events tend to be more shallow, but both reach a maximum depth of 10 m. This event magnitude also has a simple, single shear surface detachment. In addition to rotational slides, the 100 year event can also develop translational slides, since one translational slide was registered in the study site (Table 13).

Lastly, the very rare > 300 year event, an event size that was not registered in the study site, was defined as a complex, multi-stepped and self-amplifying and -triggering landslide of up to 500 m length and unknown depth. This event was initially based on the Villa Tina landslide from 1987, which showed a depth of 1.0-8.0 m (medium 6.0 m), a length of approx. 60 m and a width of approx. 50 m, resulting in a volume of approx. 20,000 m³ (TOKUHIRO 1988, HERMELÍN 2005, MONTERO-OLARTE 2007). This event had a long runout due to an increasingly steep slope located just below the end of the detachment, accelerating the movement and, therefore, the reach (MONTERO-OLARTE 2007). Since a slope that steep is not present in the study site, the size of a typical event of the > 300 year magnitude was increased, being larger than the largest event in the study site (15,000 m²), and transferred into this complex multi-event structure. Both translational and rotational sliding surface geometries are possible, also both versions at once due to the complex nature of this event magnitude.

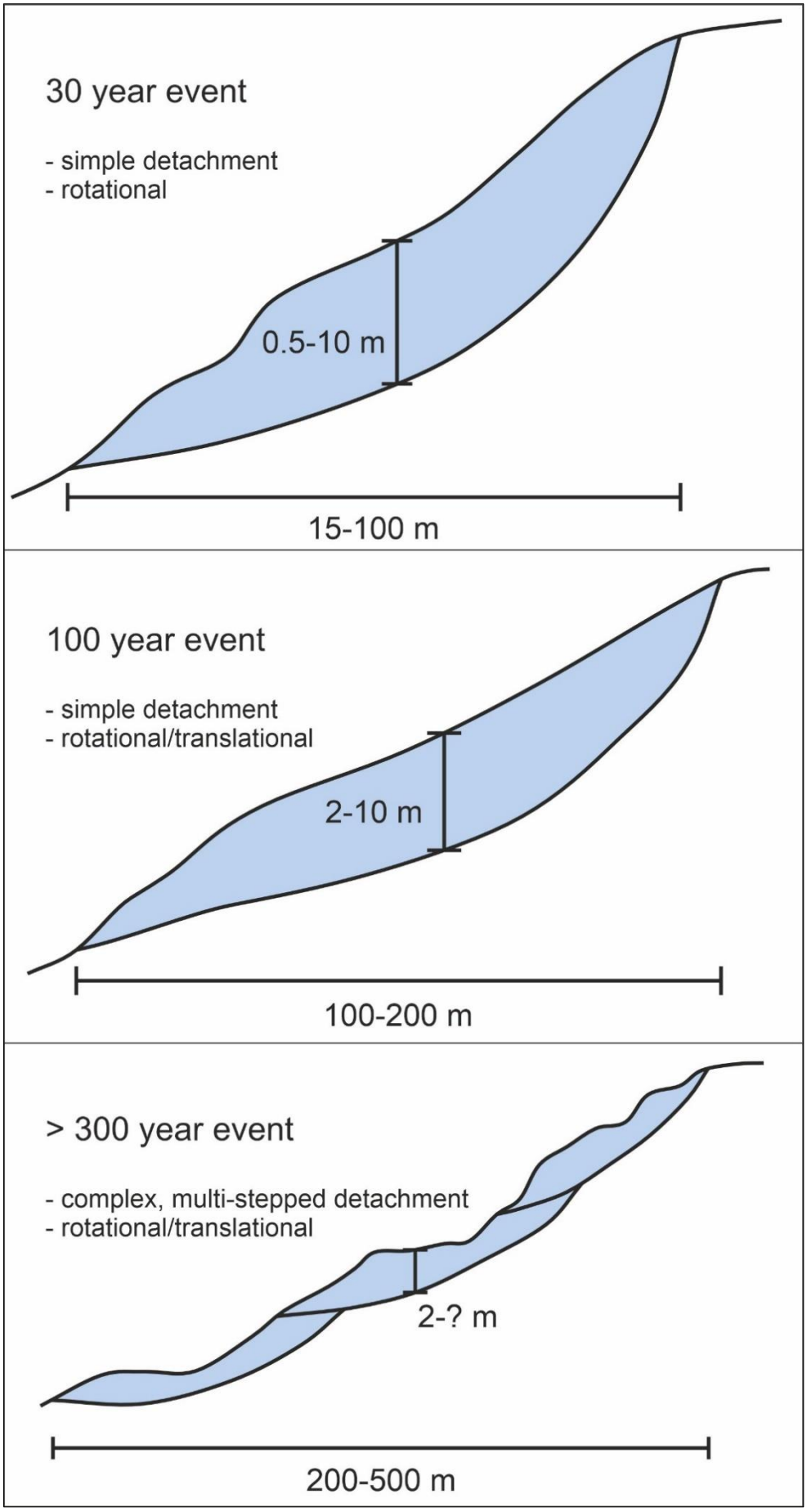

Figure 41: Sketch of the typical appearance of the three event magnitudes in the study site.

All three event magnitudes were categorized according to the Swiss model (BAFU 2016), which is depicted in Figure 42. This schema uses the probability and the intensity, both in low, medium and high, of an event to determine the hazard, depicted in red (high hazard), blue (medium hazard), yellow (low hazard), and yellow-white striped (residual hazard). The 30 year event was evaluated as having a high probability (30 years) and a medium intensity due to its size, plotting in field 6 (high/medium hazard). The 100 year event was evaluated as having a medium probability (100 years) and a high intensity, also due to its size, plotting in field 8 (high hazard). The > 300 year event was finally evaluated as having a high intensity due to its size, but a very low probability, resulting in a categorization as residual hazard instead of high hazard due to at least low probability, as a typical 300 year event would. A 300 year event with this low probability and plotting between the 100 year event and the > 300 year event was not expected and, therefore, not considered.

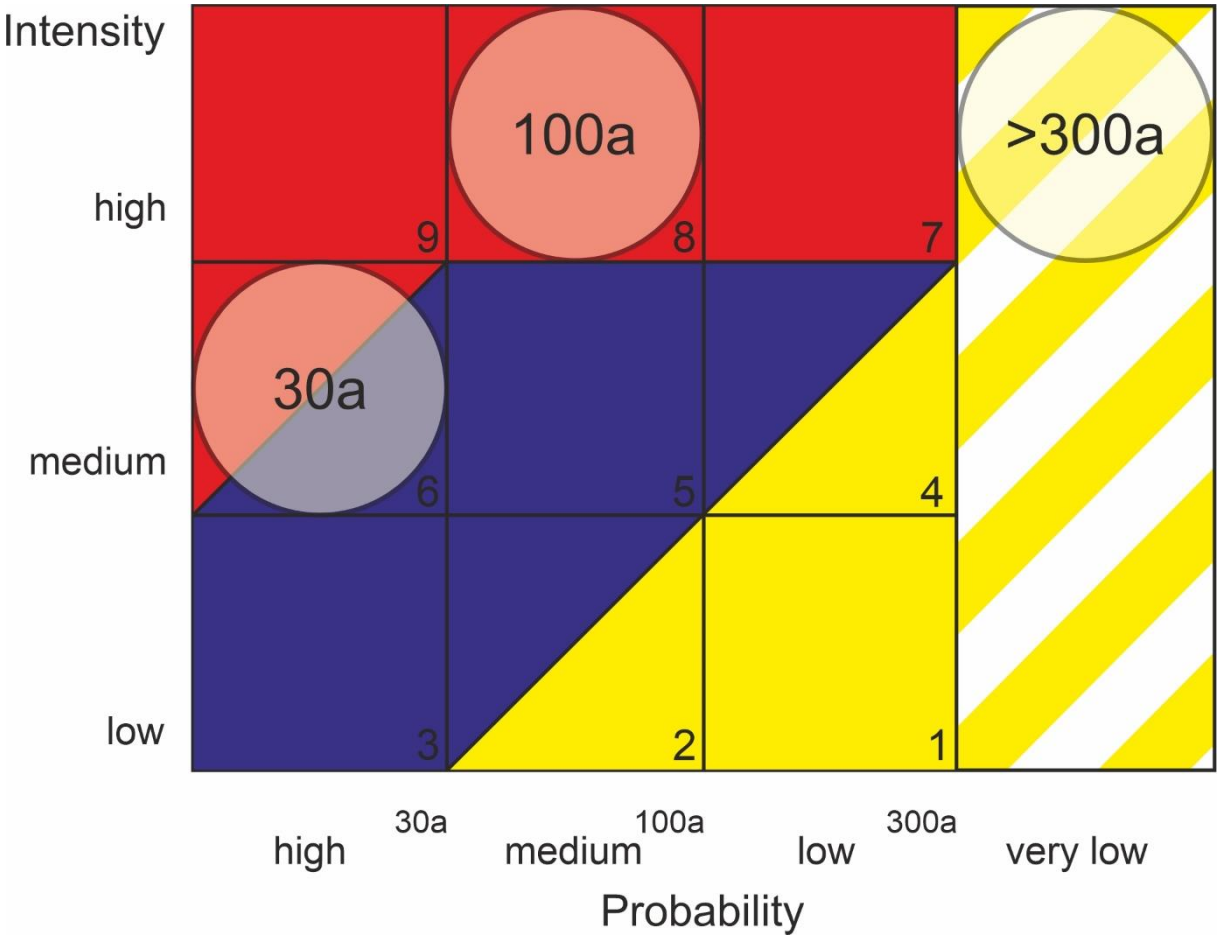

Figure 42: Hazard assessment after the Swiss model with the three event magnitudes of the project (after BAFU 2016).

The 30 year event plots in an indecisive field, being either of medium or high hazard (blue/red). Due to its impact in the neighborhood as being the most frequent event and the color blue not expressing as much urgency on a hazard map as the color red, the 30 year event was categorized as high hazard and depicted in red in the hazard map, although in a lighter red than the 100 year event (chapter 6.3.2, Figure 43, Figure 44).

6.3.2 Hazard Map

From the size of a possible landslide and the friction angles determined in the shear tests and registered in the SIMMA database (www-14) three hazard maps for the three magnitudes were derived. As described in chapter 4.8, the areas with in-situ rock were excluded from the hazard zone, only saprolite and block-in-matrix structure were assumed to be prone to landslides. The areas with a slope angle of ≥ 20° were considered to be areas at risk of an event in general (SIMMA database, www-14). Depending

on the magnitude of the event of the hazard map, these areas were then further condensed by taking the size of a typical event of the respective magnitude into account; Areas, that were too small for an event of the respective magnitude to occur, were excluded from the hazard zone of the respective magnitude. The hazard area ends, where the maximum detachment area of an event of that magnitude does not include a slope angle of 20 ° or more anymore The runout, as described in chapter 4.8, was determined as starting at the end of the smallest possible event of the respective magnitude and ending, where the whole event of the respective magnitude reaches a slope angle of ≤ 5°. Therefore, the starting and ending point, and the size and shape of the runout area changes depending on the magnitude, as is visible in the hatched areas in the following hazard maps.

The results of this approach are depicted in the three hazard maps for the 30 year event (Figure 43), the 100 year event (Figure 44), and the > 300 year event/residual hazard (Figure 45). Since the 30 year event and the 100 year event were both categorized as high hazard (chapter 6.3.1) they are depicted in two different shades of red, the > 300 year event/residual hazard in light yellow (yellow-white striped was visually problematic). As a final hazard map, these three magnitude maps were overlaid and depicted in the synthesis map or final hazard map of the study site, as can be seen in Figure 46 and Figure A8.

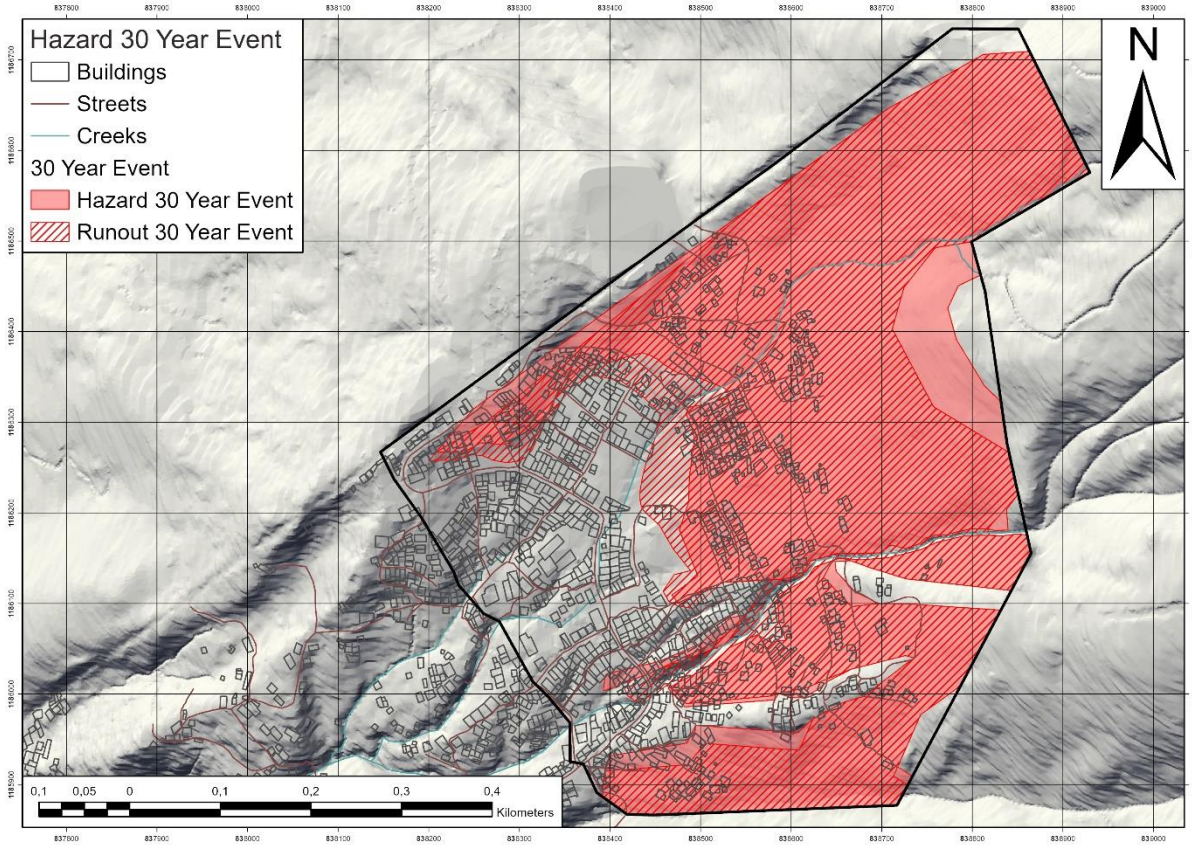

Figure 43: Hazard map depicting the hazard and runout area for 30 year events (after BREUNINGER et al. 2023a and WERTHMANN et al. 2024).

For the distribution of the sensor system, this synthesis hazard map was additionally categorized regarding the slope angle, depicting areas with a slope angle of < 25°, 25-30°, and > 30°, visible in Figure 47. This categorization allowed an even more hazard-related distribution of single sensors into the areas of higher hazard due to a higher slope angle. Since most areas with a slope angle of > 30° are located above the buildings, these areas are mostly monitored using a CSM cable line, while the areas with a higher slope angle within the populated area are monitored using point measurement devices (LoRa nodes). The final sensor distribution map, developed by AGR, is visible in Figure 54 in chapter 9, including the slope inclination hazard map depicted in Figure 47 in the background.

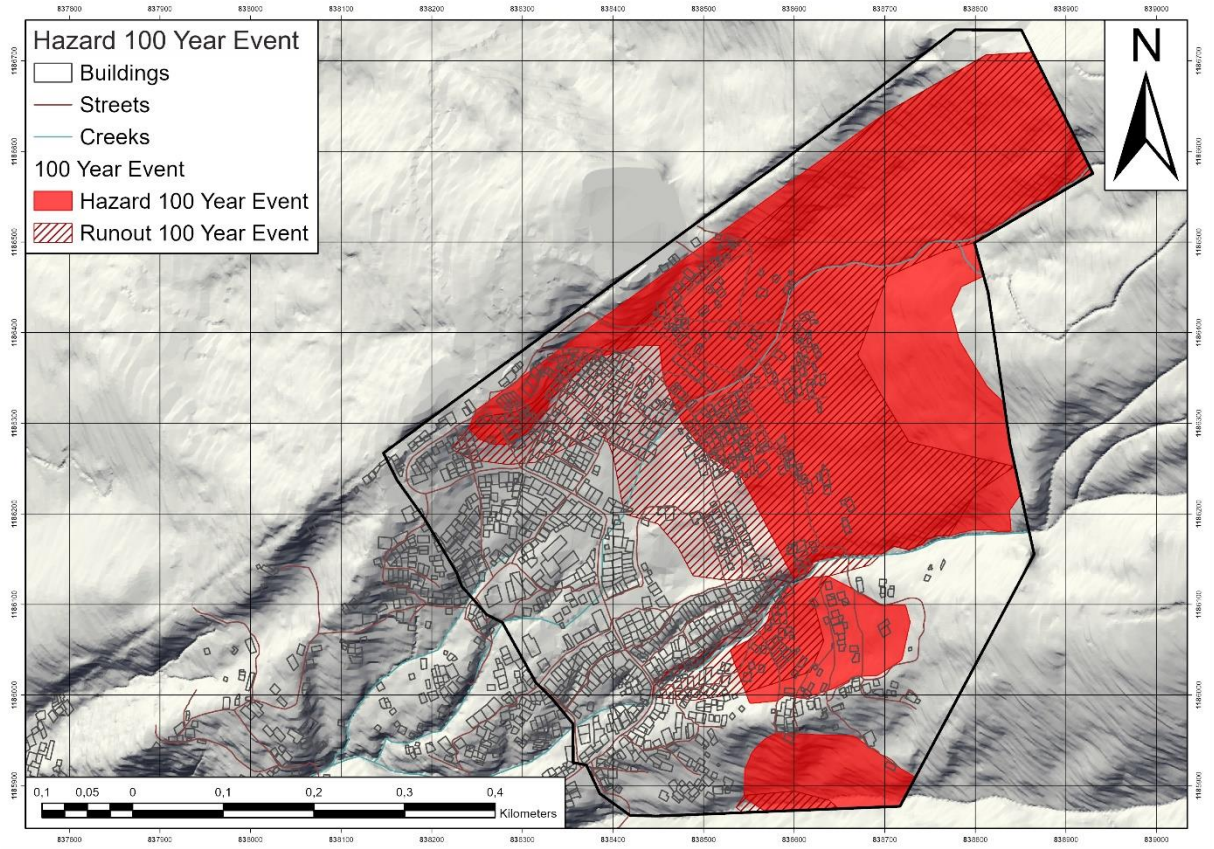

Figure 44: Hazard map depicting the hazard and runout area for 100 year events.

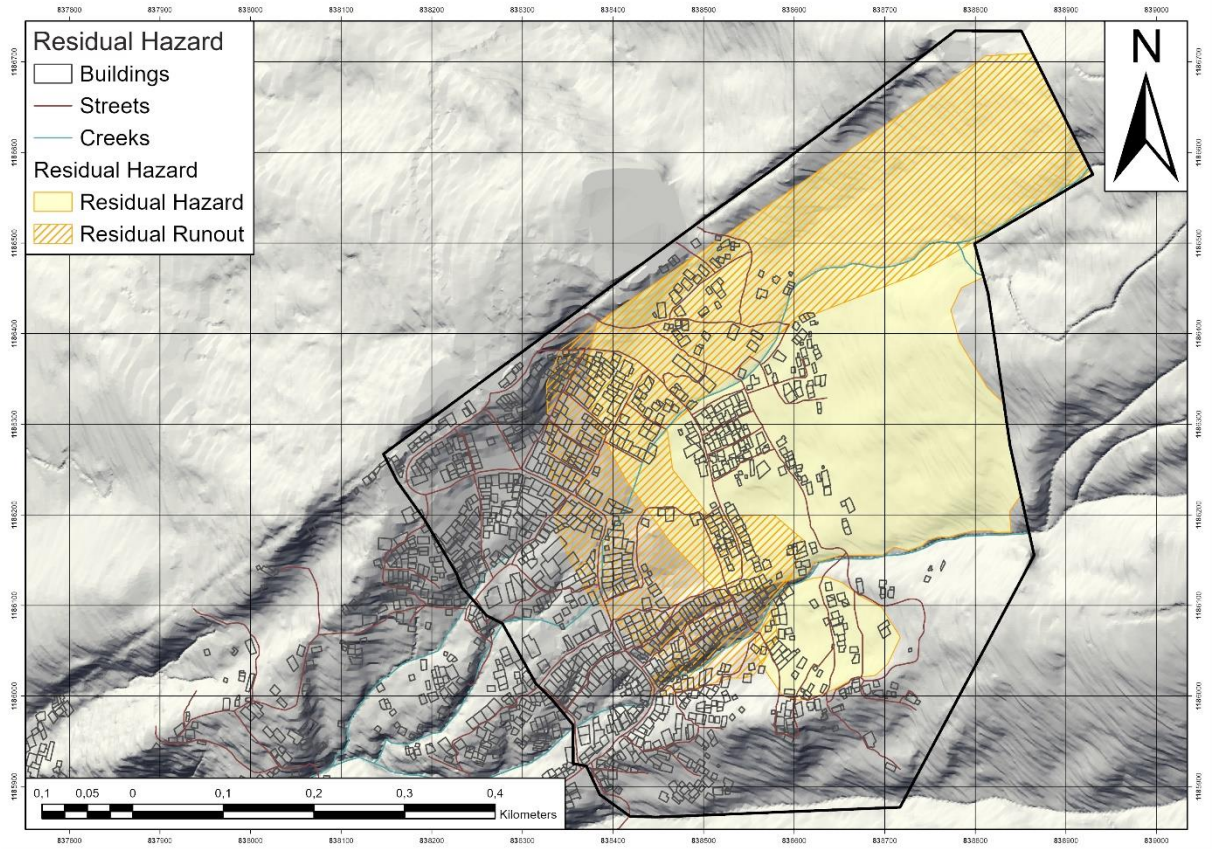

Figure 45: Hazard map depicting the hazard and runout area for the residual hazard.

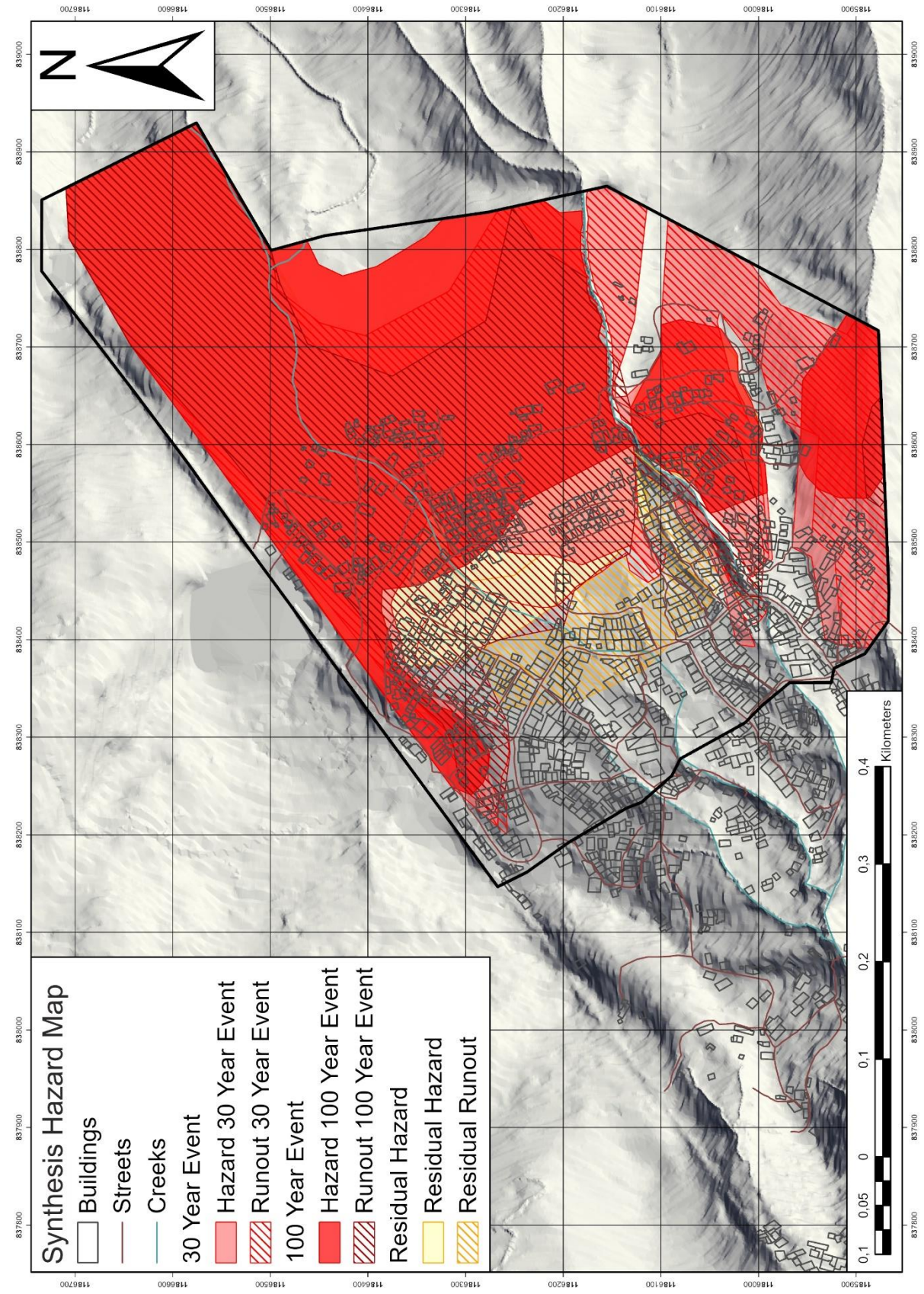

Figure 46: Synthesis hazard map of the study area.

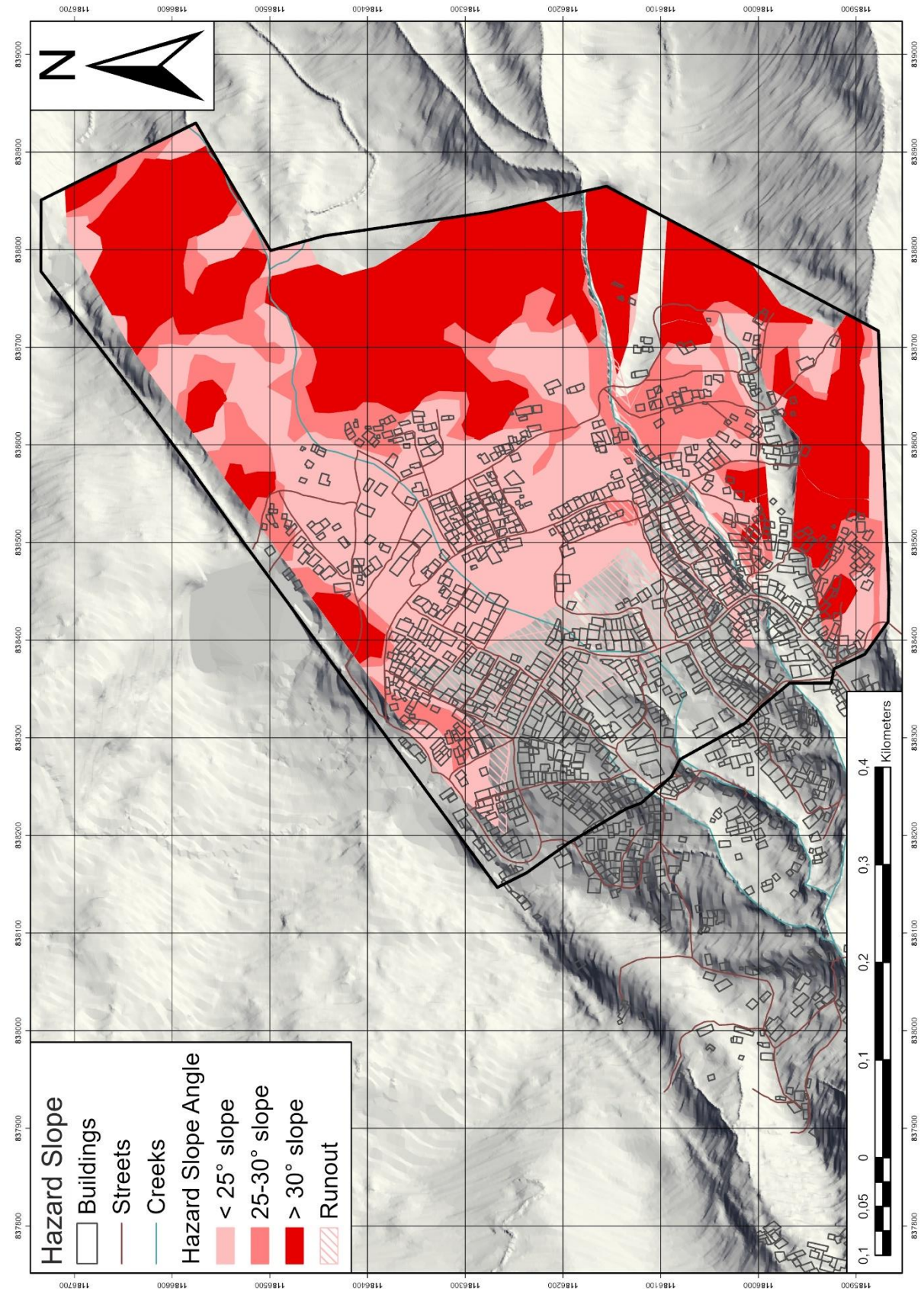

Figure 47: Synthesis hazard map of the study area, categorized regarding the slope inclination.

7 Discussion

7.1 Underground Model

During the investigations of the study site, the understanding of the subsurface changed significantly and numerous times.

Before the first investigations it was expected, that the subsurface would show the typical weathering profile with decreasing weathering and increasing grain size with depth (Figure 52a) (WERTHMANN & ECHEVERRI (2013). This meant a layering of soil and colluvial material on top, saprolite below and decreasingly weathered bedrock at the bottom of the profile. This image was still thought to be valid to some degree after the first field campaign in August 2019 (ERT profiles, process mapping) (THURO et al. 2020), which is depicted in Figure 48. This figure shows the first visual interpretation of ERT transect BO-01 in summer 2020. The only information available at that time and, therefore, used for the creation of this subsurface profile was the resistivity profile from the ERT measurement. This measurement showed a high degree of weathering of the bedrock in great depth due to the low resistivity values encountered. Other than this, the concept of a layering of the subsurface remained. The uppermost layer was believed to be already moved material (landslide mass) due to its mixture of matrix and blocks visible on the surface. Below that unit the saprolite was expected, with a clear boundary to the landslide mass (possible former landslide shear surface). The bedrock below showed much lower resistivity values than expected, as mentioned above, but was still thought to be intact. One area of higher resistivity values than the surrounding area interpreted as saprolite was believed to be a big rock or block within the unit of the saprolite.

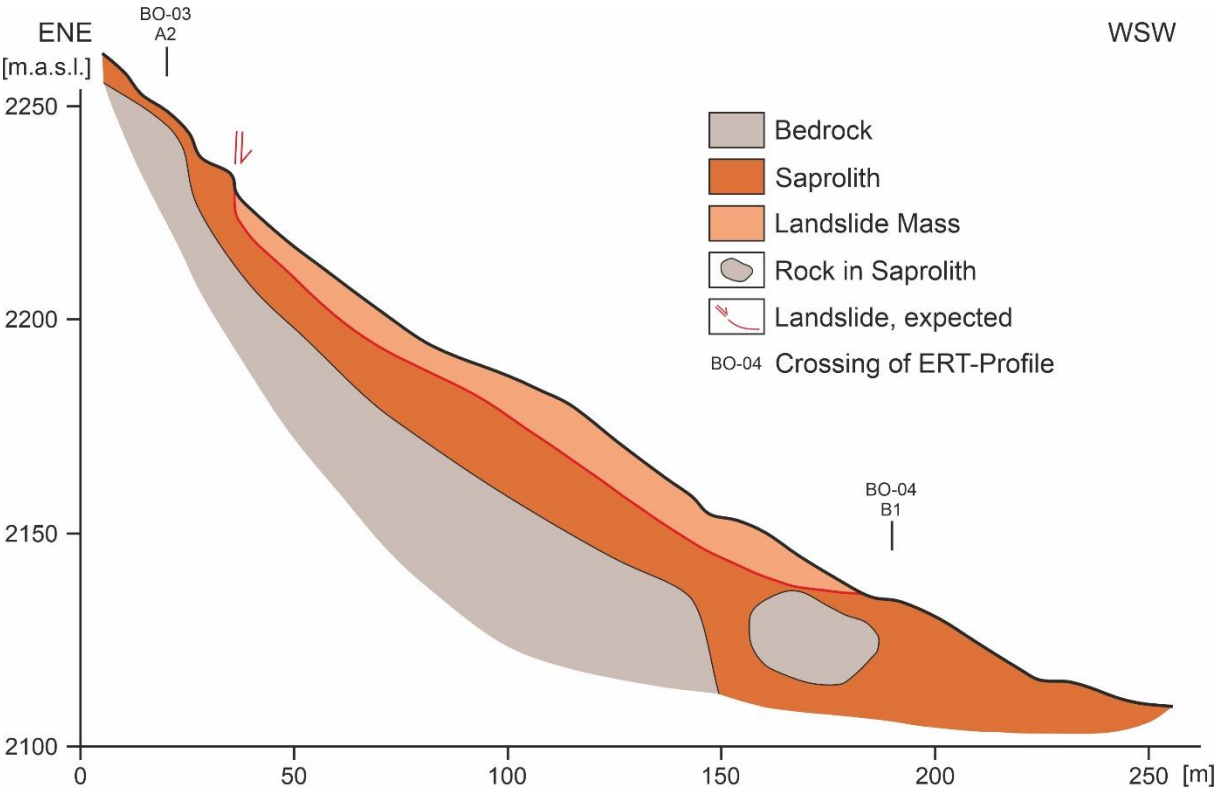

Figure 48: First attempt at a profile through the study site, along ERT transect BO-01 (after GAMPERL et al. in review).

After the second field campaign in February 2020 this picture changed. The geological mapping revealed that most of the area in the study site is dominated by a block-in-matrix structure, not only created by former landslide processes, but mainly by in-situ weathering. This was evident due to a directional bedding of most of the blocks, suggesting no movement of the blocks in the past. Since this was not conform with the subsurface understanding after the first investigation (Figure 48), the subsurface conditions were reevaluated. Figure 50 shows the first version of the colluvial map of the study site after

the geological mapping and before the drillings. As the final colluvial map (Figure 39) this first draft shows the areas of in-situ rock, saprolite and the thickness of the colluvial material (block-in-matrix structure). At this point it was expected that the thickness of the colluvial material was much higher, over 30 m in one area (brown). This overestimation originated in a new interpretation of the ERT transects; the areas of low resistivity in the profiles were now considered to be colluvial material and no longer heavily weathered dunite rock.

To illustrate this new understanding of the subsurface, some geological profiles through the study area were created, one of them being presented in Figure 49. This profile shows a cross section from the northwestern to the southeastern border of the study site, visible as a black line in Figure 50. The units were derived from the geological map on the surface and then extrapolated into the depth according to the resistivity values from ERT transect BO-04, that runs partly parallel to the profile.

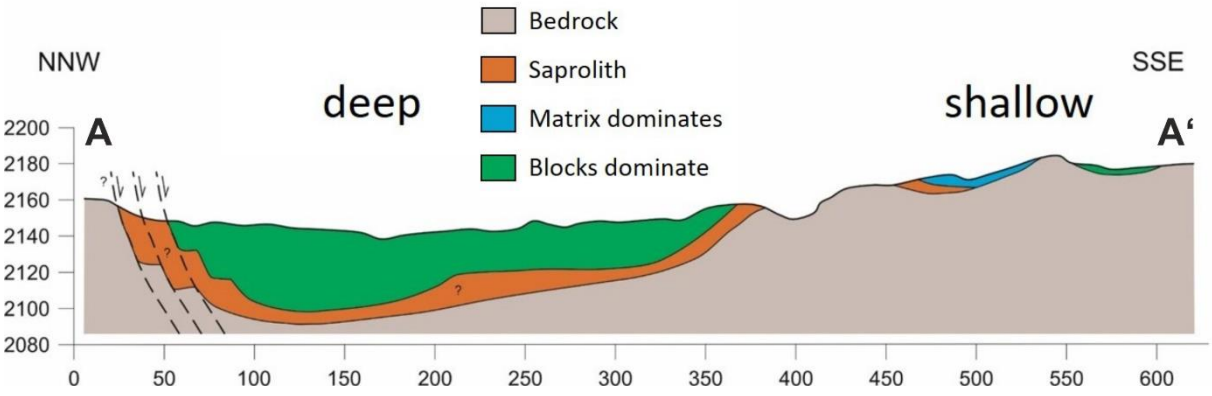

Figure 49: Second attempt at the depiction of the subsurface along the profile line depicted in Figure 50.

This second version of the subsurface depiction suggested a deep depression just north of the center of the study site and a high potential for a deep seated and widespread landslide in that area. However, there was no sign or information from the community members of an event of that size ever having occurred in the study site. The drilling locations were chosen to confirm or falsify this thickness of the colluvial material in that area (Figure 12, chapter 4.3).

The first three drillings and their laboratory tests in fall 2020 suggested that the thickness of the colluvial material was overestimated before (chapter 5.3). All drillings showed less loose material at the surface and a much higher degree of weathering of the rock than expected, evident from the visual interpretation (chapter 5.3) and the rock strength tests (chapter 5.6.1). In addition, pseudokarst structures were present in the drilling cores (soil material in between solid rock parts, oxidation and serpentinization in up to 50 m depth) and the high degree of core loss (possible cavities). This core loss might also have other reasons, but during the drilling process the drilling rig dropped occasionally in all drillings, suggesting a cavity at that depth.

This new information led to a completely new interpretation of the ERT transects and a new and final version of the subsurface profiles (Figure 36, Figure 37, Figure 38, chapter 6.2.1) and the typical weathering profile of the study site (Figure 52c). As was evident from the drillings, there is no clear layering of colluvial material, saprolite and bedrock. The weathering, especially the pseudokarst, reaches very deep and leads to cavities, either open or filled with fine-grained weathering material (matrix). These processes create loose blocks of up to 10 m in diameter (as encountered in the drillings), with fine-grained material in between, leading to low resistivity values in the ERT measurements due to their water storing abilities. There is a smooth transition from these large blocks in matrix to heavily weathered and fractured but connected dunite, that cannot be distinguished in the ERT measurements or the drillings. As is visible in Figure 52b, the karst structures in the dunite were already known (TOBÓN-HINCAPIÉ et al. 2011), but the degree of fracturing and the extremely rough surface of the dunite bedrock were underestimated in the study site.

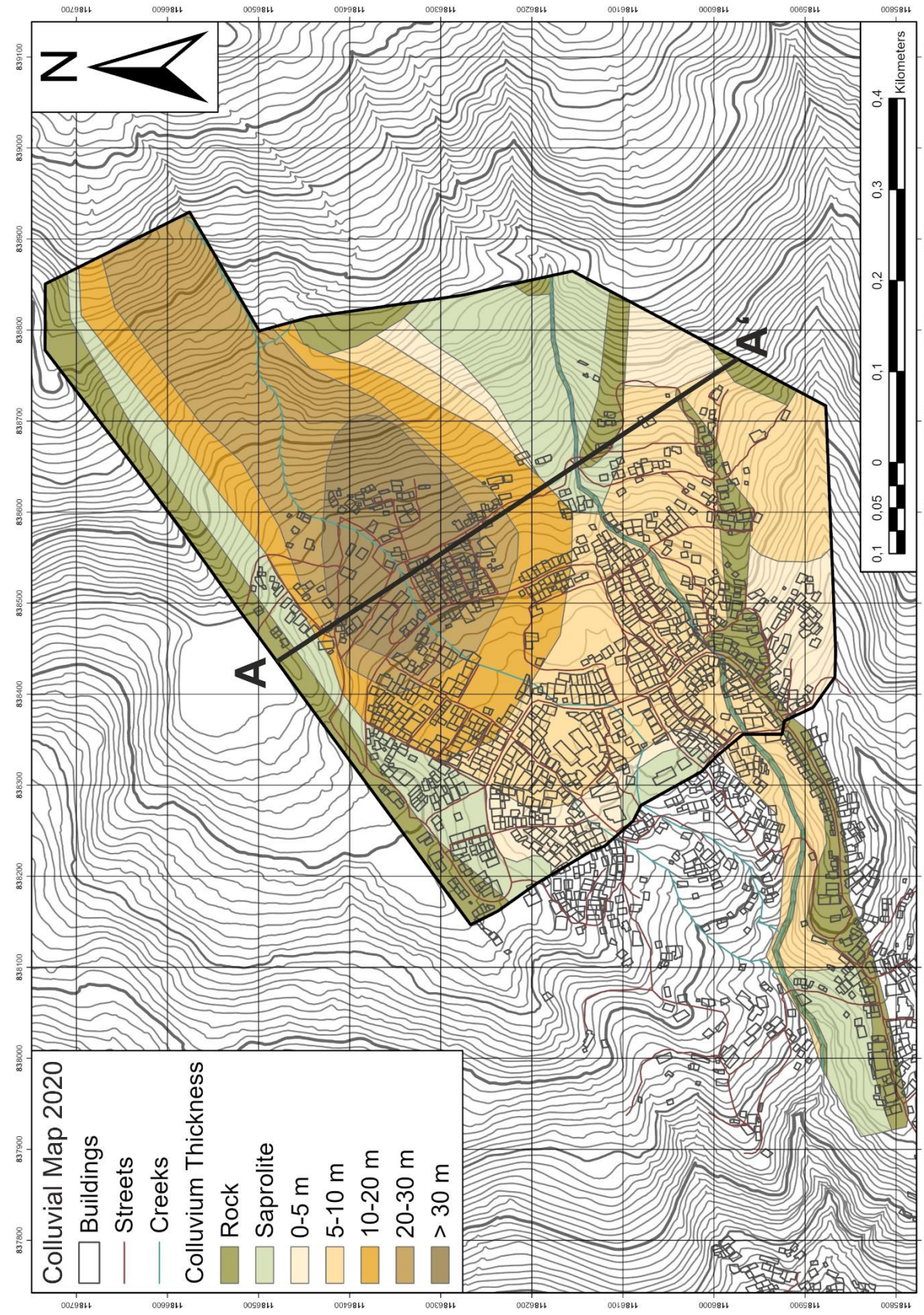

Figure 50: Colluvial map before the drillings with the profile line shown in Figure 49.

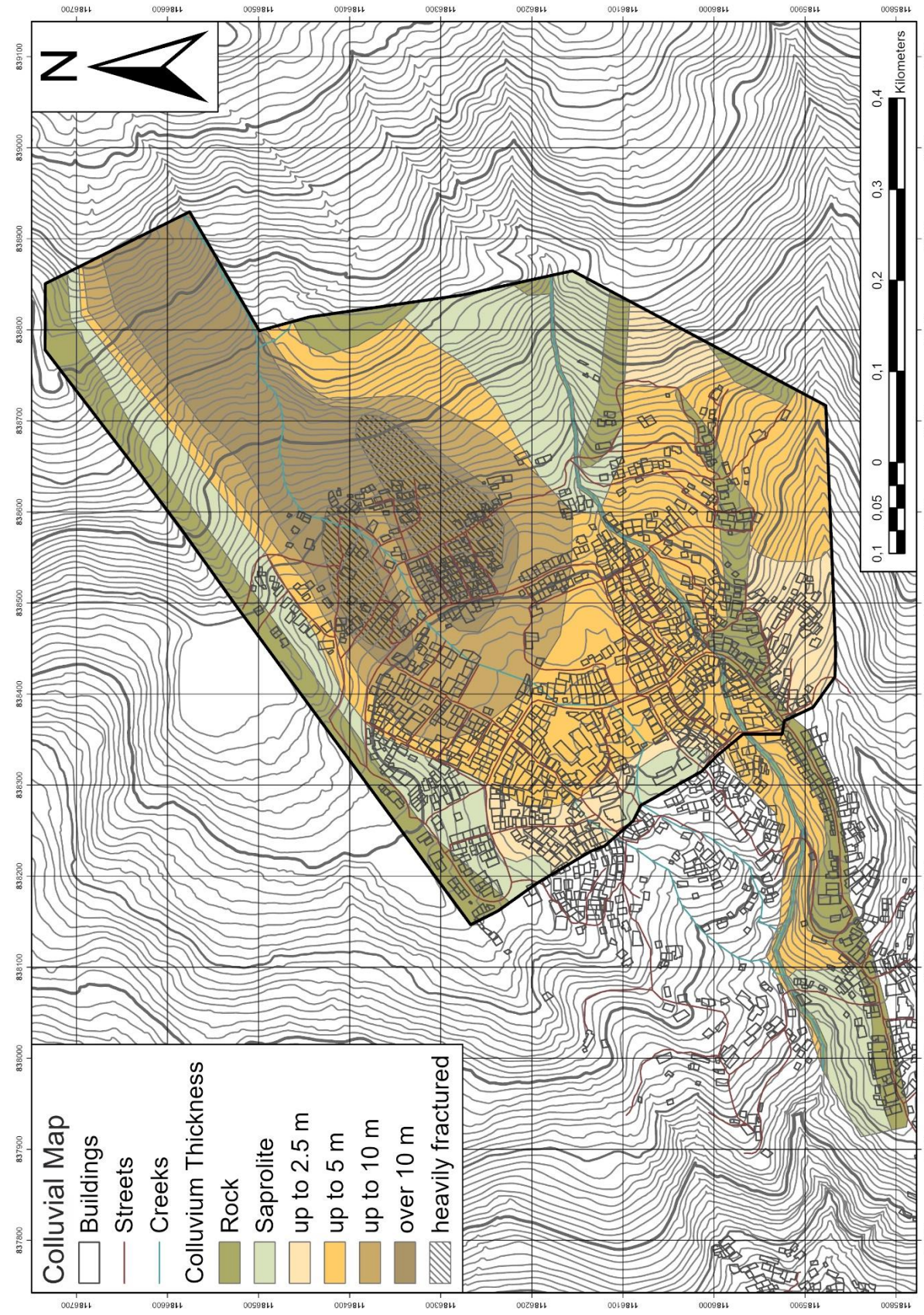

Figure 51: Final colluvial map, as depicted in Figure 39 and Figure A7, in comparison.

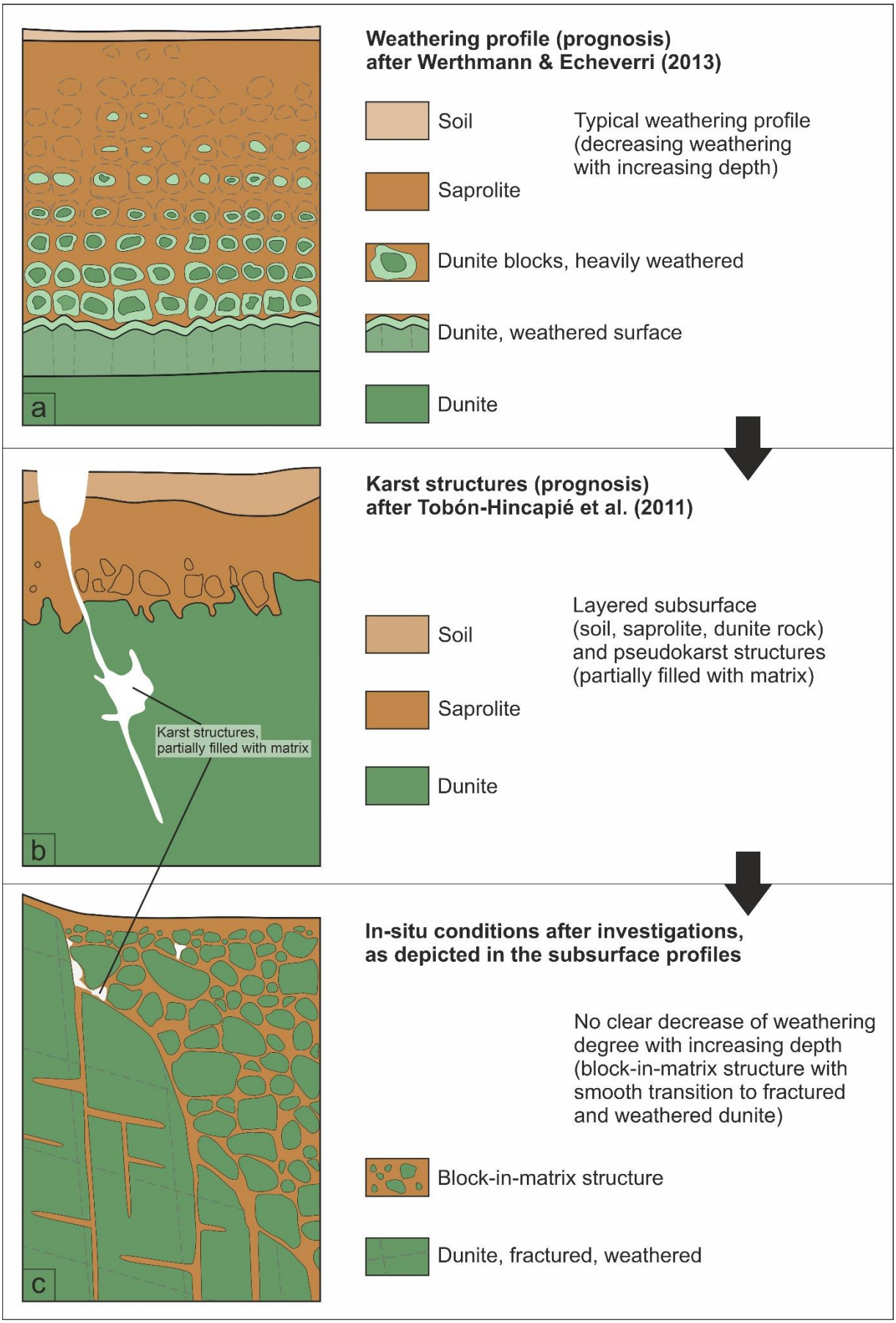

Figure 52: Development of the understanding of the weathering profile during the project: (a) weathering model after WERTHMANN & ECHEVERRI (2013), (b) pseudokarst model after TOBÓN-HINCAPIÉ et al. (2011), (c) in-situ conditions encountered during the investigations (after GAMPERL et al. in review).

Due to this new interpretation of the low resistivity values of the ERT measurements as blocks in matrix and heavily fractured and weathered rock, respectively, the depth of the colluvial material was adjusted in the colluvial map to a maximum of 20 m. After the fourth drilling B2 in fall 2021, the depth was adjusted again since this drilling was located in the middle of the deep depression and revealed an even lower thickness of the colluvial cover (just over 10 m) and a higher degree of fracturing in the depth at this location (Figure 39, chapter 6.2.2). Figure 51 shows the final colluvial map again in comparison to the old version in Figure 50. The rock and saprolite areas did not change, only the estimated colluvial thickness of the block-in-matrix structure.

The temporarily considered possibility of a high potential for a deep seated and widespread landslide in the study site was subsequently reduced to a very low probability and depicted as the residual hazard in the hazard map (Figure 45, Figure 46, chapter 6.3.2). As already suspected after the mapping of past events (Figure 14, chapter 5.1), the final underground model shows, that the typical events are much more shallow (up to 10 m). This is most likely due to (1) the large blocks in the colluvial material, that obstruct the forming of a shear surface in greater depths, and (2) the rough surface of the weathered and fractured bedrock, that does, therefore, not act as a deepest possible shear surface, as suspected before the investigations. As is evident from the Villa Tina landslide with a maximum depth of 8 m, the depth of a possible event is not always the main factor of magnitude in the Aburrá Valley. The steep slope beneath the landslide led to an acceleration of the movement (chapter 6.3.1). Since the study area does not have such a steep slope, the depth of a possible event is considered to be the main factor for the magnitude of said event, which further decreases the possibility of a large event.

Another influencing factor encountered in the investigations, besides the determination of the depth of the colluvial material, are the pseudokarst structures. Before the investigations it was assumed, that the groundwater table rises from the bottom to the top of the profile, building up on top of the unweathered bedrock into the soil material. The piezometers inside the drillings and installed elsewhere in the study site as part of the EWES did not detect a water table anywhere in the slope. This suggests that the water accumulates in a different way and at other locations. It is possible, that the pseudokarst reaches much deeper than the deepest drilling in the study site (60 m, RENDÓN-GIRALDO 2020), possibly even as deep as to the thrust fault to the underlying La Espadera Amphibolite. This would mean, that the water rushes through the slope through open karst cavities, exiting the slope at springs downhill, and being dammed by filled karst cavities, which makes it impossible for a normal groundwater table to develop. It is rather the case, that there are multiple local groundwater lenses of unknown size distributed throughout the slope. Their locations cannot be detected and are also very likely to change if a filled karst cavity gets unclogged or an open karst cavity gets filled with matrix.

Since water infiltration is the main trigger for the landslides in the Aburrá Valley (chapter 3.2) these hydrological circumstances present a problem for the prediction of a landslide event in the study site. It is not possible to determine the location of a matrix-filled and water-saturated karst cavity, where a shear surface could develop. This is most evident in the slope stability encountered in the study site; there are slopes of 30-40° inclination that seem to be unmoved in the recent past and considered stable, while slopes of 20-25° inclination show signs of movement and past landslide events. This fits with the discrepancy between the shear parameters of the samples and those of the SIMMA database (www-14), showing values of 26.9-39.4° and 20-25°, respectively (chapter 5.6.2, chapter 6.1, chapter 6.3). It was suggested to take both ranges of values into account for a hazard assessment, which meant to consider all slopes with an inclination of $\geq 20°$ to be at risk of an event (chapter 6.3.2). This discrepancy can be explained by the local groundwater accumulation in the slope rather than a rising groundwater table. Depending on the conditions of the karst cavities (filled/open), the slopes show a locally differing water content in the karst cavities and, therefore, differing water saturation and, consequently, slope stability. These circumstances lead to stable slopes of 30-40° inclination with potentially mostly unfilled karst cavities, where rainwater is transported and not dammed, and unstable slopes of 20-25° inclination on the other hand, with potentially mostly matrix-filled karst cavities, where rainwater is stored, increases the pore water pressure, decreases the friction angle of the material, and destabilizes the slope, initiating

and event. Therefore, areas with slope angles of 20-25° have to be considered at risk of a landslide in general, especially if no subsurface investigations were conducted.

In addition to the unknown location of matrix-filled, water-saturated karst cavities in the subsurface, another unknown factor in the study site is the infiltration of water from leaking or burst water pipes in the slope. As mentioned in chapter 2.3, these pipes cross the entire slope in and , especially, above the inhabited area of the barrio and are very prone to leakage and destruction due to their insufficient materials and their very shallow embedding into the soil. This unpredictable water intake into the slope and other anthropogenic factors like embankment cuttings during construction processes and dig ups for crop planting present another problem for the EWES and the hazard assessment of the study site and the entire area, since these anthropogenic factors are very similar in all informal settlements in Medellín and other parts of Colombia and mountainous regions around the world in general.

These unknown variables are expected in all inhabited areas of the Medellín Dunite, that are similar to the study site. However, in other geological units in Medellín, the problems of the pseudokarst and deep weathering in general are not expected to be as extreme as they are in this particular unit, since ultramafic rocks, such as dunite, are extremely prone to chemical weathering due to their mineralogical composition (ÜNDÜL et al. 2015, ÜNDÜL & TUĞRUL 2016). Other units in Medellín and the Aburrá Valley are not expected to have these weathering levels, and, therefore, not the same subsurface conditions as the study site. Therefore, this subsurface model might only valid for the study site and can, therefore, not easily be transferred to other areas in Medellín or the Aburrá Valley.

7.2 Hazard Assessment

Since the subsurface model was the basis for the hazard assessment, the problems encountered in the development of that model were also an issue during the creation of the hazard maps.

Besides landslides, there are signs of debris flows in the form of levees in the study site along the two major creeks best visible in the process map (Figure 14, chapter 5.1). These levees were not observed during field investigations due to the dense vegetation, but during hillshade analyses in ArcGIS. According to the community members working within the project, no debris flows have been observed since the area is inhabited; the creek channels do transport a high amount of water during heavy rainfall, but no debris. Due to this information, the debris flows were classified as a minor process with very low impact and, therefore, not included in the hazard assessment. With rotational, occasionally translational landslides being the only expected events in the study site (chapter 3.2, chapter 5.1), the hazard assessment focused solely on those events and did not take other phenomena into account.

The original approach to understand the behavior of the landslides at the study site was to back-model the mapped events with the software slide2D from rocscience. This was done in spring 2020, after the second field campaign and the creation of the geological map (chapter 5.2). At this point, it was still believed, that the subsurface was layered in loose material, saprolite and bedrock and had an evenly rising groundwater table (chapter 7.1). With slide2D it was possible to back-model the events from the process map (chapter 5.1) under the assumption of a layered subsurface and an adjustable groundwater table, with a maximum depth of the events of 10 m, as was estimated during the mapping. It was also possible to forward-model several potential events at different locations. However, when the underground model was adjusted regarding the subsurface not being layered and no typical groundwater table rising in the slope, the results of this modelling were no longer valid.

Several approaches to model the subsurface according to the actual conditions encountered during the investigations failed due to (1) the software not being able to depict the complex subsurface, especially the pseudokarst structures and groundwater lenses, in general, (2) the fact, that the locations of cavities (filled and open) and groundwater lenses are unknown and not detectable by direct or indirect measures due to their small and variable size, and (3) the most frequent events (shallow, < 4,000 m²) not being initiated in the model with the typical inclination and water content from the back-modelling as input variables. Without a representative underground model, slide2D and other well-known modeling codes

cannot produce reliable values. In fact, no software was found, that was able to depict the actual subsurface conditions of the study site. In addition, the problem of locating cavities remains, regardless of the software used.

The slide2D profiles created during the project do not depict the real subsurface conditions, since there is no layering of units and no rising groundwater table. While the back-modelling of historic events produced reliable data, since the conditions of the movements were known, the forward-modelling of possible future events cannot be successful. Therefore, the modelling of events was not further pursued. Instead, the hazard assessment was solely conducted using historic events as a measure for the size, runout, and frequency of future events (chapter 6.3.2).

Since the Swiss model for event definition represents of the conditions of slopes in mountainous regions very well and is also the main approach to landslide hazard assessment in the Alpine region (e.g. the landslides of Randa 1991 and Brienz 2023, both Switzerland), it was convenient to work with this model, due to the high level of experience with it. It did also fit very well with the events registered in the study site, since it was easily possible to categorize them temporally and regarding their size (chapter 6.3.1).

The calculation of the size, depth and age of the mapped events was mainly done with the information gained from the community members, since most of the landslide features are either overgrown with dense vegetation or anthropogenically changed (buildings, streets, plantations etc.) (chapter 4.1). Due to the very similar data obtained from the SIMMA database (www-14) from all over the Aburrá Valley, the information was deemed reliable and was, therefore, used for the determination of the different event magnitudes.

Although half of the larger events in the study site (three out of six) have happened in the past 30 years (Figure 40, chapter 6.3.1), they were still categorized as 100 year events due to their low number. The eleven 30 year events, categorized as those, are packed very densely in the diagram, within 22 years and < 4,000 m² in size and can, therefore, naturally be grouped as one magnitude. The distinction between the 100 year events and > 300 year events/residual hazard is less clear. No event in the study site was big enough to be categorized as the maximum magnitude. Therefore, the size of such an event was defined as > 15,000 m², bigger than the biggest event registered in the study site (chapter 6.3.1). An event > 15,000 m² is not unlikely to happen frequently in the Medellín Dunite in general, but it is very unlikely in the study site due to its very limited colluvial areas regarding size and depth, that are too small for a detachment of that size to develop frequently. However, in other parts of the Medellín Dunite, that show larger and deeper areas of continuous colluvial material on the surface, an event > 15,000 m² might still be in the category of the 100 year magnitude. Therefore, the definition of the event magnitudes might only be valid for the study area and not for other parts of the Medellín Dunite, the city of Medellín or the Aburrá Valley.

Figure 53 shows the hazard map with the hazard areas categorized according to the slope inclination, as was presented in Figure 47, with the outlines of the landslides recorded in the study site (Figure 14, chapter 5.1). As was mentioned in chapter 4.8 and chapter 6.3.2, all landslides are located in the block-in-matrix structure (colluvium) or the saprolite, which is why the areas of in-situ rock were not considered at risk of a landslide when creating the hazard maps. This is clearly visible in Figure 53, since all landslides (at least those within the borders of the study area) are located within the hazard areas. However, two landslide at the eastern border of the study site are located in an area of in-situ rock, in Figure 53 visible as an area of no hazard. These landslides originated above the rock, in an area considered to consist of saprolite, and are now only visible due to accumulative ridges below the rock. The information about their size and age was given by the community members accompanying the mapping process. Due to the limits of the study site, the area of origin of these landslides was not mapped. Landslides originating from the slope above the limits of the study area were considered to be either too small to reach the inhabited area of the study site or so big, that they still trigger the sensors inside the study area. Therefore, these events were considered to be of no immediate importance to the EWES.

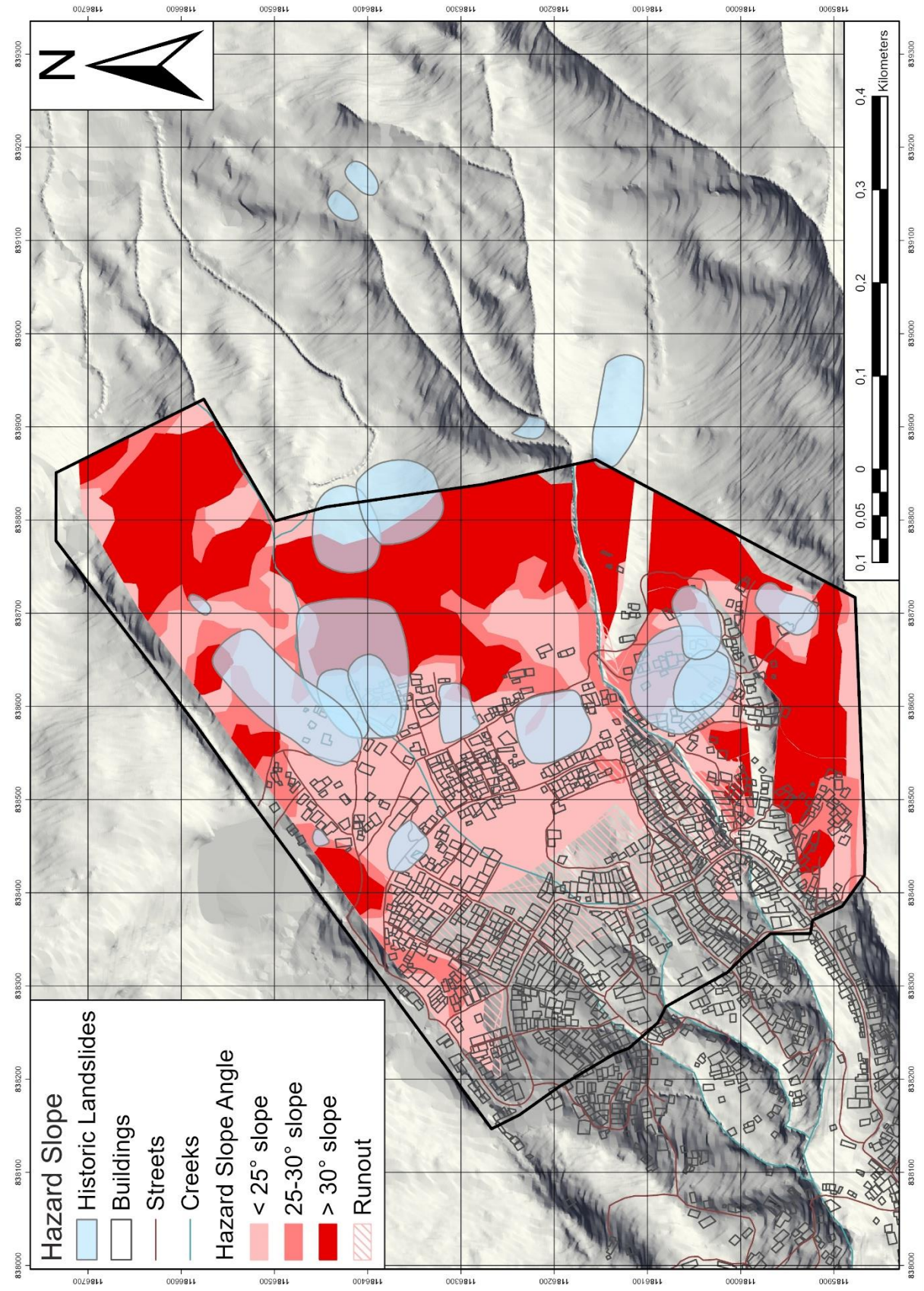

Figure 53: Synthesis hazard map depicting the slope inclination, including the outlines of the registered landslide events, as presented in Figure 14.

The hazard areas on the hazard maps were created regarding the slope angle (≥ 20°) and geological composition (saprolite, block-in-matrix structure). Areas of in-situ rock, regardless of degradation, were

excluded from the hazard zone in general (chapter 4.8, chapter 6.3.2). Due to the extreme fracturing and weathering of the rock and the continued chemical weathering, the rock ridges in the study site might be destabilized due to these factors in the future and would then have to be included in the hazard areas.

The minimal critical slope angle of 20° was derived from the SIMMA database (www-14) and the mapped events in the study site. So far, there were no events registered in areas with a slope inclination of < 20° in the study site, therefore, the value was considered valid. However, events in areas with < 20° inclination might not be visible anymore due to the high level of anthropogenic intervention in that part of the slope, and dense vegetation. It is possible for an event to occur in areas with lower slope inclination, since the matrix in the study site consists of fine-grained material (chapter 5.6.2), that gets liquefied when saturated, which decreases the friction angle of the material drastically. Due to the high number of large blocks within the matrix in most parts of the study site, it is highly likely, that those blocks act as a blockage in these cases. Those blocks only start to move, when the amount of matrix is so high, that the blocks start to float in it, or when the slope inclination reaches a certain angle. These factors seem to be in place, since an event in areas of < 20° slope inclination has not been registered in the past and was also not observed by the community members in the study site. Due to these circumstances, the minimal critical slope angle of 20° can be considered valid in the study area. In other parts of the Medellín Dunite and the Aburrá Valley, the minimal critical slope angle might be different due to the local geology, the rock's level of degradation, the soil content and depth, and also other factors not considered yet. Practically speaking, the minimal critical slope angle cannot be transferred to other parts of the city and the area, it may only be valid for the study site.

8 Conclusion

In chapter 1.2 the three main questions of the dissertation were presented. The conclusion is taking up these questions and answers them using the information obtained in chapters 2-7:

What are the specific mineralogical, geological, and geotechnical factors promoting the landslide processes in the study site?

The study site lies within the geological unit of the Medellín Dunite, that is very prone to chemical weathering due to its mineralogical composition of olivine, pyroxene, and amphibole (chapter 3.1, chapter 5.6.3, chapter 6.1). Additionally, the unit is already heavily altered by hydration and weathering and, therefore, contains serpentine, talc, chlorite, magnesite, mica, and iron oxides (chapter 3.1, chapter 5.6.3). Most of the examined samples are dominated by serpentine, suggesting a transformation of the rock into serpentinite (chapter 5.6.3). Even though the samples were taken from the surface and can, therefore, not be classified spatially, their heterogeneous mineral content supports the theory of a very inhomogeneous composition of the dunite (chapter 3.1, chapter 5.6.3, chapter 6.1). The examined soil samples (x-ray diffractometry) underline the heterogeneity of the subsurface, since they show very differing mineral contents (chapter 5.6.4, chapter 6.1), suggesting differing educts and differing alteration levels. The high content of minerals highly susceptible to weathering and their high degree of alteration (hydration, weathering) weaken the rock and promote the formation of weathering products and, ultimately, the highly landslide prone block-in-matrix structure. Additionally, the heterogeneity of the mineralogical composition leads to locally differing degrees of weathering and alteration in general and, therefore, to locally differing stabilities of the rock and characteristics of the block-in-matrix structure (depth, block size, matrix content, etc.). This is clearly visible in the geological map of the study site (Figure 15, chapter 5.2); Due to the differing mineral content, the alteration of the rock advances at different speed, leading to areas of in-situ rock (slowest alteration), saprolite, and different types of block-in-matrix structure (fastest alteration). The mineral content determines the degree of alteration and, therefore, the susceptibility to landslides.

In addition to the mineralogical factors, the unique structure of the Medellín Dunite influences the predisposition to landslides as well. The long tectonic history of the Medellín Dunite, mentioned in chapter 2.2 and chapter 3.1, has left the rock extremely fractured, as is evident from the surface mapping (chapter 5.2), the evaluation of the drilling cores (chapter 5.3), and the joint recordings (chapter 5.4 and chapter 6.1). All joint sets mentioned in chapter 3.1, depicting the tectonic structure of the region, have been encountered during the investigations (chapter 5.4 and chapter 6.1). These fractures or joint sets promote the weathering processes of the minerals, as mentioned above, deep into the subsurface of the rock and have led to the phenomenon of the pseudokarst, explained in chapter 3.1 and confirmed by the drilling evaluations (chapter 5.3 and chapter 6.1). The higher the fracture rate in a certain part of the rock, the stronger and deeper the weathering and the pseudokarst formation at that location. Therefore, increased fracture rates, leading to increased weathering and pseudokarst formation, promote the destabilization of the rock and the probability of landslides. As is the case with the heterogeneity of the mineralogical content, differing fracture rates lead to differing influence of weathering and pseudokarst in the subsurface, leading to differing degrees of stability.

The rock tests in chapter 5.6.1 (uniaxial compressive strength test, Brazilian test) confirm this extreme and deep weathering of the Medellín Dunite in the study site. None of the drillings, where the samples were taken, show a continuous increase of rock strength with depth, as would be the case in a normal weathering profile. Even seemingly unweathered samples show low strength values, confirming the locally high degree of alteration of the rock (mostly serpentinization). The values themselves vary to a high degree, especially the uniaxial compressive strength, with values between 10 MPa and 132 MPa. These strength differences are considered to correlate directly with the degree of alteration (ÜNDÜL et al. 2015, ÜNDÜL & TUĞRUL 2016), which is a direct result of the mineralogical composition and the fracture rate, as discussed above, emphasizing the important role of the heterogeneity of the subsurface for the stability of the slopes in the study site.

As a result of the extreme weathering and alteration, the ground contains a high amount of fine-grained soil material, encountered in the drillings (chapter 5.3) and the geological map (chapter 5.2). The low amount or even total absence of coarse-grained material (chapter 5.6.2) confirms mainly chemical weathering instead of mechanical forces being responsible for the disintegration of the rock (chapter 6.1). There is no correlation between grain size and sampling depth or location. Most soil samples taken from the drillings and the surface show a considerable plastic behavior, the values also do not correlate with the depth or the sampling location (chapter 5.6.2). The expression of both factors, grain size and plasticity, depend on the local mineralogical composition and its respective susceptibility to weathering; The amount of soil depends on the degree of weathering, which is dependent on the fracture rate. Especially the high liquid limit of most soil samples indicates a high water absorption capacity, which promotes the probability of a landslide.

The study site shows stable slopes of over 35° inclination, corresponding with the values of the friction angle derived from the shear tests on the trench and drilling samples (chapter 5.6.2), while the typical angle of failure for the landslides in the study site is 20-25° (chapter 6.1, chapter 6.3, chapter 7.1). These differing slope stabilities depend on the degree of alteration and fracturing, the size and number of karst cavities, the amount and grain size of the soil material (matrix), and its water absorption and storing capacity (chapter 7.1).

The high degree of alteration of the mafic minerals (hydration, serpentinization), the extreme fracturing, and the resulting pseudokarst structures and fine-grained, highly water absorbent material in the slope promote the landslide probability in the study site, as explained above. In all these processes, the heterogenic composition and structure of the rock lead to locally differing expressions of these variables and ultimately to differing slope stabilities.

What landslide processes are to be expected at the study site and what is their typical size and depth?

The landslides in the study site are mostly rotational slides, only one translational slide was registered (chapter 5.1). Their size is typically maximum 15,000 m², most slides have a size of < 4,000 m², and their depth does not exceed 10 m (chapter 5.1). Since there are no signs of landslides deviating from these values and observations, it is expected, that future landslides do show the same or similar dimensions and behavior (chapter 6.3.1, chapter 7.2). The landslides were organized in three categories: 30 year events (< 4,000 m²), 100 year events (4,000-15,000 m²), and > 300 year events/residual hazard (> 15,000 m²), with a typical 300 or > 300 year event not having happened in the study site in the past, but considered possible (chapter 6.3.1). There are signs of debris flows to be found in the study site, but since no debris flow was registered since the area is inhabited, they were dismissed (chapter 7.2).

These dimensions and probability categorizations may only be valid for the study site and cannot directly be transferred to other parts of Medellín, the Aburrá Valley or the Andean region without thorough investigations beforehand (chapter 7.1).

Which areas of the study site are most prone to landslides and which areas have the highest hazard potential?

Due to the high degree of degradation and the high soil content, the block-in-matrix structure is the most landslide-prone area in the study site (chapter 3.1, chapter 4.7, chapter 4.8, chapter 6.3). The saprolite is considered to be less susceptible but still unstable (chapter 4.8, chapter 6.3.2, chapter 7.2). Both structures, as mapped in the geological map (chapter 5.2), are potential hazard areas and those are the only areas marked as hazard areas in the hazard maps. The synthesis hazard map is visible in Figure 46 (chapter 6.3.2).

The infrastructure and building development were not taken into account during the creation of the hazard maps. Therefore, some houses are only partly located in a hazard area, partly in a safe area, as is visible in the maps (chapter 6.3.2). In these cases, the whole house (or other structure) was categorized as being at risk and included in the evacuation plan developed by LUH and the Colombian partners. The

analysis of the distribution of the population and exposed buildings by LUH resulted in a vulnerability of the population per hazard type: 49 % of the population live in the areas of high hazard (red), 23 % of the population live in the areas of residual hazard (yellow), and 28 % of the population do not live in a hazard area (WERTHMANN et al. 2024).

The underground model as well as the hazard assessment were solely developed for the study area and cannot be transferred to other parts of the city (chapter 7). The methodology, however, has proven to be efficient and can be applied anywhere in the region.

9 Outlook and Future of the Project

As was already explained throughout the thesis (chapter 1, chapter 4, chapter 6.3.2) the underground model and the hazard assessment were the basis for the distribution of the sensor system of the EWES. Figure 47 in chapter 6.3.2, the synthesis hazard map categorized regarding the slope inclination, was used by AGR to choose the steepest locations within the hazard area as the main focus of surveillance by the system. This sensor system was installed in two steps; first a test installation in the second half of 2021, followed by the final installation starting in winter 2021/2022. The main installation process lasted until summer 2022 due to several problems regarding shipment and import through the Colombian customs office.

In Figure 54 the final sensor installation plan is depicted. The system consists of (1) three gateways for the gathering, storing, and sending of data from the single sensors, (2) several measurements nodes (LoRas = infrastructure nodes on houses, INCLI = subsurface nodes, LCI = low cost inclinometers, piezometer and extensometer nodes), (3) CSM cables, horizontally along trenches and vertically in the four drillings, and (4) wire extensometers, also along the CSM trenches and the in the drillings for redundancy. The development of the system and the sensors and their distribution and installation was planned and conducted by AGR and was subject of the dissertation of Moritz Gamperl.

The sensors are largely functional; some subsurface probes, installed in a depth of up to 6 m, have problems with energy supply. Some infrastructure nodes (LoRas) at private houses were removed by the owners and not reinstalled properly (chapter 5.7), but those were the only problems encountered. No vandalism on any of the sensors was found, even years after the installation process ended, proofing the success of the approach of social integration in the project (chapter 5.7).

Since the beginning of the project, the project leaders of both countries (Christian Werthmann of LUH and Alejandro Echeverri of Urbam) as well as all the other project partners had several meetings, in person in Medellín and via video call, with the authorities of Medellín (mayor and their office) and SIATA (regional warning agency) and DAGRD (municipal disaster management agency) to make sure, that the system and the responsibility for it would be transferred to the city at the end of the project (March 2023). Due to several changes in leadership over the course of the project (elections every two years) no final commitment could be obtained to this date (June 2024).

In chapter 7 and chapter 8 it was already made clear, that the subsurface is too heterogenic to simply transfer the underground model to other parts of Medellín, and, therefore, the definition of events and the criteria for slope failure can also not easily be applied elsewhere in the Aburrá Valley. The methodology and the sensor system, however, can be applied anywhere in the city, the country, and the Andean region, but only provided, that there is a similarly intensive social approach to include the community in the project and the EWES. This last mile of the project was vital for the execution and success of all operations in the study site and cannot be underestimated for similar future projects, as is evident in the outcome of the evaluation of the social integration (chapter 5.7).

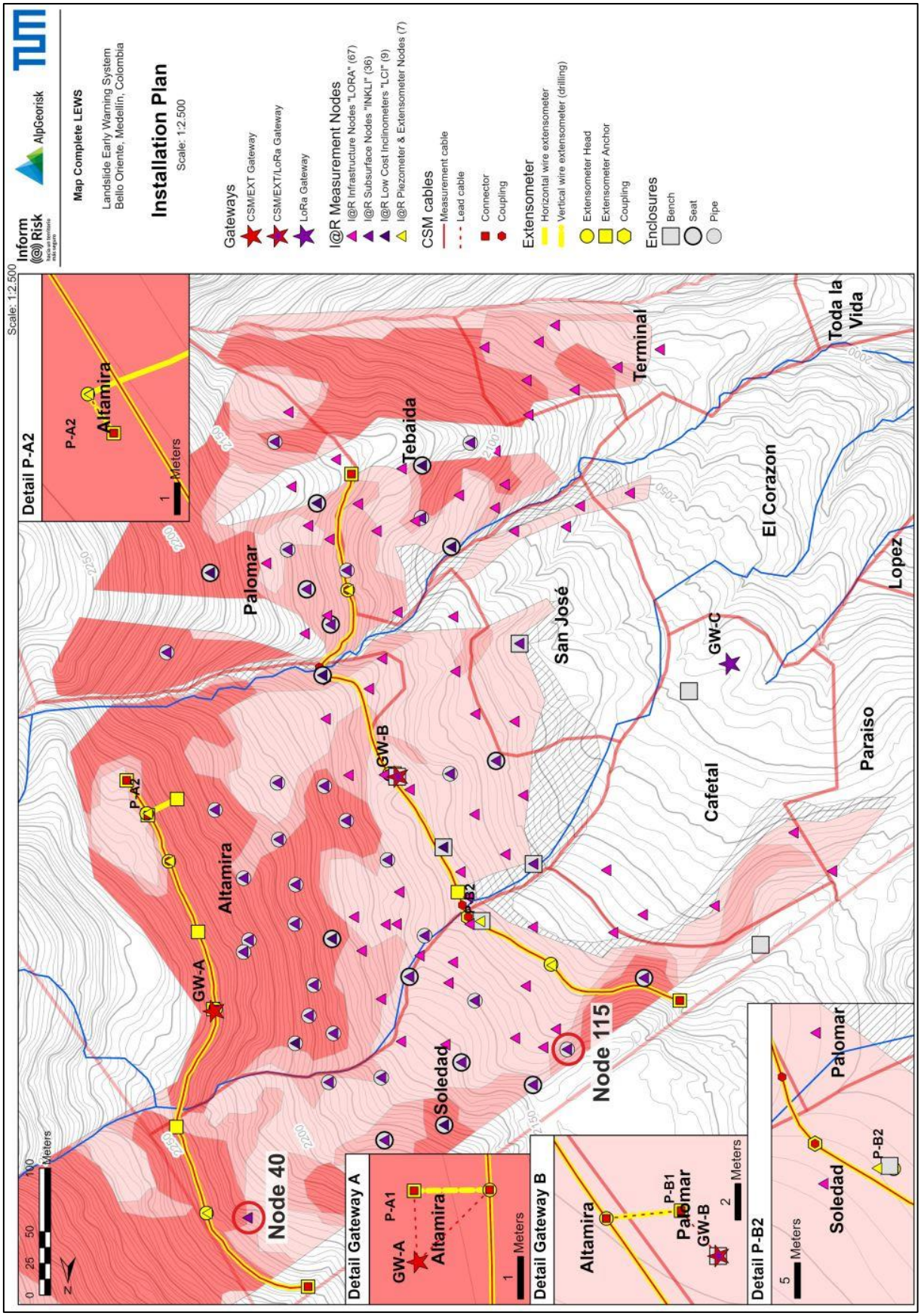

Figure 54: Final installation plan of the EWES in Bello Oriente, created by AGR, on the basis of the inclination hazard map of Figure 47, as seen in the background (GAMPERL et al. 2023).

Bibliography

ÁLVARES-AGUDELO, J. (1987): Tectonitas dunitas de Medellín, departamento de Antioquia, Colombia. – Bol. Cienc. Tierra 28: 9-44.

AMBOS, P. (2020): Petrographische Analyse der ultramafischen Gesteine am Osthang der Stadt Medellín. – 76 p., Bachelor's Thesis, Chair of Engineering Geology, Technical University of Munich, Munich.

ARISTIZÁBAL, E. & YOKOTA, S. (2008): Evolución geomorfológica del Valle de Aburrá y sus implicaciones en la ocurrencia de movimientos en masa. – Boletín de Ciencias de la Tierra, 24: 5–17.

ARISTIZÁBAL, E., GARCÍA, E. & MARTÍNEZ, C. (2015): Susceptibility assessment of shallow landslides triggered by rainfall in tropical basins and mountainous terrains. – Nat Hazards, 78(1): 621–634.

ARISTIZÁBAL, E., MARTÍNEZ-CARVAJAL, H. & GARCÍA-ARISTIZÁBAL, E. (2017): Modelling Shallow Landslides Triggered by Rainfall in Tropical and Mountainous Basins. – In: MIKOŠ, M., CASAGLI, N., YIN, Y. & SASSA, K. (eds.): Advancing Culture of Living with Landslide, 207-212, WLF 2017, Cham (Springer).

ARISTIZÁBAL, E. & GARCÍA-ARISTIZÁBAL, E. (2020): The relationship between rainfall and landslide in the Aburrá Valley, northern Colombian Andes. – Proceedings of the 13th International Symposium of Landslides, Cartagena, Colombia, 22nd-26th February 2021: 9 p.

ARISTIZÁBAL, E., GARCIA, E.F., MARIN, R.J., GÓMEZ, F. & GUZMÁN-MARTÍNEZ, J. (2022): Rainfall-intensity effect on landslide hazard assessment due to climate change in north-western Colombian Andes. – Revista Facultad de Ingeniería Universidad de Antioquia, 103, 51-66.

BOTERO-ARANGO, G. (1963): Contribución al Conocimiento Geológico de la Zona Central de Antioquia. – 102 p., Universidad Nacional de Colombia, Facultad de Minas, Medellín.

BRAGG, W.H. & BRAGG, W.L. (1915): X rays and crystal structure. – London (Bell).

BREUNINGER, T., GAMPERL, M., MENSCHIK, B. & THURO, K. (2021a): First Field Findings and their Geological Interpretations at the Study Site Bello Oriente, Medellín, Colombia: Project Inform@Risk. – Proceedings of the 13th International Symposium of Landslides, Cartagena, Colombia, 22nd-26th February 2021: 7 p.

BREUNINGER, T., GARCIA-LONDOÑO, C., GAMPERL, M. & THURO, K. (2021b): Initial Experiences of Community Involvement in an Early Warning System in Informal Settlements in Medellín, Colombia. – In: SASSA, K., MIKOŠ, M., SASSA, S., BOBROWSKY, P.T., TAKARA, K. & DANG, K. (eds.): Understanding and Reducing Landslide Disaster Risk: Volume 3 – Monitoring and Early Warning: 597-602, WLF 2020, ICL Contribution to Landslide Disaster Risk Reduction, Cham (Springer).

BREUNINGER, T., MENSCHIK, B., DEMHARTER, A., GAMPERL, M. & THURO, K. (2021c): Investigation of Critical Geotechnical, Petrological and Mineralogical Parameters for Landslides in Deeply Weathered Dunite Rock (Medellín, Colombia). – Int. J. Environ. Res. Public Health 2021, 18, 11141, https://doi.org/10.3390/ijerph182111141.

BREUNINGER, T., GAMPERL, M. & THURO, K. (2023a): Geologische Vorerkundung für ein Hangbewegungsfrühwarnsystem in den informellen Siedlungen von Medellín, Kolumbien. – Conference Proceedings, DGGT Conference, 12.-13. September 2023, Würzburg, Germany, 60-66.

BREUNINGER, T., MENSCHIK, B., GAMPERL, M. & THURO, K. (2023b): Determination of Crucial Shear Parameters in Highly Landslide Prone Tropical Soils in Bello Oriente, Medellín, Colombia. –

In: Wang, S., Huang, R., Azzam, R. & Marinos, V.P. (eds.): Engineering Geology for a Habitable Earth, 947-953, Proceedings of the IAEG XIV Congress 2023, Chengdu, China: Volume 2: Geohazard Mechanisms, Risk Assessment and Control, Monitoring and Early Warning, Singapore (Springer).

BRINDLEY, G.W. & BROWN, G. (1982): Crystal Structures of Clay Minerals and their X-Ray Identification. – vol. 5, 494 p., Hertfordshire (The Mineralogical Society of Great Britain and Ireland).

BAFU (2016): Schutz vor Massenbewegungsgefahren. Vollzugshilfe für das Gefahrenmanagement von Rutschungen, Steinschlag und Hangmuren. –Umwelt-Vollzug Nr. 1608, 98 S., Bundesamt für Umwelt, Bern.

CAILLAUD, J., PROUST, D. & RIGHI, D. (2006): Weathering Sequences of Rock-Forming Minerals in a Serpentinite: Influence of Microsystems on Clay Mineralogy. – Clays and Clay Minerals, 54(1): 87–100.

CASAS, J.D.H. & MONSALVE, G. (2018): Geological inferences about the upper crustal configuration of the Medellín – Aburrá Valley (Colombia) using strong motion seismic records. – Geodesy and Geodynamics, 9(1): 67–76.

CEDIEL, F. & SHAW, R.P. (eds.) (2019): Geology and Tectonics of Northwestern South America: The Pacific-Caribbean-Andean Junction. – Frontiers in Earth Sciences, 1001 p.; Cham (Springer).

CORREA-MARTÍNEZ, A.M. (2009): Petrogênese e Evolução do Ofiolito de Aburrá, Cordilheira Central dos Andes Colombianos. – Dissertation., Instituto de Geociências, Departamento de Mineralogia e Petrologia, Universidade de Brasília, 204 p.; Brasília.

CORREA-MARTÍNEZ, A.M. & MARTENS, U. (2000): Caracterización Geológica de las Anfibolitas de los Alrededores de Medellín. – Bachelor's Thesis, Universidad Nacional de Colombia (Medellín), Facultad de Minas.

CROSTA, G.B. & FRATTINI, P. (2008): Rainfall-induced landslides and debris flows. – Hydrological Processes: An International Journal, 22(4): 473–477.

CROZIER, M.J. (2010): Deciphering the effect of climate change on landslide activity: A review. – 428 Geomorphology, 123(3-4): 260-267, https://doi.org/10.1016/j.geomorph.2010.04.009.

DEERE, D.U. (1964): Technical description of rock cores for engineering purposes. – Rock Mechanics and Engineering Geology, 1(1), 17-22 p., Vienna (Springer).

DEMHARTER, A. (2021): Geological-geotechnical characterization of the "Medellín Dunite" along the eastern slope of the city of Medellín, Colombia. – 143 p., Master's Thesis, Chair of Engineering Geology, Technical University of Munich, Munich.

DESLATTES, R.D. & HENINS, A. (1973): X-Ray to Visible Wavelength Ratios. – Physical Review Letters, 31(16), 972.

ECHEVERRI, A., VÉLEZ, A.E., WERTHMANN, C. (eds.) (2012): Re habitar la ladera: operaciones en áreas de riesgo y asentamiento precario en Medellín. – 135 p., Universidad EAFIT, Medellín.

ERMRICH, M., & OPPER, D. (2011): X-Ray Powder Diffraction. – XRD for the analyst, Getting acquainted with the principles, 63-85, Kassel (PANalytical GmbH).

FROUDE, M.J. & PETLEY, D.N. (2018): Global fatal landslide occurrence from 2004 to 2016. – Nat. Hazards Earth Syst. Sci., 18(8): 2161–2181.

GARCIA-CASCO, A., RESTREPO, J.J., CORREA–MARTÍNEZ, A.M., BLANCO-QUINTERO, I.F., PROENZA, J.A., WEBER, M. & BUTJOSA, L. (2020): The petrologic nature of the "Medellín Dunite" revisited: An algebraic approach and proposal of a new definition of the geological body. – In

Gómez, J., Pinilla–Pachon, A.O., (eds.): The Geology of Colombia—Publicaciones Geológicas Especiales 36,Volume 2 Mesozoic, Servicio Geológico Colombiano: Bogotá, Colombia: 45–75, https://doi.org/10.32685/pub.esp.36.2019.02.

GAMPERL, M., SINGER, J. & THURO, K. (2021): Internet of Things Geosensor Network for Cost-Effective Landslide Early Warning Systems. – Sensors 21(8), 2609.

GAMPERL, M., SINGER, J., GARCIA-LONDOÑO, C., SEILER, L., CASTAÑEDA, J., CERÓN-HERNANDEZ, D. & THURO, K. (2023): Recommendations for Landslide Early Warning Systems in Informal Settlements Based on a Case Study in Medellín, Colombia. – Land, 12(7): 1451, https://doi.org 10.3390/land12071451.

GAMPERL, M., BREUNINGER, T., THURO, K., CERÓN-HERNANDEZ, C. & MENSCHIK, T. (in review): Improvement of landslide investigation in deeply weathered ultramafites by parallelizing ERT with direct field observations. – Frontiers in Earth Science. – In: GAMPERL, M. (2024): Implementation of a Landslide Early Warning System considering informal settlements in Medellín (Colombia). – 197 p., Ph.D.-Thesis, Chair of Engineering Geology, Technical University of Munich, Munich, URL: https://mediatum.ub.tum.de/1721464.

GILG, H.A. (2024): Personal Communication. – 26th February 2024, Chair of Engineering Geology, Technical University of Munich, Munich, Bavaria, Germany.

GONZÁLEZ, I.H. (2001): Memoria explicativa: Mapa Geológico del Departamento de Antioquia. Escala 1 : 400 000: Geología, Recursos minerales y amenazas potenciales. – 241 p.; Bogotá (Ingeominas).

GU, D., ANDREEV, K. & DUPRE, M.E. (2021): Major Trends in Population Growth Around the World. – China CDC Weekly, 3(28): 604-613, doi: 10.46234/ccdcw2021.160.

HERMELÍN, M. (2005): Desastres de Origin Natural en Colombia 1979-2004. – 248 p., Medellín (Universidad EAFIT Medellín).

HERMELÍN, M. (ed.) (2016): Landscapes and Landforms of Colombia – World Geomorphological Landscapes, 218 p., Cham (Springer).

HERNÁNDEZ-GONZÁLEZ, J.S. (2014): Mineralizaciones de Cr y elementos del grupo del platino (EGP) asociadas a las Metaperidotitas de Medellín, Colombia. – Doctoral dissertation, Universidad de Barcelona and Universidad Autónoma de Barcelona, Barcelona, Spain.

HIDALGO, C.A. & VEGA, J.A. (2014): Hazard estimation for landslides triggered by earthquakes and rainfall (Aburrá Valley-Colombia). – Revista EIA/English version, 11(22): 93–107.

HIDALGO, C.A. & VEGA, J.A. (2015): Risk Estimation in Urban Buildings by Landslides Triggered by Earthquakes and Rainfall (Medellín-Colombia). – From Fundamentals to Applications in Geotechnics, 2892-2899, IOS Press.

HUNGR, O., LEROUEIL, S. & PICARELLI, L. (2014): The Varnes classification of landslide types, an update. – Landslides, 11, 167–194.

JAYASINGHA, P. (2016): Social Geology and Landslide Disaster Risk Reduction in Sri Lanka. – Journal of Tropical Forestry and Environment, 6(2): 1-13.

KLIMEŠ, J., RIOS ESCOBAR, V. (2010): A landslide susceptibility assessment in urban areas based on existing data: an example from the Iguaná Valley, Medellín City, Colombia. – Nat. Hazards Earth Syst. Sci., 10(10), 2067–2079.

KOPP, R. E., EASTERLING, D. R., HALL, T., HAYHOE, K., HORTON, R., KUNKEL, K., LEGRANDE, A. (2017): Potential Surprises – Compound Extremes and Tipping Elements. – In: WUEBBLES, D.J., FAHEY, D.W., HIBBARD, K.A., DOKKEN, D.J., STEWART, B.C. & MAYCOCK, T.K. (eds.):

Climate Science Special Report: A Sustained Assessment Activity of the U.S. Global Change Research Program, 608-635.

LEIBNIZ UNIVERSITY HANOVER (2018): Inform@Risk – Leitantrag Client II BMBF. – 95 S.

LEISGANG, I. (2021): Risk-Based Selection and Positioning of Sensors for a Geosensor Network for Landslide Monitoring, in Medellín (Colombia). – 102 p., Master's Thesis, Chair of Engineering Geology, Technical University of Munich, Munich.

LIU, F., WANG, B., OUYANG, Y., WANG, H., QIAO, S., CHEN, G., DONG, W. (2022): Intraseasonal variability of global land monsoon precipitation and its recent trend. – Climate and Atmospheric Science 5(1): 30.

MACKENZIE, W.S. & ADAMS, A.E. (1995): Minerale und Gesteine in Dünnschliffen. – 191 S., Stuttgart (Ferdinand Enke Verlag).

MARKL, G. (2015): Minerale und Gesteine. – 608 S., 3. Aufl., Berlin (Springer).

MEHRA, O.P. & JACKSON, M.L. (2013): Iron Oxide Removal from Soils and Clays by a Dithionite-Citrate System Buffered with Sodium Bicarbonate. – Clays and Clay Minerals, 7: 317–327.

MONTERO-OLARTE, J. (2007): Deslizamiento y flujo de tierra Villatina, Medellín, Antioquia, Colombia. – In: PROYECTO MULTINACIONAL ANDINO: GEOCIENCIAS APA LAS COMUNIDADES ANDINAS: Movimientos es Masa de la Región Andina: Una Guía para la Evaluación de Amenazas, A.18, 262-268, Sevicio Nacional de Geología y Minería, Publicación Geológica Multinacional, No. 4.

MOREIRAS, S.M. & PONT, I.P.V.D. (2017): Climate Change Driving Greater Slope Instability in the Central Andes. – In: MIKOŠ, M., VILÍMEK, V., YIN, Y. & SASSA, K. (eds): Advancing Culture of Living with Landslides, 5: 191-197, WLF 2017, Cham (Springer).

NADIM F. & INTRIERI E. (2011): Early warning system for landslides: challenges and new monitoring technologies. – In: Proceedings of the 5th Canadian Conference on Geotechniques and Natural Hazards, 1-15, 15th-17th May 2011, Kelowna, BC, Canada.

OJEDA, J., & DONNELLY, L. (2006): Landslides in Colombia and their impact on towns and cities. – 10th IAEG Congress 2006, Nottingham, paper no. 112, 1-13.

OKRUSCH, M. & MATTHES, S. (2014): Mineralogie - Eine Einführung in die spezielle Mineralogie, Petrologie und Lagerstättenkunde. – 726 S., 9. Aufl., Berlin (Springer).

OTTO, J.C. & SASS, O. (2006): Comparing geophysical methods for talus slope investigations in the Turtmann valley (Swiss Alps). – Geomorphology 76(3-4: 257-272.

PEÑA, G.L.R. (2017): Las amenazas por movimientos en masa de Colombia, una visión a escala 1:100.000, Servicio Geológico Colombiano, https://doi.org/10.32685/9789589952887.

PETZI, J. (2022): Geological-geotechnical characterization of the "Medellín Dunite" along the eastern slope of the city of Medellín, Colombia. – 74 p., Master's Thesis, Chair of Engineering Geology, Technical University of Munich, Munich.

PRIEST, S.D. (1993): Discontinuity Analysis for Rock Engineering. – 473 p., Springer (New York).

RENDÓN-GIRALDO, D.A. (2020): Personal Communication. – 18th November 2020, Departamento de Geociencias y Medio Ambiente, Universidad Nacional de Colombia, Medellín, Antioquia, Colombia.

RESTREPO J.J. (2008): Obducción y Metamorfismo de Ofiolitas triásticas en el flanco occidental del Terreno Tahamí, Cordillera Central de Colombia. – Boletín de ciencias de la tierra, 22: 49–100; Medellín.

RESTREPO, J.J, IBAÑEZ-MEJIA, M. & GARCÍA-CASCO, A. (2012): U-Pb zircon ages of the Medellin Amphibolites (Central Cordillera of Colombia) reveal mid-Cretaceous tectonic juxtaposition of Triassic and mid-cretaceous metamorphic complexes. – Abstr. VIII South Am. Symp. Isot. Geol.; Medellín, Colombia, pp. 201-202, http://dx.doi.org/10.13140/2.1.4463.6969.

RESTREPO, J.J. & TOUSSAINT, J.F. (1984): Unidades Litológicas de Los Alrededores del Valle de Aburrá. – Mem. Conf. Sobre Riesgos Geológicos Val, Sociedad Colombiana de geología, Aburrá, Medellín, 1984, 1-26.

RIETVELD, H.M. (2010). The Rietveld Method: a retrospection. – Journal for Crystallography – Crystalline Minerals, 225, 545-547, https://doi.org/10.1524/zkri.2010.1356.

RODRÍGUEZ, G., GONZÁLEZ, H., ZAPATA, G., COSSIO, U. & CORREA-MARTÍNEZ, A.M. (2005): Memoria explicativa: Geología de la Plancha 147 Medellín Oriental. Escala 1 : 100 000. – 312 p.; Bogotá (Ingeominas).

SEPÚLVEDA, S.A & PETLEY, D.N. (2015): Regional trends and controlling factors of fatal landslides in Latin America and the Caribbean. – Nat. Hazards Earth Syst. Sci., 15(8): 1821–1833.

SERVICIO GEOLÓGICO COLOMBIANO (SGC) (2015): Guía metodológica para estudios de amenaza, vulnerabilidad y riesgo por movimientos en masa. – 179 p., Libros del Servicio Geológico Colombiano, Bogotá.

SINGER, J., THURO, K., GAMPERL, M., BREUNINGER, T. & MENSCHIK, B. (2021): Technical Concepts for an Early Warning System for Rainfall Induced Landslides in Informal Settlements. – In: CASAGLI, N., TOFANI, V., SASSA, K., BOBROWSKY, P.T. & TAKARA, K. (eds.): Understanding and Reducing Landslide Disaster Risk, ICL Contribution to Landslide Disaster Risk Reduction Ser, 209–215, Cham (Springer).

STINY, J. (1922): Technische Geologie. – 789 S.; Stuttgart (Enke).

THURO, K., SINGER, J., MENSCHIK, B., BREUNINGER, T.& GAMPERL, M. (2020): Development of an early warning system for landslides in the tropical Andes (Medellín, Colombia). – Geomechanics and Tunnelling, 13(1): 103–115.

TOBÓN-HINCAPIÉ, M.P., JOYA-CAMACHO, A.M., MARCÍAS-TORRES, C.E., GOMEZ-GALLO, M.H., ZAPATA-WILLS, C. & VELÁSQUEZ, A. (2011): Medidas de mitigación de la Ladera Oriental del Valle de Aburrá entre las Quebradas La Poblada y La Sandín. – 218 p.; Medellín (Alcaldía de Medellín - Secretaria del Medio Ambiente).

TOKUHIRO, H. (1988): Landslide in Villa Tina, Medellín City, Colombia. – Jpn. Landslide Soc. Landslide News 2: 12-13.

TRÖGER, W.E. (1969): Optische Bestimmung der gesteinsbildenden Minerale: Teil II. – 822 S., 2. Aufl., Stuttgart (Schweizerbart'sche Verlagsbuchhandlung).

TRÖGER, W.E. (1982): Optische Bestimmung der gesteinsbildenden Minerale: Teil I.: Bestimmungstabellen. – 188 S., 5. Aufl., Stuttgart (Schweizerbart'sche Verlagsbuchhandlung).

UCHIMURA, T., TOWHATA, I., WANG, L., NISHIE, S., YAMAGUCHI, H., SEKO, I. & QIAO, J. (2015): Precaution and early warning of surface failure of slopes using tilt sensors. – Soils and Foundations, 55(5): 1086–1099.

ÜNDÜL, Ö., TUĞRUL, A., ÖZYALIN, Ş. & ZARIF, İ.H. (2015): Identifying the changes of geo-engineering properties of dunites due to weathering utilizing electrical resistivity tomography (ERT). – J. Geophys. Eng. 12(2): 273–281, https://doi.org/10.1088/1742-2132/12/2/273.

ÜNDÜL, Ö. & TUĞRUL, A. (2016): On the variations of geo-engineering properties of dunites and diorites related to weathering. – Environ. Earth Sci. 75: 1326, https://doi.org/10.1007/s12665-016-6152-x.

VAN WESTEN, C.J. & TERLIEN, M.T.J. (1996): An approach towards deterministic landslide hazard analysis in GIS. A case study from Manizales (Colombia). – Earth surface and landforms 21(9), 853–868.

VEGA, J.A., HIDALGO, C.A., MARÍN, N.J. (2017): Landslide Risk: Economic Valuation in The North-Eastern Zone of Medellin City. – IOP Conf. Ser.: Mater. Sci. Eng. 245, 1 p., 062010, IOP Publishing.

WERTHMANN, C. & ECHEVERRI, A. (2013): Rehabitar la Montaña: estrategias y procesos para un hábitat sostenible en las laderas de Medellín. – 301 p.; Medellín (Universidad EAFIT).

WERTHMANN, C. (2019): Status Meeting Inform@Risk, 05.11.2019. – 109 p., unpublished presentation, Leibniz University Hanover/Universidad EAFIT Medellín, Hanover/Medellín.

WERTHMANN, C., SAPENA, M., KÜHNL, M., SINGER, J., GARCIA, C., BREUNINGER, T., GAMPERL, M., MENSCHIK, B., SCHÄFER, H., SCHRÖCK, S., SEILER, L., THURO, K. & TAUBENBÖCK, H. (2024): Insights into the development of a landslide early warning system prototype in an informal settlement: the case of Bello Oriente in Medellín, Colombia. – 42 p., Nat. Hazard Earth Syst., https://doi.org/10.5194/nhess-24-1843-2024.

WIECZOREK, G.F. (1997): Landslide Triggering Mechanisms. – In: NATIONAL RESEARCH COUNCIL (ed.): Landslides: Investigation and Mitigation, Transportation research record Public transit, 247: 76-90, Washington, DC (National Acad. Press).

ZIEGLER, J. (2020): XRD Analysis of the Weathered Material from the Igneous Rocks on the Eastern Slope of Medellín (Inform@Risk). – 60 p., Bachelor's Thesis, Chair of Engineering Geology, Technical University of Munich, Munich.

Standards

ASTM D 2487—17e1 (2017): Standard Practice for Classification of Soils for Engineering Purposes (Unified Soil Classification System) – ASTM International:(West Conshohocken, PA, USA).

ASTM D 3282 (2015): Standard Practice for Classification of Soils and Soil-Aggregate Mixtures for Highway Construction Purposes. – ASTM International:(West Conshohocken, PA, USA).

ASTM D 3967 (2016): Standard Test Method for Splitting Tensile Strength of Intact Rock Core Specimen. – ASTM International:(West Conshohocken, PA, USA).

ASTM D 7012-14e1 (2014): Standard Test Methods for Compressive Strength and Elastic Moduli of Intact Rock Core Specimens under Varying States of Stress and Temperatures. – ASTM International (West Conshohocken, PA, USA).

ASTM E 100 (2019): Standard Specification for ASTM Hydrometers. – ASTM International (West Conshohocken, PA, USA).

DGGT (DEUTSCHE GESELLSCHAFT FÜR GEOTECHNIK) 2022a: Empfehlung Nr. 1: Einaxialer Druckversuche an zylindrischen Gesteinsprüfkörpern. – Empfehlungen des Arbeitskreises Versuchstechnik Fels, 1-20.

DGGT (DEUTSCHE GESELLSCHAFT FÜR GEOTECHNIK) 2022b: Empfehlung Nr. 10: Indirekter Zugversuch an Gesteinsproben – Spaltzugversuch. – Empfehlungen des Arbeitskreises Versuchstechnik Fels, 115-122.

DIN 1055-2 (2010): Actions on structures – Part 2: Soil properties. – Berlin (Beuth).

DIN EN ISO 14688-1 (2020): Geotechnical investigation and testing — Identification and classification of soil — Part 1: Identification and description (ISO 14688-1:2017); German version EN ISO 14688-1:2018. – Berlin (Beuth).

DIN EN ISO 14688-2 (2020): Geotechnical investigation and testing — Identification and classification of soil — Part 2: Principles for a classification (ISO 14688-2:2017); German version EN ISO 14688-2:2018. – Berlin (Beuth).

DIN EN ISO 14689 (2018): Geotechnical investigation and testing - Identification, description and classification of rock (ISO 14689:2017); German version EN ISO 14689:2018. – Beuth (Berlin).

DIN EN ISO 17892-4 (2017): Geotechnical investigation and testing - Laboratory testing of soil – Part 4: Determination of particle size distribution (ISO 17892-4:2016); German version EN ISO 17892-4:2016. – Berlin (Beuth).

DIN EN ISO 17892-10 (2019): Geotechnical investigation and testing - Laboratory testing of soil - Part 10: Direct shear tests (ISO 17892-10:2018); German version EN ISO 17892-10:2018– Berlin (Beuth).

DIN EN ISO 17892-12 (2020): Geotechnical investigation and testing - Laboratory testing of soil - Part 12: Determination of liquid and plastic limits (ISO 17892-12:2018); German version EN ISO 17892-12:2018. – Berlin (Beuth).

I.N.V. E-123 (2013): Análisis granulométrico de suelos por tamizado. – Institución Nacional de Vías (INVIAS).

I.N.V. E-124 (2013): Análisis granulométrico por medio del hidrómetro. – Institución Nacional de Vías (INVIAS).

I.N.V. E-125 (2013): Determinación del limite liquido de los suelos. – Institución Nacional de Vías (INVIAS).

I.N.V. E-126 (2013): Limite plastico e indice de plasticidad. – Institución Nacional de Vías (INVIAS).

I.N.V. E-154 (2013): Determinación de la resistencia al corte metodo de corte directo (cd) (Consolidado drenado). – Institución Nacional de Vías (INVIAS).

SN 670 010b (1998): Bodenkennziffern. – Association of Swiss Road and Traffic Engineers (eds.), Zurich.

Internet Sources

www-01: https://www.google.com/maps/@4.9615585,-76.0645273,2392421m/data=!3m1!1e3?entry=ttu, last accessed on 11.02.2024.

www-02: https://www.bpb.de/kurz-knapp/lexika/kosmos-weltalmanach/65710/kolumbien/, last accessed on 11.02.2024.

www-03: https://www.colombiaenmapas.gov.co/#, last accessed on 11.02.2024.

www-04: https://de.wikipedia.org/wiki/Datei:Colombia_relief_location_map.jpg, last accessed 03.08.2020.

www-05: https://www.liportal.de/kolumbien/ueberblick/?fs=12, last accessed 31.07.2020.

www-06: https://www.medellin.gov.co/es/centro-documental/proyecciones-poblacion-viviendas-y-hogares/, last accessed on 11.02.2024.

www-07: https://www.medellin.gov.co/irj/go/km/docs/wpccontent/Sites/Subportal%20del%20Ciudadano/Plan%20de%20Desarrollo/Secciones/Informaci%C3%B3n%20General/Documentos/POT/medellinPoblacion.pdf, last accessed on 11.02.2024.

www-08: https://www.google.com/maps/place/Medell%C3%ADn,+Departamento+de+Antioquia,+Kolumbien/@6.2338907,-75.6913192,37300m/data=!3m1!1e3!4m6!3m5!1s0x8e4428dfb80fad05:0x42137cfcc7b53b56!8m2!3d6.2476376!4d-75.5658153!16zL20vMDF4XzZz?entry=ttu, last accessed on 11.02.2024.

www-09: https://upload.wikimedia.org/wikipedia/commons/2/2a/Comunas_de_Medellin.svg, last accessed 29.02.2024.

www-10: http://www.ideam.gov.co/web/tiempo-y-clima/clima, last accessed on 11.02.2024.

www-11: https://mayorsmigrationcouncil.org/news/medellns-holistic-housing-for-refugees/, last accessed 05.03.2024.

www-12: https://www.refugeesinternational.org/reports-briefs/a-forgotten-response-and-an-uncertain-future-venezuelans-economic-inclusion-in-colombia/, last accessed 05.03.2024.

www-13: https://www.planat.ch/en/specialists/risk-management/what-has-to-be-done, last accessed 06.03.2024.

www-14: https://simma.sgc.gov.co/#/public/basic/, last accessed 22.05.2024.

Annex

Figures

Figure A1: Drilling Core Evaluation, Drilling A1, DIN A1.

Figure A2: Drilling Core Evaluation, Drilling A2, DIN A1.

Figure A3: Drilling Core Evaluation, Drilling B1, DIN A0.

Figure A4: Drilling Core Evaluation, Drilling B2, DIN A0.

Figure A5: Process Map, DIN A3.

Figure A6: Geological Map, DIN A3.

Figure A7: Colluvial Map, DIN A3.

Figure A8: Synthesis Hazard Map, DIN A3.

Tables

Table A1: Results of the uniaxial compressive strength test and the tensile strength test.

Table A2: Results of the grain size analysis and the Atterberg limits analysis.

Table A3: Sample conditions and results of the direct shear test.

Table A4: Results of the thin section analysis.

Table A5: Results of the XRD analysis.

Drilling profile

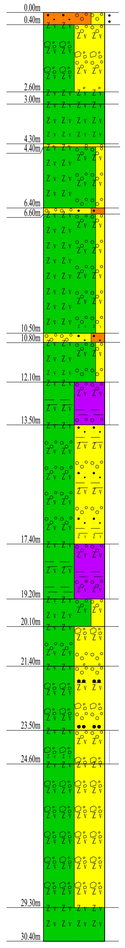

Core loss

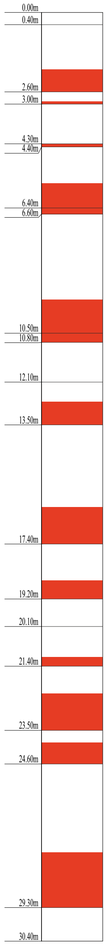

Weathering profile

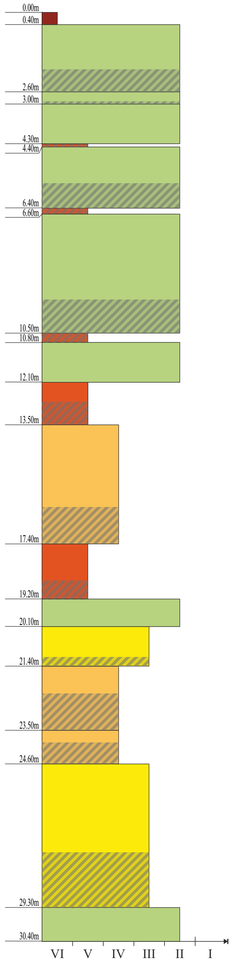

Quality (RQD)

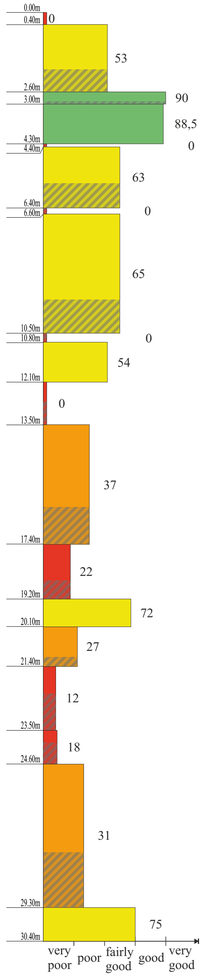

Fracture ratio

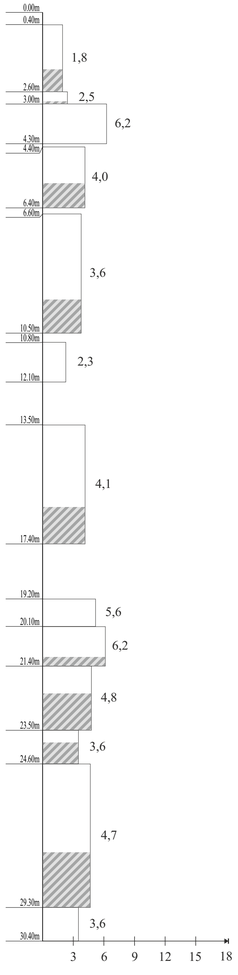

Joint set
(simplyfied tadpole-depiction)

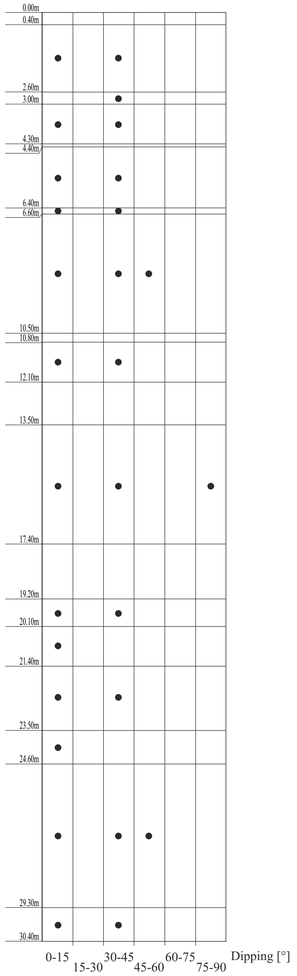

Alteration type

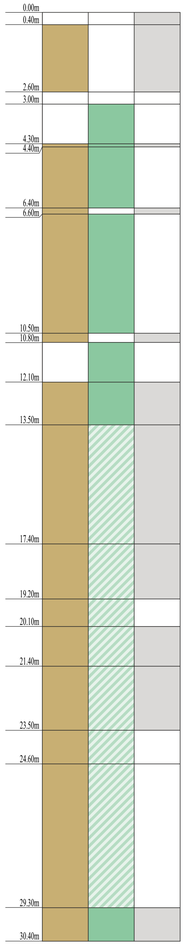

Homogeneous areas

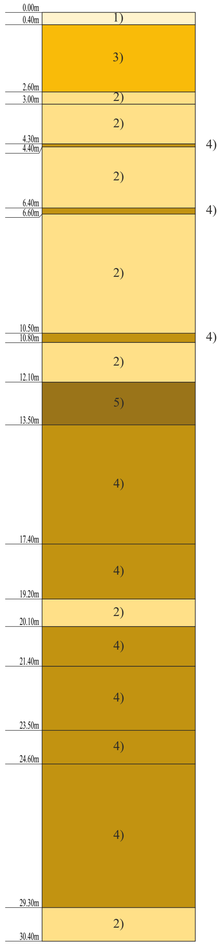

Drilling profile

Core loss

Weathering profile

Quality (RQD)

Fracture ratio
after STINY (1922)

Joint set
(simplyfied tadpole-depiction)

Alteration type

Homogeneous areas

Core recovery	Core loss
20,53 m	9,87 m
67,50 %	32,50 %

Description of joints (weathering, quantitative)	
I)	fresh
II)	light
III)	moderate
IV)	high
V)	extreme
VI)	soil

after DIN EN ISO 14689 (2018)

RQD	
0 - 25	very poor
25 - 50	poor
50 - 75	fairly good
75 - 90	good
90 - 100	very good

after DEERE (1964)

Alteration type	
	brown colored
	serpentinized
	fragmented

Homogeneous areas	
0)	Core, fresh *(here not encountered)*
1)	Top soil
2)	Core, lightly weathered
3)	Core, (highly) fractured, lighty weathered
4)	Core, highly fractured, highly weathered
5)	Core, loose, completley fractured, with clay
6)	Core, extremely fragile *(here not encountered)*

Figure A1: Drilling 2020-A1 Bello Oriente, Medellín (Colombia)

Scale 1:100

edited by: Agnes Demharter, Tamara Breuninger

Drilling profile

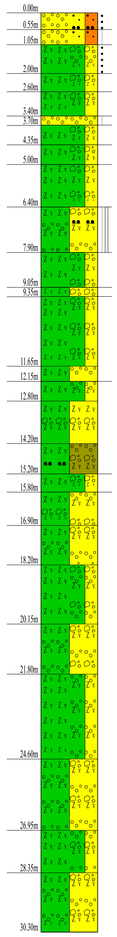

Core loss

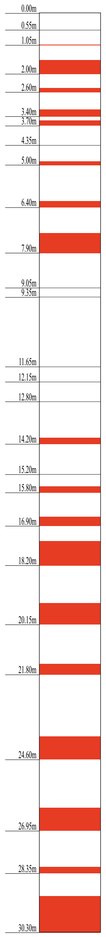

Weathering profile

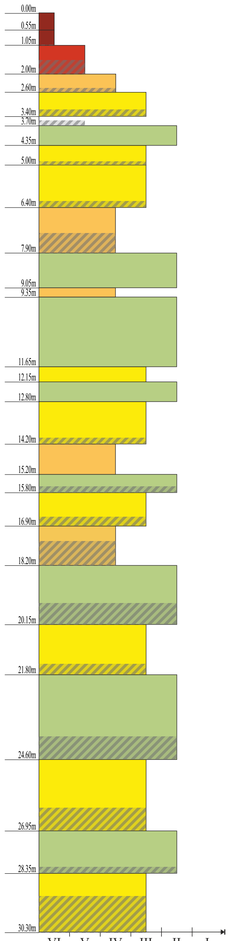

Quality (RQD)

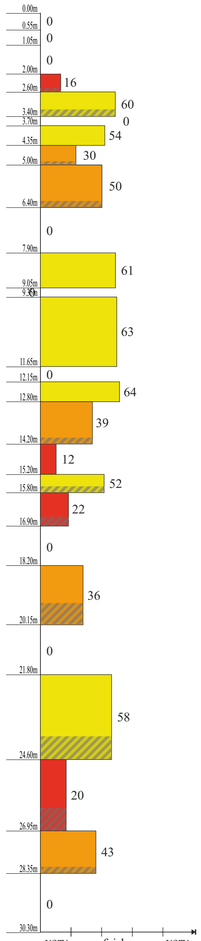

Fracture ratio

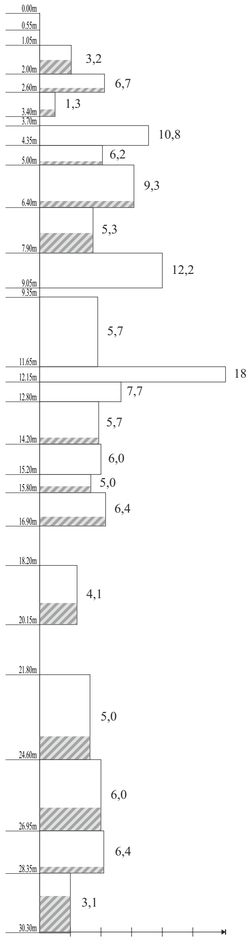

Joint set
(simplyfied tadpole-depiction)

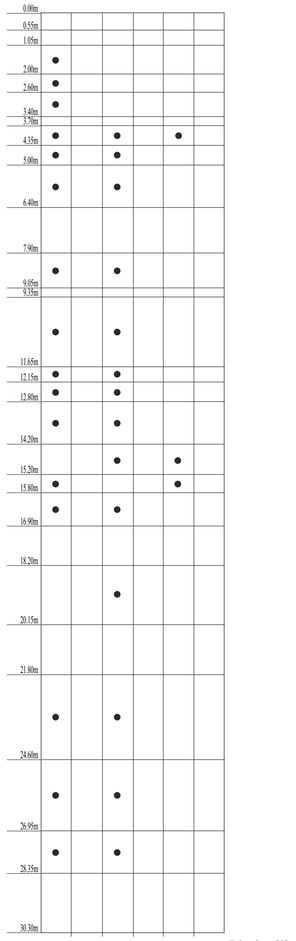

Alteration type

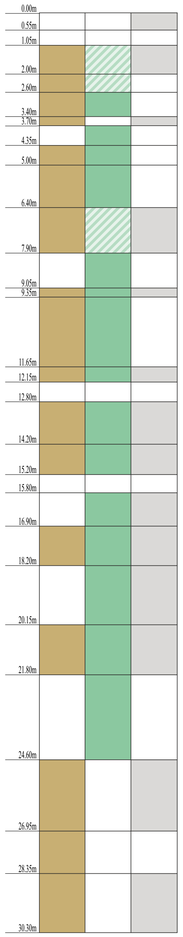

Homogeneous areas

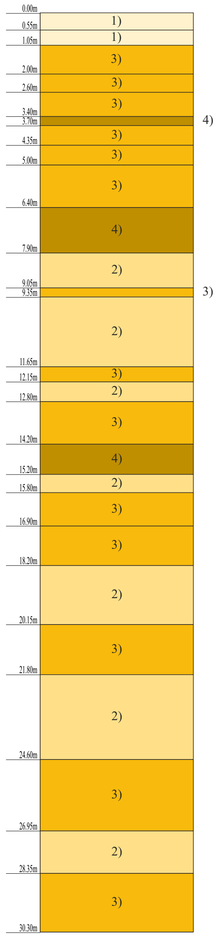

Drilling profile

Core loss

Weathering profile

Quality (RQD)

Fracture ratio
after STINY (1922)

Joint set
(simplyfied tadpole-depiction)

Alteration type

Homogeneous areas

Core recovery	Core loss
20,53 m	9,87 m
67,50 %	32,50 %

Description of joints (weathering, quantitative)	
I)	fresh
II)	light
III)	moderate
IV)	high
V)	extreme
VI)	soil

after DIN EN ISO 14689 (2018)

RQD	
0 - 25	very poor
25 - 50	poor
50 - 75	fairly good
75 - 90	good
90 - 100	very good

after DEERE (1964)

Alteration type	
	brown colored
	serpentinized
	fragmented

Homogeneous areas	
0)	Core, fresh *(here not encountered)*
1)	Top soil
2)	Core, lightly weathered
3)	Core, (highly) fractured, lighty weathered
4)	Core, highly fractured, highly weathered
5)	Core, loose, completley fractured, with clay
6)	Core, extremely fragile *(here not encountered)*

Figure A2: Drilling 2020-A2
Bello Oriente, Medellín (Colombia)

Scale 1:100

edited by: Agnes Demharter, Tamara Breuninger

Drilling profile

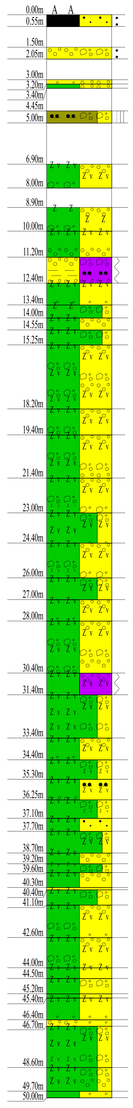

Core loss

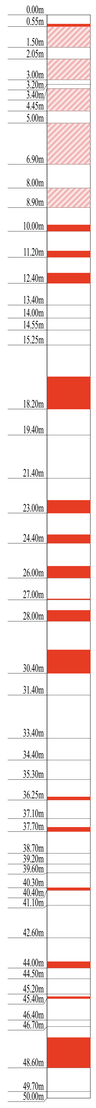

Weathering profile

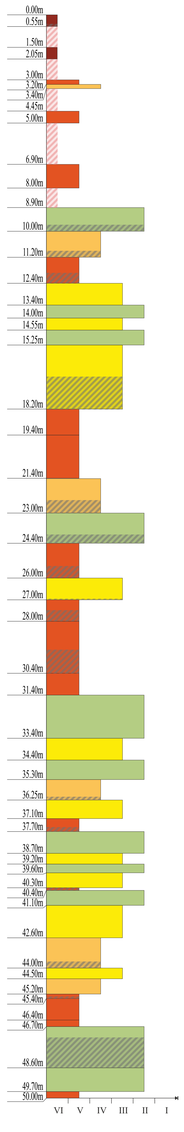

Quality (RQD)

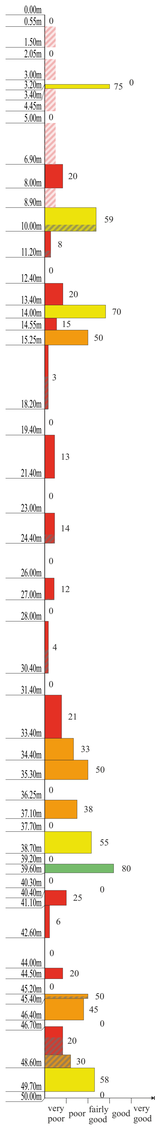

Fracture ratio

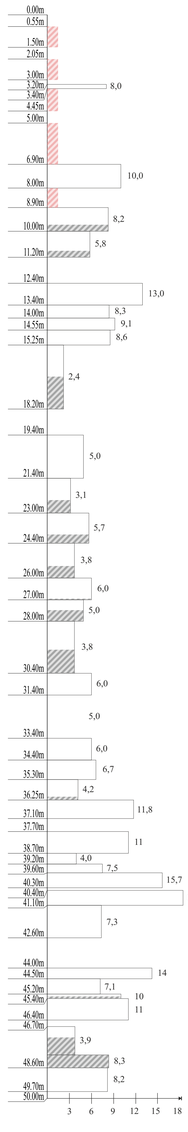

Joint set
(simplyfied tadpole-depiction)

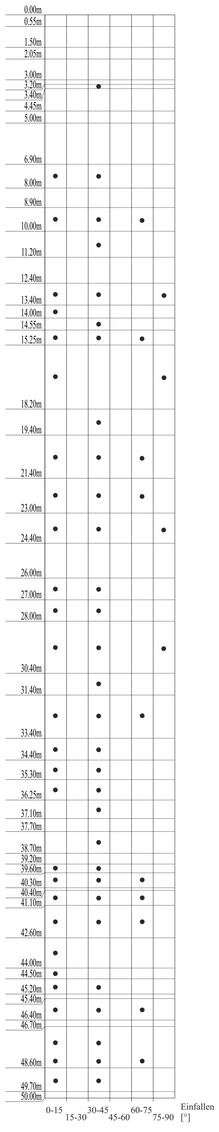

Alteration type

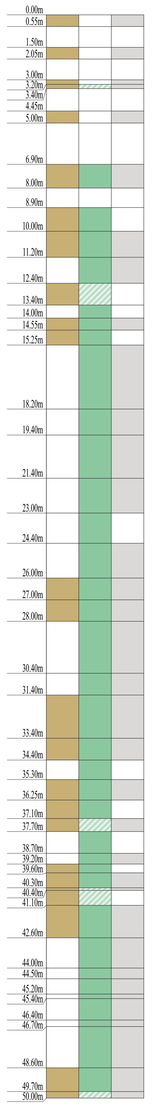

Homogeneous areas

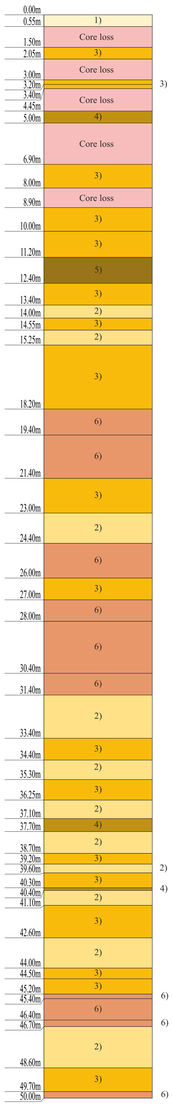

Drilling profile

Core loss

Core recovery	Core loss
36,11 m	13,89
72,22 %	27,78 %

Weathering profile

Description of joints (weathering, quantitative)	
I)	fresh
II)	light
III)	moderate
IV)	high
V)	extreme
VI)	soil

after DIN EN ISO 14689 (2018)

Quality (RQD)

RQD	
0 - 25	very poor
25 - 50	poor
50 - 75	fairly good
75 - 90	good
90 - 100	very good

after DEERE (1964)

Fracture ratio

after STINY (1922)

Joint set

(simplyfied tadpole-depiction)

Alteration type

Alteration type
brown colored
serpentinized
fragmented

Homogeneous areas

Homogeneous areas	
0)	Core, fresh *(here not encountered)*
1)	Top soil
2)	Core, lightly weathered
3)	Core, (highly) fractured, lighty weathered
4)	Core, highly fractured, highly weathered
5)	Core, loose, completley fractured, with clay
6)	Core, extremely fragile

Figure A3: Drilling 2020-B1
Bello Oriente, Medellín (Colombia)

Scale 1:100

edited by: Agnes Demharter, Tamara Breuninger

Drilling profile

Starting point:2130.00 m

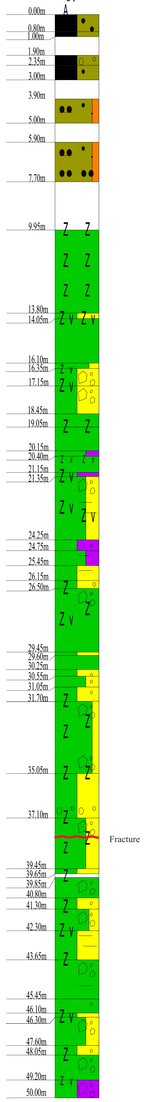

Core loss

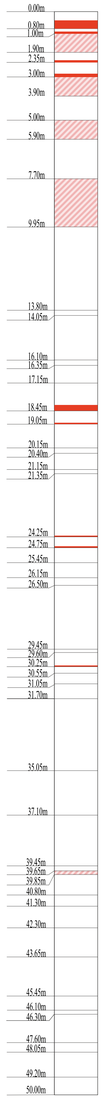

Weathering profile

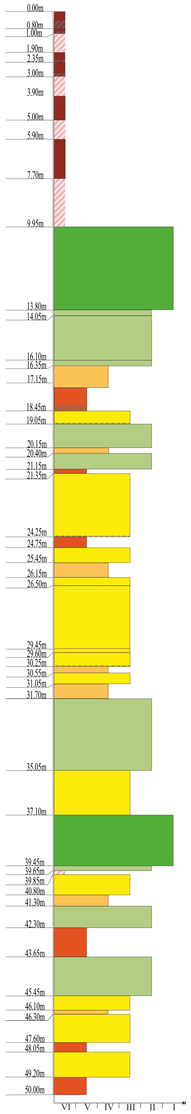

Quality (RQD)

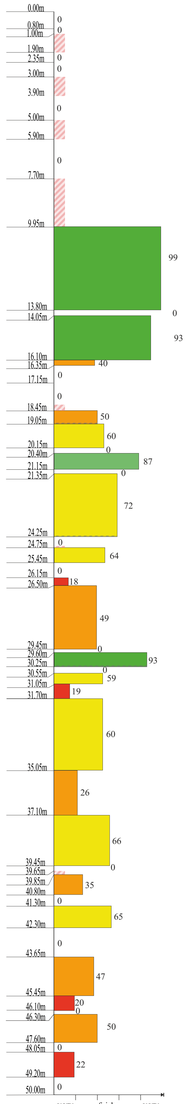

Fracture ratio

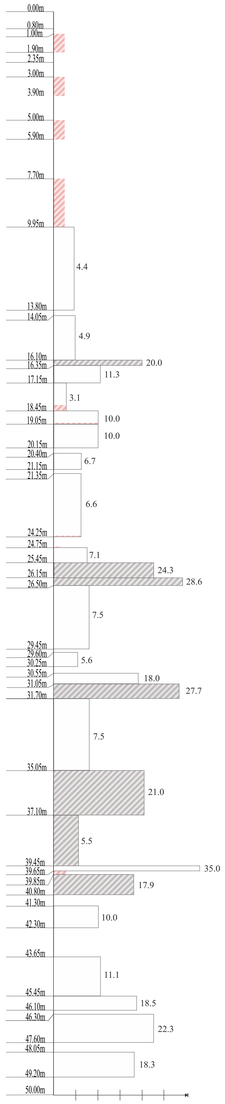

Joint set

(simplyfied tadpole-depiction)

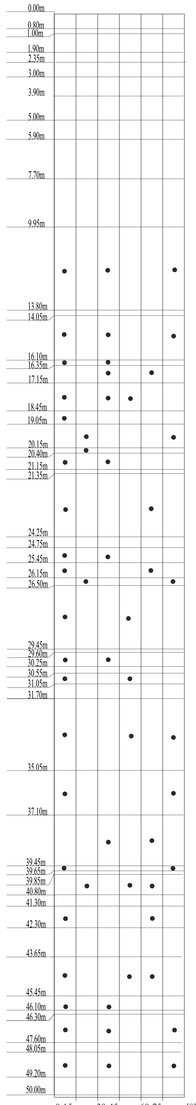

Alteration type

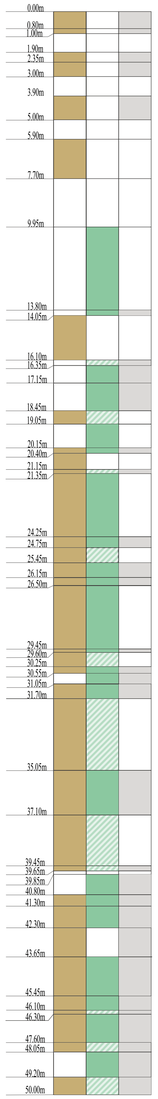

Homogeneous areas

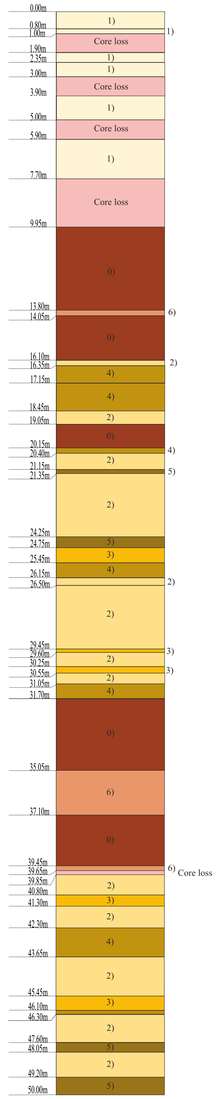

Drilling profile

Core loss

Core recovered	Core lost
43.13 m	6.87
86.26 m	13.74 %

Weathering profile

Description of joints (weathering, quantitative)	
I)	fresh
II)	light
III)	moderate
IV)	high
V)	extreme
VI)	soil

after DIN EN ISO 14689 (2018)

Quality (RQD)

RQD	
0 - 25	very poor
25 - 50	poor
50 - 75	fairly good
75 - 90	good
90 - 100	very good

after DEERE (1964)

Fracture ratio

after STINY (1922)

Joint set

(simplyfied tadpole-depiction)

Alteration type

Alteration type	
	brown colored
	serpentinized
	fragmented

Homogeneous areas

Homogeneous areas	
0)	Core, fresh
1)	Top soil
2)	Core, lightly weathered
3)	Core, (highly) fractured, lighty weathered
4)	Core, highly fractured, highly weathered
5)	Core, loose, completley fractured, with clay
6)	Core, extremely fragile

Figure A4: Drilling 2021-B2
Bello Oriente, Medellín (Colombia)

Scale 1:100

edited by: Julia Petzi, Tamara Breuninger

Figure A5: Process Map

- Historic Landslides
- Sliding Direction
- Tear-Off Edge
- Accumulative Ridge
- Buildings
- Streets
- Creeks

N

0,1 0,05 0 0,1 0,2 0,3 0,4 Kilometers

Figure A6: Geological Map

- Buildings
- Streets
- Creeks

Geology

- Rock
- Saprolite
- Matrix
- Block-in-Matrix Structure (Matrix dominates)
- Block-in-Matrix Structure (Blocks dominate)
- Blocks

N

0,1 0,05 0 0,1 0,2 0,3 0,4 Kilometers

Figure A7: Colluvial Map

- Buildings
- Streets
- Creeks

Colluvium Thickness

- Rock
- Saprolite
- up to 2.5 m
- up to 5 m
- up to 10 m
- over 10 m
- heavily fractured

N

0,1 0,05 0 0,1 0,2 0,3 0,4 Kilometers

Figure A8: Synthesis Hazard Map

- Buildings
- Streets
- Creeks

30 Year Event

- Hazard 30 Year Event
- Runout 30 Year Event

100 Year Event

- Hazard 100 Year Event
- Runout 100 Year Event

Residual Hazard

- Residual Hazard
- Residual Runout

N

0,1 0,05 0 0,1 0,2 0,3 0,4

Kilometers

837800 837900 838000 838100 838200 838300 838400 838500 838600 838700 838800 838900 839000

1186700 1186600 1186500 1186400 1186300 1186200 1186100 1186000 1185900

Table A1: Results of the uniaxial compressive strength test and the tensile strength test.

Drilling	Uniaxial Compressive Strength			Tensile Strength	
	Depth	UCS [MPa]	E-Modul	Depth	Tensile Strength [Mpa]
A1	4.45	40.64	13.01	2.70	13.64
	10.00	86.71	12.99	6.50	16.43
	11.60	85.71	20.78	13.70	8.58
	19.30	41.10	9.35	16.00	6.95
	27.00	65.76	13.82	21.30	9.86
	29.60	62.93	17.51	30.30	8.23
A2	8.85	94.37	12.35	7.90	10.64
	10.00	42.77	20.43	13.00	17.51
	13.15	95.86	26.82	14.40	10.43
	15.30	47.51	9.58	16.00	4.76
	23.30	132.00	23.53	19.45	14.18
	27.80	86.00	10.85	27.05	13.15
B1	9.25	37.79	8.94	4.40	5.58
	13.45	75.16	15.82	15.10	10.50
	23.10	10.19	0.88	30.90	4.06
	32.50	56.27	14.32	33.50	9.22
	39.15	91.88	17.42	45.50	14.10
	46.85	120.30	17.12	48.60	4.92
B2	12.50	43.24	6.55	12.50	12.00
	23.20	76.54	7.86	23.20	7.73
	33.70	62.96	10.17	33.70	14.47
	38.50	39.01	8.16	38.50	8.56

Table A2: Results of the grain size analysis and the Atterberg limits analysis.

Samples Drillings												
Drilling	**Depth [m]**	**DIN EN ISO 14688-1 (2020)**	**DIN 4022**	**Gravel [%]**	**Sand [%]**	**Silt [%]**	**Clay [%]**	**Plastic Limit [%]**	**Liquid Limit [%]**	**Plasticity Index [%]**	**USCS (ASTM D 2487-17e1 2017)**	**DIN EN ISO 14688-2 (2020)**
A1	19.50	sagrSi	U, g*, s	32	21	47	-	26	53	27	SC	ClH
	21.45	sagrSi	U, g, s'	19	14	67	-	20	31	11	CL	ClL
	25.30	sagrSi	U, g, s'	15	12	73	-	21	32	11	CL	ClL
	26.00	sasiGr	G, u*, s	48	15	37	-	27	45	18	GM	GU*/SiM
A2	3.40	sagrSi	U, g*, s	33	19	48	-	31	49	18	SM	SIM
B1	2.30	saSi	U, s	2	17	81	-	72	106	34	MH	SiV
	5.25	saSi	U, s	0	7	93	-	56	77	21	MH	SiV
B2	4.00	saclSi	U, t, s	0	27	44	29	40	60	20	MH	SiH
	4.90	clsaSi	U, s, t	0	28	45	27	44	62	18	MH	SiH
	7.15	sasiCl	T, u, s	0	15	39	46	43	63	20	MH	SiH

Samples Trenches											
Sample	**DIN EN ISO 14688-1 (2020)**	**DIN 4022**	**Gravel [%]**	**Sand [%]**	**Silt [%]**	**Clay [%]**	**Plastic Limit [%]**	**Liquid Limit [%]**	**Plasticity Index [%]**	**USCS (ASTM D 2487-17e1 2017)**	**DIN EN ISO 14688-2 (2020)**
Test_03	clsaSi	U, s', t'	3.8	13.7	75.5	7.0	62	89	27	MH	SiV
Test_05	clsagrSi	U, g, s', t'	31.4	13.6	41.5	13.5	37	51	14	MH	SiH
Test_08	grsaclSi	U, t, s', g'	5.2	14.8	60.0	20.0	50	75	25	MH	SiV
Test_10	grsaclSi	U, t, s, g'	7.8	15.5	49.5	27.2	47	70	23	MH	SiH/SiV
Test_13	saclSi	U, t, s'	2.5	10.5	63.3	23.7	46	73	27	MH	SiV
Low_01	clgrsaSi	U, s, g', t'	13.8	22.2	57.3	6.7	55	72	17	MH	SiV
Low_03	grsaclSi	U, t*, s, g'	6.0	16.0	40.0	38.0	45	66	21	MH	SiH
Up_01	clgrsaSi	U, s, g, t	18.4	18.6	47.0	16.0	30	54	24	MH	SiH
Up_02	saclsiGr	G, u, t, s'	3.73	8.8	28.2	25.7	35	53	18	MH	SiH
Up_03	clgrsaSi	U, s, g, t'	17.0	20.0	57.5	5.5	44	59	15	MH	SiH
Up_04	sasiCl	T, u*, s'	1.7	12.3	40.0	46.0	41	70	29	MH	SiH/SiV
Up_05	saSi	U, s	4.1	17.9	75.0	3.0	93	116	23	MH	SiV
Up_06	sasiCl	T, u*, s'	1.7	14.3	40.5	43.5	61	81	20	MH	SiV
Up_07	saSi	U, s	0.0	16.0	81.3	2.7	146	164	18	MH	SiV

Table A3: Sample conditions and results of the direct shear test.

Samples Drilling B2														
Sampling Depth [m]	Shear parameters		Water content [%]						Density [g/m³]					
			Stress level 1 (40.3 kPa)		Stress level 2 (80.4 kPa)		Stress level 3 (160.5 kPa)		Stress level 1 (40.3 kPa)		Stress level 2 (80.4 kPa)		Stress level 3 (160.5 kPa)	
	Friction angle φ [°]	Cohesion c [kPa]	Before	After	Before	After	Before	After	Before	After	Before	After	Before	After
4.00	31.3	37.7	40.39	40.60	39.14	41.65	37.53	38.75	1.855	1.869	1.811	1.842	1.824	1.874
4.90	36.0	30.0	40.42	43.27	38.56	38.33	38.28	36.87	1.783	1.808	1.878	1.870	1.889	1.898
7.15	35.0	35.0	55.05	55.95	53.97	53.75	53.56	55.48	1.707	1.703	1.731	1.730	1.680	1.689

Samples Trenches														
Sample	Shear parameters		Water content [%]						Density [g/m³]					
			Stress level 1 (40.3 kPa)		Stress level 2 (80.4 kPa)		Stress level 3 (160.5 kPa)		Stress level 1 (40.3 kPa)		Stress level 2 (80.4 kPa)		Stress level 3 (160.5 kPa)	
	Friction angle φ [°]	Cohesion c [kPa]	Before	After	Before	After	Before	After	Before	After	Before	After	Before	After
Test_03	28.6	41.7	37.19	37.64	36.08	38.12	36.41	37.86	1.704	1.755	1.707	1.750	1.701	1.749
Test_05	33.1	20.1	27.46	2925	23.13	26.87	24.89	22.61	1.744	1.789	1.725	1.776	1.802	1.894
Test_08	26.9	19.9	35.02	37.65	33.67	37.19	34.81	36.16	1.588	1.645	1.601	1.658	1.650	1.725
Test_10	34.6	13.0	34.88	37.12	35.70	36.30	35.32	35.13	1.597	1.663	1.613	1.680	1.614	1.680
Test_13	30.0	11.0	36.18	39.85	38.01	39.92	39.81	40.00	1.555	1.627	1.534	1.598	1.481	1.576
Low_01	37.3	19.6	46.60	46.78	44.63	50.60	38.49	43.57	1.701	1.715	1.612	1.612	1.639	1.679
Low_03	30.6	18.4	54.26	54.45	57.46	59.43	55.14	54.19	1.642	1.684	1.575	1.627	1.593	1.621
Up_01	29.7	36.0	35.99	42.15	35.84	39.70	33.60	36.89	1.694	1.777	1.744	1.813	1.776	1.864
Up_03	39.0	3.2	42.58	48.54	42.19	47.72	43.96	48.71	1.701	1.771	1.697	1.772	1.581	1.722
Up_04	39.4	12.9	38.31	46.53	38.51	47.17	42.53	46.87	1.698	1.761	1.671	1.756	1.627	1.735
Up_05	38.4	4.4	82.18	103.25	89.48	101.78	72.02	94.56	1.249	1.356	1.237	1.334	1.264	1.411
Up_06	32.1	17.8	57.50	66.26	57.13	64.02	54.74	60.87	1.490	1.570	1.540	1.638	1.537	1.620
Up_07	31.3	17.5	109.04	136.05	119.39	145.26	112.15	147.23	1.169	1.298	1.077	1.262	1.057	1.267

Table A4: Results of the thin section analysis.

Mineral	Surface Samples										
	D-01	D-02	D-03	D-04	D-05	D-06	D-07	D-08.1	D-08.2	D-09	D-10
Olivine	x	x	x	x	x	x	x	x	x	x	x
Serpentine	x	x	x	x	x	x	x	x	x	x	x
Pyroxene	-	x	x	x	x	-	x	x	x	x	x
Amphibole	-	-	x	-	x	-	x	-	x	x	-
Chlorite	x	x	x	x	x	x	x	x	x	x	x
opaque phase	x	x	x	x	x	x	x	x	x	x	x
Quartz	-	-	-	-	-	-	x	-	-	-	-
Goethite	x	-	-	x	x	x	-	-	-	x	-

Table A5: Results of the XRD analysis.

	Surface Samples							
Mineral	**L-01**	**L-02**	**L-03**	**L-04**	**L-05**	**L-06**	**L-07**	**L-08**
Chlorite	x	x	x	x	x	x	x	x
Amphibole (tremolite)	x	x	x	x	x	x	x	x
Serpentine (lizardite)	x	x	x	x		x		x
Gibbsite	x					x		
Magnetite						x		
Quartz	x	x	x	x	x	x	x	x
Goethite	x	x	x	x	x	x		x
Hematite	x	x	x	x	x	x	x	x
Olivine (forsterite)								x
Clay minerals (nontronite)							x	

	Trench Samples									
Mineral	**Test_03**	**Test_08**	**Test_13**	**Low_01**	**Low_02**	**Low_03**	**Up_01**	**Up_03**	**Up_05**	**Up_07**
Chlorite	37.9	26.5	42.5	4.3	5.1	4.5	-	8.8	-	-
Amphibole	-	-	-	27.5	22.6	4.9	32.5	12.3	22.7	-
Serpentine	-	-	-	-	-	26.0	-	-	50.4	-
Quartz	-	-	-	-	-	-	1.9	12.4	16.5	27.8
Goethite	57.3	56.5	52.9	53.9	48.7	23.0	-	66.5	-	-
Hematite	4.8	17.0	4.7	-	-	-	-	-	-	-
Clay Minerals	-	-	-	-	-	7.6	-	-	10.4	-
Feldspar	-	-	-	14.2	22.1	34.0	-	-	-	31.3
Spinel	-	-	-	-	1.4	-	-	-	-	-
Cordierite	-	-	-	-	-	-	-	-	-	40.9
Talc	-	-	-	-	-	-	65.6	-	-	-